Plasma-catalytic processes with copper manganese oxide catalysts for the abatement of volatile organic compounds

Plasmakatalytische processen met koper-mangaanoxidekatalysatoren voor de afbraak van vluchtige organische stoffen

Zhiping Ye

Promotors: Prof. dr. R. Morent, Prof. dr. J.-F. Lamonier, Dr. J.-M. Giraudon
Proefschrift ingediend tot het behalen van de graad van Doctor in de Ingenieurswetenschappen: Toegepaste Natuurkunde

Vakgroep Toegepaste Fysica
Voorzitter: Prof. dr. ir. C. Leys
Faculteit Ingenieurswetenschappen en Architectuur
Academiejaar 2017-2018

N° d'ordre : 42549

UNIVERSITE de LILLE – SCIENCES ET TECHNOLOGIES

ECOLE DOCTORALE SCIENCES DE LA MATIERE, DU RAYONNEMENT ET DE L'ENVIRONNEMENT

THÈSE

présentée par

Zhiping YE

pour l'obtention du

TITRE DE DOCTEUR EN CHIMIE ET CHIMIE PHYSIQUE

intitulée

PLASMA-CATALYTIC PROCESSES WITH COPPER MANGANESE OXIDE CATALYSTS FOR THE ABATEMENT OF VOLATILE ORGANIC COMPOUNDS

Soutenue le 18 Décembre 2017

Rapporteurs:	**Catherine BATIOT-DUPEYRAT**, Professeur, Université de Poitiers
	Jeriffa De CLERCQ, Professeur, Université de Gand
Examinateurs:	**Filip De TURCK**, Professeur, Université de Gand
	Anne GRIBOVAL-CONSTANT, Maître de Conférences, Université de Lille
	Nathalie De GEYTER, Professeur, Université de Gand
	Cuong PHAM-HUU, Directeur de Recherche, CNRS, Université de Strasbourg
Directeurs de thèse:	**Jean-François LAMONIER**, Professeur, Université de Lille
	Rino MORENT, Professeur, Université de Gand
Co-Encadrant de thèse:	**Jean-Marc GIRAUDON**, Maître de Conférences, Université de Lille
Invité:	**Stéphane SIFFERT**, Professeur, Université du Littoral Côte d'Opale

LEDEN VAN DE EXAMENCOMMISIE

Prof. Dr. Ir. Filip De Turck - Chair
Department of Information Technology
Faculty of Engineering and Architecture - Ghent University

Dr. Anne Griboval Constant – Co-Chair
Unite de Catalyse et Chimie du Solide
Universit éde Lille

Prof. Dr. Rino Morent – Promoter
Department of Applied Physics
Faculty of Engineering and Architecture - Ghent University

Prof. Dr. Jean-Fran çois Lamonier – Promoter
Unite de Catalyse et Chimie du Solide
Universit éde Lille

Dr. Jean-Marc Giraudon – Promoter
Unite de Catalyse et Chimie du Solide
Universit éde Lille

Prof. Dr. Catherine Batiot Dupeyrat
Institut de Chimie des Milieux et Mat ériaux de Poitiers
Universit éde Poitiers

Prof. Dr. Ir. Jeriffa De Clercq
Department of Materials, Textiles and Chemical Engineering
Faculty of Engineering and Architecture - Ghent University

Prof. Dr. Ir. Nathalie De Geyter
Department of Applied Physics
Faculty of Engineering and Architecture - Ghent University

Dr. Cuong Pham-Huu
Director of Research, CNRS
Institut de Chimie et Proc éd és pour l'Énergie, l'Environnement et la Sant é
Universit éde Strasbourg

UNIVERSITEIT GENT 200 JAAR
FACULTEIT INGENIEURSWETENSCHAPPEN EN ARCHITECTUUR

Universiteit Gent
Faculteit Ingenieurswetenschappen en Architectuur
Vakgroep Toegepaste Fysica EA17
Onderzoeksgroep Plasmatechnologie

Sint–Pietersnieuwstraat 41, B–9000 Gent

This research was supported by a grant from “Region Nord pas de Calais”.

This research was supported by a grant from “Interreg”.

This research was supported by a grant from “GoTtoS3”.

This research was supported by a grant from “Union Européenne Europese Unie”.

Summary

Semiconductor, power, chemical industries, etc. use volatile organic compounds (VOC) as solvents, thinners, liquid fuels, cleaning agents, etc. So the process waste air is frequently contaminated with VOCs. Release of VOC laden air into the environment represents a relevant contribution to air pollution. This causes the formation of tropospheric ozone and photochemical smog, enhancing the greenhouse effect and the destruction of the stratospheric ozone layer. Moreover, most of them are toxic and/or carcinogenic. Due to the ever more stringent global national legislation there is urgent need of adequate techniques for a radical reduction of VOC emissions. The conventional methods for the removal of VOCs in flue gases like thermal oxidation, catalytic oxidation and biological oxidation are linked with high energy costs, especially for large volume flows with low levels of VOCs.

Non-thermal plasma techniques (NTPs) offer interesting perspectives for the removal of low concentrations of pollutants in air at high flow rates. They are quite different from thermal plasmas such as those generated by plasma torches and arc discharges. In a non-thermal plasma most of the input electrical energy is added selectively to the plasma electrons, so preventing feed gas heating. Electron-impact dissociation and ionization of the background gas cause radical production and the formed reactive species decompose the targeted VOCs. Non-thermal plasma techniques allow the treatment of mixed waste streams.

Although NTP technology for air cleaning was often proposed in literature, undesired by–product formation hinder industrial applications. Therefore, the combination of NTP and heterogeneous catalysis is studied and is called plasma–catalysis. In a plasma–catalytic system, the catalyst can be located inside the discharge region (in-plasma catalysis – IPC) or downstream of the plasma reactor (post-plasma catalysis – PPC). In this work, both types of reactors are studied.

This PhD thesis first gives an overview of the literature to summarize our present state of knowledge using MnOx based catalysts for toluene abatement in PPC configuration. The context of this study is briefly sum-up. After briefly screening the main depollution methods, the principles of PPC are exposed based on the coupling of two mature technologies such as NTP and catalysis. In that respect the presentation of the abundant manganese oxides will be firstly given.

Then in a second step the main features of MnO_x allowing better performances in the reactions expected to occur in the abatement of toluene in PPC process are reviewed including ozone decomposition, toluene ozonation, CO oxidation and toluene total oxidation. Finally the current status of the applications of PPC using MnOx on toluene abatement are discussed. In a first step, the selected variables of the hybrid process related to the experimental conditions of toluene abatement in air are identified. The selected variables are those expected to play a role in the performances of the two-stage plasma-catalyst system towards toluene abatement. The descriptors correlated to the performances of the hybrid process in terms of efficiency are also presented. In a second step the effects of the variables on the experimental outcomes (descriptors) are discussed.

In a first experimental chapter, the decomposition of toluene using a packed bed DBD reactor has been systematically studied in air streams with different relative humidity. Optical emission spectroscopy (OES) showed that with increasing humidity, less N_2 excited states are present in the discharge, which can be attributed to the increased quenching of these states due to collisions with water molecules before they undergo spontaneous emission to a lower excited state. Unfortunately, it was not able to derive any conclusions on the effect of RH on the amount of excited oxygen atoms as well as excited OH radicals since no corresponding emission peaks have been observed. OES was however able to determine the nitrogen rotational temperature which was found to be equal to 450 ± 50 K for the highest discharge power used in this work (5.0 W). At the same time, under these conditions, the DBD reactor wall temperature was found to be 323 ± 3 K, which is significantly lower than the nitrogen rotational temperature due to the fact that this rotational temperature is an overestimation of the bulk gas temperature as it only gives an indication of the temperature in the core of the microdischarges. It was also observed that nor the nitrogen rotational temperature nor the reactor wall temperature was influenced by the RH of the gas stream. After characterizing the discharge itself, toluene decomposition experiments were also performed thereby limiting the discharge power to 5.0 W andhigher discharge powers were found to result in the formation of the unwanted by-product NO_2. It was observed that the highest toluene removal efficiency was observed at a RH of 40% most likely due to the fact that the OH radical amount in the plasma is the highest under these experimental conditions. In addition, all gaseous products in the plasma reactor outlet have been identified and the main products of the toluene decomposition process were found to be CO_2, CO, N_2O, O_3 (both dry and humid air) and HCOOH (dry air only). Increasing the RH of the air stream was found to completely suppress the formation of formic acid while the formation of ozone was also found to decrease. In contrast, the CO selectivity was found to increase

with RH, while the CO_2 selectivity was unaffected by the addition of water to the air stream. The highest N_2O concentration was observed at a RH of 40%: this observation in combination with the observed relatively high amounts of CO_2, CO and O_3 molecules in the gas outlet at a RH of 40% confirm the observed highest removal efficiency at this experimental condition. It can thus be concluded that toluene decomposition in the examined packed bed DBD reactor is the most efficient at a RH of 40%.

In a next chapter, Cu-Mn oxide catalysts were synthesized by two different routes: conventional and redox co-precipitation. Catalysts $CuMn_2O_4$-P4, CuOx-P4 and MnOx-P4 were prepared as references for conventional co-precipitation, while CuMnOx-R3, CuMnOx-R2 and MnOx-R3 were used to evaluate the calcination temperature (200 or 300 ℃) and Cu ions effect in the redox method. In addition, the performances of Cu-Mn oxides synthetized by the redox method, calcined at 300 ℃ and doped with noble metal (Pt and Pd) were also evaluated. Four important conclusions were made from this work: (1) Regardless of the synthesis route, the CuMnOx catalysts outperformed the reference single oxides in total toluene oxidation. Moreover, the CuMnOx-R2 catalyst outclassed the Purelyst MD101 commercial catalyst over time on stream. (2) The dispersed copper manganese oxides resulting from the redox-precipitation route exhibit a much higher activity as compared to the one of the spinel $CuMn_2O_4$-P4 oxide prepared by conventional co-precipitation. This superior performance of the redox derived Cu-Mn materials was attributed to improved textural properties such as high specific surface areas, amorphous state and structural disorder (presence of oxygen vacancies). (3) Catalytic experiments performed in a free oxygen atmosphere showed that surface adsorbed oxygen (O_{ads}) and subsurface oxygen played a role in the activity of the catalyst. (4) ToF-SIMS analysis after the catalytic test allowed to detect metal (M = Mn,Cu) organic secondary ions indicating a strong adsorption of partial oxidation/decomposition products of toluene on active sites which induce catalyst partial deactivation.

In the final experimental chapter, trichloroethylene (TCE) abatement was investigated in moist air with NTP using a 10-pin-to-plate negative DC corona discharge and with PPC using Cu-Mn mixed oxides as catalysts. In comparison to the total catalytic oxidation and NTP process, PPC was found to be the best process to convert TCE into CO_2 with a catalyst temperature of 150 ℃. A remarkable increase of CO_2 yield has been observed and explained by the facile oxidation of polychlorinated by-products (adsorbed at the surface) by oxygen active species coming from the O_3 decomposition. Copper manganese oxide prepared by redox-precipitation method (CuMnOx-R3) showed higher TCE conversion into CO_2. However the performance of the catalyst deteriorated by

continuous usage due to chlorine poisoning. The catalyst prepared by conventional co-precipitation method ($CuMn_2O_4$-P4) showed better stability in the PPC process for TCE abatement.

Samenvatting

Onder andere de chemische, halfgeleider-en energie-industrie gebruiken vluchtige organische stoffen (VOS) als solventen, verdunners, brandstoffen, reinigingsmiddelen, etc. Hierdoor is de afvallucht van deze industrieën frequent gecontamineerd met VOS. Het vrijkomen van deze afvallucht in het milieu vertegenwoordigt een relevante bijdrage aan de luchtvervuiling. Dit veroorzaakt de vorming van troposferische ozon en fotochemische smog, wat het broeikaseffect en de vernietiging van de stratosferische ozonlaag versterkt. Verder zijn de meeste VOS toxisch en/of kankerverwekkend. Door de strengere wetgeving is er een dringende behoefte aan adequate technieken voor een radicale reductie van VOS-uitstoot. De conventionele technieken voor de verwijdering van VOS in afvalgassen, zoals thermische oxidatie, katalytische naverbranding en biologische oxidatie, hebben een hoge kost, zeker voor grote volumes met lage hoeveelheden VOS. Thermische oxidatie vereist een verwarming van het gas tot ongeveer 1000 K. Door het gebruik van een geschikte katalysator, is slechts één derde nodig van de energie in vergelijking met thermische oxidatie, omdat VOS oxidatie dan gebeurt bij temperaturen rond 500 K.

Niet-thermische plasmatechnieken bieden goede perspectieven voor de verwijdering van lage concentraties van verontreinigende stoffen in lucht bij hoge gassnelheden. Niet-thermische plasma's (NTP's) zijn verschillend van thermische plasma's zoals deze gegenereerd door plasmatoortsen en vlambogen. In NTP's wordt het meeste van de geleverde elektrische energie selectief aan de plasma-elektronen gegeven, wat de opwarming van het volledige verontreinigde gas voorkomt. De dissociatie en ionisatie van het gas door de impact van de elektronen veroorzaakt de productie van radicalen en de gevormde reactieve deeltjes zorgen voor ontbinding van de VOS. Niet-thermische plasmatechnieken laten de behandeling van gemengde afvalstromen toe.

NTP technologie voor luchtreiniging is vaak voorgesteld in literatuur, maar de vorming van ongewenste bijproducten verhindert industriële toepassingen. Daarom wordt de combinatie van NTP's met heterogene katalyse bestudeerd. Dit noemt men plasmakatalyse. In een plasmakatalytisch systeem kan de katalysator gelokaliseerd worden in de ontladingsregio (in-plasma katalyse - IPC) of nadat het gas de plasma reactor is gepasseerd (post-plasma katalyse - PPC). In dit werk worden beide types van reactors bestudeerd.

Deze PhD thesis geeft eerst een overzicht van de literatuur om de huidige kennis omtrent MnOx gebaseerde katalysatoren voor tolueenafbraak in PPC

samen te vatten. Na een korte screening van de belangrijkste afbraaktechnieken worden de principes van PPC beschreven gebaseerd op de koppeling van twee mature technieken zoals NTP en katalyse zijn. Eerst wordt een overzicht gegeven van de mangaanoxides. In een tweede stap worden de hoofdkenmerken gegeven van MnOx die een betere performantie toelaten tijdens de reacties, reacties waarvan we verwachten dat ze optreden tijdens de afbraak van tolueen in PPC processen zoals ozonafbraak, tolueen ozonizatie, CO oxidatie en totale tolueenoxidatie. Tot slot wordt de huidige toestand van de toepassingen van PPC met MnOx in het geval van tolueenafbraak beschreven. Eerst worden de verschillende experimentele parameters van het hybride 2-stapsproces plasma-katalyse van tolueenafbraak in lucht geïdentificeerd. Ook worden de begrippen geïntroduceerd die de efficiëntie van het proces beschrijven. In een tweede stap worden de effecten van de parameters op de experimentele resultaten becommentarieerd.

In het eerste experimentele hoofdstuk wordt de decompositie van tolueen door een packed-bed dielektrische barrière ontlading systematisch bestudeerd in luchtstromen met verschillende relatieve vochtigheid (RV). Optische emissie spectroscopie (OES) toonde aan dat er minder geëxciteerde N_2-toestanden aanwezig waren in de ontlading bij een stijgende vochtigheid, wat kan toegeschreven worden aan de verhoogde quenching van deze toestanden door interacties met watermoleculen voordat ze spontane emissie ondergaan naar lager geëxciteerde toestanden. Het was echter niet mogelijk om conclusies te trekken over het effect van de RV op de hoeveelheid van geëxciteerde zuurstofatomen en OH-radicalen aangezien er geen corresponderende emissiepieken werden waargenomen. Met OES was het echter wel mogelijk om de rotationele temperatuur van stikstof te bepalen. Voor het hoogste ontladingsvermogen (5.0 W) was deze temperatuur gelijk aan 450 ± 50 K. Onder deze condities was de temperatuur van de reactorwand gelijk aan 323 ± 3 K, wat significant lager is dan de rotationele temperatuur van stikstof omdat deze rotationele temperatuur een overschatting is van de temperatuur van het bulkgas aangezien deze temperatuur een indicatie is van de temperatuur in de kern van de micro-ontladingen. Verder werd er geobserveerd dat de RV van de gasstroom geen invloed had op de rotationele temperatuur van stikstof en de temperatuur van de reactorwand. Na de karakterisering van de ontlading zelf, werden experimenten naar de decompositie van tolueen uitgevoerd. Hierbij werd het ontladingsvermogen gelimiteerd tot 5.0 W omdat het ongewenste bijproduct NO_2 werd gevormd bij hogere vermogens. De hoogste verwijderingefficiëntie van tolueen werd geobserveerd bij een RV van 40%, wat hoogstwaarschijnlijk wordt veroorzaakt doordat de hoeveelheid van OH-radicalen in het plasma het hoogste is voor deze experimentele condities. Daarnaast zijn alle gasvormige producten

in de plasma reactor uitlaat geïdentificeerd. De hoofdproducten van het decompositieproces van tolueen waren CO_2, CO, N_2O, O_3 (bij zowel droge als vochtige lucht) en HCOOH (alleen bij droge lucht). Het verhogen van de RV van de luchtstroom onderdrukte volledig de vorming van HCOOH en ook de vorming van ozon daalde, terwijl de CO selectiviteit steeg met een verhoogde RV. De CO_2 selectiviteit werd niet beïnvloed door de toevoeging van water aan de luchtstroom. De hoogste N_2O concentratie werd geobserveerd bij een RV van 40%: deze observatie in combinatie met de relatief hoge hoeveelheid van CO_2, CO en O_3 molecules in de gasuitlaat bij een RV van 40% bevestigde dat de hoogste verwijderingefficiëntie werd bekomen bij deze experimentele conditie. Het kan dus geconcludeerd worden dat de decompositie van tolueen het meest efficiente is bij een RV van 40% in de onderzochte packed-bed dielektrische barrière ontlading.

In het volgende hoofdstuk wordt de synthese van Cu-MnOx-katalysatoren via twee verschillende syntheseroutes aangepakt: conventionele en de redox co-precipitatie. De katalysatoren $CuMn_2O_4$-P4, CuOx-P4 en MnOx-P4 werden gesynthetiseerd als referenties voor de conventionele co-precipitatie methode, terwijl CuMnOx-R3, CuMnOx-R2 en MnOx-R3 werden gebruikt om de calcinatie temperatuur (200 of 300 °C) en het Cu-ionen effect te evalueren in de redox methode. Verder werden de prestaties van CuMnOx katalysatoren gesynthetiseerd via de redoxmethode, gecalcineerd bij 300 °C en gedopeerd met edelmetalen (Pd, Pt) geëvalueerd. Er werden vier belangrijke conclusies gemaakt in dit werk: (1) De CuMnOx katalysatoren overtroffen de katalysatoren gebruikt als referentie in de volledige oxidatie van tolueen, ongeacht de syntheseroute. Verder overklaste de CuMnOx-R2 katalysator de commercieel verkrijgbare katalysator Purelyst MD 101 op het gebied van gebruikstijd in de stroom. (2) De verspreide CuMnOx verkregen door de redox-precipitatie route hebben een veel hogere activiteit dan de spinel $CuMn_2O_4$-P4 oxide verkregen door conventionele co-precipitatie met TMAH als neerslagmiddel. Deze superieure resultaten van de Cu-Mn materialen gesynthetiseerd met de redoxmethode kunnen toegeschreven worden aan verbeterde texturele eigenschappen zoals grote specifieke oppervlakte, de amorfe toestand en structurele wanorde (aanwezigheid van zuurstofvacatures). (3) Katalytische experimenten in een vrije zuurstof atmosfeer toonden aan dat oppervlaktegeadsorbeerde zuurstof (O_{ads}) en suboppervlakkige zuurstof een rol spelen in de activiteit van de katalysator. (4) ToF-SIMS analyse na de katalytische test laten het toe om metaal(M = Mn, Cu)-organische secundaire ionen te detecteren, wat wijst op een sterke adsorptie van partiële oxidatie/decompositieproducten van tolueen op actieve sites die partiële deactivatie van de katalysator induceren.

In het laatste experimentele hoofdstuk wordt de afbraak van trichloroethyleen (TCE) onderzocht in vochtige lucht met NTP, waarbij gebruikt wordt gemaakt van een pin-tot-plaat negatieve DC corona ontlading en van PPC met Cu-Mn gemengde oxiden als katalysatoren. In vergelijking met de totale katalytische oxidatie en het NTP proces, was PPC met een katalysetemperatuur van 150 ℃ het beste proces om TCE om te zetten in CO_2. Een opmerkelijke stijging van CO_2-opbrengst werd geobserveerd en verklaard door de gemakkelijke oxidatie van polygechloreerde bijproducten (geadsorbeerd op het oppervlak) door actieve zuurstofdeeltjes afkomstig van de decompositie van O_3. CuMnOx verkregen door de redox-precipitatie methode (CuMnOx-R3) vertoonde hogere een hogere conversie van TCE in CO_2. De prestatie van de katalysator verslechterde echter door continu gebruik door chloorvervuiling. De katalysator verkregen door de conventionele coprecipitatie methode ($CuMn_2O_4$-P4) vertoonde een betere stabiliteit (oppervlakteverrijking van Mn minder uitgesproken) in het PPC proces voor het terugdringen van TCE in vochtige lucht.

Résumé

Les industries chimiques, de l'énergie, des semi-conducteurs, etc. utilisent des composés organiques volatils (COV) comme solvants, diluants, combustibles liquides, agents nettoyants, etc. Ainsi les effluents gazeux issus de ces procédés industriels sont souvent contaminés par des COV. Ces rejets dans l'environnement contribuent notablement à la pollution de l'air. Les COV concourent à la formation d'ozone troposphérique et de smog photochimique, à l'augmentation de l'effet de serre et à la destruction de la couche d'ozone stratosphérique. De plus, la plupart des COV sont toxiques et /ou cancérigènes. En raison de législations nationales toujours plus strictes, il y a un besoin urgent de techniques adéquates pour une réduction efficace des émissions de COV dans l'atmosphère. Les méthodes conventionnelles d'élimination des COV comme l'oxydation thermique, l'oxydation catalytique et l'oxydation biologique présentent des coûts énergétiques relativement élevés, en particulier pour les débits importants d'effluents gazeux contenant de faibles quantités de COV. L'oxydation thermique nécessite le chauffage du gaz à environ 1000 K. En utilisant un catalyseur, on estime qu'un tiers de l'énergie est nécessaire en comparaison de l'oxydation thermique, puisque l'oxydation des COV peut se faire vers 500 K.

Les techniques de traitement par plasma non thermique (NTP) offrent d'intéressantes perspectives pour l'élimination de faibles concentrations de polluants dans l'air à des débits élevés. Ces techniques sont très différentes de celles par plasmas thermiques tels que ceux générés par des torches à plasma et des décharges d'arc. Dans un plasma non thermique, la majeure partie de l'énergie électrique introduite est fournie sélectivement aux électrons du plasma, évitant ainsi le chauffage des gaz. La dissociation par impact électronique et l'ionisation du gaz de fond provoquent la production de radicaux et les espèces réactives formées décomposent les COV ciblés. Les techniques de plasma non thermique permettent le traitement d'un mélange gazeux de différents COV.

La technologie NTP est souvent proposée pour le traitement de l'air, cependant la formation indésirable de sous-produits entrave les applications industrielles d'un tel procédé. Par conséquent, la combinaison d'un plasma non thermique avec la catalyse hétérogène est étudiée et se nomme plasma-catalyse. Dans un système plasma-catalyse, le catalyseur peut être situé à l'intérieur de la zone de décharge (Catalyse in-plasma : IPC) ou en aval du réacteur à plasma (Catalyse post-plasma : PPC). Dans ce travail, les deux types de réacteurs ont été étudiés.

Cette thèse de doctorat donne d'abord un aperçu de la littérature pour résumer l'état actuel des connaissances concernant l'utilisation de catalyseurs d'oxydes de manganèse (MnOx) pour l'élimination du toluène en configuration PPC. Le contexte de cette étude est brièvement résumé. Après un bref examen des principales méthodes de dépollution, les principes de la catalyse post-plasma sont donnés sur la base du couplage de deux technologies matures que sont le plasma non thermique et la catalyse. A cet égard, la présentation des différents types d'oxydes de manganèse est tout d'abord exposée. Les principales caractéristiques des MnOx permettant les meilleures performances dans les réactions attendues dans l'élimination du toluène dans le procédé PPC sont ensuite examinées, et concernent la décomposition de l'ozone, l'ozonation du toluène, l'oxydation du CO et l'oxydation totale du toluène. Enfin, dans une dernière partie, l'état actuel des applications de la catalyse post-plasma qui utilisent MnOx pour l'élimination du toluène est discuté. Dans une première étape, les variables du procédé hybride en lien avec les conditions expérimentales pour l'élimination du toluène dans l'air ont été identifiées. Les variables sélectionnées sont celles qui devraient jouer un rôle dans les performances du système plasma-catalyse en deux étapes pour l'élimination du toluène. Les descripteurs corrélés aux performances du procédé hybride en termes d'efficacité sont également présentés. Dans une deuxième étape, les effets des variables sur les résultats expérimentaux (descripteurs) sont discutés.

Dans le premier chapitre expérimental, la décomposition du toluène a été étudiée à l'aide d'un réacteur DBD comprenant un lit de garnissage sous flux d'air ayant des humidités relatives différentes. La spectroscopie d'émission optique (SEO) a montré que l'augmentation de l'humidité conduisait à moins d'états N_2 excités dans la décharge, ce qui peut être attribué à une extinction accrue de ces états due aux collisions avec les molécules d'eau avant qu'ils ne subissent une émission spontanée à un état excité inférieur. Malheureusement, il n'a pas été possible de tirer de conclusions de l'effet de l'humidité relative sur la quantité d'atomes d'oxygène excités ainsi que sur les radicaux OH excités car aucun pic d'émission correspondante n'a été observé. La SEO a cependant permis de déterminer la température de rotation de l'azote à 450 ± 50 K pour la puissance de décharge la plus élevée utilisée dans ce travail (5 W). Dans ces mêmes conditions expérimentales, la température de la paroi du réacteur DBD était de 323 ± 3 K, valeur significativement inférieure à la température de rotation de l'azote du fait que cette température de rotation est une surestimation de la température du gaz qui donne seulement une indication de la température au sein des micro-décharges. Il a été également observé que ni la température de rotation de l'azote ni celle de la paroi du réacteur n'étaient influencées par l'humidité relative du flux gazeux. Après la caractérisation de la décharge elle-

même, des expériences de décomposition du toluène ont également été réalisées, en limitant la puissance de décharge à 5,0 W car des puissances de décharge plus élevées entraînaient la formation du sous-produit indésirable NO_2. La plus grande efficacité d'élimination du toluène a été observée pour une humidité relative de 40%, probablement en raison du fait que la quantité de radicaux OH dans le plasma était la plus grande dans ces conditions expérimentales. De plus, tous les produits gazeux en sortie de réacteur ont été identifiés et les principaux produits du procédé de décomposition du toluène ont été CO_2, CO, N_2O, O_3 (air sec et humide) et HCOOH. L'augmentation de l'humidité relative dans l'air supprime totalement la formation d'acide formique et diminue la formation d'ozone. En revanche, la sélectivité en CO augmente avec l'humidité relative, tandis que celle en CO_2 n'est pas affectée. La plus forte concentration de N_2O a été observée avec une humidité relative de 40% : cette observation combinée aux quantités relativement élevées observées pour le CO_2, le CO et l'O_3 en sortie de réacteur pour une humidité relative également de 40% confirment la plus grande efficacité d'élimination du toluène dans ces conditions expérimentales. Ainsi la décomposition du toluène dans le réacteur DBD comprenant un lit de garnissage est la plus efficace pour un taux d'humidité relative dans l'air de 40%.

Dans le chapitre suivant, des oxydes simples et mixtes de Cu et de Mn ont été synthétisés par deux voies différentes: les co-précipitations conventionnelles et redox. Les catalyseurs $CuMn_2O_4$-P4, CuOx-P4 et MnOx-P4 ont été préparés comme référence par co-précipitation conventionnelle, tandis que les matériaux $CuMnO_x$-R3, $CuMnO_x$-R2 et MnO_x-R3 ont été synthétisés afin d'évaluer les effets de la température de calcination (200 or 300 °C) et des ions Cu dans la méthode redox. Les performances des oxydes mixtes de Cu et de Mn préparés par la méthode redox, calcinés à 300 °C et dopés par des métaux nobles (Pd, Pt) ont également été évaluées. Quatre conclusions importantes ont pu être tirées de ce travail : (1) indépendamment de la voie de synthèse, les performances des catalyseurs CuMnOx ont surpassé celles des oxydes simples dans l'oxydation totale du toluène. De plus, le catalyseur CuMnOx-R2 a surclassé le catalyseur commercial Purelyst MD101 lors d'un test longue durée ; (2) les oxydes mixtes de manganèse et de cuivre préparés par la méthode redox présentent une activité beaucoup plus élevée que celle des oxydes mixtes obtenus par co-précipitation conventionnelle. Cette performance accrue des matériaux Cu-Mn dérivés de la méthode redox a été attribuée à des propriétés texturales améliorées telles que des surfaces spécifiques élevées, un état amorphe et un désordre structural (présence de lacunes d'oxygène) ; (3) des expériences catalytiques réalisées sous atmosphère gazeuse sans oxygène ont montré que l'oxygène adsorbé en surface (O_{ads}) et l'oxygène sous la surface joue un rôle dans l'activité du catalyseur ; (4) l'analyse ToF-SIMS des matériaux après le test catalytique a permis de détecter

des ions secondaires organiques contenant des métaux M (M = Mn, Cu) indiquant une forte adsorption des produits d'oxydation et/ou de décomposition partielle du toluène sur des sites actifs induisant une désactivation partielle du catalyseur.

Dans le dernier chapitre expérimental, l'élimination du trichloroéthylène (TCE) a été étudiée dans de l'air humide sous plasma non thermique utilisant une décharge corona négative DC à 10 broches et en configuration PPC en utilisant des oxydes mixtes Cu-Mn comme catalyseurs. En comparaison de l'oxydation catalytique totale et au procédé NTP, le procédé PPC s'est avéré être le meilleur pour convertir le TCE en CO_2 avec une température de catalyseur de 150 °C. Une augmentation remarquable du rendement en CO_2 a été observée et expliquée par l'oxydation facile de sous-produits poly-chlorés (adsorbés en surface) par des espèces oxygénées issues de la décomposition de l'ozone. L'oxyde mixte de Mn et de Cu préparé par la méthode redox (CuMnOx-R3) a montré la meilleure conversion de TCE en CO_2. Cependant, la performance de ce catalyseur se détériore dans le temps suite à un empoisonnement au chlore. Le catalyseur préparé par la méthode de co-précipitation conventionnelle ($CuMn_2O_4$-P4) a montré une meilleure stabilité dans le processus PPC pour l'élimination du TCE.

Acknowledgements

There is an old saying: the bad news is time flies, the good news is you are the pilot. I have stayed in France/Belgium for almost 4 years. Comparing to me from 4 years ago, I'm so glad I have better understanding of my research filed, I have so many fantasy experiences and I become more confident and patient to do things. All of these are ascribed to the experiences with you all: my supervisors, my friends and my families.

First of all, I would like to express my sincere gratitude towards Prof. dr. R. Morent, Prof. dr. J.-F. Lamonier, Assistant Professor dr. J.–M. Giraudon for offering me overseas opportunity to study in Ghent University and Lille University of Science and Technology.

I would like to express my appreciation to Assistant Professor dr. J.–M. Giraudon, you are so wealthy of knowledge. You always can give me clear guidance and I always can learn knowledge after discussion with you. I appreciate your patient instructions and kind understanding. I also want to say thank you to Prof. dr. J.-F. Lamonier. I still remembered the first time I arrived at France. I appreciated you picked me up at the train station and helped me to find a comfortable room. There was tough time, thank you and Assistant Professor dr J.-M. Giraudon to support and believe in me. I want to thank you for all-time support and understanding.

I also would like to express my appreciation to Prof. dr. R. Morent. I still remembered you encouraged me to pursue my Ph.D studying when I hesitated at the beginning of my studying, and you always encouraged and supported me to attend inspirational and interesting symposiums or workshops. You took my reports seriously every time, and I can benefit from your comments on every occasion. I also want to express my appreciation to Prof. dr. N. De Geyter for all her kind support and guidance, especially with plasma experiments.

There is an old saying in China: even someone is your teacher for only a day, you should respect him like your father for the rest of your life. I will also remember all your instructions in heart and try my best to be a student who you may be proud of in the future. Once again, I'm grateful you all gave me this precious opportunity to learn what scientific research is and what the methodology and attitude towards my research field are. All of these will be the most valuable treasure for me.

Moreover, I would like to thank all my co-authors for the effort they put into my work. A special thanks goes to Dr. A. Nikiforov for OES analysis, O. Gardoll for the TPR analyses, Dr. P. Simon and M. Trentesaux for XPS analysis, L. Burylo for XRD measurements.

I also wish to thank friends in UCCS, T. Kane, Dr. Y. Boyjoo, G. Rochard, Dr. C. Carmen, Dr. D. Chlala, H. Malbieres, P. Peyravi, H. Siaka, Dr T. Li, J. Sha, S. Chen, B. Gu, Dr. X.-F. Yi, and those Chinese students studying in France. I will cherish the memory of working with you and having fun with you all. I enjoyed the time when I was hanging out with you all. Thanks to Tanu, Yash for the encouragements. At last, I will miss the tea time, the international meals, the BBQ, tours in France/Belgium and other unforgettable moments.

I would like to thank Dr. A. Vandenbroucke, S. KaliyaPerumalVeerapandian, T. Vandenbrande, S. Sultana, Dr. P. cools, Dr. G Aziz for helping me to adapt the research life in Ghent and teaching me new skills and knowledge. Thank to Arne teaching me to use the plasma setup, thanks to Savita helping me for the plasma experiments and thanks to Gaelle for the layout of dissertation. I'm so glad and honor to be with you all in the same research team at Ghent University.

At last but not least, I would like to say thank you to my fiancé Qi Yang. Thank you for your unlimited patience in 4-year long distance relationship, your love and care supported me to face the difficulty, and Thank you for coming into my life and giving me happiness. I also want to say thank you to my parents, my sister and my lovely nephew. You all always believe in me and support me without reserve.

All in all, I would like to say thank you all from the bottom of my heart. Time flies, but not memories.

List of Acronyms

AC
Activated carbon....31
AOS
Average oxidation state....21
BET
Brunauer–Emmett–Teller....21
BJH
Barrett-Joyner-Halenda....82
C
Capacitor....57
CNS
Central Nervous System....16
CP
Coprecipitation....16
D_p
Diameter of pore....45
DBD
Dielectric barrier discharge....7
DC
Direct current....34
DCAC
Dichloroacetylchloride....106
ED
Energy density....36
E-R model
Eley-Rideal model....22
EXAFS
Extended X-ray absorption fine structure....24
EY
Energy yield....7
FID
Flame Ionization Detector....84
FTIR
Fourier-transform infrared spectroscopy....48
GHSV
Gas hourly space velocitymer....29
HDTMABr
Hexadecyltrimethylammonium bromide....45
HCl
Hydrochloric acid....106

List of publications

A.1 International journal publications

1. **Z. Ye,** S. Kaliya Perumal Veerapandian, I, Onyschchenko, A, Nikiforov, N. De Geyter, J.-M. Giraudon, J.-F. Lamonier, R. Morent

An in-depth investigation of toluene decomposition with a glass beads packed bed DBD reactor

Industrial & Engineering Chemistry Research, 56 (37), pp 10215–10226, 2017

IF 2016: 2.8432.

2. **Z. Ye,** J.-M. Giraudon, N. Nuns, P. Simon, N. De Geyter, R. Morent, J.-F. Lamonier

Influence of the preparation method on the activity of copper-manganese oxides for toluene total oxidation

Applied Catalysis B: Environmental, (223), pp 154-166, 2018

IF 2016: 9.446

3. **Z. Ye,** J.-M. Giraudon, N. De Geyter, R. Morent, J.-F. Lamonier

The Design of MnOx Based Catalyst in Post-Plasma Catalysis Configuration for Toluene Abatement.

Catalysts, 8(2), 91

IF 2016: 3.0824.

4. S. Sultana, **Z. Ye**, S. Kaliya Perumal Veerapandian, A. Löfberg, N. De Geyter, R. Morent, J.-M. Giraudon, J.-F. Lamonier,

Synthesis and catalytic performances of K-OMS-2, Fe/K-OMS-2 and Fe-KOMS-2 in post plasma-catalysis for dilute TCE abatement

Catalysis today, in press, 2017

IF 2016: 4.636

C.4 Active conference participations

1. 15th FEA Research Symposium, Ghent University, Belgium. (2014)

"Poster presentation"

2. International Workshop on Plasmas for Energy and Environmental Application, Liverpool, UK. (2016)

"Oral presentation"

TABLE OF CONTENTS

CHAPTER 1: GENERAL INTRODUCTION

VOCs (Volatile Organic Compounds) are widely used and produced by industrial process, transportation and domestic activity. However, VOCs are toxic to humans causing different symptoms, cancers or death. VOCs can also be the source of atmospheric pollutions such as photochemical smog and destruction of the ozone. Toluene is one of the most widely used VOCs as industrial feedstock and solvent, and the global production is estimated to reach 19.6 million tons by 2020, increasing by 5.2% annually. It is noteworthy to mention that ~86% of the toluene produced is eventually released into the biosphere. Meanwhile, trichloroethylene (TCE), as an example of chlorinated VOCs, is also extensively used due to the use of industrial degreaser, synthesis feedstock and solvent. It has been assumed that 82% of the sold TCE is used for metal degreasing and that 70% of TCE used during metal degreasing is released to the environment. Therefore, with the progressive increase in toluene and TCE emissions because of the increase of consumption, there must be a significant effort and efficient technology to control them.

Non-thermal plasma (NTP) has been largely reported to treat those harmful VOCs. NTP chemistry is an interdisciplinary field including high energy physics, physicochemical discharge and reaction engineering. The application of NTP on VOCs abatement has been attracting more and more attention because of its relatively high removal efficiency, energy yields and good economy. Generally, NTP consists of electrons, ions, active radicals, neutral particles and UV photons. These species are the products when a sufficiently strong electric field is applied in a gas discharge. High energetic electrons can promote the production of other species, including: ionization, excitation, dissociation and attachment of low energy electrons. Therefore, the secondary reactions with VOCs will be initiated by those dissociated molecules, active radicals and ions. Packed-bed DBD (Dielectric Barrier Discharge) reactors have proven to achieve stable performance and higher energy efficiency for pollutant removal than conventional non-thermal plasma reactors. Dielectric beads help to reduce the breakdown voltage, which is favorable for industrial application because higher input power can be obtained at the same applied voltage. Therefore in Chapter 5, a glass beads packed bed DBD reactor was used for toluene abatement. However, it is also well known that NTP technology often results in incomplete VOC oxidation in the formation of unwanted by-products. Nevertheless, a thorough identification and quantification of these created by-products is often indispensable to elucidate the breakdown mechanism of toluene by NTP. In addition, when the packed bed reactor needs to be filled with catalytic pellets in a next step to perform in-plasma catalytic experiments, it is also of great importance to know all the by-products of the NTP treatment alone to understand the possible synergy between NTP and the used catalyst and to fulfill complete

toluene oxidation at a minimal energy cost. As a result, it is thus crucial to first examine toluene abatement in the packed bed DBD reactor alone before combining it with a catalyst.

Catalytic combustion is also one of the attractive methods for VOC control. The advantage of using catalysts based on transition metals instead of noble metals is their lower cost. Among transition metals, bulk and supported manganese-based catalysts have received increased attention, as they are considered as cheap, environmentally friendly and active materials. Thus, it has been widely reported that manganese oxides such as Mn_3O_4, Mn_2O_3 and MnO_2 exhibit high activity for the complete oxidation of hydrocarbons. In an attempt to get the most promising catalyst formulations for toluene oxidation, one effective strategy can be the investigation of binary metal oxides containing manganese. Among the different A-Mn-O systems, the Cu-Mn-O system has been found to be attractive since the mixture of manganese and cupric oxides have led to the discovery of the general name "hopcalite" catalysts, of prime importance for CO oxidation at ambient temperature, O_3 destruction as well as VOCs oxidation. This indicates that Cu-Mn oxides can be potential catalysts for post plasma catalysis process because of their ozone decomposing property. Meanwhile, the catalytic activity of Cu-Mn oxide catalysts for toluene control is affected by the preparation methods. Hence, a co-precipitation method and a redox-precipitation method of Cu-Mn oxides were evaluated in this work for toluene oxidation.

NTP and catalytic oxidation still have their limits, such as unwelcomed byproducts for the NTP technique and high energy consumption for catalytic oxidation. In order to further improve the techniques for VOC abatement, the combination of catalysts with NTP seems to be a prospective technique. Additionally, the synergy effect has been demonstrated by using plasma-catalysis, which improved the energy efficiency. The undesired byproducts, such as CO, ozone and other organic byproducts, decreased in a plasma-catalytic process. There are two ways to introduce the catalysts into the plasma: in plasma catalysis (IPC) or post plasma catalysis (PPC). In this thesis, we investigated the PPC process with Cu-Mn oxides for TCE abatement.

CHAPTER 2: THE DESIGN OF MnO_X IN PPC CONFIGURATION FOR TOLUENE ABATEMENT

The results of chapter 2 were published in the following international peer-reviewed journal:

Z. Ye, J.-M. Giraudon, N. De Geyter, R. Morent J.-F. Lamonier

The Design of MnOx Based Catalyst in Post-Plasma Catalysis Configuration for Toluene Abatement

Catalysts 2018, 8(2), 91, 2018

2.1. Introduction

With the increasing consumption of toluene in commercial and industrial applications [1], toluene emission problem becomes of serious concern for causing environmental problem as well as inducing negative health effects on humans [2, 3]. So it is highly desired to find an economical and green technique for toluene emission control. Comparing to traditional techniques such as high-temperature-based combustion and catalytic oxidation, non-thermal plasma (NTP) technology is capable of operating at room temperature and ambient pressure. Meanwhile, easy operation is another main advantages of NTP technique [4]. However, the energy efficiency and CO_2 selectivity still need to be improved for further industrial application. Hence, plasma-catalysis, including in plasma catalysis (IPC) and PPC configurations, can be a promising approach for toluene abatement having the advantages of higher toluene removal efficiency and lower unwanted byproducts at a low operating temperature, at which it is normally not possible to activate the catalysts [5, 6].

To begin with, the physico-chemical properties of toluene are presented and its negative effects on environment and human being are given. Then, after briefly screening the most encountered VOCs (Volatile Organic Compounds) depollution methods, the principles of PPC are exposed based on the coupling of two mature technologies such as NTP and catalysis. The design of manganese oxides is discussed in a fourth part. The choice of based MnOx as potential catalysts in PPC configuration was motivated due to the fact that except metals of the platinum group, characterized by their high price, the metal oxide catalysts containing manganese oxide exhibit the highest activity in decomposition of gaseous ozone and also in catalytic oxidation of pollutants. In that respect, the presentation of the abundant manganese is firstly given. Then, the important features of MnO_x allowing better performances in the main reactions expected to occur in the abatement of toluene in a PPC process are reviewed including catalytic oxidation of toluene, ozone decomposition, toluene ozonation and CO oxidation. Finally in a last part the current status of the applications of PPC using MnOx based type catalysts on toluene abatement is discussed. The selected variables of the hybrid process related to the experimental conditions of toluene abatement in air are first identified. The selected variables are those expected to play a role in the performances of the two-stage plasma-catalyst system towards toluene abatement. The descriptors linked to the performances of the hybrid process in terms of process efficiency are also presented. In a second step the effects of the variables on the experimental outcomes (descriptors) are discussed.

2.2. The properties, applications and hazardous effects of toluene

Toluene ($C_6H_5CH_3$) is widely investigated as a representative VOCs of the BTX (Benzene, Toluene and Xylene) family. Toluene is a colorless liquid with an aromatic odor. It is a mono-substituted benzene derivative, consisting of a CH_3 group attached to a phenyl group. The basic properties of toluene are presented in Table 2.1.

Table 2.1 The physicochemical properties of toluene

Property	Value
Chemical formula	C_7H_8
N° CAS	108-88-3
Molar mass (g/mol)	92.14
Density (g/ml)	0.87 (20°C)
Melting point (°C)	-95
Boiling point (°C)	111
Solubility in water (g/l)	0.52 (20°C)
Vapor pressure (kPa)	2.8 (20°C)
Odor threshold (ppm_v, Parts Per Million by volume)	0.17
Auto ignition temperature (°C)	480
Conversion factors	1 ppmv = 3.76 mg/m^3 (in air, 25 °C)

Toluene can react as an aromatic hydrocarbon in electrophilic aromatic substitution [7]. The methyl group has a greater electron-releasing property than that of H atom in the same position. Sulfation, chlorination and halogenation have been undergone via this property. Importantly, comparing to the phenyl group, methyl group is more susceptible to oxidation [8].

Toluene has numerous commercial and industrial applications: for example, toluene is used as a precursor in the synthesis of chemicals, such as xylene, benzene, toluene diisocyanate (TDI) for the manufacture of polyurethane foam and trinitrotoluene (the explosive TNT). Toluene is used as an octane booster in gasoline fuels, which are used in internal combustion engines. In addition, toluene is widely used as a solvent because of its favorable properties, such as high solvency, low flammability, non-corrosiveness and high stability. In many commercial products, toluene is present in paint thinners, silicone sealants, nail polish remover, glues, disinfectants and correction fluid. The global demand for toluene valued at over USD 25.1 billion in 2015, is expected to reach above USD

31.8 billion in 2021[9]. Toluene worldwide production is estimated to be 19.6 million tons in 2020 comparing to 12.4 million in 2010 [10].

However, it is noteworthy to mention that ~86% of the toluene produced is eventually released into the biosphere (primarily in the troposphere) due to high volatility and low solubility in water. There are several man-made sources of emissions to the atmosphere, including the following [11]:

- Inadvertent sources (65%), such as emissions from motor vehicles and aircraft exhaust, losses during gasoline marketing activities, chemical spills, cigarette smoke, and household products.
- Industrial processes in which toluene is used (33%)
- Toluene production (2%)

Toluene is believed to be one of the most prevalent hydrocarbons in the troposphere. Its dispersion is largely dependent upon meteorological conditions and its atmospheric reactivity. The lifetime of toluene ranges from 4 days (at high-altitudes during the summer) to several months (at low-altitudes during the winter). The average half-life of toluene resulting from atmospheric oxidation is estimated to be 12.8 hours [3]. So the contribution of toluene to the photochemical smog is considerable.

The presence of toluene in air has a negative impact on human health. Toluene is a main contributor of indoor environmental pollution. Different sources such as paints, adhesives and cigarette are known to contribute to the increase of toluene concentration in indoor air.

Health effects	Oral	Dermal
Death	•	
Acute	•	•
Intermediate		
Chronic		
Immunologic/Lyphoretic		
Neurologic		
Reproductive		
Developmental		
Genotoxic		•
Cancer		

Figure 2.1. Existing information on health effects of toluene (black dot: existing data); adapted from reference [2].

The report entitled "toxicological profile for toluene" published in 2000 conducted by U.S. department of health and human services presents the health effects of toluene [2]. As shown in figure 1, there are three main exposure routes for human: inhalation, oral and dermal. Among them, a lot of data deal with toluene incorporation throughout inhalation. The high hazard profile of toluene is highlighted as it covered all the possible health effects listed in Figure 2.1. For example, in Virginia, it was reported that 39 deaths were attributed to inhalant abuse from 1987 to 1996, and Hobara *et al.* [12] estimated 1 hour of exposure to 1,800–2,000 ppm toluene may be fatal to humans via inhalation. Regarding oral route, only cases of death and acute effect have been reported. Concerning the dermal route, it has been found that exposure of toluene caused the acute effect and genotoxic effect. Due to the adverse effects on human health, WHO (Word Health Organization) has published guideline for the toluene exposure limit. European Union has followed the instruction of WHO [1]: The lowest-observed-adverse-effect level on the central nervous system (CNS) from occupational studies, is approximately 332 mg/m^3 (88 ppmv) and the limit of occupational exposure for 8 hour of work is 188 mg/m^3 (46 ppmv) in European Uunion (EU).

2.3. The treatment techniques for the removal of toluene

The dangerousness of toluene involves researching an economic and green technique for its abatement. There have been developing a few traditional types of VOCs abatement techniques, mainly focus on two directions: one deals with non-destructive methods (adsorption, condensation, membrane separation), the other one concerns destructive methods (biochemical method, thermal and catalytic oxidations). The limits based on VOCs concentration and flow rate for these conventional methods have been depicted in Figure 2.2. Since every type of treatment technology has advantages and disadvantages, none is really satisfactory.

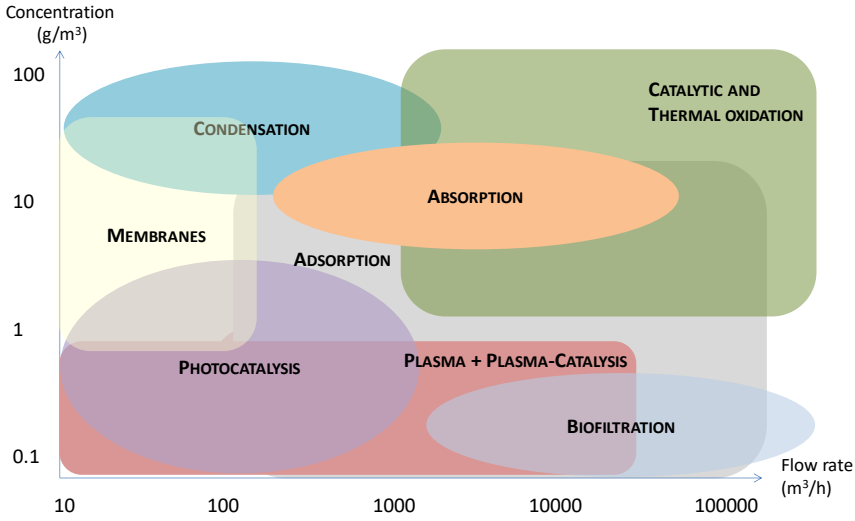

Figure 2.2. Classification of various air pollution control technologies based on air flow rate and initial VOC concentration.

Comparing to conventional methods, NTP technology has been claimed to be an alternative method for reducing VOCs due to its wide applicable range of 10-50000 $Nm^3.h^{-1}$ and (ppb level)-10,000 ppmv [13-16], especially effective for concentrations lower than 100 ppmv [17]. The application of NTP on toluene abatement has attracted considerable interest because of easy on/off operation and inexpensiveness [18, 19]. Generally, NTP consists of energetic electrons, ions, active radicals, neutral particles and UV photons as shown in Figure 2.3. These species are produced when a sufficient strong electric field was applied allowing gas discharge. The electron energy is usually considered to range from 1 to 20 eV while the temperature of the carrier gas keeps close to room temperature. These high energetic electrons can promote toluene abatement via a primary process such as charge transfer, ionization, excitation, dissociation reactions [20]. The secondary process is characterized by the subsequent chemical reactions involving the products of primary process (electrons, radicals, ions, and excited molecules). However, the overall process is not selective into the desired target which is CO_2. To overcome lack of CO_2 selectivity, researchers have focused on emerging techniques resulting from the coupling of two mature VOCs abatement technologies. Among those, plasma-catalysis is one of the most promising. Attractiveness of this hybrid process stems from the possibility to take full advantages of the two technologies: high selectivity from catalysis and the easy operation from NTP. Thus previous works have emphasized the beneficial role of plasma-catalysis in VOCs removal allowing to decrease the

energy cost as well as minimizing the production of hazardous by-products [17, 21, 22].According to the location of catalyst, the plasma catalysis system can be divided into two categories, namely, IPC and PPC configurations. In this study we will focus only on PPC applied to toluene removal.

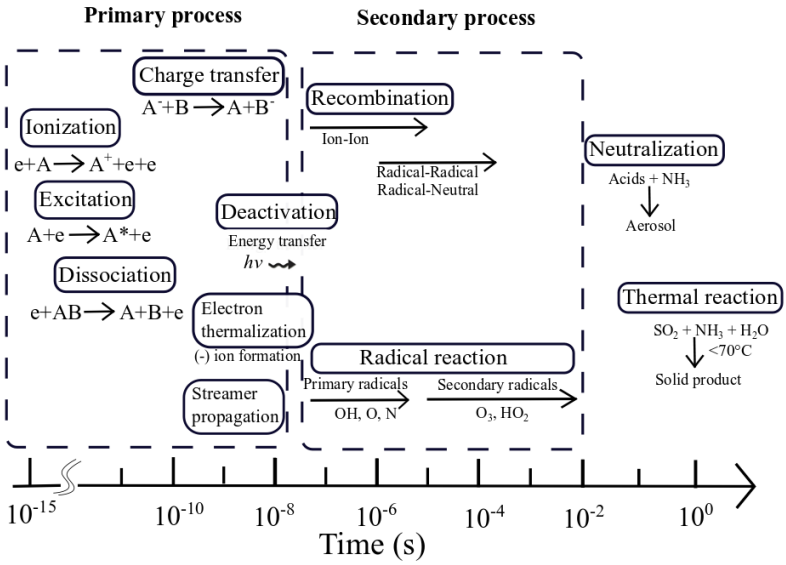

Figure 2.3. Time-scale of elementary processes in a non thermal process [20].

2.4. Design of catalysts for toluene abatement in PPC process

2.4.1. Introduction

In PPC configuration the catalyst is located downstream from the non-thermal plasma reactor. In that way homogeneous complex reactions occur between plasma and the carrier gas molecules such as O_2, N_2, possible H_2O and the VOC whose number and extent can be tuned by changing the energy put in the plasma. Due to the low selectivity of the NTP, along the VOC oxidation into CO_2, its transformation is always accompanied by the formation of unwanted hazardous byproducts (e.g. plasma generated VOCs (reaction intermediates), CO, O_3, and NO_x). This problem can be resolved *a priori* through the high selectivity of the catalyst. For instance, the proper catalyst should be able to oxidize the plasma generated organic by-products and the plasma non processed initial VOC as well as CO to CO_2 and decompose O_3 and NO_x generally in moist air at a temperature close to room temperature or moderate (≤ 150 ℃) at the same time.

The basic idea is to take advantage of the O_3 decomposition efficiency of the catalyst to supply active species enabling the total oxidation of plasma non processed hazardous species. When regarding the nature of the catalysts, noble metals and transition metal oxides have been found to be the most active substances for ozone decomposition. However among the developed catalysts, MnOx are considered to be the most efficient and cost-effective for ozone decomposition. Additionally the possibility of increasing moderately the temperature of the catalyst allows to activate some oxygen of the catalyst. Based on that observation, efficient catalysts for total oxidation of VOC cannot be discarded. Again, the same families of catalysts should be taken into account and again MnOx can be good candidates for total oxidation of toluene. Lastly MnOx are also recognized as efficient catalysts in CO oxidation which is also an important reaction to consider.

This review attempts to summarize our present state of knowledge using MnOx based catalysts for toluene abatement in PPC configuration. In that respect the presentation of the abundant manganese oxides will be firstly given. Then in a second step the main features of MnO_x allowing better performances in toluene total oxidation, ozone decomposition, toluene ozonation and CO oxidation will be successively briefly reviewed. Finally in the last part the current status of the applications of PPC using MnOx on toluene abatement will be discussed.

2.4.2. Presentation of the main manganese oxide polymorphs

Manganese (Mn) is a multivalent element. Each valence state has a characteristic oxide or oxides. MnOx occur naturally as minerals in at least 30 different crystal structures in a range of manganese oxidation states. Manganese oxides are technologically important materials and have widely been used as effective and inexpensive catalysts and as electrode materials for batteries. Interestingly, some MnOx crystal structures exhibit tunnel- and/or layered structures with varied proportions of Mn in different oxidation states (2+, 3+, and 4+). The known binary oxides of manganese include MnO, Mn_2O_3, Mn_3O_4 and MnO_2. Like many monoxides, MnO adopts the rock salt structure, where cations and anions are both octahedrally coordinated. The α-Mn_2O_3 phase is named bixbyite. The Mn^{3+} ions are octahedrally coordinated, while the O ions have 4 Mn neighbors. The bixbyite structure can be viewed as a close-packed lattice of Mn with O ions filling three quarters of the tetrahedral interstitials in a pattern with Ia3 symmetry. Hausmannite Mn_3O_4 has a spinel structure having a composition formula $Mn^{2+}(Mn^{3+})_2O_4$, where Mn^{2+} ions occupy the tetrahedral sites and Mn^{3+} the octahedral sites [23].

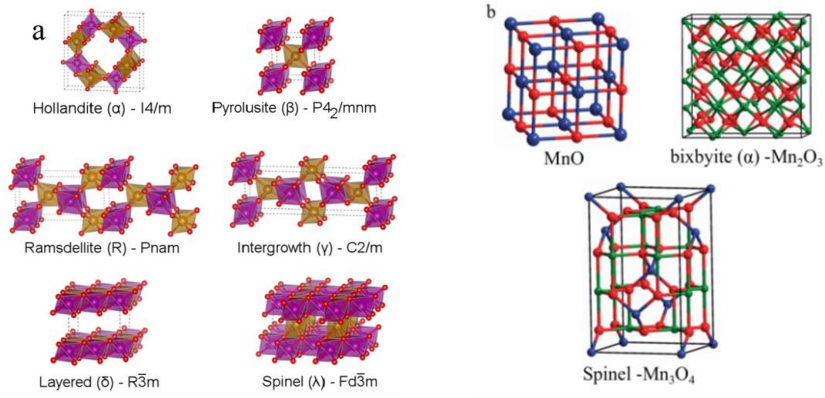

Figure 2.4. Illustration of the crystal structures of selected common manganese oxides: (**a**) MnO_2 including: α-$Mn^{IV}O_2$ (hollandite); rutile β-$Mn^{IV}O_2$ (pyrolusite); R-$Mn^{IV}O_2$ (ramsdellite); γ-$Mn^{IV}O_2$ (intergrowth); δ-$Mn^{IV}O_2$ (birnessite); λ-$Mn^{IV}O_2$ (spinel); Here, The purple and yellow atoms represent spin-up and spin-down Mn, respectively, while the red atoms represent O [24]; (**b**) Crystal structures of MnO, α-Mn_2O_3 and Mn_3O_4. The green, blue, and red atoms represent Mn^{III}, Mn^{II}, and O^{2-}, respectively [25].

Along these oxides is the metastable layered Mn_5O_8 having a compositional formula ($(Mn^{2+})_2(Mn^{4+})_3O_8$). Manganese dioxide, MnO_2, for its own part, shows polymorphism. MnO_2 has several crystalline structures, including α-,β-, γ-, δ-, and λ-MnO_2. The different tunnel structures can be described by the size of their tunnels determined by the number of octahedral subunits (n×m), as depicted in Figure 2.4. α-MnO_2 (hollandite) consists of double chains of edge-sharing MnO_6 octahedra, which are linked at corners to form 1D (2×2) and (1×1) tunnels in the tetragonal unit cell. The size of the (2×2) tunnel is 0.46 nm, which is a large tunnel for insertion/extraction of alkali cations. β-MnO_2 (pyrolusite) is composed of single strands of edges haring MnO_6 octahedra to form a 1D (1×1) tunnel. Because of the narrow (1×1) tunnel size (0.189 nm), β-MnO_2 cannot accommodate cations. The structure of γ-MnO_2 is random intergrowths of ramsdellite (1×2) and pyrolusite (1×1) domains. δ-MnO_2 is a 2D layered structure with an interlayer separation of 0.7 nm. It has a significant amount of water and stabilizing cations such as Na^+ or K^+ between the sheets of MnO_6 octahedra. λ-MnO_2 is a 3D spinel structure.

The richness in MnOx structures thus provides a rigorous test system to explore the significance of atomic positions on the catalytic efficiency towards toluene oxidation.

2.4.3. MnOx in catalytic oxidation of toluene

The high reactivity of MnOx towards VOCs abatement is generally ascribed to easy variation of manganese oxidation state (Mn^{2+}, Mn^{3+}, Mn^{4+}), oxygen storage capacity in the crystalline lattice and high mobility of lattice oxygen [26]. Kim and Shim [27] investigated the effect of O/Mn stoichiometry using Mn_3O_4, Mn_2O_3 and MnO_2. It was found that the catalytic activity decreased in the order of Mn_3O_4 > Mn_2O_3 > MnO_2 in line with the decrease of the specific surface areas and oxygen mobility of the MnOx. Mn_3O_4 [28], Mn_2O_3 [29, 30] and MnO_2 [28] were also previously investigated separately by different research teams for toluene oxidation. F. Wang *et al.* [31] reported on the external morphology effect of MnOx (rod-, wire-, tube-, and flower-like morphologies) for the oxidation of toluene. It was found that the oxygen ad-species concentration (related to the Mn^{3+} concentration) and low-temperature reducibility decreased in the order of rod-like α-MnO_2 > tube-like α-MnO_2 > flower-like Mn_2O_3 > wire-like α-MnO_2, in good agreement with the sequence of the catalytic performance of these samples. The best-performing rod-like α-MnO_2 catalyst could effectively catalyze the total oxidation of toluene at low temperatures (T_{50} = 210 °C and T_{90} = 225 °C at a GHSV of 20,000 $ml.g^{-1}.h^{-1}$). It was concluded that the excellent catalytic performance of α-MnO_2 nanorods might be associated with the high oxygen ad-species concentration and low-temperature reducibility. Verykios *et al.* [32] showed that γ-MnO_2 which was less affected by the presence of water than other MnO_2 polymorphs could be suitable for toluene removal. This catalyst was claimed to be more active than noble metal catalysts.

In a same way, various structures of MnO_2 *i.e.* α-, β-, δ-MnO_2 were prepared and their catalytic performances in toluene oxidation were assessed to those of a γ-like MnO_2 obtained by the selective removal of La^{3+} from an acid-treated three-dimensional macroporous and mesoporous $LaMnO_3$ [33]. The best performance of this γ-like MnO_2 over the other MnO_2 polymorphs was ascribed both to the open three-dimensional macroporous and mesoporous morphology leading to higher BET surface areas than conventional syntheses, enhanced surface adsorbed oxygen (O_{ads}) to lattice oxygen (O_{latt}) molar ratio (O_{ads}/O_{latt}) and easier reducibility. Similarly Liao *et al.* [34] investigated the external morphology effect over Mn_3O_4 having hollow and solid sphere morphologies for toluene abatement. The better catalytic activity when using hollow spheres of Mn_3O_4 was claimed to result from beneficial combined effects such as the cavity morphology leading to high surface area, higher O_{ads}/O_{latt} molar ratio, believed to

be proportional to active oxygen, and higher Mn average oxidation state (AOS). MnOx supported catalysts were affected by the same factors too. To conclude catalytic activity is generally associated with several factors, such as the BET surface area, presence of oxygen vacancies, reducibility, and external morphology of the catalyst.

The common oxidation catalytic reactions generally involved three types of mechanism [35]: Langmuir-Hinshelwood, Eley-Rideal and Mars-Van Krevelen (MkV) mechanism [33]. It is well known that MnOx exhibit strong oxygen storage/release ability due to the fact that they easily undergo a rapid reduction–oxidation cycle through the interaction with reducing or oxidant agents, accompany by the formation of manganese ions in various oxidation states. The involvement of lattice oxygen of catalysts in total oxidation of toluene and the strong correlation between labile lattice oxygen and catalytic activity suggest that the reaction could proceed via the MvK model [8, 36]. In the case of VOCs catalytic oxidation, the first step corresponding to the reduction of the catalyst surface is generally the rate determining step [37].

2.4.4. MnOx in ozone decomposition

Decomposition of ozone in the gas phase was carried out on various metal oxides by S. Imamura *et al.* [38]. It was shown that the activity of the metal oxide catalysts increased roughly in the order of the increase in their surface area and in the amount of surface oxygen on them. These observations are very interesting as these characteristics resemble to those of total oxidation catalysts because low surface area and a small amount of surface oxygen are generally targeted for partial oxidation catalysts. Interestingly metal oxide conductance increased throughout ozone introduction for the most reactive oxides such as $Ag_2O \approx NiO$, CuO, Co_3O_4 which are p type oxides suggesting that negatively charged oxygen species were formed on their surface. Ag_2O was claimed to be the most effective catalyst in decomposing ozone, increasing its activity as the reaction proceeds while some transition-metal oxides are deactivated during the reaction due to accumulation of oxygen species that cover their active sites. The high reactivity of the oxygen species on Ag was invoked to be due to the especially weak bond between oxygen and silver compared with those between oxygen and other metals. Additionally the high reactivity of such catalyst for CO oxidation was believed to occur thanks to the production of very active oxygen such as oxygen ion O^- without totally discarding oxygen (O) and ozonide ion (O_3^-) resulting from the decomposition of O_2^-.

In that way, a comprehensive survey of different oxides (MnO_2, Co_3O_4, NiO, Ag_2O, Fe_2O_3, Cr_2O_3, CeO_2, MgO, V_2O_5, CuO and MoO_3) supported on γ-Al_2O_3

for ozone decomposition, but this time in the presence of water (RH (Relative humidity): 40%), was performed by B. Dhandapani *et al.* [39]. It is found again that p-type oxide semiconductors are the most active substances for ozone decomposition. Among the investigated transition metal oxides MnO_2 showed the highest activity explaining its prevalence in patent disclosures. Ozone decomposition pathway over MnOx supported on γ-Al_2O_3 was investigated by T. Oyama *et al.*. The reaction proceeds through two irreversible steps, the adsorption of ozone on the catalyst surface and the desorption of molecular oxygen [40, 41]**.** Ozone is first decomposed/reduced by Mn^{n+} cation into O^{2-} and O_2. Then production of active O_2^{2-} and O_2 was proposed via reaction of O^{2-} with another O_3 molecule in the presence of $Mn^{(n+2)+}$. Next, unstable O_2^{2-} reduced $Mn^{(n+2)+}$ back into Mn^{n+} and desorption of an oxygen molecule occured [42, 43]:

$$O_3 + Mn^{n+} \rightarrow O^{2-} + Mn^{(n+2)+} + O_2 \quad (1)$$

$$O_3 + O^{2-} + Mn^{(n+2)+} \rightarrow O_2^{2-} + Mn^{(n+2)+} + O_2 \quad (2)$$

$$O_2^{2-} + Mn^{(n+2)+} \rightarrow Mn^{n+} + O_2 \quad (3)$$

Oyama *et al.* found that difference in the structure of the manganese active center was the origin of support effect on the activity. At low Mn loadings (< 6 wt%) the active phase was to be well dispersed on Al_2O_3 but not well understood. Significant progresses were achieved in 2001 by R. Radhakrishnnan *et al.* by using extended X-ray absorption fine structure (EXAFS) to evaluate the local bonding environment in the MnO_x/γ-Al_2O_3 catalyst [43]. The catalyst (3 wt%) was prepared throughout incipient wetness impregnation using manganese acetate precursor. After heating at 170 ℃ for 6 h, the solid was calcined at 400 ℃. Based also on *in situ* Raman spectroscopy analysis performed before and during ozonation reaction and *ab Initio* calculations as complementary tools a four mononuclear species was postulated as the manganese active center with a Mn-O distance of 210 pm as shown in Figure 2.5. During the ozone decomposition reaction, an adsorbed peroxide species was observed on the catalyst surface (Raman line at 880 cm^{-1}).

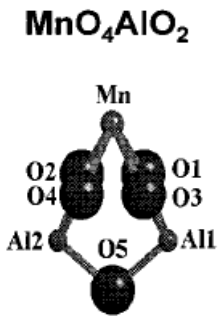

Figure 2.5. Geometry-optimized four oxygen coordinate Mn structure using the HF/6-311G method [43].

Only a few works have investigated the activity of manganese dioxides with specific crystal phase [44, 45]. Ma *et al.* [46] proposed a scheme of ozone decomposition over transition metal doped cryptomelane–type manganese oxide catalysts (α-MnO_2) implying the $Mn^{3+/4+}$ mixed valence in the decomposition/reduction of O_3 into O_2 and O^-. Consequently, the main differences here stem in the nature of the implied redox couple of manganese and in the nature of the reactive oxygen species: O^- instead of O_2^{2-}.

$$O_3 + [Mn^{3+}] \rightarrow O_2 + O^-_{ads}[Mn^{4+}] \quad (4)$$

$$O_3 + O^-_{ads}[Mn^{4+}] \rightarrow 2O_2 + [Mn^{3+}] \quad (5)$$

This scheme highlights the importance of the mixed valence ($Mn^{4+/3+}$) in α-MnO_2 catalysts. Based on this mechanism the higher content of Mn^{3+} (surface oxygen vacancies) cations present at the surface of the catalyst is expected to promote ozone decomposition.

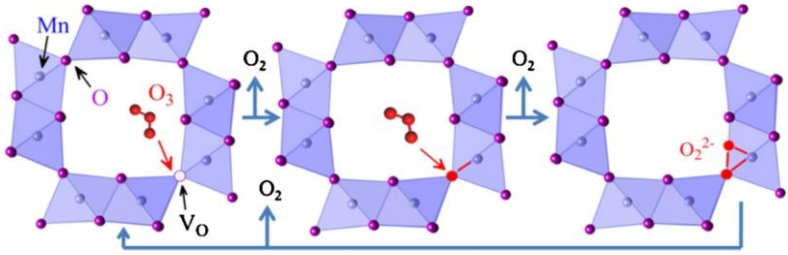

Figure 2.6. Ozone decomposition mechanism based on the involvement and recycling of oxygen vacancy (V_O) [44].

Interestingly, the effect of MnO_2 structure on ozone decomposition was recently investigated on α-, β- and γ-MnO_2. The activity of these three MnO_2 polymorphs for ozone decomposition followed the order of α- > γ- > β-MnO_2. The superior performances of α-MnO_2 were explained by the combined largest specific surface area and the lowest Mn AOS. Additionally it was found that the catalytic activity of MnO_2 strongly depended on the density of oxygen vacancies in line with the presence of Mn^{3+}. The ozone decomposition mechanism based on the involvement and recycling of oxygen vacancy (V_O) was proposed below and the pertinent points were grasped in Figure 2.6. Once Mn^{3+} appears in the manganese dioxide, oxygen vacancies were generated to maintain electrostatic balance according to the following process (Eq. 6):

$$4Mn^{4+} + O^{2-} - Opea^{4+} + 2e^{-}/V_O + 1/2O_2 \rightarrow 2Mn^{4+} + 2Mn^{3+} + V_O + 1/2O_2 \quad (6)$$

$$O_3 + V_O \; V/_2 + O^{2-} \quad (7)$$

$$O_3 + O^{2-} - O/_2 + O_2^{2-} \quad (8)$$

$$O_2^{2-} -)O_2 + V_O \quad (9)$$

When ozone gas flows through MnO_2, the ozone molecule binds to MnO_2 surface by inserting an O atom into an oxygen vacancy site. The oxygen vacancy is 2-electron donor and transfers 2 electrons to an O atom of ozone [47, 48], thus forming an oxygen species (O^{2-}) in the oxygen vacancy site and an oxygen molecule, which desorbs into the air (see (Eq. 7)). Then another ozone molecule reacts with O^{2-} to produce a gas-phase oxygen molecule and a bridging O_2 dimer (peroxide, O_2^{2-}), which was observed by *in situ* Raman spectroscopy (see (Eq.8)). Finally, the peroxide species (O_2^{2-}) decomposes to release an oxygen molecule (see (Eq. 9)). The decomposition of peroxide species was believed to be the rate-limiting step.

This study brings important guidelines for the design of future MnO_2 based-type catalyst for ozone removal.

2.4.5. MnOx in ozonation reactions

Catalytic ozonation is an innovative method for oxidation of pollutants in liquid or gas phase. Ozonation reactions mainly referred to catalytic VOCs oxidation by ozone. As this reaction consists of ozone decomposition in the presence of an organic substrate it is not surprising that MnOx, which are among

the most active transition metal oxides for low temperature decomposition of ozone to generate active oxygen species, are required for oxidation of VOCs by ozone. Application of this method in gas phase has opened a new catalytic approach for low temperature oxidation of VOCs at trace concentration levels. Results of the literature review show that apparent activation energy of VOCs oxidation can be greatly reduced by use of ozone compared to that of oxygen, making total oxidation of VOCs possible at temperatures as low as 100 ℃ or even lower.

Effect of manganese loading on total oxidation of toluene by ozone using $MnOx/\gamma\text{-}Al_2O_3$ was investigated by E. Rezai *et al.* [49]. Activities of four loadings of Mn (1, 5, 10 and 20 %) were studied in the temperature range of 22-100 ℃. A direct relationship between Mn loading and average oxidation state of manganese was found. Catalysts at lower loadings, up to 10%, were mostly composed of Mn_2O_3 while a mixture of MnO_2 and Mn_2O_3 was present in catalysts with loadings higher than 10%. All catalysts became deactivated at room temperature and their activities were improved by an increase of temperature. It was observed that lower Mn loadings have higher activity in oxidation of toluene. It was proposed that lower oxidation states of manganese are more favorable in decomposition of ozone resulting in higher rate of toluene oxidation. A Langmuir–Hinshelwood mechanism based on activation of toluene molecule via abstraction of hydrogen from the methyl group was postulated to occur over $MnOx/\gamma\text{-}Al_2O_3$ (10 wt%) catalyst [50] explaining the effect of toluene and ozone partial pressures on toluene oxidation rate. Hence the C–H bond cleavage was assumed to be the relevant kinetic step in the oxidation of toluene by ozone.

The mechanism of oxidation of VOCs by ozone is based on ozone decomposition due to Eqs. 10-14 generating atomic oxygen to react with VOCs in the oxidation reaction (Eq. 14) assuming that VOCs are adsorbed on Mn sites (Eq. 13) and the reaction proceeds based on Langmuir-Hinshelwood mechanism between adsorbed species (Eq. 14) [49].

$$O_3 + Mn \rightarrow O_2 + O\text{-}Mn \quad (10)$$

$$O_3 + O\text{-}Mn \rightarrow O_2 + O_2\text{-}Mn \quad (11)$$

$$O_2\text{-}Mn \rightarrow O_2 + Mn \quad (12)$$

$$VOC + Mn \rightarrow VOC\text{-}Mn \quad (13)$$

VOC-Mn + O-Mn → Products (14)

It is believed that higher dispersion of Mn atoms in catalysts with lower loading levels decreases oxidation state of Mn.

XRD studies showed the presence of β-MnO_2 and Mn_2O_3 (bixbyite) in the Mn loading of 10 %. The percentages of Mn_2O_3 and MnO_2 in the catalyst estimated from XANES spectra were 91.0 and 9.0 %, respectively. The activation energy of the reaction was determined to be 31 kJ/mol obtained by a power law model. The power law model also determined the reaction orders with respect to toluene and ozone as -1 and 2, respectively [50].

Ozonation of toluene catalyzed by MnOx supported on siliceous MCM-41was also investigated by the same team [51]. The performances were found to be similar to those of MnO_2/γ-Al_2O_3 at room temperature, the activity decreasing with reaction time as the supported alumina catalyst.

MnO_2/graphene samples were developed for catalytic ozonation of toluene by M.Hu *et al.* [52]. The hydrothermal method was used as an effective way to prepare tightly anchored birnessite-type MnO_2 on graphene. The highest toluene degradation rate of $7.89.10^{-6}$ $mol.min^{-1}.g^{-1}$ obtained over the 64.6 wt.% MnO_2/graphene sample was attributed to a synergetic effect of graphene and MnO_2. This synergetic effect was attributed to the tight connection between the active sites on graphene for adsorption of toluene and decomposition of ozone, and the MnO_2 on graphene for decomposition of ozone to form atomic oxygen species. Additionally MnO_2/graphene can be regenerated at 325 ℃.

MnOx dispersed on HZSM-5 (Mn/HZSM-5; Mn: 4 wt%) was shown to be an efficient catalyst for oxidation of 20 ppmv of toluene in the presence of 2000 ppmv of ozone at 30 ℃ [53]. It was shown by DRIFTS analysis a toluene and ozone conversions of about 78% and 70%, respectively, over Mn/HZSM-5 with a COx (CO + CO_2) selectivity of 70%. Additionally the catalytic performances were promoted by Ag which was attributed to induce more oxygen vacancies. The high activity of these catalysts was mainly attributed to the reactive oxygen species generated from ozone decomposition over the oxygen vacancies of these catalysts. Based on the obtained results the possible reaction pathways with or without ozone were given in Figure 2.7. The toluene can be partially oxidized into benzyl alcohol by the lattice oxygen, but it can be further oxidized into benzaldehyde, benzoic acid and maleic anhydride, ultimately, mineralized to CO_2 by O_3 at room temperature.

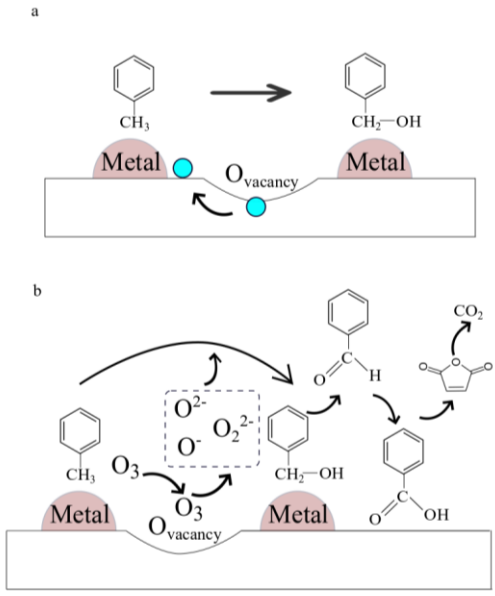

Figure 2.7: The pathway of toluene oxidation without ozone (a), with ozone (b) at room temperature adapted from [53].

Commercial honeycomb ozone decomposition catalyst (consisting of MnO_2 as the main active phase with SiO_2 and TiO_2) immobilized on a nonwoven fabric was investigated for O_3 and toluene removal in dry and humid conditions [54]. It was shown that O_3 was rapidly decomposed only around the entrance of the honeycomb ozone decomposition catalyst. However the amount of converted toluene decreased with time because water molecules competed on the catalyst surface decreasing O_3 and toluene adsorption. To overcome this inhibition MnO_2 catalyst were mixed with alumina or zeolite, which were functional adsorbents, to increase the contact between O_3 and the ozone decomposition catalyst (ODC) surface but however only a small percentage of VOCs reacted.

Table 2.2 exhibits the salient results in ozonation reactions towards toluene abatement. As mentioned above the active phase is mainly MnO_2 well dispersed on a support which is generally γ-Al_2O_3, TiO_2/SiO_2, graphene and HZSM-5. It has to be mentioned that graphene allows to dispersed huge amount of Mn (60 wt%) as compared to γ-Al_2O_3 where the Mn content does not exceed the value of 20 wt% [49, 55]. All given reactions here are conducted at room temperature. Direct comparison of the different catalyst performances is complicated due to the discrepancy of the operating parameters such as the ratio of generated ozone

to the inlet toluene ratio which ranged from 0.55 to 8.75. Beneficial effect is noticeable when this ratio is allowed to increase. Additionally ozone consumption decreases whatever the catalyst under concern indicating partial deactivation of the catalyst. This decrease is always accompanied to a decrease of the toluene removal efficiency in line with poor carbon mass balance.

Alcohols, aldehydes and organic acids were identified as intermediates in the reaction process. Heat treatment and excessive ozone feeding favored catalyst generation.

As catalytic ozonation proceeds at lower temperature compared with conventional catalytic oxidation processes, catalyst stability under mild conditions remains a problem. Although aromatic compounds can be oxidized by manganese oxide catalysts at room temperature in an ozone feed, the catalysts generally suffer from severe deactivation because of the build-up of less-reactive by-product compounds on the catalysts.

Table 2.2 **Overview of ozonation results for toluene abatement.**

Catalyst	Active Phase	Flow Rate (mL/min)	GHSV ($mL.h^{-1}.g^{-1}$)	Temperature (°C)	CC_7H_8 (ppm)	CO_3 (ppm)	O_3/C_7H_8	$\eta_{Toluene}$ (%)	η_{Ozone} (%)	By-products	Reference
20% MnO_2/Al_2O_3	MnO_2	100 (dry air)	60,000	20	177	98	0.55	~25 (160 min) then deactivation	From 100 to 80% in 160 min	Benzoic acid, benzaldehyde, and benzyl alcohol.	[55]
10% MnOx/γ-Al_2O_3	MnO_2 and Mn_2O_3	1000 (dry air)	300,000	20	120	1050	8.75	From 100 to 40% in 330 min	From 100 to 20% in 330 min	Acetic acid, oxalic acid, benzene and maleic anhydride Carbon balance: ~20%	[49]
65 wt. % MnO_2/graphene	MnO_2	150 (dry air)	112,500	20	200	400	2	~33.6 (400 min) then deactivation	~84.3 (400 min), then deactivation	Organic byproducts	[52]
$MnO_2/TiO_2/SiO_2$ honeycomb	MnO_2	1000 (dry air)	-	20	10	38	3.8	~72 (100 min)	-	Carbon balance: ~22%	[54]
	MnO_2	1000 (RH: 70%)	-	20	10	38	3.8	~35 (100 min)	-	Carbon balance: ~50%	
Mn/HZSM-5	MnOx	100 (dry air)	150,000	30	20	200	10	78	70	benzaldehyde, benzoic acid and maleic anhydride	[53]

2.4.6. The ability of MnOx for CO removal

Catalytic oxidation of CO has long been studied on various MnOx catalysts due to their high CO oxidation ability and low cost in contrast to the expensive noble metal catalysts [56]. Like Cr, Mn has also been used in association with other elements, such as Cu, Co, Ni, and La, to form manganites, which are very active for CO oxidation [57].

In the study of CO oxidation by various bulk MnOx at low temperature (RecNum>141</RecNu*et al.* [56] reported that the ranking for CO oxidation in a mixture of unit ratio of O_2/CO by decreasing activity followed the sequence: $Mn_2O_3 > MnO_2 \geq MnO$. The CO oxidation over MnO_2 and Mn_2O_3 occurred *via* Langmuir–Hinshelwood mechanism while over MnO a MvK mechanism prevailed. More energy was needed for activating the CO–Mn^{2+} bond in the reaction which accounted for the low activity of MnO. By opposition, the high reactivity for Mn_2O_3 was attributed not only to the moderate strength of CO–Mn^{3+} bond but also to the abundant defects/oxygen vacancies on its surface phase.

Interestingly, Wang *et al.* [58] compared the catalytic behavior of three manganese oxides (MnO_2, Mn_3O_4 and Mn_2O_3) doped or not by gold. Mn_2O_3 appeared to be the most active oxide (T_{50}: +135 ℃), reducing at the lowest temperature and undergoing exceptional promotion by gold (T_{50}: -62 ℃ on 2.9 %Au/Mn_2O_3). Imamura *et al.* [59] in their investigation of Pd/Mn_2O_3 catalysts found a similar high activity for the bare support. The role of Mn_2O_3 would be to permit the incorporation of O_2. The slow step would be the surface reaction of CO, which is promoted by Pd.

MnO_2 was also the subject of numerous investigations for CO oxidation [60-62]. As discussed above, MnO_2 has 4 kinds of polymorphs, denoted as α-, β-, δ-γ-MnO_2. α- and δ- MnO_2 were found to be the most active phases for CO oxidation, whereas β- and γ-MnO_2 are much less active [60]. The order of activity was well-correlated to the Mn-O bond strength ($\alpha < \delta < \gamma < \beta$), the higher Mn-O bond strength, the lower the activity.

Liang *et al.* [60] also suggested that the oxidation state of manganese constantly oscillates between Mn^{4+} and Mn^{3+}. The γ- and β-MnO_2 polymorphs would be less active because the re-oxidation of Mn^{3+} into Mn^{4+} would be more difficult than in α- and δ-MnO_2. This was also confirmed by the work of Iablokov *et al.* [63].

Among the most common Mn based oxides, Mn_2O_3 was the most reactive in CO oxidation, and among the different polymorphs of MnO_2, α- and δ- MnO_2 were found to be the most active phases. It should be noted, however, that Iablokov *et al.* [63] were able to prepare an efficient MnOx ($1.61 < x < 1.67$) oxide, more active in CO oxidation than Mn_2O_3, via calcination of a manganese oxalato precursor in 10 % O_2 at 525 °C.

2.5. MnOx in PPC for toluene abatement

PPC is a two-stage plasma-catalysis system, including two reactors in series with the catalytic reactor located downstream of NTP. The operating mode is the following: the gaseous effluent, consisting of the VOC generally diluted in moist air, is processed by the NTP. The chemical effects occurring within the plasma are the result of an energy injection into the gas effluent by way of electron-impact processes under an electric field. Complex homogeneous reactions take place between the plasma generated reactive species enabling the more or less complete decomposition of the initial VOC. The nature and extent of these homogeneous reactions depend mainly on the energy put per liter in the plasma and to the type of discharge all other things otherwise remaining equal. Usually the NTP can degrade the VOC to some extent but the main drawbacks are high energy consumption and its non-selectivity. Consequently organic intermediates which can be more harmful than the starting VOC, along with hazardous substances such as O_3 and NO_2, can evolve from the NTP reactor. By opposition to IPC where the catalyst is integrated in the reactor, the plasma produced short-lived reactive species do not achieve to reach the catalytic reactor in PPC configuration.

Hence the NTP process can lead to the formation of a complex gaseous product distribution. At that stage the design of the catalyst plays a key role to improve CO_2 selectivity. Indeed the catalyst should be able to transform all the hazardous species into CO_2 taking advantage of active oxygen species from ozone decomposition. Hence once more the catalyst should exhibit high performances in ozone decomposition. Comparing to ozonation reactions where the plasma plays only the role of ozone supplier (ozoner), in PPC, plasma processes alter the gas composition that is fed to the catalyst in a complex manner. In a previous study A. Gervasini *et al.* investigated the role of the plasma as ozoner and in PPC configuration for the abatement of various VOCs [64]. It resulted that plasma driven catalysis was more efficient than gaseous ozonation for waste gas treatment due to an “ionizing effect”. It was put forwards that plasma could decompose or shatter the organics arranging molecules to be

more easily destroyed by the catalyst. Anyway some additional works have to be carried out to ascertain such assumptions.

2.5.1. Current applications of MnOx catalysts in PPC systems on toluene abatement

2.5.1.1. The characteristics of MnOx in PPC

This part reviewed the performances of post-plasma catalysis towards toluene abatement focusing in particular on the characteristics of MnOx used as catalyst downstream the plasma reactor. Two Tables have been included in this part for ease of reading. Table 2.3a compiles information on the synthesis and physico-chemical properties of the catalysts while Table 2.3b includes the salient parameters generally considered to play a role in the performances for toluene removal in PPC. From a close look at Table 2.3a it is found that the catalytic formulations, when considering homemade catalysts, include bulk MnOx as single transition metal (TM) oxide [65, 66] or as manganese phosphate Mn-O-P [67] or more usually in a combination with another TM (Cu [65, 68-71], Co [66, 72], Fe [68, 73, 74]) with the possible use of Ag as additive [75]. The active phase can be dispersed on a support such as γ-Al_2O_3, AC (activated carbon) [74], Ni foam [76] and ZSM-5 [72].

Bulk MnOx were prepared by the conventional precipitation method at pH 9-10 using Mn(II) nitrate as precursor. L. Ye *et al.* [66] obtained a mixture of Mn_2O_3 and of the metastable Mn_5O_8 with a specific surface area close to 28 m^2/g after calcination at 400 °C. Quoc An *et al.* [65] reported the preparation of bulk α-MnO_2 (OMS-2) by the redox method performed at 100°C for 24h at pH 1.2 using $KMnO_4$ and $MnSO_4$ as Mn precursors in hydrothermal conditions. Magureanu *et al.* reported the synthesis of manganese phosphate [67]. Three amorphous Mn-O-P catalysts with Mn/P ratios of 1:1.5 (Mn-1), 1: 0.04 (Mn-2) and 1:1 (Mn-3) were prepared from the reaction of MnO_2 with concentrated H_3PO_4 in aqueous/aminoalcohol medium via hydrothermal treatment (Mn-1) but under microwave conditions (Mn-2; Mn-3) using structure directing agents. The final catalysts were obtained after calcination at 550 °C. The increase of Mn loading led to an increase in specific surface area (4.5, 20 and 85 m^2/g for Mn-1, Mn-2 and Mn-3, respectively) accompanied with a change in the pore size distribution from microporous to mesoporous. The XPS Mn AOS showed values less than 4 due to Mn reduction in the presence of the template.

As MnOx exhibit many structures the characterization of the catalyst can be very tricky when dispersed on a support. The parameters which are the most relevant to affect the structure and dispersion are the nature of the Mn precursor, the mode of impregnation, the temperature of calcination, the nature of the

support and the Mn content. As shown in Table 2.3a, the MnOx/γ-Al_2O_3 have all been prepared via wetness impregnation of Al_2O_3 with manganese nitrate and calcined at temperature in the range 350-400 ℃ with Mn amount ranging from 7 to 10 wt% [66, 74, 77]. It has been found that the nitrate precursor leads to mainly β-MnO_2 for a Mn loading of 10 wt% over γ-Al_2O_3 at a calcination temperature of 400 ℃ for 4h [78]. However decreasing the temperature of calcination is expected to increase the dispersion and change the Mn AOS.

Manganese (Mn: 3wt%) was also dispersed by wet impregnation using manganese (II) acetate as Mn precursor on an activated carbon (AC) developing very high surface area (1308 m^2/g) [74]. The MnO/AC catalyst was obtained after calcination at 300 ℃ in N_2 for 2h. The low Mn content, the counter-anion nature of the Mn precursor as well as the conditions of calcination ensured a good Mn dispersion combined to a low Mn AOS. Mn_2O_3 deposited on nickel foam was reported by H. Huang *et al.* [76]. The Ni foam was a special support having a thin and porous structure enabling the pressure drop in the reactor to be greatly reduced. The formation of Mn_2O_3 resulted here from a calcination of the Mn nitrate dispersed on Ni foam at a temperature of 600 ℃.

Although Ag-Mn/HZSM5 showed good activity in the ozonation of toluene, low cost Ag-free multi-component catalysts were investigated to increase the performances. As previously noticed, a second transition metal (TM such as Cu, Fe and Co) can be integrated in combination with Mn. Among the three TM oxides, Fe_2O_3 and Co_3O_4 are p-type metal oxides recognized for having high activity in ozone decomposition by opposition to CuO which is a n-type oxide [39]. However mixing Cu with Mn could lead to hopcalite catalysts recognized as efficient catalysts in O_3 removal [79] and CO oxidation at room temperature [80]. The occurrence of the two redox couples Cu^{2+}/Cu^{+} and Mn^{4+}/Mn^{3+} in the solid was believed to play a role in these catalytic reaction [81]. Additionally, the Cu-Mn-O system was remarkably active in toluene oxidation [8, 82-89]. Beside, enhanced ozone decomposition over Fe-Mn oxides was explained by a lower MnO_2 crystallite mean size, a more defective structure and improved textural properties [90].

Quoc An *et al.* [65] reported the dispersion of copper (5 wt%, 10 wt% and 15 wt%) on α-MnO_2 using wetness impregnation method with nitrate Cu precursor followed by a calcination at 500 ℃ for 4h. However no physico-chemical characterizations can help to the comprehension of the structure of these catalysts. Ye *et al.* reported the synthesis of Co-Mn oxides (Co/Mn atomic ratio of 1:6, 1:1 and 6:1) using the co-precipitation at pH 9-10 using Mn and Co nitrate precursors [66]. The calcination step was performed at 400 ^{o}C for 2 h.

XRD analysis revealed Mn_3O_4, $Co_3Mn_3O_4/Co_3O_4$ and Co_3O_4 for the three increasing Co/Mn ratios, respectively. Hence the Co/Mn ratio of 1.0 allowed a good mixing of Mn and Co in the presence of segregated oxides. Textural properties were improved for the stoichiometric and Co rich catalyst allowing to double the specific surface area in comparison with the MnOx reference catalyst. Additionally the XPS Mn AOS increased when incorporating Co in line with larger number empty d-states and greater reducibility (electron accepting nature) of the active center.

Recently, Y. Huang reported the synthesis of 10 wt% of CoMnOx and CeMnOx (M/Mn = 1; M = Co, Ce) active phases supported on ZSM-5 and of a reference MnOx/ZSM-5 catalyst [72]. The textural properties of the porous support ZSM-5 were the following: BET surface area of 306 m^2/g and average pore size of 9.1 nm. These catalysts resulted from a coprecipitation at pH 9-10 using nitrate precursors followed by a calcination step at 400^oC for 5h. The reference MnOx/ZSM-5 revealed a complex mixture of Mn_3O_4, Mn_2O_3 and MnO_2. The Co based catalyst exhibited the mixed $Co_3Mn_3O_4$ phase in accordance with Ye *et al.* [66]. By opposition only single oxides such as Ce_2O_3, MnO_2, and Mn_3O_4 were observed on the Ce-containing catalyst.

Table 2.3a. The characteristics of Mn oxides in PPC.

Exp.	Catalyst	The Shape of Catalyst	The State of Catalyst	The Support	The Nature of Catalyst	Structure(s) (XRD)	The Synthesis Method/Commercial Company	S_{BET} (m^2/g)	Dp [1] (nm)	Added Characterizations	Reference
1	Cu-Mn/Al_2O_3	Powder	Supported	Al_2O_3	Cu-Mn	-	Heraeus, Hanau, Germany	-	-	-	[70]
2	(a) N 150 (MnO_2–Fe_2O_3)	Pellet	Bulk	-	60 wt. % Fe_2O_3 & 40 wt. % MnO_2	MnO_2	Süd-Chemie (Munchen, Germany)	219	-	-	[74]
	(b) MnO_2/γ-Al_2O_3	**Powder**	**Supported**	**γ-Al_2O_3**	**9 wt. % MnO_2**		**Incipient wetness impregnation, Precursor: Mn nitrate, calcined at 350 °C for 2 h under 100 mL/min air**	**169**			
	(c) MnO/AC			**AC [2]**	**3 wt. % MnO_2**		**Wet impregnation, Precursor: Mn acetate, calcined at 300 °C for 2 h under N_2**	**1024**			
3	(a) Mn-1 (Mn-P-O)	Powder	Bulk	-	Mn-P-O	Amorphous phase	Hydrothermal: MnO_2 with H_3PO_4 (85 wt. %) (Mn:P 1:1.5) in 50 mL distilled water + dimethylaminoalcohol, 170 °C for 48 h	4.5	-	XPS: Mn $2p_{3/2}$: oxidation state of Mn < 4; P $2p_{3/2}$: inorganic phosphates	[67]
	(b) Mn-2 (Mn-P-O)				**Mn-P-O**		**Hydrothermal treatment under microwaves: starting gel: 1.00 P: 0.04 Mn: 0.48 HDTMABr [3]: 0.48 TMAOH [4]: 174.00 H_2O, 60 °C (1 h), 80 °C (1 h), and 300 °C (3 h) then calcination at 550 °C**	**21**	**1.1**		

	(c) Mn-3 (Mn-P-O)				**Mn-P-O**		**Starting gel: 1.00 P: 1.00 Mn: 0.48 HDTMABr : 0.48 TMAOH: 174.00 H_2O, same operating mode than above**	**85**	**3.4, 50**		
4	$CuMn/TiO_2$	Pellets	Supported	TiO_2	3% Cu, 6.8% MnO_2	-	Heraeus, Hanau, Germany	50	-	-	[71]
5	MnO_2/Al_2O_3	Pellets	Supported	Al_2O_3 [5]	7 wt. % MnO_2	-	Wetness impregnation Precursor: Mn nitrate, calcined at 400 °C	-	-	-	[77]
6	Mn_2O_3/Ni foam	Foam	Supported	Ni foam	Mn_2O_3	Mn_2O_3	Impregnation Precursor: Mn nitrate, calcined at 600 °C	10.8	-	XRD: before 400 °C, ultra-fine or amorphous features of phase. After 500 °C, Mn_2O_3	[76]
7	(a) $Cu–Mn/TiO_2$ (a)	Pellet (1.5 mm)	Supported	TiO_2	CuO (3 wt. %) MnO_2 (6.8 wt. %)	-	Hereaus Hanau, Germany	32	-	-	[68]
	(b) Cu–Mn/TiO_2 (b)					-		**50**	-	-	
	(c) Fe_2O_3-MnO_2 (N 150)	**Pellet (6 mm)**	**Bulk**	-	**>40 wt. % Fe_2O_3 >25 wt. % MnO_2**	-	**Süd-Chemie (Munchen, Germany)**	**100**	-	-	
	(d) CuO-MnO_2 (N 140)	**Pellet (5 mm)**			**>15 wt. % CuO >25 wt. % MnO_2**	-		**100**	-	-	
8	Fe_2O_3-MnO_2	Honeycomb [6]	Bulk	-	60 wt. % Fe_2O_3, 30 wt. % MnO_2	-	Süd-Chemie (Japan)	-	-	-	[73]
9	(a) MnO_2/Aluminum honeycomb	Honeycomb	Supported	Aluminum honeycomb	MnO_2	-	Honeycle ZA (Nichias Corporation)	-	-	-	[69]
	(b) MnO_2-CuO	**Pellet (4–6 mesh)**	**Bulk**	-	**MnO_2-CuO**	-	**Moleculite (Molecular Products Limited)**	**20–30**	-	-	

10	(a) OMS-2	Powder	Bulk	-	α-MnO_2	-	Hydrothermal treatment, Redox method, Precursors: $KMnO_4$ + $MnSO_4$ 100 °C for 24 h, pH: 1.2, calcined in static air using a range of time and temperature	-	-	-	[65, 91]
	(b) Cu-OMS-2		**Supported**	**OMS-2 [7]**	**5 wt. % Cu**	-	**Wetness impregnation, Precursor: $Cu(NO_3)_2$ Calcined at 500 °C for 4 h**	-	-	-	
	(c) Cu-OMS-2				**10 wt. % Cu**	-		-	-	-	
	(d) Cu-OMS-2				**15 wt. % Cu**	-		-	-	-	
11	Ag-Mn-O	Powder	Bulk	-	10 wt. % Ag-MnOx	Mn_3O_4 + Ag	Ag-Mn-O: Co-precipitation, pH 10, Precursors: $Mn(NO_3)_2$ + $AgNO_3$ dried at 110 °C for 12 h	-	-	-	[75]
12	a) MnOx	Powder	Bulk		MnOx	Mn_3O_4 + Mn_5O_8	**Precipitation, pH 9-10,** Precursor: Mn nitrate, then calcined at 400 °C for 2 in air.	27.9	-	XPS: lattice oxygen 53.1%	[66]
	b) Co_3O_4-MnO_2				**1:6 = Co:Mn**	**Mn_3O_4**	**Coprecipitation at pH 9-10, Precursor: Mn and Co nitrates calcined at 400 °C for 2 h under in air.**	**29.5**		**XPS: lattice oxygen 56.2%**	
	c) Co_3O_4-MnO_2				**1:1 = Co:Mn**	**$Co_3Mn_3O_4$ + Co_3O_4**		**53.4**		-	
	d) Co_3O_4-MnO_2				**6:1 = Co:Mn**	**Co_3O_4**		**61.6**		-	
13	a) MnOx/ZSM-5	Powder	Supported	ZSM-5	10 %wt MnOx	MnO_2,Mn_2O_3, and Mn_3O_4	Precipitation, pH 9-10, calcined at 400 °C for 2 h in under air. Then wet impregnation with ZSM-5, calcined at 400 °C for 5 h	290.7	3.4	XPS: lattice O at 532.9 eV: 55.2%	[72]
	b) CoMnOx/ZSM-				**10%wt CoMnOx**	$Co_3Mn_3O_4$, MnO_2 and	Coprecipitation. Same experimental procedure	302.8	2.9	XPS: lattice O at 532.9 eV: 59.2%	

5		(Co/Mn =1)	Mn_3O_4	than above			
c) CeMnOx/ZSM-5		**10%wt CeMnOx** (Ce/Mn=1)	**CeO_2,** Ce_2O_3, MnO_2, and Mn_3O_4		**305.6**	**2.9**	**XPS: lattice O at 532.9 eV: 58.3%**

[1] Pore diameter; [2] Activated carbon; [3] Hexadecyltrimethylammonium bromide; [4] Tetramethylammonium hydroxide; [5] Al_2O_3: diameter of granules being 3–4 mm and total surface area being 180 m^2/g; [6] Diameter: 15 mm, length: 75 mm, 500 cells per inch; [7] OMS-2: cryptomelane type manganese octahedral molecular sieve.

2.5.1.2. The performances in toluene abatement using MnOx in PPC

In a first step, the selected variables of the hybrid process related to the experimental conditions of toluene abatement in air were identified. The selected variables were those expected to play a role in the performances of the two-stage plasma-catalyst system towards toluene abatement. The descriptors linked to the performances of the hybrid process in terms of efficiency of the process were also presented. In a second step the effect of these variables on the experimental outcomes (descriptors) was discussed.

Based on data given in the literature the pertinent variables which can play a role have been identified and are related to the NTP reactor (geometry and type of discharge), the (specific) energy density at maximum of toluene conversion, nature of the gaseous effluent, type, shape and weight of the catalyst, GHSV, carbon balance and identified gaseous by-products. Information on the nature of the gaseous effluent includes variables such as kind of the carrier gas, flow rate, inlet toluene concentration and inlet ozone concentration injected into the catalytic reactor. When possible the same type of information is delivered in similar NTP experiments for easier comparison. Information on PPC performances towards toluene abatement includes the following descriptors: toluene removal efficiency associated with the energy put per plasma liter, CO_2/CO selectivity (S_{CO2}/S_{CO}), CO_2 yields (Y_{CO2}) and energy yield (EY).

Table 2.3b compiles the salient information on the application of post-plasma catalysis using MnOx based type catalysts for toluene abatement in air in accordance with the above paragraphs.

First of all, the types of discharges were briefly discussed based on the information given in Table 2.4. Two discharge types were commonly used, such as DBDs (dielectric barrier discharges) with tubular/cylindrical configuration of the NTP reactor [65-67, 72-75] or packed bed DBDs (packing material: glass [69] or $BaTiO_3$ [77]) and positive DC (direct current) corona discharge with pin-to-plate configuration [68, 70, 71].

The most important characteristic of DBDs is that non-equilibrium plasma conditions can be provided in a much simple way. At about atmospheric pressure electrical breakdown occurs in many independent thin current filaments due to the presence of the dielectric. The reactors are generally of tubular/cylindrical forms. These short-lived micro-discharges have properties of transient high pressure glow discharges with electron energies ideally suited for exciting or dissociating background gas atoms and molecules. The flexibility of the NTP reactor with respect to geometrical configuration, operating medium and

operating parameters is well recognized. Efficient available low cost power supplies and additionally easy scaling up for laboratory experiments to large industrials installations taking into account the drawback of high pressure drop make DBDs attractive [92].

The presence of a packing material in the reactor leads to a packed bed DBD reactor. The promising utilization of such reactor is that the dynamics of plasma discharges are predominantly influenced by the properties of the packing material in terms of its dielectric constant. Increasing the dielectric constant enhances the electric field in the vicinity of pellets contact points [93]. Consequently the dielectric constant of a packing material determines the amount of energy that the reactor can store during a single discharge [94].

A corona discharge is an electrical discharge brought on by the ionization of a fluid such as air surrounding a conductor that is electrically charged. Corona discharges take place at or near atmospheric pressure using relatively low power. Corona discharge is a self-sustained discharge which occurs in sharply non-uniform electric field, typically operated in needle-to-plate or wire-to-plate configuration. Corona discharge mainly produces burst pulses corona, then streamer corona, glow corona and spark discharge as the applied voltage increases. Once the streamer corona discharge is formed in a closed chamber, a low temperature dense plasma environment can be generated over a large volume [92**]**. Hence, corona discharge is another approach that can avoid spark formation in streamer channels. The streamers propagation affects the NTP reactions like ionization, excitation, dissociation for VOCs abatement [20].

The experiments listed in Table 2.3b are all carried out at room temperature and atmospheric pressure except Exp.5 for which the catalyst has been heated at 330 ℃. Dry air is used as carrier gas if nothing is mentioned otherwise. The total flow rate and the toluene concentration ranges from 67 to 133,600 $ml.min^{-1}$ and 0.5 ppmv (indoor pollution) to 800 ppmv (range of industrial emission), respectively. The GHSV range from about 10.000 to 40.000 $ml.g^{-1}.h^{-1}$. These extreme values show the wide range of plasma-catalysis application in terms of volume and VOC concentration for treating a waste gas containing toluene. However it has to be mentioned that initial toluene concentration is close to 100 ppmv in most reported studies. The concentrations of ozone at the inlet of the catalytic reactor vary tremendously from 70 to 6000 ppmv depending on the nature of the NTP and to the inlet concentration of toluene. To get read of the influence of the initial toluene concentration the inlet ozone/ inlet toluene molar ratio has been given. The values exhibited in Table 2.3b range herein from 1.3 to 200.

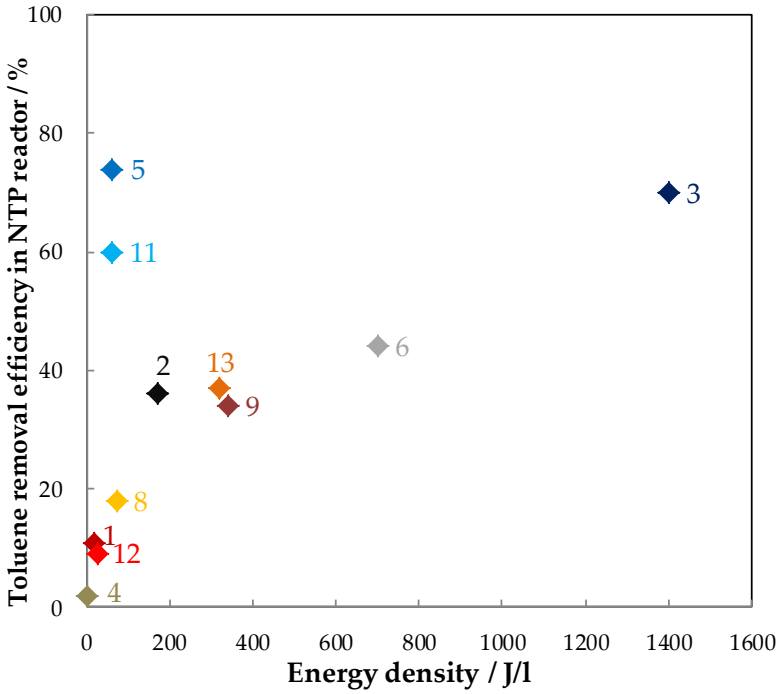

Figure 2.8. Toluene removal efficiency as a function of ED for NTP reactor. The figures mentioned inside the graph refer to the number of the experiment (see Tables 2.3a and 2.3b).

To evaluate the efficiency of the NTP reactors in terms of geometry-discharge, the toluene conversion has been plotted as a function of ED as shown in Figure 2.8. With that respect the characteristics of the NTP reactors have been recalled in terms of geometry and discharge and initial inlet toluene concentration $[C_7H_8]_0$ as shown in Table 2.4. The gap between the 2 electrodes ranges from 2 to 10 mm. The reactor volume V_R ranges from 8.5 to 250 ml and the corresponding residence time (t_r) ranges from 1.4 to 2.5 s except in Exp.1 for which the residence time is very short ($4.5.10^{-4}$ s). The toluene removal efficiencies using corona discharge (Exp.1 and Exp.4) are relatively low compared to those of DBD (Exp.5 and Exp.11) for similar energy density. However this observation has to be tempered as the inlet toluene concentrations associated to corona discharge are rather low (45-0.5 ppmv) compared to those for DBD (100-500 ppmv). However among DBD reactors it is found that Exp.3 and Exp.5 lead to similar toluene conversion but with an energy density ratio ED(Exp.5)/ED(Exp.3) of about 24 noticeably higher than the inlet toluene concentration ratio of 2.5. The $BaTiO_3$ packed bed DBD reactor (Exp.5)

exhibited herein the highest toluene removal efficiency (74 %) at the lowest ED (60 J/L) thanks to the presence of $BaTiO_3$ which enhances the average electric field and to the temperature of the catalytic reactor at 330 °C. In this set of experiments, the effect of the residence time t_r in the NTP reactor is difficult to apprehend as the range of values is too narrow to allow a pertinent discrimination.

Table 2.4. Characteristics of the NTP reactors.

Exp	**1** [70]	**2** [74]	**3** [67]	**4** [71]	**5** [77]	**6** [76]	**7** [68]
	Positive DC Corona discharge (pin-plate)	Glass beads packed bed DBD (cylindrical reactor)	DBD (cylindrical reactor)	positive DC Corona (pin-plate)	$BaTiO_3$ packed bed DBD (cylindrical reactor)	DBD (wire-plate)	Positive DC corona discharge (pin-plate)
C_{tol} (ppm_v)	45	240	200	0.5	500	100	0.5
Gap (mm)	9	6	2	20	-	10	-
V_R[1]/ml (t_r[2]/s)	72 ($4.5.10^{-4}$)	13.2 (2.5)	8.5 (1.7)	250 (1.5)	-	-	250 (1.5)
Exp	**8** [73]	**9** [69]	**10** [65]	**11** [75]	**12** [66]	**13** [72]	
	DBD (tubular reactor)	Multistage reactor	DBD (tubular reactor)	DBD (tubular reactor)	DBD (tubular reactor)	DBD (tubular reactor)	
C_{tol} (ppm_v)	85	70	800	109	107	107	
Gap (mm)	5.65	-	-	2	2.5	4	
V_R[1]/l (t_r[2]/s)	-	-	-	11.9 (1.4)	14.9 (1.8)	-	

[1] Reactor volume; [2] Residence time

In order to investigate the benefit of adding a catalytic reactor downstream the NTP, toluene removal efficiency from PPC experiments has been plotted in Figure 2.9 as a function of toluene removal efficiency from separated NTP experiments. It is remarkable that all the points lie above the bisector showing the beneficial role of integrating a MnOx based catalyst downstream the NTP reactor. All the more the points deviate from the bisector; all the more the catalyst plays a beneficial role when integrated in the PPC process all other things being otherwise equal. The most improvement is obtained in Exp.12 with

a decreasing beneficial effect, depending on the nature of the catalyst, as follows: Exp.12c > Exp.12b > Exp.12d > Exp.12a. Hence, in this case, a direct comparison of the catalyst performances can be undertaken. It is thus found a beneficial role of integrating Co to Mn in equal amount (Exp.12c). The presence of $Co_3Mn_3O_4$, along with a segregated Co_3O_4 spinel phase, promotes toluene removal efficiency compared to the reference MnOx solid. Similarly the catalysts in Exp.13 can be ranked by decreasing activity: Exp.13b > Exp.13c > Exp.13a or more clearly: 13b (10 wt% CoMnOx/ZSM-5, Co/Mn=1) > 13c (10 wt% CeMnOx/ZSM-5, Ce/Mn=1) > 13a (10 wt% MnOx/ZSM-5). Thus, good performances for toluene abatement can be obtained over CoMnOx, as bulk or dispersed on the ZMS-5 support. It was claimed that the mixture of $Co_3Mn_3O_4$, MnO_2 and Mn_3O_4 phases in enhancing structural defects significantly promotes the toluene abatement reaction. Likewise, the different catalysts investigated in Exp.2 can be ranked as follows: MnO/AC (Exp.2c) > MnO_2/Al_2O_3 (Exp.2b) > MnO_2-Fe_3O_4 (Exp.2a). This study underlined the important role of the support as the activity of the catalyst depends mainly on the support. When regarding MnO/AC, the low Mn content, the high surface area of the support, the nature of the counter-anion of the Mn precursor (OAc) as well as the conditions of calcination (in N_2 at 300 °C) ensured a good Mn dispersion combined to a low Mn AOS. These two properties are responsible for toluene oxidation into CO_2 in an effective way. A series of *CuO/MnO₂* catalysts with different *Cu* loadings were synthesized by the incipient wetness impregnation method in Exp.10. Higher activity of 10wt% CuO/MnO_2 can be attributed to a better dispersion of the active phase. However caution must be exercised in the interpretation of these results due to lacking key information such as the $[O_3]/[Toluene]_0$ ratio defined above as well as the CO_2 yield. Additionally the 100% toluene conversion achieved over Ag-Mn-O (Exp.11) has also to be highlighted but however the high silver content (10 wt%) can be a drawback.

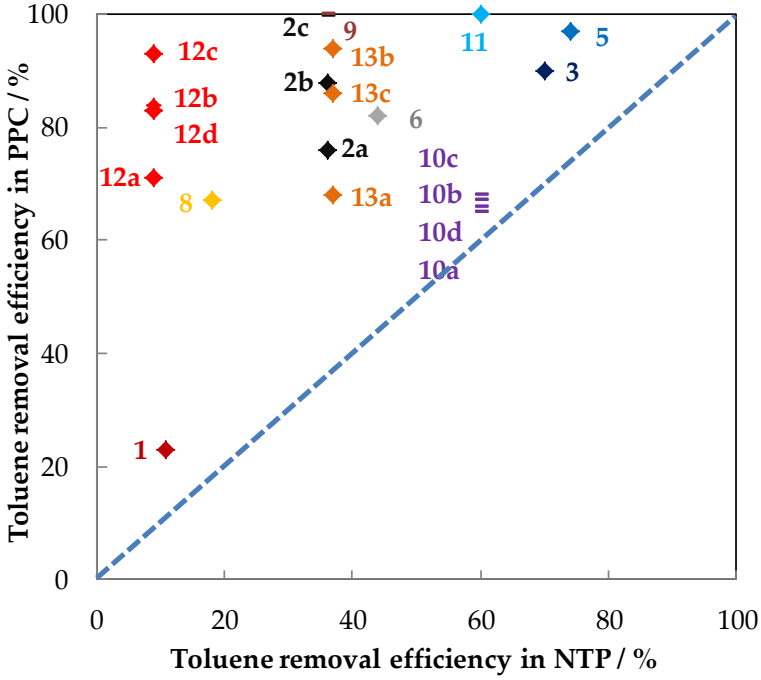

Figure 2.9. Toluene removal efficiency in PPC as a function of Toluene removal efficiency in NTP reactor.

To achieve a better insight in terms of efficiency of the process, which means the total oxidation of toluene into CO_2 and H_2O, the toluene conversion into CO_2 (CO_2 yield) has been drawn as a function of toluene removal efficiency (see Figure 2.10). This representation highlights more accurately the efficiency of the PPC process as the toluene removal efficiency takes only account for the amount of toluene removed making no distinction between CO_2 and other possible organic by-products. The representation allows to distinguish two sets of PPC processes: set 1 delimited by the blue circle and set 2 consisting in the remaining ones. The set 1 includes the most efficient PPC configurations 13b, 3a, and 13c, namely (DBD; CoMnOx/ZSM5), (DBD; Mn-P-O, Mn-1), and (DBD; CeMnOx/ZSM5). Set 2 includes the PPC configurations 2c, 9c, 9a, 9b, 2b, 2a and 13a, namely (Glass packed bed DBD; MnO/AC), (multistage DBD; MnO_2-CuO + MnO_2/Aluminum honeycomb), (multistage DBD; MnO_2/Aluminum honeycomb), (multistage DBD; MnO_2-CuO), (Glass packed bed DBD; MnO_2/γ-Al_2O_3), (Glass packed bed DBD; N150 (MnO_2-Fe_2O_3)) and (DBD; MnOx/ZSM-5). A direct comparison is unfortunately restrictive as it is not possible to get the

information in terms in CO_2 yield from numerous papers as in many papers mineralization rate (or COx selectivity) is given.

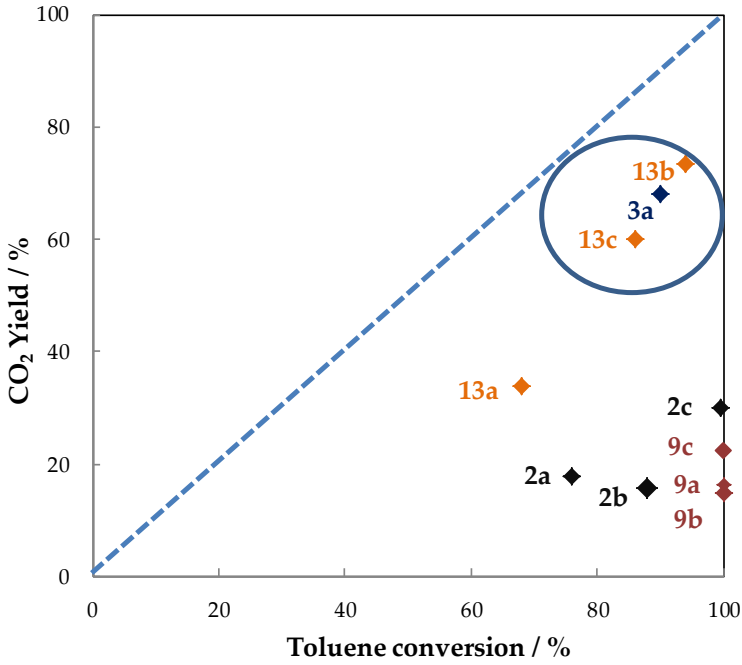

Figure 2.10. CO_2 yield as a function of Toluene removal efficiency in PPC.

Improving the global efficiency of the PPC process requires that the NTP works at low ED while minimizing the formation of undesirable by-products. CO_2 yield as a function of reactor energy density given shown in Figure 2.11 emphasizes the efficiency of the CoMnOx/ZSMS-5 (Exp.13b) and CeMnOx/ZSM-5 (Exp.13a) catalysts located downstream of a DBD reactor to convert toluene into CO_2 at low ED. Additionally as a good performance in terms of CO_2 yield is also achieved with a pulsed DBD reactor in combination with the manganese phosphate catalyst [67] a quite high ED results in an energy yield of 1.84 g/kWh (see below) with a factor of about 2 lower than that of Exp.13 of 4.2 g/kWh.

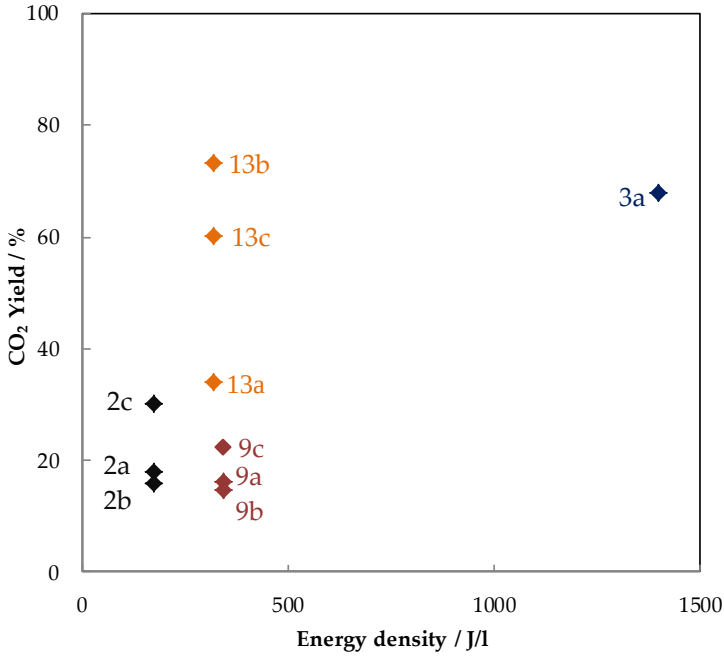

Figure 2.11. CO_2 yield as a function of energy density in PPC.

When considering PPC, the ratio R = $[O_3]_{in}/[Tol]_0$ ($[O_3]$: concentration of ozone injected in the catalytic reactor; $[Tol]_0$: concentration of toluene injected in the NTP reactor) is a key parameter as the O_3 may be in a sufficient amount enabling total mineralization of toluene. Considering the mode of decomposition of O_3 over MnOx the reaction of toluene abatement by O_3 can be formally written as follows:

$$C_7H_8 + 18O_3 \rightarrow 7CO_2 + 4H_2O + 18O_2 \quad (15)$$

The fundamental assumption is that each O_3 is converted to a single O radical and that toluene is oxidized only by active oxygen species on the surface of the catalyst. However, at low toluene conversion, active oxygen species mainly degrade the plasma non processed toluene while at higher conversion they are mainly implied in the degradation of the gaseous carbonaceous by-products produced in the course of the NTP treatment whose relative distribution is dependent on the nature of the NTP all things being equal.

R has been represented as a function of toluene conversion into CO_2 in Figure 2.12. Despite the very limited set of values it is observed a clear linear dependence of R as a function of toluene conversion into CO_2. This shows the

efficiency of these catalysts to decompose ozone when the value of R is higher than 18.

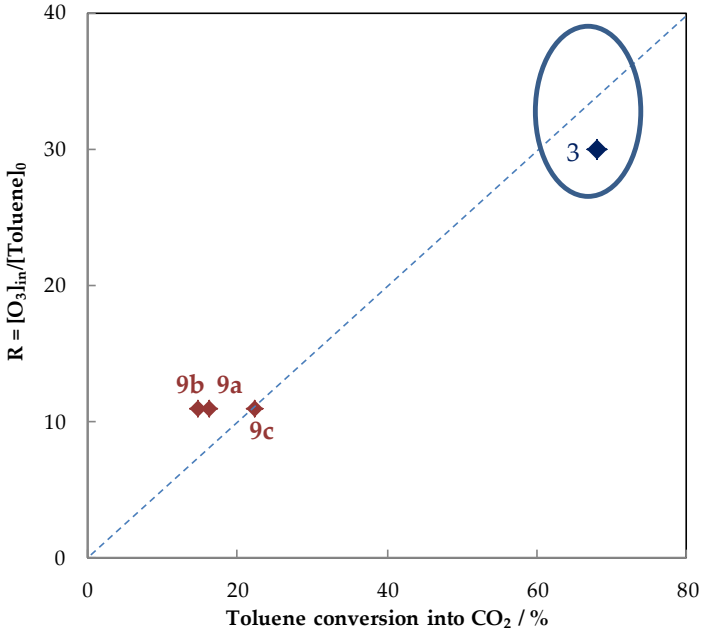

Figure 2.12. R = $[O_3]_{in}/[Tol]_0$ as a function of CO_2 yield in PPC.

Good performances are obtained with a pulsed dielectric barrier discharge (DBD) at atmospheric pressure and room temperature in combination with manganese phosphate catalyst (Mn-1) placed downstream.

CO and N_2O can be detected as by-products. Benzaldehyde, formic acid, methylbenzoquinone, benzyl alcohol, benzoic acid, and benzyl benzoate constitute some examples of organic by-products which can be identified as intermediates on the surface in the reaction process. These by-products derived from the partial oxidation of toluene. The detection of such ad-species in a strong interaction with the catalyst can cause a decrease in activity of the catalyst in the course of the reaction and leads to a decrease of the carbon mass balance. In the experiments given here no O_3 is detected at the catalytic reactor confirming the efficiency of the catalysts in O_3 decomposition.

The efficiency of the process has also been evaluated in terms of energy yield expressed in grams of toluene removed by kWh (g/kWh). The histogram given in Figure 2.13 sums up the results. The ranking of PPC configurations in terms of

decreasing energy efficiency for the most efficient configurations is: Exp.12 (22-28) ≈ Exp.11 (24) > Exp.2 (14-19) > Exp.8 (11) > Exp.1 (8) > Exp.13 (3-4) ≈ Exp.9 (1.7-3.1). The energy yields can vary from a factor 20 considering all the configurations.

The stability of the based Mn oxide catalysts in the reactive gaseous mixture over time was investigated in few PPC processes. Durability test carried out for 43 h showed good stability for Ag-Mn-O (Exp.11) [75] in terms of either CO_2 generation, toluene decomposition and ozone degradation. The strong interaction between metallic Ag and Mn_3O_4 was postulated to promote the oxidation of intermediate compounds at room temperature. Durme *et al.* [71] also reported that no deactivation of the commercial catalyst Cu-Mn/TiO_2 (10 g, 3 wt% Cu, 6.8 wt% MnO_2) was observed for 48h on stream in PPC configuration at room temperature. The reasons were ascribed to two points. Firstly, no significant amounts of active sites were blocked due to low amount of toluene (0.5 ppmv). Secondly, adsorbed degradation products may also be oxidized efficiently due to high ozone decomposition ability of Cu-Mn/TiO_2. Therefore, the high ozone decomposition ability of metal-MnOx (e.g. Ag, Cu) can prevent catalyst deactivation.

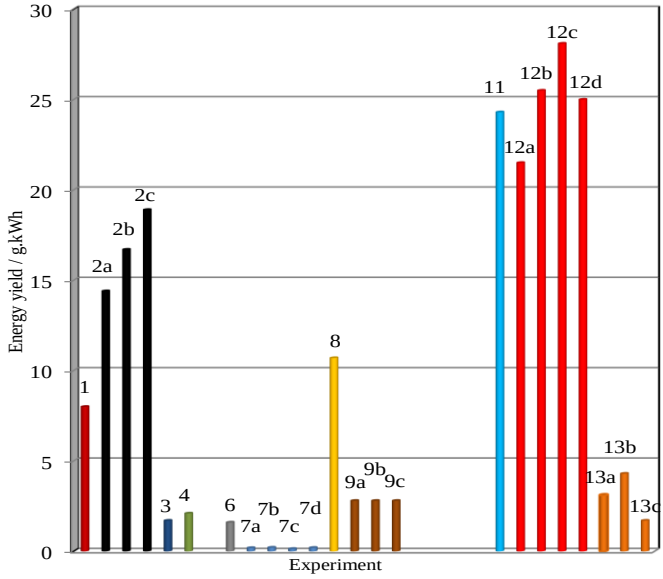

Figure 2.13. Energy yield as a function of the PPC process.

Table 2.3b. Overview on toluene removal with MnOx based catalysts in PPC.

Exp.	Discharge Type (NTP Reactor)	Catalyst (weight/g)	Configuration	Carrier Gas Flow Rate (mL/min)	Toluene (ppm)	RH (%)	Inlet Ozone (ppm)	Inlet Ozone/Inlet Toluene	GHSV ($mL.g^{-1}.h^{-1}$)	MRE [1] (%)	ED [2] (J/L)	EY [3] (g/kWh)	$S_{CO2}/(S_{CO})$ (%)	Y_{CO2} (%)	By-Products CB [4]	Reference
1	Positive Corona discharge (pin-plate)	Cu-Mn/Al_2O_3 (-)	PPC	Air 133,600	45	-	60	1.3	-	22.8	18.7	8	-	-	-	[70]
		-	NTP	Air 133,600	45	-	-	-	-	10.8	18.7	4	-	-	-	
2	Glass beads packed bed DBD (cylindrical reactor)	(a) N 150 (MnO_2–Fe_2O_3) (1)	PPC	Air 315	240	-	-	-	18,900	76	172	14.4	23.5 (16.5)	17.9	CB [2]: 52.6%; O_3: 3.9 ppm	[74]
		(b) MnO_2/γ-Al_2O_3 (1)				-	-	-		88		16.7	18 (14)	15.8	CB: 36.3% O_3: 14.6 ppm	
		(c) MnO/AC (1)				-	-	-		99.7		18.9	30.2 (24.8)	30.1	CB: 55%. O_3: 8 ppm	
		-	NTP	Air 315	240	-	-	-	18,900	36	172	6.9	6	2.2	S_{CO}: 8%, CB: 38.8% O_3: 8 ppm	
3	DBD (Cylindrical reactor)	(a) Mn-1 (Mn-P-O) (0.2)	PPC	Air 300	200	-	6000	30	90,000	90–95	1400	1.7–1.8	73 (27)	65.7 – 69.4	CB: ~100%	[67]
		(b) Mn-2 (Mn-P-O) (0.2)				-		30					72 (28)	64.8 – 68.4	CB: ~100%	
		(c) Mn-3 (Mn-P-O) (0.2)				-		30					68 (32)	61.2 – 64.6	CB: ~100%	
		-	NTP	Air 300	200	-	-	-	90,000	70–75	1400	1.3–1.4	-	-	-	
4	Positive DC corona discharge (Pin-plate)	CuOMnO_2/TiO_2 (10)	PPC	Air 10,000	0.5	-	~18	36	60,000	78	2.5	2.1	-	-	NO_2: ~550 ppm at 15 J/L	[71]
		-	NTP	Air 10,000	0.5	27	-	-	60,000	4	2.5	0.1	-	-	-	
5	$BaTiO_3$	7 wt. %	PPC	Air	500	-	-	-	60,000	97 [5]	60	-	-	-	CO: ~300 ppm	[77]

	packed bed DBD (Cylindrical reactor)	MnO_2/Al_2O_3 (7 mL)	NTP	1000 Air 1000	500	-	-	-	8600 h^{-1}	74 [5]	60	-	-	-	-	
6	DBD (wire-plate)	Mn_2O_3/Ni foam (-)	PPC	Air 200	100	-	150	1.5	-	82	700	1.6	-	-	Ozone: 9 ppm	[76]
		-	NTP			-	-	-	-	44	700	0.8	-	-	-	
7	Positive DC corona discharge (pin-plate)	(a) Cu–Mn/TiO_2(a) (15)	PPC	Air 10,000	0.5	50	~70	140	40,000	40	14	0.19	-	-	-	[68]
		(b) Cu–Mn/TiO_2(b) (15)					~100	200		63	20	0.21	-	-	-	
		(c) Fe_2O_3-MnO_2 (N 150) (15)					~82	164		34	15.8	0.14	-	-	-	
		(d) CuO-MnO_2 (N 140) (15)					-	-		47	-	0.20	-	-	-	
8	DBD (tubular reactor)	Fe_2O_3-MnO (-)	PPC	Air 2500	85	-	330	3.9	-	67	72	10.7	-	13 [4]	Gas: Benzene Solid: benzaldehyde, methylbenzoquinone, benzyl alcohol, benzoic acid, and benzyl benzoate	[73]
		-	NTP	Air 2500	85	-	-	-	-	18	72	2.8	-	7 [4]	Formic acid, Acetic acid and benzene	
9	Multistage reactor	(a) MnO_2/Aluminum honeycomb (-)	PPC	Air +10,000	70	-	766	10.9	-	100	342	2.8	16.3	16.3	CO: 48 ppm; N_2O:18 ppm	[69]
		(b) MnO_2-CuO (-)						10.9	-	100			14.7	14.7	CO: 8 ppm; O_3: 117 ppm; N_2O: 21 ppm	
		c) MnO_2/Aluminum honeycomb+ MnO_2-CuO (-)						10.9	-	100			22.4	22.4	CO: 10 ppm; N_2O: 18 ppm	
		-	NTP	Air 10,000	70	-	-	-	-	~36	342	1.0	10.8	3.9	CO: 16 ppm; O_3: 1327 ppm; N_2O: 23 ppm	
10	DBD (Cylindrical reactor)	(a) OMS-2 (0.2)	PPC	80% N_2 +20% O_2 +	800	-	-	-	20,000	65	18 kV and	-	-	-	-	[65, 91]

				66.67						50 Hz						
		(b) 5 wt. % Cu-OMS-2 (0.2)				-	-	-		67		-	-	-	-	
		(c) 10 wt. % Cu-OMS-2 (0.2)				-	-	-		68		-	-	-	-	
		(d) 15 wt. % Cu-OMS-2 (0.2)				-	-	-		66		-	-	-	-	
		-	NTP	80% N_2 + 20% O_2 + 66.67	800	-	-	-	20,000	60		-	-	-	-	
11	DBD (tubular reactor)	Ag-Mn-O (0.2)	PPC	Air + 498	108	-	650	6.0	150,000	100	60	24.3	-	-	N_2O and CO	[75]
		-	NTP	Air +498	108	-	-	-	150,000	60	60.	14.6	-	-	O_3:650 ppm N_2O and CO	
12	DBD (tubular reactor,)	(a) MnOx	PPC	Air + 500	107	-	580	5.4	32,233 h^{-1}	71	48	21.5	-	-	O_3: 280 ppm N_2O, CO	[66]
		(b) (1:6) Co_3O_4-MnO_2						5.4		84		25.5	-	-	O_3: 180 ppm N_2O, CO	
		(c) (1:1) Co_3O_4-MnO_2						5.4		93		28.1	-	-	O_3: 90 ppm N_2O, CO	
		(d) (6:1) Co_3O_4-MnO_2						5.4		83		25.0	-	-	O_3: 110 ppm N_2O, CO	
		-	NTP	Air + 500	107	-	-		32,233 h^{-1}	~24	48	7.3	-	-	-	
13	DBD (tubular reactor)	(a)MnOx/ZSM-5	PPC	Air + 1000	107	12 mL/min air bubbling water	-	-	-	68	320	3.1	50 (8)	34	N_2O, O_3: 370 ppm	[72]
		(b)CoMnOx/ZSM-5					-	-		94		4.3	78 (8)	73.3	N_2O, O_3: 200 ppm	
		(c)CeMnOx/ZSM-5					-	-		86		3.9	70 (8)	60.2	N_2O, O_3: 260 ppm	
		-	NTP	Air + 1000	107		-	-	-	~37	320	1.7	-	-	-	

[1] MRE: Maximum removal efficiency; [2] ED: Energy density; [3] EY: Energy yield; [4] Carbon balance; [5] PPC and NTP experiments performed at 330 °C; [6] YCOx (CO + CO_2)

2.6. Conclusion

The desire to increase the efficiency of toluene depollution processes by reducing their energy consumptions while simultaneously reducing toluene emission to meet the more stringent limits has motivated considerable research in advanced toluene oxidation processes. Among them PPC is a promising method which takes full advantages of the two technologies: high selectivity from catalysis and the easy operation from NTP allowing the hybrid system to work at ambient temperature. A greater CO_2 selectivity can be achieved due to the production of active oxygen produced from plasma generated O_3 catalytic decomposition to remove the by-products. Recent progress in the research on *noble* metal-free catalysts has highlighted the importance of manganese oxide based formulations to be involved in such a process. This is because manganese oxides are low-cost, easily synthesized, environmentally friendly and efficient catalysts in ozone decomposition and toluene ozonation.

The best catalytic formulations include Ag-Mn-O, amorphous manganese phosphate, 10 wt%(CoMnOx)/ZSM-5 and MnO/AC. Besides, Co, Ce and Ag are the most efficient additives to promote O_3 decomposition in interaction with manganese oxide. Furthermore Co allows to get good performances in moist air which opens encouraging perspectives. It has to be mentioned that some Ag has to be introduced in the formulation to promote the desorption of organic ad-species and to ensure a good time-on-stream-stability. In terms of energy yields, the PPC configuration of the DBT tubular reactor with Co_3O_4-MnO2 (Co:Mn=1:6) catalyst downstream ensures an efficient use of the energy.

Despite the promising improvements resulting from several studies about using related Mn based oxides active phases, there are still open issues to be addressed regarding the design of the catalyst in order to develop an efficient hybrid process. To improve the efficiency of the catalysts many strategies can be pursued, such as external morphology control, doping, optimization of the active Mn related phase with the nature of the support. Interestingly, the effect of the external morphology of MnOx which is easily to tune has to be deeply investigated as it may have a significant impact on the density of vacancies, of defects, as well as on the Mn average oxidation state and textural properties of the materials. The role of additives has not been cleared up sufficiently and the effect of other TM oxides has to be investigated in order to minimize CO, NOx, N_2O and possible O_3 as by-products.

Finally, the stability of the based Mn oxide catalysts in the reactive gaseous mixture over time has to be investigated more deeply. The carbon balance has to

be carried out. Although the beneficial cleaning effect of Ag has been evidenced, the decrease of Ag loading has to be performed while maintaining satisfactory catalytic performances. In regard the effect of inhibitors such as water as also to be investigated.

CHAPTER 3: MATERIALS AND METHODS

3.1. Introduction

Throughout this chapter, the abatement of two VOCs (toluene and trichloroethylene (TCE)) in combination with different catalysts and/or in combination with non-thermal plasma is discussed in details in 3 different parts:

The first part is dedicated to the abatement of toluene with non-thermal plasma (NTP). All experiments described in this section were conducted at Ghent University.

The second section focuses on the catalytic abatement of toluene with Cu-Mn oxides being the catalyst of choice. The experiment itself consisted of catalyst preparation and characterization as well as set-up optimization and experimental process analysis. All experiments described in this section were conducted at the University of Lille.

The last part describes the post-plasma catalytic (PPC) abatement of TCE using either CuMnOx-R3 or $CuMn_2O_4$-P4 as the catalyst material. This part describes both the setup and the experimental process. The experiments of this part were conducted at Ghent University.

3.2. Plasma-assisted experiment

3.2.1. Objective

Toluene was chosen as the VOC model for the experiments involving only plasma. The environmental and health problems associated with toluene have been already discussed in details in chapter 2.

A packed-bed DBD system is the reactor that has been adopted since it was shown to exhibit considerably higher energy efficiency in terms of VOC abatement compared to the conventional NTP reactors. This is due to the presence of beads that help to reduce the breakdown voltage, which is favorable for the production of micro-discharges between the packed materials. As a result, both the process stability and the performance are considerably enhanced.

Along with the PPC experiments, single plasma experiments were also conducted. This allowed for a better understanding of the principles of plasma production, the reactions between the active species and the VOC, and the effects of humidity on the abatement efficiency.

3.2.2. Setup description

A schematic representation of the experimental setup is given in **Figure 3.1**. It consists of three main parts: (1) the reaction gas supply system, (2) the DBD packed bed plasma reactor and (3) the analytical instrumentation. Each of these parts will be described in details in the following paragraphs.

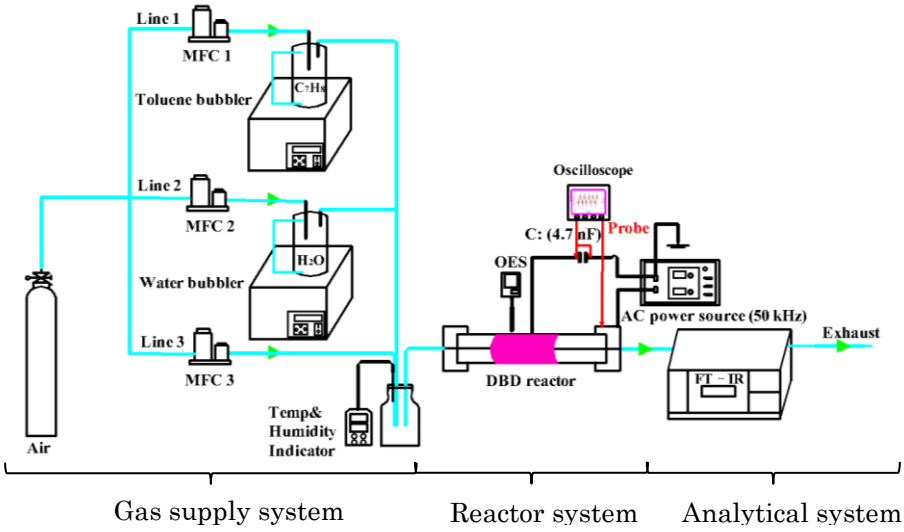

Figure 3.1. Experimental set-up used for plasma-assisted toluene abatement (OES: optical emission spectroscopy; C: capacitor)

3.2.2.1. Plasma treatments

Dry air (Alphagaz 1, Air Liquide) was adopted as the carrier gas in the experiments. Toluene (99.5%) was acquired from Carl Roth (Belgium) and was stored in a glass gas-bubbler. Distilled water (Eurowater), also stored in a gas-bubbler, was used to adjust the humidity in the DBD reactor. The bubblers were kept in a water bath of 31 °C, as depicted in **Figure 3.2a**, in order to keep toluene and distilled water at a constant temperature. The flows of air, water and toluene were adjusted and maintained by 3 separate mass flow controllers (MFC) (Bronkhorst®, El Flow®) as depicted in **Figure 3.2b**.

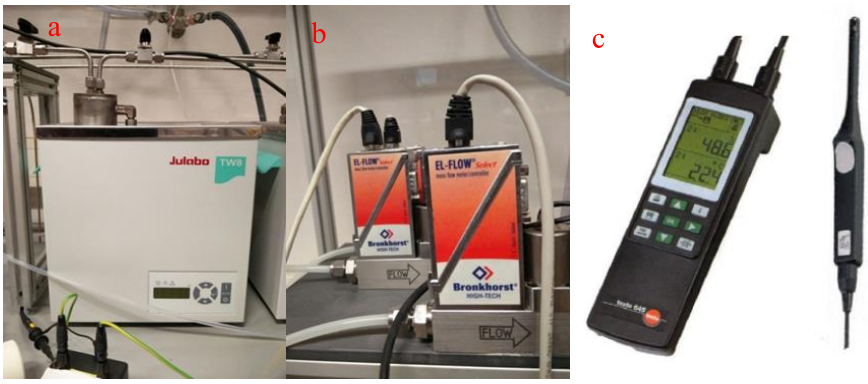

Figure 3.2. Gas supply system with (a) water bath device, (b) MFC, (c) Testo 445 climate measurement device with temperature/humidity probe

Humidity determination

The humidity was controlled by varying the flow of dry air through the distilled water. As described above, the container filled with distilled water was placed in a water bath at 31 ℃ to maintain a good reproducibility. The different flow rates used during the experiments are listed in **Table 3.1**. A humidity indicator was used to monitor the induced changes in RH %. (**Figure 3.2 c**). The temperature/humidity probe (TESTO 445) was located in a closed vessel in which the feed gas can circulate. The vessel was placed between the gas supply system and the reactor inlet (**Figure 3.1**).

Table 3.1. The flow rate of MFC in different RH %

RH (%)	MFC 1 (L/min)	MFC 2 (L/min)	MFC 3 (L/min)	Total flow (L/min)
0	1.000	0	0.0075	1.0075
20	0.805	0.195	0.0075	1.0075
40	0.620	0.380	0.0075	1.0075
60	0.500	0.500	0.0075	1.0075

3.2.2.2. DBD reactor

DBD packed bed plasma reactor

The DBD plasma reactor itself is schematically presented in **Figure 3.3** and 3.4. It consists of a quartz cylinder having a diameter of 22 mm, a length of 250 mm and a wall thickness of 3 mm. The inner electrode made up of a stainless steel rod with a diameter of 8 mm, is fixed along the reactor axis. A stainless

steel iron mesh, acting as the outer electrode, is placed on the outer surface of the quartz tube over a length of 86 mm. The discharge gap between the two parallel electrodes is filled with 30 g of glass beads having a diameter of 3 mm. The beads are kept in place by using quartz wool on the sides. The volume of the discharge is 3.83 cm^3 and the corresponding residence time of the gas in the plasma zone is 0.23 s.

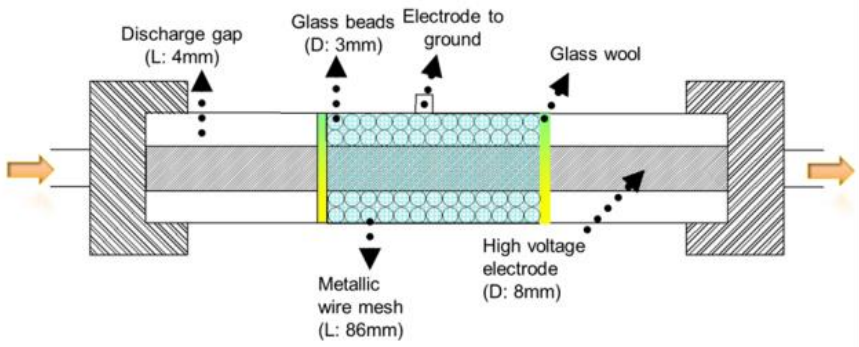

Figure 3.3. Schematic representation of the packed bed DBD reactor

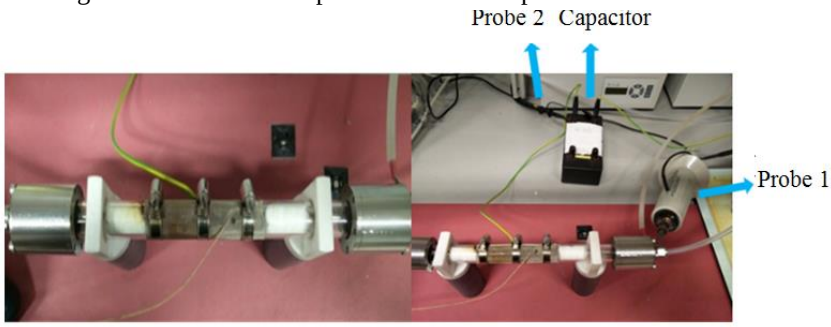

Figure 3.4. DBD systems with (a) DBD reactor; (b) voltage-current measurement circuit

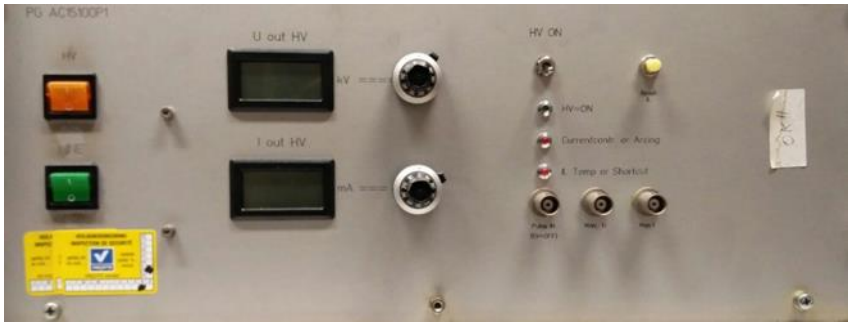

Figure 3.5. Photo of AC power source

An AC high voltage source (**Figure 3.5**) with amplitudes ranging between 5.5 and 7.0 kV and with a fixed frequency of 50 kHz is connected to the inner electrode. The outer electrode is connected to the ground through a capacitor of 7.9 nF (**Figure 3.4 b**).

Energy measurement

The I-V graph was used to measure the discharge energy, as seen in **Figure 3.6**. The current-voltage plots were obtained from the oscilloscope data as described in the following paragraph. These plots were used to determine the discharge power in the DBD reactor, as the electrical energy consumed per current discharge cycle equals the voltage multiplied by the current per discharge cycle. The discharge power P was then calculated by multiplying the electrical energy by the frequency of the feeding voltage (50 kHz).

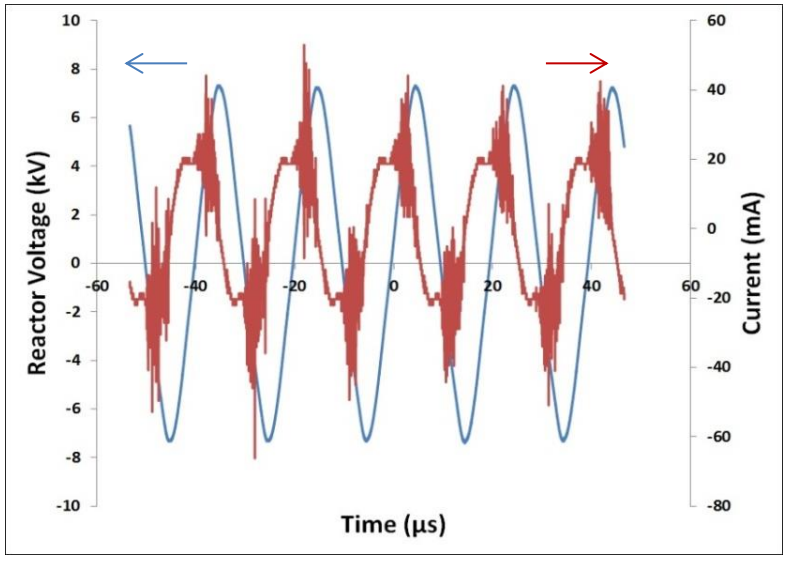

Figure 3.6. I-V graph measured at power of 3.6 w

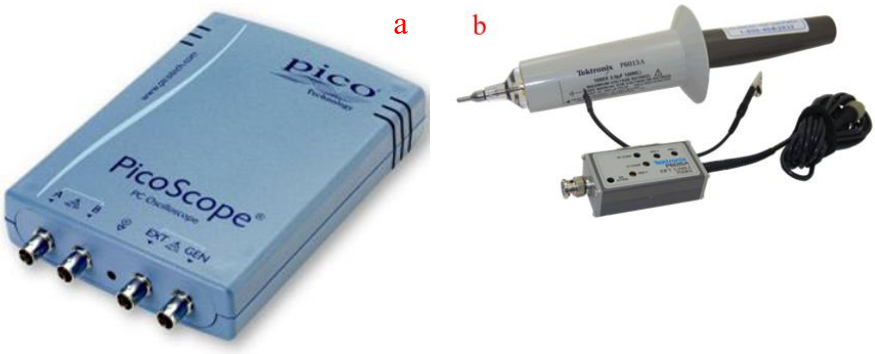

Figure 3.7. The energy measurement device with (a) oscilloscope, (b) high voltage probe

The applied high voltage was measured using a 1000:1 high voltage probe (Tektronix P6015A, **Figure 3.7 b**). The charge stored on the electrodes was monitored by measuring the voltage across the capacitor connected in series to the ground electrode. The resulting voltage-charge waveforms were recorded via a digital oscilloscope (PicoScope 3204A, **Figure 3.7 a**).

The applied energy used to maintain the discharge in DBD reactor was calculated according to equations 1-4. The amount of charge transported across the capacitor equals the charge transported across the DBD reactor, and can be calculated as follows:

$$Q_{reactor} = Q_{capacitor} = I_{reactor} \cdot dt = I_{capacitor} \cdot dt \quad \text{(Eq. 3.1)}$$

Q being the charge stored in the capacitor; I the current across the capacitor and dt the time.

The energy of the total discharge, also referred to specific input energy (SIE), can be calculated according to the following equations:

$$E = \frac{1}{T}\int_{t=0}^{T} VI \cdot dt \quad \text{(Eq. 3.2)}$$

$$P = E \times f \quad \text{(Eq. 3.3)}$$

$$\text{SIE (J/l)} = \frac{discharge\ power\ (W)}{gas\ flow\ rate\ (l/s)} \quad \text{(Eq. 3.4)}$$

E being the discharge energy, T the discharge time, V the voltage across the reactor, I the current of the capacitor, P the discharge power and f the discharge frequency.

Optical emission spectroscopy (OES)

The excited atoms and ions present in a plasma discharge are known to generate a unique emission spectrum specific to each element. Numerous characteristic emission spectral lines can be defined for each element. By identifying and quantifying these peaks, it is possible to acquire crucial information on the influence of the humidity on the excited species generated by the discharge.

Two types of optical emission spectrometers were used in this series of experiments. All optical emission spectra were collected through an optical fiber placed perpendicularly to the axis of the quartz tube and located a few millimeters away from the middle of the discharge region. Overview spectra of the discharge were recorded in a spectral range of 200 to 900 nm using an Ocean Optics spectrometer S2000 with a resolution of 1.3 nm. High resolution spectra were obtained for gas temperature determination using a second spectrometer (Avantes AvaSpec-3048) with a resolution of 0.05 nm.

3.2.2.3. Gas analyzing instrumentation

To analyze the chemical composition of the gaseous stream, FT-IR spectroscopy (Bruker, Tensor 27) was employed with the configuration shown in figure 3.8. Infrared spectroscopy is based on molecular vibration resonance. When exposed to infrared radiations, molecules will selectively absorb specific wavelength radiations which cause a change in their dipole moment. Consequently, the vibrational energy levels of the molecules will transfer from a ground state to an excited state.

The frequency at which the molecule will adsorb the radiation is determined by the vibrational energy gap. The number of possible absorption peaks is directly related to the number of vibrational freedoms of the molecule. The intensity of absorption peaks is related to the extent of the change in dipole moment and the possibility of the transition of energy levels. Therefore, by analyzing the infrared spectrum, one can readily obtain abundant structural information of a molecule.

Figure 3.8. Gas analyzing instrumentation with (a) FT-IR, (b) cell in FT-IR (c) gas cell

The following experimental conditions were used to measure the FT-IR spectra of both the background and the sample. After a steady-state was observed, the next measurement was conducted automatically.

- Instrument type: Tensor 27 Sample Compartment RT-DLaTGS
- Accessory: General Type-Transmittance
- Gas cell: 20 cm optical path length
- Resolution: 4 cm^{-1}
- Sample scan number: 10 scans
- Background scan number: 20 scans
- Saved data from 4000 cm^{-1} to 600 cm^{-1}

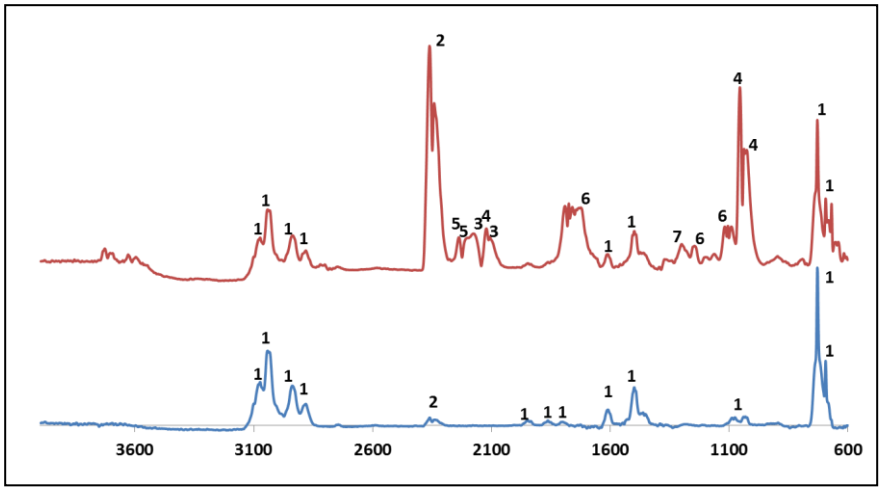

Figure 3.9. FTIR (Fourier-transform infrared spectroscopy) spectra showing the inlet gas (blue) and after abatement at SIE 230 J/l (red) in dry air (1: toluene, 2: CO_2, 3:CO, 4: O_3, 5: N_2O, 6: HCOOH)

Figure 3.9 shows an example of spectra of the gas before and after discharge in dry air. After discharge, the peak of toluene decreased, and other byproducts started to appear in the red spectrum. The methodology was used for identifying and quantifying the byproducts, the description is in next section.

3.2.3. Calibration experiments

Toluene calibration

A gas cylinder (Air products, 200 bar) containing a predefined mixture of 552 ppm of toluene in air was connected to the setup to calibrate the intensity of the absorption peaks. During calibration, a flow rate of 1 L/min (identical to the flow rate applied during the experiments) was maintained. **Figure 3.10 b**. shows an FT-IR spectrum of toluene under calibration conditions. Compared to the standard spectrum of the National Institute of Standards and Technology (NIST) (**Figure 3.10 a**), the representative peaks are located at almost the same positions. The peak area lying from 3060.2 to 3019.4 cm^{-1} was chosen for toluene concentration integration. The different steps performed during the calibration process are described below:

1. After measuring the background of FT-IR spectrometer, the calibration gas (552 ppm of toluene in air) was fed into the system until the complete cylinder was empty.

2. After recording the FT-IR spectrum, the peak area in the range of 3060.2 to 3019.4 cm^{-1} was recorded for 10 minutes.
3. A linear regression was applied to the average integration area as a function of time, and the slope (K1) was used to calculate toluene concentration.

   The explanation of K1:

$$K1=\frac{C_{toluene}}{S_{toluene}}=1665.3 \quad \text{(Eq. 3.5)}$$

Where $C_{toluene}$ is the predefined concentration of toluene (ppm) and $S_{toluene}$ the absorbance of the integration area.

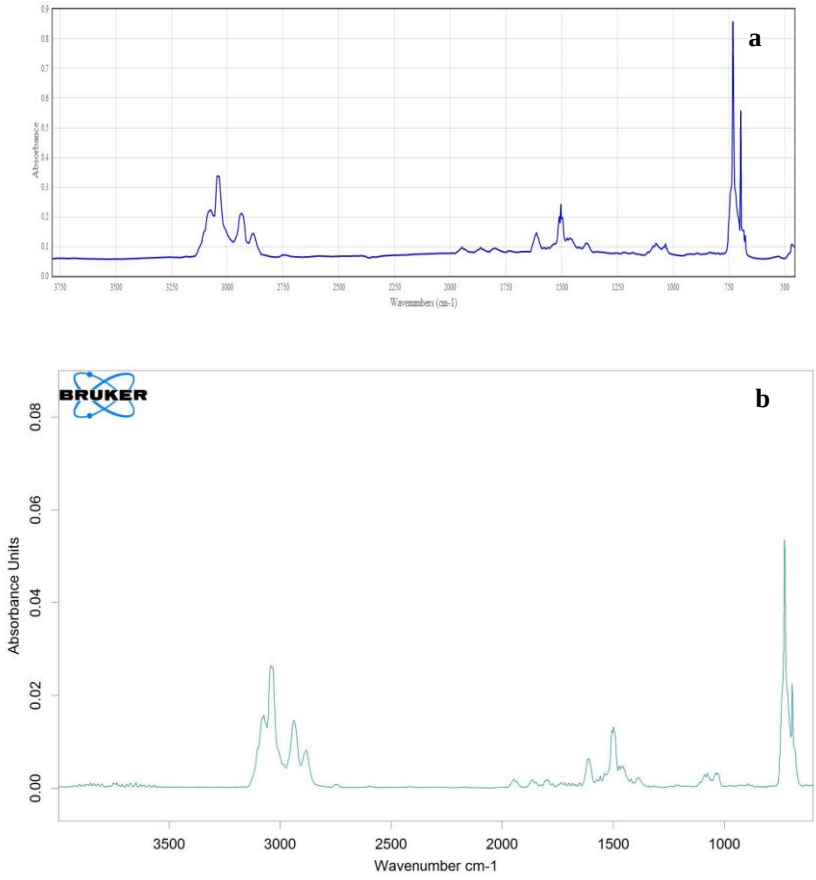

Figure 3.10. FT-IR spectrum with (a) toluene spectrum from NIST [95], (b) calibration experiment result (toluene cylinder: 522 ppm)

CO_x calibration

A cylinder (Air Products, 200 bars) containing a predefined mixture of CO_x was used for CO_2 and CO calibration. The composition of the calibration gases was:

CO_2: 250 ppm, CO: 250 ppm, TCE: 500 ppm.

The cylinder of mixed gases was fed into the system at a flow rate of 1 L/min, as seen in figure 3.11 d. When comparing the spectrum of figure 3.11 d. to the spectrum of CO_2, CO and TCE from NIST (**Figure 3.11 a, b, c**), one can notice that they are located at similar wavenumbers. After identifying the compounds of CO_x, an integration process was performed as following:

1. After determination of the FT-IR spectrometer background, the calibration gas was fed into the system.
2. The peak areas between 2388.4-2287.2 cm^{-1} (CO_2) and 2140.32-2071.37 cm^{-1} (CO) were integrated.
3. During the calibration experiment, the integration data were recorded continuously to avoid any experimental error.
4. Linear regression analysis was applied to the integration area values, and the slopes of lines K2 and K3 were used to calculate the CO_x concentrations. K2 and K3 were defined as following:

$$K2 = \frac{C_{co2}}{S_{co2}} = 128.1 \quad \text{(Eq. 3.6)}$$

$$K3 = \frac{C_{co}}{S_{co}} = 8660.5 \quad \text{(Eq. 3.7)}$$

C_{COx} being the concentration present in the calibration gas (ppm) and S_{COx} the absorbance of the integration area.

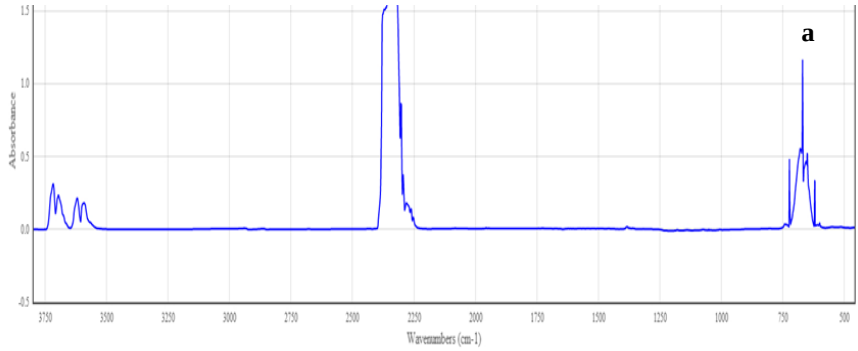
a
Absorbance
Wavenumbers (cm-1)

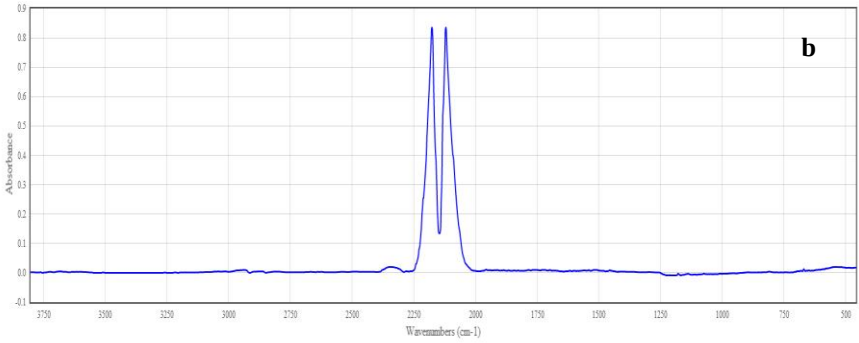
b
Absorbance
Wavenumbers (cm-1)

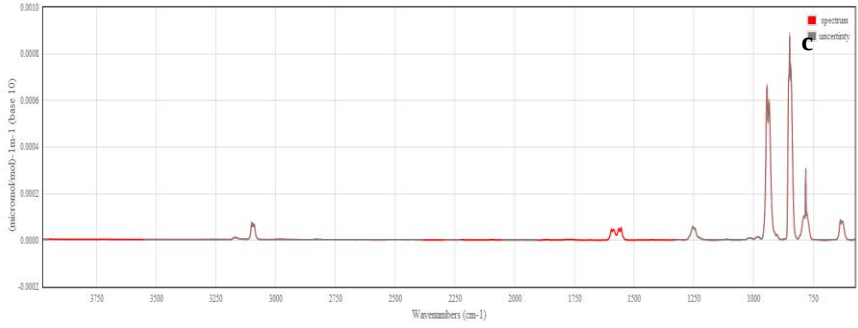
c
spectrum
uncertainty
(micromol/mol)-1m-1 (base 10)
Wavenumbers (cm-1)

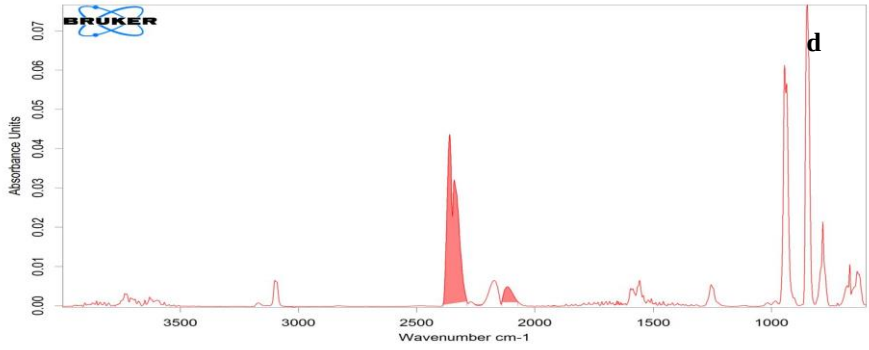
BRUKER
d
Absorbance Units
Wavenumber cm-1

Figure 3.11. FT-IR spectrum with the (a) CO_2 spectrum from NIST [96], (b) CO spectrum from NIST [97], (c) TCE spectrum from NIST [98]and (d) calibration experiment result (condition as described above)

O_3 calibration

The calibration of ozone was done differently compared to the other gaseous compounds, because ozone is not commercially available as a calibration gas since it is highly unstable. The ozone present during the experiments was generated in-situ by the plasma discharge.

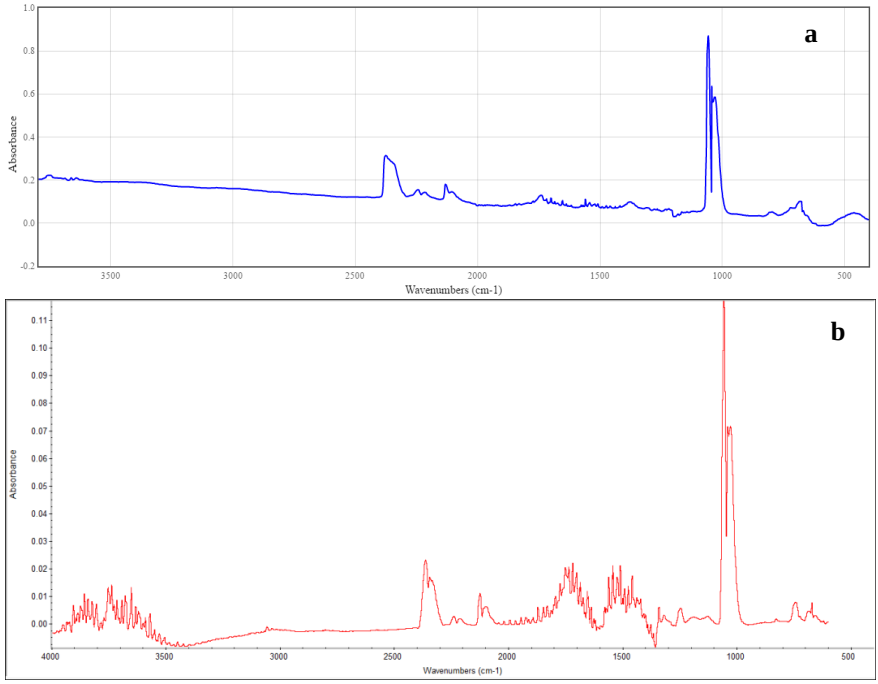

Figure 3.12. FT-IR spectrum with (a) O_3 spectrum from NIST [99], (b) calibration experiment result (Flow rate:1 L/min; Discharge voltage: 5.5 kV)

To identify the adsorbed peaks of ozone, the discharge voltage was set at 5.5 kV and the flow rate of dry air was set at 1 L/min. The resulting FT-IR spectrum is given in **Figure 3.12 b**. Based on the available ozone spectra from NIST (**Figure 3.12 a**), the characteristic ozone peaks can be identified in the range of 1067.17 to 1043.78 cm^{-1}, which was the area selected for integration.

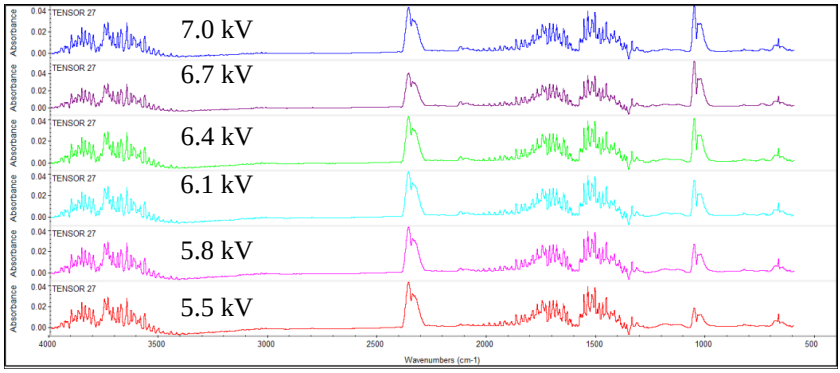

Figure 3.13 FT-IR spectrums with different voltage discharge

To quantity the amount of generated ozone during the abatement experiments, an ozone monitor was connected to the system (Envitec, model 450, 0-1000 ppm, see **Table 3.2** for more details). Dry air was fed into the DBD reactor at a flow rate of 1L/min. Different discharge voltages (5.5 kV, 5.8 kV, 6.1 kV, 6.4 kV, 6.7 kV and 7.0 kV) were studied, as shown in **Figure 3.13**. The ozone-enriched gas was passed through the FT-IR spectrometer and the measurements were conducted in threefold for each voltage. The effluent gas was passed through the ozone monitor continuously, thus measuring the ozone concentration in situ. Based on the measurements at different discharge voltages, the ozone concentration is obtained via linear regression, similar to what has been described for the other calibration processes:

Linear regression analysis was applied to the integration area values. The slope of line K4 was used to calculate the O_3 concentrations. K4 was defined as the following:

$$K3 = \frac{C_{O3}}{S_{O3}} = 1138.3 \qquad \text{(Eq. 3.8)}$$

Table 3.2 The parameters of the ozone monitor

Measurement rage (ppm)	Detectable limit (ppm)	Sample flow rate (L/min)	Accuracy (%)	Resolution (ppm)
0-1000	0.003	1-2.5	±0.1	0.01

NO_x calibration

The NO_x calibration curve was determined similarly to the ozone calibration process. A flue gas analyzer (Testo 350, for more detailed information see **Table 3.3**) was mounted onto the outlet of FT-IR. This device can record the concentration of the NO_x in real-time and can calculate the average concentration

over a certain time-period. Due to the high concentrations of NO_x present during the experiments, a dilution factor of five, automatically processed by the Testo device, was applied.

Table 3.3 The parameters of Testo 350 flue gas analyzer

Compounds	Measurement rage (ppm)	Accuracy (%)	Resolution (ppm)
NO	1500-20000	± 5	10
NO_2	500-2500	± 5	1

Dry air was fed at a rate of 1 L/min into the DBD reactor, and measurements were performed at a fixed series of discharge voltages to establish the calibration curves. Each FT-IR lasted 5 minutes per one discharge power. Similarly to what has been described for the other calibration processes, a linear regression analysis was applied to the integration area values, and the slopes of lines K5 and K6 were used to calculate the NO_x concentrations. K5 and K6 were defined as following:

$$K5 = \frac{C_{NO2}}{S_{NO2}} = 4568.2 \quad \text{(Eq.3.9)}$$

$$K6 = \frac{C_{NO}}{S_{NO}} = 20834 \quad \text{(Eq.3.10)}$$

In summary, the calibration parameters for all compounds are listed in **Table 3.4**. All concentration calculations that will be further described in the chapter are based on this table.

Table 3.4 The summary of calibration parameters

Compound	Formula	Wavenumber (cm^{-1})	K
Toluene	$C_6H_5CH_3$	3060.2-3019.4	1665.3
Carbon dioxide	CO_2	2388.4-2287.2	8660.5
Carbon monoxide	CO	2140.32-2071.37	128.1
Ozone	O_3	1067.17-1043.78	1138.3
Nitrogen dioxide	NO_2	1640.24-1622.7	4568.2
Nitrogen oxide	NO	1928.92-1882.9	20834

3.2.4. Plasma experiment process

Experimental process for the dry air experiments

1. The reactor was filled with a fixed mass (25 g) of glass pellets (3 mm).

2. Dry air was sent in at a flow of 1 L/min for 15 min until a steady-state was obtained

3. Background spectra were measured for the FT-IR spectrometer

4. Toluene was bubbled in at a rate of 7.5 ml/min equaling a concentration of ~350 ppm as discussed at the beginning of the chapter. Toluene concentration was sampled in intervals of 30 s for at least 1 hour to guarantee a stable toluene gas flow.

5. The AC power supply was turned on and the energy was calculated as described above.

6. The effluent gas was sampled at intervals of 30 s for 1 hour by the FT-IR spectrometer. Meanwhile, the concentration of CO_x and NO_x and the conversion of toluene were recorded.

7. When the experiment was finished, the AC power supply was turned off and a final check was done to see if the effluent of the reactor matched the effluent before the experiment.

Plasma experiment in humid air

For the humidity experiments, the same steps were followed as described above, except for step 2 that was changed as following:

The flow rates of dry air through the water gas-bubbler were set according to the values given in **Table 3.1**. As mentioned before, the total flow rate of air and water was kept constant at 1 L/min. After a stabilization period of 10-15 min, step 3 was started.

3.3. Catalysis experiment

3.3.1. Catalyst preparation

Preparation of $CuMn_2O_4$ by co-precipitation method

$CuMn_2O_4$ was prepared by hydrolysis of metal nitrates in aqueous solutions as inspired by the work of Einaga et al [100] (co-precipitation). By following their synthesis strategy, the dissolution of Cu^{2+} species in the mother solution could be avoided.

For the co-precipitation synthesis of the $CuMn_2O_4$, the following chemicals were used: $Cu(NO_3)_2 \cdot 3H_2O$ (Sigma-Aldrich, >99%), $Mn(NO_3)_2 \cdot 4H_2O$ (Sigma-Aldrich, >97%) and $NMe_4OH \cdot 5H_2O$ (Sigma-Aldrich, >97%) (pH regulator).

The molar ratio of Cu/Mn in the catalyst is 1:2. The main reactions occurring during the synthesis were the following:

$$2\ NMe_4OH + Mn^{2+} + 2NO_3^- = Mn(OH)_2 + 2\ NMe_4NO_3 \quad \text{(Eq. 3.11)}$$

$$2\ NMe_4OH + Cu^{2+} + 2NO_3^- = Cu(OH)_2 + 2\ NMe_4NO_3 \quad \text{(Eq. 3.12)}$$

The start concentrations of the different chemicals used during the co-precipitation synthesis are listed in **Table 3.5**.

Table 3.5 The required amount of chemicals for the co-precipitation synthesis

	$Cu(NO_3)_2 \cdot 3H_2O$	$Mn(NO_3)_2 \cdot 4H_2O$	$NMe_4OH \cdot 5H_2O$	$CuMn_2O_4$
n(mol)	0.005	0.01	0.03	0.005
M(g/mol)	241.60	251.01	181.23	240.62
m_{req}(g)	1.208	2.510	5.437	1.203
Purity (%)	99.0	97.0	97.0	-
m_{acu}(g)	1.220	2.510	5.437	-

req: required mass, acu: actual mass

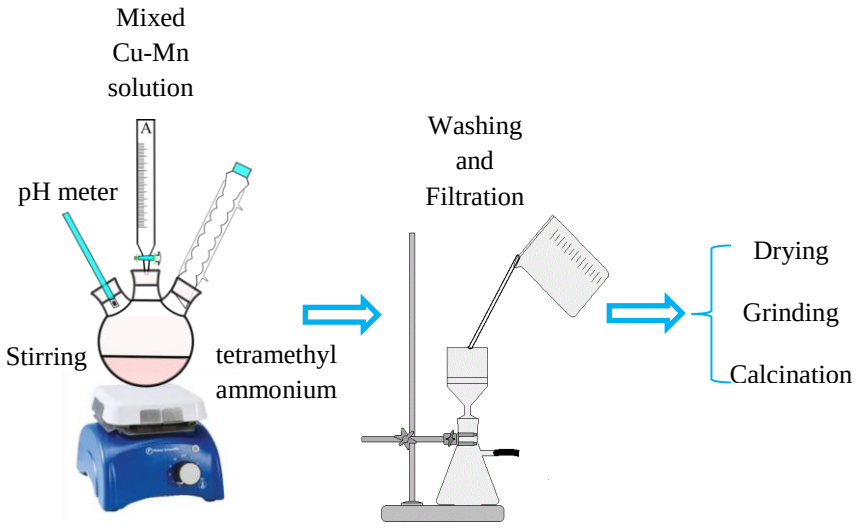

Figure 3.14 The schematic diagrams of Cu-Mn oxides in co-precipitate preparation method

1.220 g of Cu(NO3)2 3H2O was dissolved in 10 ml of distilled water, resulting in a blue solution. The concentration and pH of the $Cu(NO_3)_2$ solution were 0.5mol/L and 3.3, respectively. Next, 2.588 g of $Mn(NO_3)_2$ $4H_2O$ was dissolved in 20 ml of distilled water, which turned the solution to pink. The concentration of $Mn(NO_3)_2$ was 0.5mol/L and a pH of 2.2 was recorded. The two abovementioned solutions were mixed together and vigorously stirred for 25 min at room temperature using a magnetic stirrer (FISHER SCIENTIFIC FB15001) (figure 3.14). In a subsequent step, the mixture (pH=2.4) was added dropwise, using a burette, to an aqueous solution that contained 0.5 mol/l of (TMAH) tetramethylammonium hydroxide (pH= 11.7), as depicted in **Figure 3.14**. After the entire solution was added dropwise, an incubation time of 15-20 min at room temperature was set to obtain a complete solid-liquid separation. pH measurements were conducted periodically until a pH of 7.2, indicating a complete phase separation, was measured. The resulting colloidal particles were filtered out and washed several times with distilled water until a pH equal to 6 (the pH of the distilled water) was reached. After washing, the precipitate was kept dry at 100 ℃ for 24 h.

Once a complete precipitation of the metal hydroxides was achieved, the molar ratios of TMA to Mn^{2+} and TMA to Cu^{2+} were both equal to 2.

After co-precipitation, the hydroxides were filtered and subjected to a calcination step:

$$O_2 + 2Cu(OH)_2 + 4Mn(OH)_2 \xrightarrow{400\ H} 2\ CuMn_2O_4 + 6H_2O \qquad \text{(Eq. 3.13)}$$

During calcination, air was sent into the reactor at a flow rate of 0.3 ml/min. The calcination temperature was increased from room temperature to 400 ^{o}C at a constant heating ramp of 2 ℃/min (duration time = 187.5 min) using a temperature controller (ERALY BP19-F-78590). Once the calcination temperature was reached, it was kept constant for 5 h until a black powdered catalyst was obtained.

For comparison, the same procedure was used for single metal oxides of CuOx and MnOx.

Preparation of $CuMnO_x$ by the redox method

The following synthesis procedure was inspired from the one reported by Njagi et al [101].

For the redox synthesis of $CuMnO_x$, the following chemicals were acquired: $CuMnO_x$ catalyst, the $Cu(NO_3)_2\ 3H_2O$ (Sigma-Aldrich, >99%), $Mn(CH_3COO)_2\ 4H_2O$ (Sigma-Aldrich, >99%) and $KMnO_4$ (Sigma-Aldrich, >99%).

The molar ratio of Cu / Mn of the final catalyst is 1 :1. The main reactions occurring during synthesis were the following:

$$2KMnO_4 + 3Mn(CH_3COOH)_2 + 2H_2O \rightarrow 5MnO_2 + 2\ KCH_3COO + 4\ CH_3COOH \qquad \text{(Eq. 3.14)}$$

$$Cu^{2+} + 2OH^- \rightarrow Cu(OH)_2 \qquad \text{(Eq. 3.15)}$$

$$(X-3)O_2 + 2Cu(OH)_2 + 2MnO_2 \xrightarrow{300} 2CuMnOx + 2H_2O \qquad \text{(Eq. 3.16)}$$

The start concentrations of the different chemicals used during the redox synthesis are listed in **Table 3.6**.

Table 3.6 The required amount of chemicals for the redox synthesis

	0.01	0.006	0.004	0.01

241.60	245.09	158.03	
2.416	1.471	0.632	
99.0	99.0	99.0	-
2.440	1.486	0.638	-

req: required mass, acu: acutural mass

2.440 g of $Cu(NO_3)_2$ $3H_2O$ was dissolved in 50 ml of distilled water, resulting in a blue solution. The concentration was 0.2 mol/l and a pH of 3.9 was recorded. Next, 1.486 g of $Mn(CH_3COO)_2$ $4H_2O$ was dissolved in 50 ml of distilled water. The concentration was 0.12 mol/l and a pH of 7.2 was measured. In a following step, the two solutions were mixed together and vigorously stirred for 5 min at room temperature, using the magnetic stirrer.

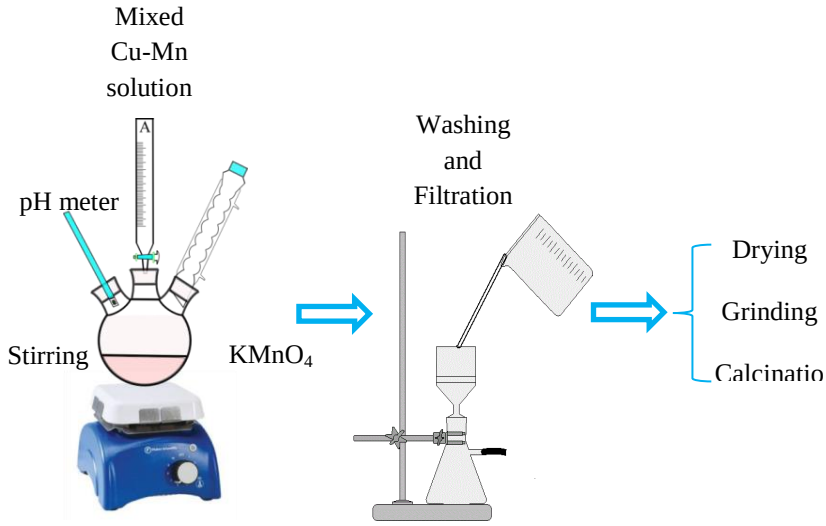

Figure 3.15. The schematic diagrams of Cu-Mn oxides in redox preparation method

Once mixed, the Cu-M aqueous solution was added dropwise to an aqueous solution containing 0.08 mol/L of $KMnO_4$. During the addition process, the $KMnO_4$ solution was stirred vigorously at 350 rpm. Before mixing, the pH of $KMnO_4$ solution was found to be 7.6. Once the mixing started, the pH of the Cu-Mn-$KMnO_4$ solution decreased progressively until a value of 4.3 was reached at the end of the reaction. The resultant precipitate was stirred continuously for 24 h at a speed of 350 rpm.

The synthesized particles were filtered out and washed several times with distilled water until a neutral pH of 6 was obtained (around 1 L of distilled water was used). After filtering, the precipitate was kept dry at 100 ℃ for 12 h.

In a final step, the catalyst was placed into a furnace for calcination. During calcination, air was sent into the reactor at a rate of 0.3 ml/min. The calcination temperature was increased from room temperature to 300 ℃ at a constant heating ramp of 2 ℃ min^{-1} (duration time: 137.5 min). Once the desired calcination temperature was reached, a steady temperature was maintained for 2 h. After calcination, a brown solid was obtained.

For comparison, the same procedure was used for single metal oxide of MnOx and CuMnOx calcined at 200 ℃.

Synthesis of M-CuMnOx-R3 (M= Pd,Pt)

The synthesis of the catalyst M-CuMnOx (M=Pd, Pt) was done via a wet impregnation method [102] as shown in **Figure 3.16**.

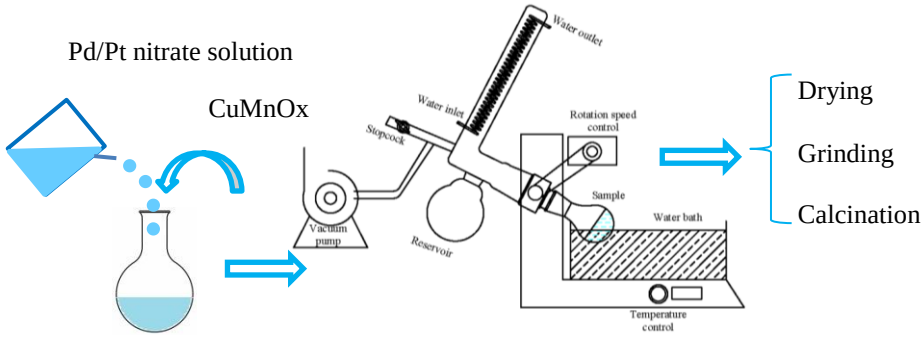

Figure 3.16. Scheme of M/CuMnOx preparation process.

0.5 wt% of M was prepared using either $Pd(NO_3)_2$ $2H_2O$ (Sigma-Aldrich, 40% Pd basis, Assay: 100%) or $Pt(NH_3)_4(NO_3)_2$ (Sigma-Aldrich, 50% Pt basis, Assay: 99.24%).

For preparing 440 mg 0.5 wt% of $Pd/CuMnO_x$, the following calculation steps were made:

$$\frac{m_{Pd}}{0.44+m_{PdO}} \times 100 = 0.5 \qquad \text{(Eq. 3.17)}$$

$$n_{Pd} = n_{PdO} \rightarrow \quad \frac{m_{Pd}}{M_{Pd}} = \frac{m_{PdO}}{M_{PdO}} \; dOm_{PdO} = \frac{M_{PdO} \times m_{Pd}}{M_{Pd}} \qquad \text{(Eq. 3.18)}$$

$M_{Pd(NO3)2\ 2H2O}$ = 266.46 g/mol; M_{Pd} = 106.42 g/mol; M_{PdO}= 122.42 g/mol

$$m_{Pd} = 0.002212\ g$$

$$m_{\mathrm{Pd(NO3)22\ H2O}} = 0.00552\ g$$

For 40% Pd basis of $Pd(NO_3)_2\ 2H_2O$:

$$m_{actual} = m_{\mathrm{Pd(NO3)2{\cdot}d(NO}} = 0.00552\ g$$

For preparing 440 mg, 0.5 wt% of $Pt/CuMnO_x$, the calculation is shown below:

$$\frac{m_{Pt}}{0.44+m_{PtO}} \times 100 = 0.5 \qquad \text{(Eq. 3.19)}$$

$$n_{Pt} = n_{PtO} \rightarrow \quad \frac{m_{Pt}}{M_{Pt}} = \frac{m_{PtO}}{M_{PtO}}\ \ tO m_{PtO} = \frac{M_{PtO} \times m_{Pt}}{M_{Pt}} \qquad \text{(Eq. 3.20)}$$

$M_{Pt(NH3)4(NO3)2}$ = 387.21 g/mol; M_{Pt} = 195.084 g/mol; M_{PtO}= 211.084g/mol

$m_{Pt} = 0.002212\ g$

$$m_{\mathrm{Pt(NH3)4(NO3)2}} = 0.00439\ g$$

For 50% Pt basis of $Pt(NH_3)_4(NO_3)_2$:

$$m_{actual} = \frac{m_{\mathrm{Pt(NH_3)_4(NO_3)_2}}}{99.24\%} = 0.00442\ g$$

The required starting concentrations for the wet-impregnation-based synthesis are summarized in **Table 3.7**.

Table 3.7 Summary of the required chemicals

	$Pd(NO_3)_2\ 2H_2O$	$Pt(NH_3)_4(NO_3)_2$	CuMnOx
n(mmol)	0.0207	0.0113	
M(g/mol)	266.46	387.21	
m_{req} (g)	0.00552	0.00439	440
Assay (%)	100.0	99.24	-
m_{acu}(g)	0.00552	0.442	-

req: required mass, acu: acutural mass

The synthesis process was similar for both Pd and Pt (figure 3.16). A predefined amount of $Pd(NO_3)_2\ 2H_2O$/ $Pt(NH_3)_4(NO_3)_2$ (table 3.8) was dissolved in 30 ml of distilled water in round-bottom flask. The obtained concentrations of $Pd(NO_3)_2$ and $Pt(NO_3)_2$ were 0.69 mmol/L and 0.377 mmol/L respectively. 440 mg of CuMnOx were added into the aqueous Pd/Pt precursor, and the resulting mixture was stirred constantly at 60 ℃, using a rotary evaporator (rotational speed: 20 rotations/min) under a pressure of 70 mbar (Büchi Rotavapor R-114).

The obtained solids were kept to dry overnight at 80 ℃. In a final step, the catalyst was put into a furnace for calcination. During calcination, air was sent into the reactor at a rate of 0.3 ml/min, while the calcination temperature was increased from room temperature to 300 ℃ at a constant heating ramp of 2 ℃ min^{-1} (duration time: 137.5 min). Once the calcination temperature was reached, the process was continued for 4 h at constant temperature.

A complete summary of all the catalysts prepared is listed in **Table 3.8**.

Table 3.8 The nomenclatures of catalysts prepared in different methods

Solid	Nomenclature
Cu-Mn oxides (co-precipitation/precipitation)	CuOx-P4
	MnOx-P4
	$CuMn_2O_4$-P4
Cu-Mn oxides (redox)	MnOx-R3
	CuMnOx-R2
	CuMnOx-R3
M/CuMnOx-R3 (doping)	Pd/ CuMnOx-R3
	Pt/ CuMnOx-R3

P: precipitation or co-precipitation, R: redox-precipitation, 2, 3 and 4 stand for calcination temperature of 200, 300 and 400 ^{o}C, respectively.

3.3.2. Catalyst characterization

Inductively coupled plasma optical emission spectrometry (ICP-OES)

ICP-OES is an analytical technique used for the detection of trace metals. ICP-OES was applied for determining the relative concentrations of Cu, Mn, Pt and Pd present in the catalyst.

For this series of experiments, an ICP-OES spectrometer (720-ES Agilent) with an axially viewing and a simultaneous CCD detection was employed. Before the actual analysis, a pretreatment was required:

10 mg of dried and grounded sample catalyst was dissolved in 1,5 mL of concentrated Aqua Regia. The solution was then heated to 50 ℃ and stirred for 12 h at a constant temperature. Afterwards, the sample volume was readjusted to 50 mL by adding ultrapure water.

To quantitatively determine the metal content in the catalysts, certified standard solutions were used for calibration. With the aid of the ICP Expert^{TM} software (version 2.0.4) it was possible to make a good approximation of the metal content by estimating the weight percentage of the component.

ICP-OES is an analytical technique used for the detection of trace metals. ICP-OES was applied for determining the relative concentrations of Cu, Mn, Pt and Pd present in the catalyst.

For this series of experiments, an ICP-OES spectrometer (720-ES Agilent) with an axially viewing and a simultaneous CCD detection was employed. Before the actual analysis, a pretreatment was required:

10 mg of dried and grounded sample catalyst was dissolved in 1,5 mL of concentrated Aqua Regia. The solution was then heated to 50 ℃ and stirred for 12 h at a constant temperature. Afterwards, the sample volume was readjusted to 50 mL by adding ultrapure water.

To quantitatively determine the metal content in the catalysts, certified standard solutions were used for calibration. With the aid of the ICP Expert™ software (version 2.0.4) it was possible to make a good approximation of the metal content by estimating the weight percentage of the component.

Sample phase analysis by X-ray powder diffraction (XRD)

XRD is a rapid, non-invasive analytical technique primarily used for phase identification of crystalline materials. XRD analysis was applied on the different catalysts to identify the presence of CuO_x, MnO_x and Cu-MnO_x, thus guaranteeing that each catalyst was composed of the desired chemical composition.

The XRD patterns of the different catalysts were obtained using a D8 Advanced Bruker AXS diffractometer. The wavelength of CuKα1 X-ray radiation was 1.5418 Å. The configuration for Bragg-Brentano diffractometer was theta-2 theta. The samples were immobilized on ceramic glass (Macor) holders. The angle (2θ) of XRD was varied between 10 and 70° with a step size of 0.02 °and an integration time of 3 s.

$$\text{Duration time} = \frac{70^o - 10^o}{0.02^o} \times 3s = 2.5\ h \qquad \text{(Eq. 3.21)}$$

Sample phase analysis by XRD as a function of temperature

To investigate the evolution of the amorphous phase as a function of the temperature (from room temperature to 800^o C) in various atmospheres (air, N_2), $CuMnO_x$ was analyzed using a Bruker D8 advanced diffractometer equipped with a High-Resolution Energy-Dispersive 1-D Detector (LYNXEYE XE) and a XRK 900 Environmental reaction chamber. The wavelength of CuKα1 X-ray radiation was 1.5418 Å. The running conditions for the X-Ray tube were 40 kV and 40 mA. The configuration for Bragg-Brentano diffractometer was theta-2 theta. Samples were immobilized on ceramic glass (Macor) holders.

During the experiment, the angle (2θ) was varied between 10 and 70° with a step size of 0.02 ° and an integration time of 3 s. The experimental test was

performed with Air/N_2 (50 ml/min). Temperature was increased from room temperature to 800 ^{o}C at a ramp rate of 10 ^{o}C/min. For each atmosphere (air, N_2), the sample was analyzed using the same condition at every 100 ^{o}C and the spectrum was captured at every temperature point (duration: 2.5 h). The total duration time of the experiment was 17.5 h.

Duration time from room temperature to 100 ^{o}C= (100-25)/(10*60)+2.5=$2\frac{5}{8}$ h

Duration time from 100-200 ^{o}C = (200-100)/(60*10)+2.5=2 $\frac{2}{3}$ h

Total duration time= 7* 2 $\frac{2}{3}$ h + $2\frac{5}{8}$ h =17h 17.5 min

X-ray photoelectron spectroscopy (XPS)

XPS is a surface-sensitive semi-quantitative spectroscopic technique that measures the elemental composition of the first few nm. When applying high-resolution settings, the chemical state of the material can also be determined via peak deconvolution analysis, allowing for the quantification of the chemical state of the catalyst. For Cu-Mn oxides, XPS measurements were performed to acquire the elemental composition and chemical states of Cu, Mn and O.

XPS experiments were performed at room temperature under ultra-vacuum conditions (pressure = 2.3×10^{-7} pa) using an AXIS Ultra DLD Kratos spectrometer equipped with a monochromatized aluminum source (Al Kα = 1486.7 eV) and a charge compensation gun. The vacuum prevented the contamination of the surface and made it possible to carry out the analysis of the emitted photoelectrons. The mode of operation of the hemispherical analyzer (ΔE / E) was constant. The power of the source was maintained at 150 W, and the passing energies of the high resolution and the overview survey were 40 eV and 160 eV with step sizes of 0.1 eV and 1 eV respectively. The detection limit is about 0.1 atomic percentage. All binding energies were referenced to the C 1s core level peak at 284.8 eV.

Simulation of the experimental photo-peaks was carried out using a mixed Gaussian/Lorentzian peak fit procedure according to the software supplied by CasaXPS. Semi-quantitative analysis was accounted for a nonlinear Shirley background subtraction. The XPS quantification was performed from the study of the peak core levels Cu2p, Mn2p, Mn3s, C1s, O1s and N1s.

The catalysts were denoted based on the AOS of Mn. The AOS of Mn was calculated based on the binding energies of the doublet separation of Mn3s (ΔE). The equation is described as follows[103]:

AOS Mn= $8.956 - 1.13\Delta E$. (Eq. 3.22)

Due to the overlapping of the Cu2p and Mn LMMb Auger peaks, the intensity of Cu2p was recalculated by removing the contribution of the Mn Auger peak from the whole envelope. The ratio of (Mn2p)/(Mn LMMb) with MnOx-P4 was used as reference in order to obtain the intensity of Mn LMMb auger peaks of Cu-Mn oxides (CuMnOx-R3/R2 or $CuMn_2O_4$-P4).

In PPC experiments, Cl is found in XPS spectra. For simulation of Cl compounds, the following principle is obeyed: the FWHM of Cl 2p3/2 and Cl 2p1/2 should be equal: $\frac{Cl\ 2p3/2}{Cl\ 2p1/2} = \frac{\sigma\ 2p3/2}{\sigma\ 2p1/2}$ and Cl 2p spin-orbit splitting (Δ=1.6 eV).

Temperature-programmed reduction (TPR)

TPR is a technique for the characterization of heterogeneous catalysts and the quantification of their reduction capacity. CuO_x, MnO_x and Cu-Mn oxides were tested by TPR to compare the relative changes in reduction capacity.

0.050 g of catalyst samples were prepared for the TPR tests. H_2-based TPR experiments were performed using a Micromeritics Autochem catalyst analyzer equipped with a quartz U-shaped microreactor. A H_2/Ar gas mixture was sent into the reactor at 50 mL/min while the reactor temperature was increased from room temperature to 500 °C at a heating rate of 5 °C/min. The Mn AOS of Cu-Mn oxides was determined by calculating the hydrogen consumption during the process, while considering the reduction of Cu (II) into Cu (0) and the reduction of Mn^{x+} into MnO. The applied calculation was done as the following:

$$Cu^{2+} + H_2 \rightarrow Cu^0 + 2H^+ \quad \text{(Eq. 3.23)}$$

$$n_{H2/Cu} = n_{Cu} \quad \text{(Eq. 3.24)}$$

$$Mn^{n+} + \frac{n-2}{2} H_2 \rightarrow Mn^{2+} + (n-2)H^+ \quad \text{(Eq. 3.25)}$$

$$n_{H2/Mn} = n_{H2/total} - n_{H2/Cu}; \quad \text{(Eq. 3.26)}$$

$$\text{AOS Mn} = 2 + 2\left(\frac{n_{H2/Mn}}{n_{Mn}}\right) \quad \text{(Eq. 3.27)}$$

Where $n_{H2/Mn}$ equals the molar H_2 consumption by Mn^{x+}, $n_{H2/Cu}$ the molar H_2 consumption by Cu^{2+}, n_{Cu}: the molar amount of Cu, n_{Mn}: the molar amount of Mn and $n_{H2/total}$ the molar H_2 consumption by Cu-Mn oxides.

Time-of-Flight Secondary Ion Mass Spectrometry (ToF-SIMS)

ToF-SIMS is a surface analytical technique based on the excitation of the surface with a focused pulsed beam of primary ions thus producing secondary ions in a sputtering process. The reference catalysts CuMnOx-R3 and $CuMn_2O_4$-

P4 were analyzed to provide essential information about the molecular, inorganic and elemental species present on the surface.

The negative and positive measurements are performed with a ToF-SIMS5 spectrometer (ION-TOF GmbH Germany) equipped with a bismuth liquid metal ion gun (LMIG). Prior to the test, a pellet preparation was needed. The catalyst powder was put between two stainless steel plates then placed in a pump chamber. Pressure inside the chamber was increased progressively until 2.5 tons was reached. After preparation, the tablet sample was introduced into the test chamber. Pressure inside the test chamber was reduced to at least 10^{-4} Pa. Once a sufficiently low pressure was reached, the tablet was bombarded with a pulsed Bi^{3+} primary ion beam (25 keV, 0.25 pA) rasterized over a 500*500 μm^2 surface area. A data acquisition time of 100s was selected, and the total fluency was kept below 1012 ions/cm^2, thus ensuring static conditions. A low-energy ($\approx$ 20 eV) pulsed electron flood gun was applied to compensate for the charge accumulation. The mass resolution ($m/\Delta m$) was about 7000 at a m/z = 63 for Cu^+. The secondary ions were identified by their exact mass and were subsequently coupled with the appropriate intensities for the expected isotope pattern.

Textural properties analysis via Brunauer–Emmett–Teller (BET) and Barrett-Joyner-Halenda (BJH)

The textural properties that are specific to the surface area and the pore size distribution, were studied via N_2 adsorption-desorption measurements at liquid nitrogen temperature (-196 ℃). BET theory aims to explain the physical adsorption of gas molecules on a solid surface and serves as the basis for the measurement of specific surface areas. BJH analysis is a pore size distribution determination method, which is typically applied to nitrogen desorption data measured on catalysts at 77 K.

Two types of surface area analyzers were employed during the course of this work: the Micromeritics Flow Sorb III serial 416 and the Micromeritics TriStar-II. The first one provided the single-point surface area measurement and was capable of measuring sample surface areas of 0.01 m^2/g to over 1,000 m^2/g. Before the test, a continuous flow of N_2 was passed over the sample at atmospheric pressure, and then the degassing process was performed at 150^o C for 30 min. After degassing, the samples were first put in liquid nitrogen, and sequentially into distilled water. The surface area can be calculated based on the equation described below:

$$S_{BET} = \frac{S_{total}}{m_{degassing}}; \quad \text{(Eq. 3.28)}$$

S_{total}: total surface area

Surface area and porosity were obtained using Micromeritics TriStar-II device. The device contains two parts: 1- a sample degas system containing a sample degasser (Micromeritics Vacprep 061) and a vacuum pump (PFEIFFER Duo 2.5), 2- an analysis system containing the surface area, a porosity analysis equipment (Micromeritics TriStar-II) and a vacuum pump (PFEIFFER Duo 2.5).

Before the analysis, the samples were degassed at 150 ℃ in vacuum for a few hours. The samples were then placed into the test chamber and the surface area and pore size distribution were calculated automatically. The total pore volume (V_{total}) was estimated from the amount adsorbed at a relative pressure of 0.99.

Thermogravimetric analysis (TGA) with mass spectrometry (MS)

Thermal analysis was performed using a thermogravimetric analyzer (TA instruments SDT 2960 simultaneous DSC-TGA). Samples were heated from room temperature to 800 ℃ at a ramp rate of 10 ℃/min and in a 20% O_2/He (100ml/min) atmosphere. The gases which desorbed from the samples during thermal treatment were monitored using mass spectrometry (Pfeiffer Vacuum OmniStar GSD 320 O_2 1-200 amu). The following chemicals were monitored: water (m/z=18), CO (m/z=28), CO_2 (m/z=44), CH_4 (m/z=15), benzene (m/z=78), benzaldehyde (m/z=105,106), benzoic acid (m/z=122) and formaldehyde (m/z=29, 30).

Scanning Electron Microscopy (SEM)

The morphologies of catalysts were examined by SEM images recorded on a Hitachi S-4700 apparatus. SEM micrographs (10,000 ×) were taken with an accelerating voltage of 7 kV. Before SEM analysis, the samples were coated with gold via a JFC-1300 Auto Fine Coater (JEOL, Belgium) in order to avoid charge effects. After applying the gold coating, the catalyst powders were studied with an InTouch Scope JSM-6010 plus/LVScanning Electron Microscope (SEM) (JEOL, Belgium).

3.3.3. Toluene abatement test

Catalytic toluene oxidation was performed at the University of Lille 1. The descriptions of the setup and the experimental process are presented below:

3.3.3.1. Experimental setup

All experiments were performed in a continuous flow at atmospheric pressure. The experimental setup consisted of three parts:

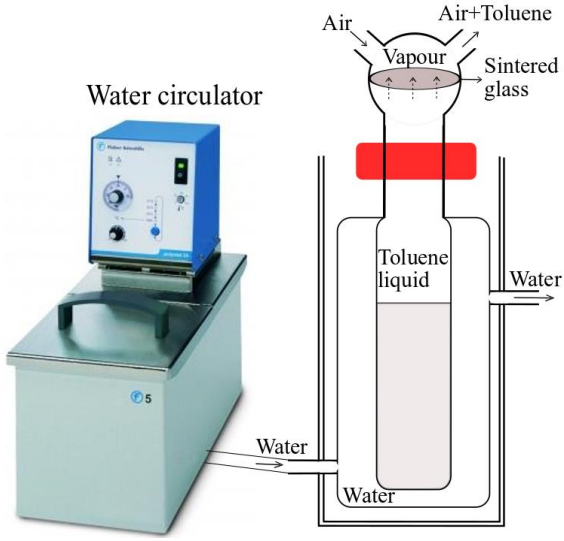

Figure 3.17. The schematic of toluene generation setup

(1) A toluene generator (made in-house) that was used to produce 800 ppm of toluene gas as shown **Figure 3.17**. A flow of dry air, controlled by MFC (Brooks 5850 series), was passed through the flask containing the toluene liquid (Sigma Aldrich, > 99,8 %). As a result, a vapor mixture of toluene and air was formed and was then fed into the catalytic reactor. A water circulator (Fisher Scientific polystat 36) was employed to keep the toluene container at a stable temperature. The desired concentration of toluene (800 ppm) was obtained by adjusting the water temperature in the water circulator. In this study, a temperature of 62 ℃ and a flow of dry air of 100 ml/min were selected to obtain the desired 800 ppm of toluene stream.

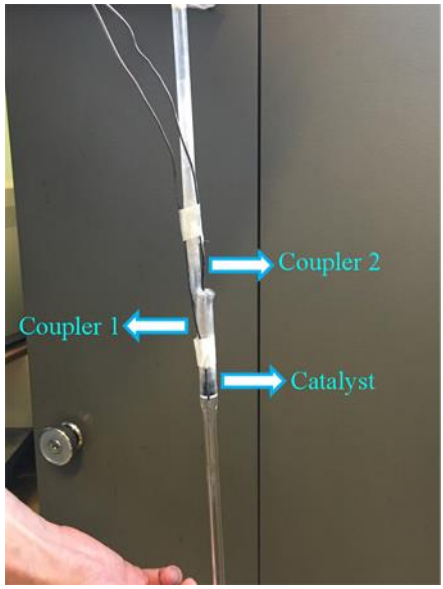

Figure 3.18. Photo of the reactor

(2) A catalytic reactor. About 0.20 g of the catalyst prepared by co-precipitation or redox method was placed inside the pyrex-glass reactor for each run. Once filled, the reactor was placed into the coaxial tubular furnace, which was temperature regulated (TEMPATRON, PID500, equipped with two thermal couplers). Coupler 1 was used to monitor the temperature of the reactor surface, and Coupler 2 was inserted into the reactor near to the catalyst surface as seen **Figure 3.18**.

(3) An analysis system. The concentrations of the gaseous species exiting from the inlet and outlet gas streams were analyzed on-line by Gas Chromatography (7860A Agilent Gas Chromatograph) equipped with a Thermal Conductivity Detector (TCD) and a Flame Ionization Detector (FID) packed with two columns: a Restek Shin Carbon ST/Silco HP NOC 80/100 micro packed, to separate permanent gases (Air, CO and CO_2) and a capillary column Cp-Wax 52CB25 m, Ø = 0.25 mm, to separate hydrocarbons and aromatic compounds. A typical example of the spectra analyzed by the TCD and FID, can be observed in **Figure 3.19**.

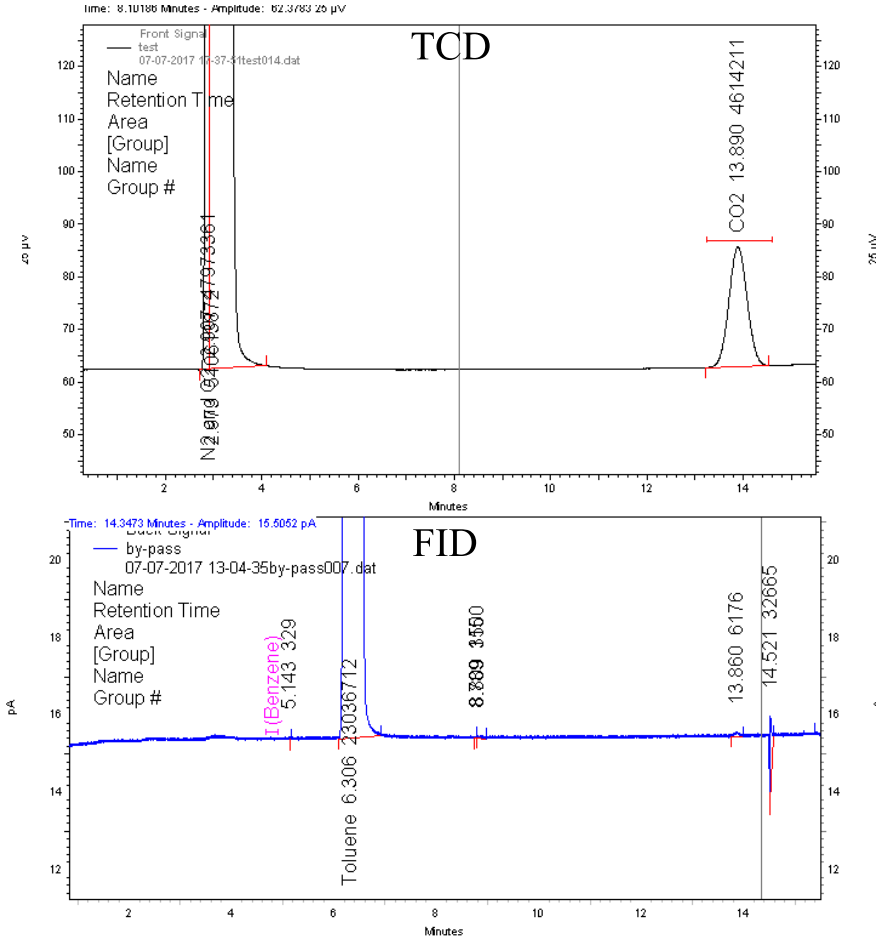

Figure 3.19. Example of the products detected by the chromatograms equipped with TCD and FID in toluene oxidation experiment

3.3.3.2. Toluene oxidation analysis in air

A catalyst activation step was introduced to eliminate the presence of H_2O, CO_2 and some chemicals possibly absorbed on the surface of the studied catalyst. Two processes were undergone in the activation part as seen in Figure **3.20**: toluene concentration stability process and catalyst activation process. A more detailed description is given below.

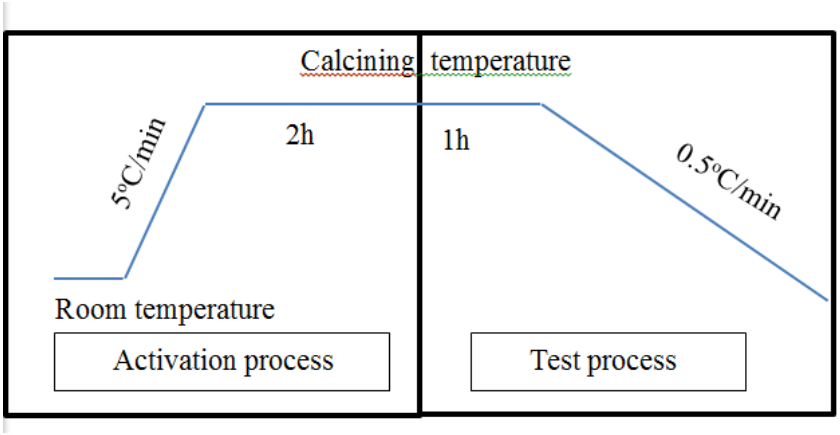

Figure 3.20. Schematic of the experiment process

1. The stability test of toluene concentration was conducted as shown in the green circuit. 100 ml/min of air were passed through toluene generator setup, then toluene/air concentration was analyzed by GC, ~800 ppm of toluene was needed in catalytic oxidation experiment. Meanwhile, the catalyst was activated in calcining temperature (CuMnOx-R3: 300 ℃ or $CuMn_2O_4$-P4: 400 ℃) as shown in the yellow circuit. Another flow of 75 ml/min was sent to the reactor for the activation (yellow circuit).

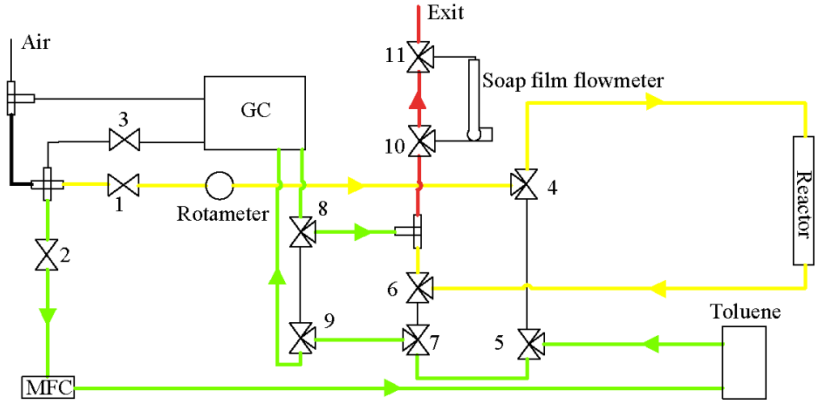

Figure 3.21 Schematic representation of the toluene bypass circuit (green) and the catalyst activation circuit (yellow). The red line shows the exhaust of the system where both flows are mixed

2. The air flow rate during activation was set at 75 ml/min and the flow rate going through toluene was set at 100 ml/min, giving a

total flow rate of 175 ml/min. A soap film flowmeter with a fixed volume of 5 ml was used to indicate the flow rate, which allowed the calculation of the total flow rate according to the following equation:

$$\text{Flow rate} = \frac{5\ ml}{1.7\ s} = \frac{2.94 ml}{s} = 176 ml/min \quad \text{(Eq. 3.30)}$$

3. Once a steady flow was obtained, the furnace was heated from room temperature to catalyst calcination temperature (CuMnOx-R3: 300 ℃, $CuMn_2O_4$-P4: 400 ℃) with a rate of 5 ℃ min^{-1}. After reaching the desired temperature, the activation process was maintained for 2 h.
4. During the activation process, air was also passed through the toluene flask as shown in figure 3.21. Once a stable toluene concentration was reached, the effluent was analyzed on line by GC equipped with TCD and FID.

Test process:

The valve setting was adjusted for the testing process (**Figure 3.22**). The desired concentration (~800 ppm) of toluene/air mixture gas was sent to the reactor, then toluene/air mixture gas was oxidized in the catalyst reactor and the exhaust gas was analyzed by GC. The test temperature was set as shown in **Figure 3.20**. Calcining temperature (CuMnOx-R3: 300 ℃, $CuMn_2O_4$-P4: 400 ℃) was maintained for 1 h, then the temperature was decreased at a cooling rate of 0.5 ℃. min^{-1}. During the test process, the air was passed through the system at a constant flow rate of 100 ml/min. Valves 10 and 11 were adjusted, and a soap film flowmeter with a fixed volume of 5 ml was used to indicate the flow rate, thus allowing for the calculation of the total flow rate according to the following equation:

Flow rate = (5 ml)/(3 s)=1.6ml/s=100 ml/min (Eq. 3.31)

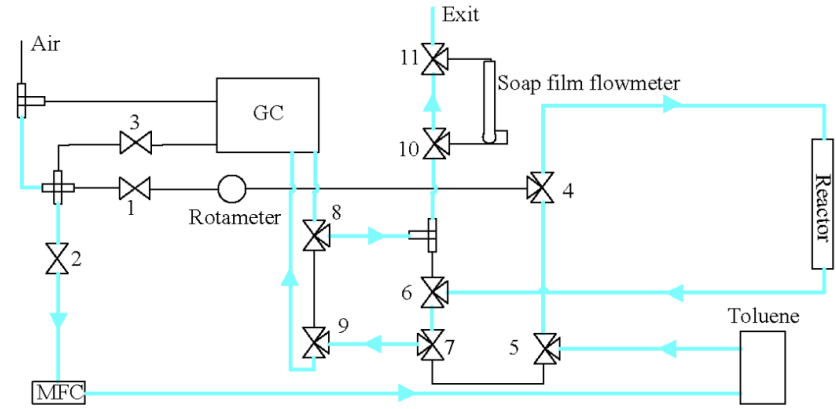

Figure 3.22. Schemes of the test flow (Cyan line is the test flow diagram)

3.3.3.3. Toluene oxidation tested in He

The experiment process performed in He differed from the process performed in air. As seen in **Figure 3.23**, the process consisted of four parts. The first step is the activation process that is similar to the one described earlier for air with the only difference being that air was replaced by He. In between the activation step and the testing procedure, a cooling step was introduced, as the experiment was conducted from a low temperature to a high temperature, unlike the test in air. The third step is the adsorption process that helps preventing undesired adsorption during the catalytic abatement of toluene. The fourth and final step was the catalytic oxidation process.

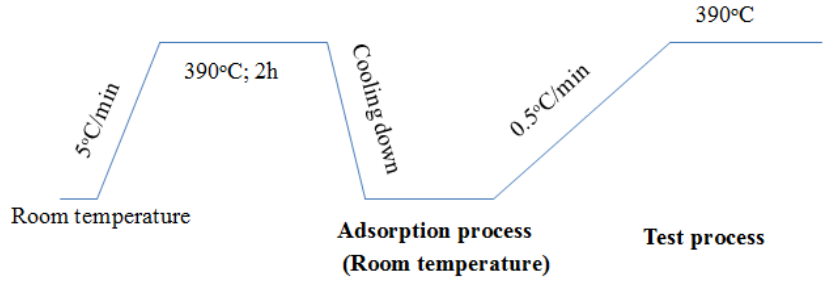

Figure 3.23. Toluene oxidation experiment in He

Activation process:

As shown in **Figure 3.24**, two types of gas supplies were connected to the system: the first one was air that was sent into the reactor for the catalyst activation and the second one was He that was sent into the toluene evaporation setup to produce a stable flow of toluene/He mixed gas. The flow rate during activation was around 75 ml/min and the flow rate that passed through the toluene container was 100 ml/min, thus giving a total flow rate of 175 ml/min.

Once a steady flow was reached, the furnace was heated from room temperature to catalyst calcination temperature (300 ℃ or 400 ℃) at a rate of 5 ℃. min^{-1}, and the activation lasted 2 h.

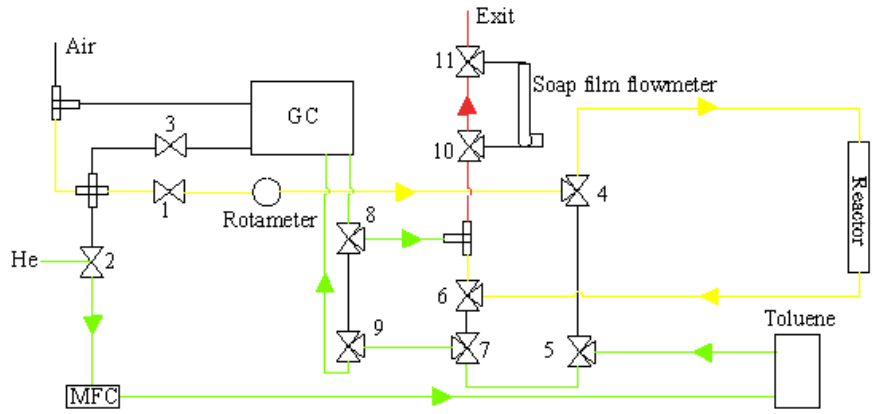

Figure 3.24. The graph of bypass and activation flow (Green line is the flow diagram of bypass; Yellow line is the flow diagram of activation; Red line is the mixture of bypass line and activation)

Cooling process:

After the catalyst activation step, the furnace was turned off and the system cooled down to room temperature, using compressed air. Once a room temperature and a steady toluene stream were reached, the adsorption step was started.

Adsorption process:

As seen in **Figure 3.25**, a He gas flow of 100 ml/min was sent through the toluene container. Possible changes in Toluene/He concentration due to adsorption processes were tracked by GC. The affinity of the effluent towards the catalysts was tested in this chapter and was found to be low, since the toluene concentration was recovering quickly.

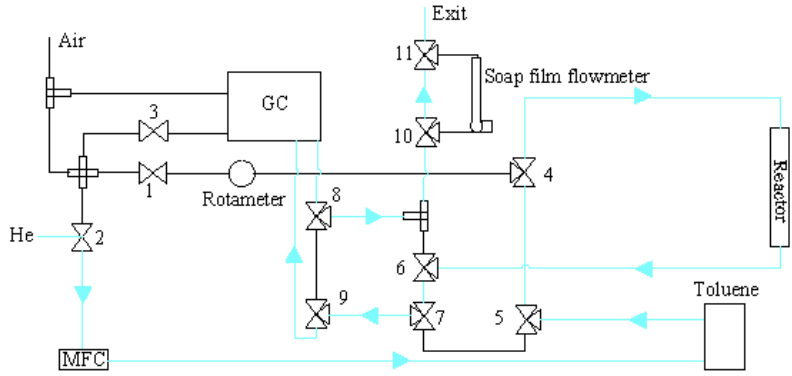

Figure 3.25. Schematic representation of the gas flow circuit during adsorption and testing

Test process:

First of all, toluene/He gas was passed through the system at a constant flow rate of 100 ml/min as shown in **Figure 3.25**, while the furnace temperature program was adjusted from room temperature to 390 ℃, with an increased rate of 0.5 ℃. min^{-1}. Valves 10 and 11 were adjusted as seen in **Figure 3.25**, and a soap film flowmeter with a fixed volume of 5 ml was used to indicate the flow rate thus allowing for the calculation of the total flow rate according to the equation 30. Then, 3 s were needed to obtain a flow rate of 100 ml/min.

3.3.3.4. Stability test

Stability tests were performed in a continuous flow fixed bed Pyrex micro-reactor operating at atmospheric pressure. About 0.20 g of the catalyst was placed in the reactor per run. The micro reactor was coaxially placed in an electrical furnace. All the lines were heated.

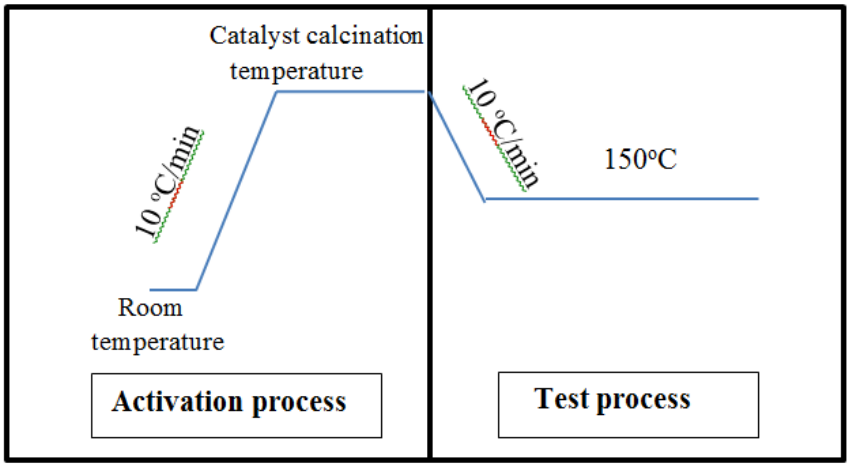

Figure 3.26 Stability experiment in air

As **Figure 3.26** shows, before each run, an activation step was required with the process being an exact copy of the process described for air. The samples were pretreated for 2 h under an air flow of 75 mL min^{-1} for every calcination temperature of the catalyst with a temperature increase of 10 ℃/ min^{-1}. In parallel, a flow of 100 ml/min was sent through the toluene container to achieve a stable toluene concentration.

After the activation step, the temperature of the furnace was decreased to 150 ° C at a rate of 10 ℃ min^{-1}. Afterwards, the reactive gas mixture was fed into the reactor at 100 mL/min. The mixture consists of 800 ppm of toluene diluted in air, corresponding to a WHSV (Weight Hourly Space Velocity) of 30000 mL g^{-1} h^{-1}. The reactor was then kept at 150 ℃ for 24 h. The effluent gas was analyzed at time intervals of 18 min by the GC equipped with TCD and FID.

3.4. Post Plasma-Catalysis of TCE

3.4.1. Introduction

As extensively described in literature, TCE, one of the most common VOCs, is known to cause severe risks towards environment and health [104]. For the abatement of VOC, it was opted to use a combination of Cu-Mn oxide catalysts with non-thermal plasma. For these experiments, a PPC configuration was chosen since it is associated with several advantages that were already discussed in details earlier, but can be summarized by the following: lower concentrations of unwanted byproducts, higher CO_x yield and better TCE removal efficiency. During this study, CuMnOx-R3 and $CuMn_2O_4$-P4 were investigated in the

following configurations: (1) catalytic oxidation without plasma and (2) plasma-assisted abatement without presence of a catalyst and (3) catalytic oxidation in combination with non-thermal plasma. Special attention was given to the possible synergetic effects occurring when combining both abatement techniques.

The section includes setup description, catalysis oxidation experiments and PPC experiments.

3.4.2. Setup description

The scheme of the used experimental set-up is presented in **Figure 3.27**. As can be seen from this figure, the complete set-up consists of three main parts: (1) Gas supply system, (2) Reactor system: negative DC glow discharge reactor and catalytic reactor (3) Analytical instrumentation. Each of these parts will be described in details in the following paragraphs.

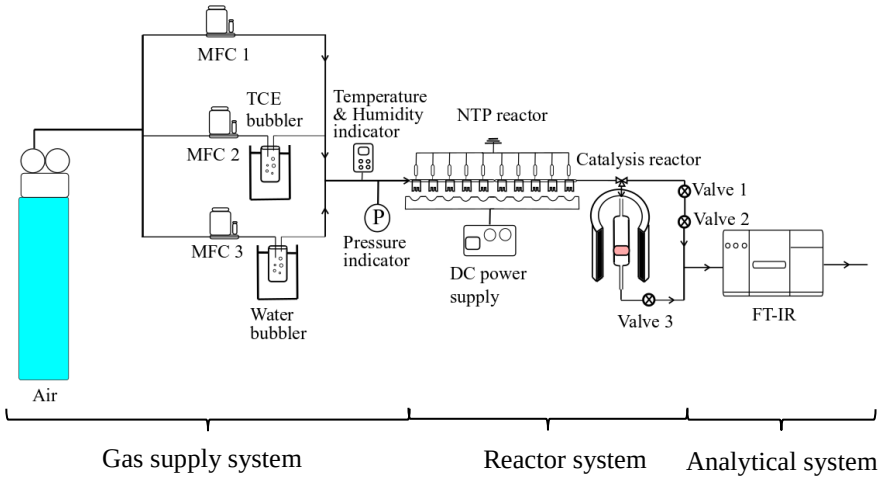

Figure 3.27. Schematic representation of the experimental set–up

3.4.2.1. Gas supply system

Chemicals

Air (Alphagaz 1, mole percentages: O_2 = 21% and N_2 = 79%, 200 bar) was acquired from Air Liquide and TCE (100ml, pof three main parts: (1) Gas supply system, (2) Ra glass gas-bubbler, similar to the systems using toluene described earlier. The gas bubbler was placed in a water bath to maintain a stable temperature during the experiments. Distilled water (Eurowater) was stored in a second gas-bubbler and placed in a water bath. The total flow rate for TCE/air was 0.5 L/min in humid conditions.

Probes

The humidity and temperature of the gas mixture were measured by a Testo 445 device (**Figure 3.2c**). The temperature/humidity probe was located in a closed vessel in which the feed gas was circulated. The vessel itself was placed between the gas supply system and the reactor inlet. The gas pressure of the air flowing through the set–up was measured via a Digital Pressure Indicator 705.

3.4.2.2. Reactor system

A photograph of the negative DC glow discharge reactor is shown in **Figure 3.28**. The cylindrical reactor is made of PTFE (Polytetrafluoroethylene), with a glass tube placed coaxially, acting as the cover. The cover itself can be closed with airtight fitting to prevent any leaking. The active plasma region was defined as 40 x 9 x 400 mm^3. The plasma reactor consists of 10 aligned, crenellated cathode pins that were positioned at 28 mm intervals. The distance between the 10 cathode pins and the single anode plate is 10 mm. A DC power supply (Technix, SR40–R–1200) provided the discharge power. The NTP was generated at atmospheric pressure and at room temperature.

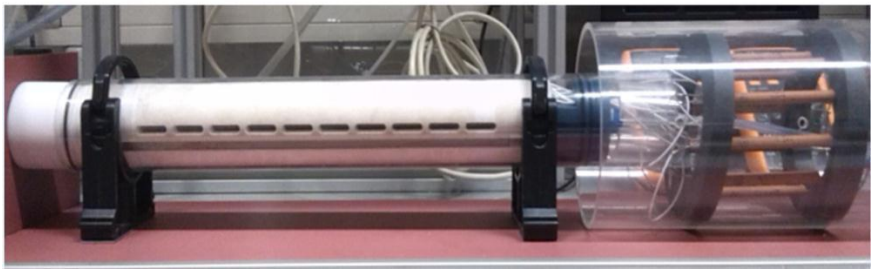

Figure 3.28. Photo of plasma reactor with 10 electrode pins

Energy measurement

As shown in **Figure 3.29**, the applied power in the reactor was measured via determination of the U_{pl} (the voltage applied to the reactor) and the discharge current. To obtain the value of U_{pl}, the total voltage U_{tot} was measured by a high voltage probe (Fluke 80 K–40, division ratio 1/1000), and the discharge current "I" was determined by recording the voltage of U_m across a 100 Ω resistor (Rm) placed in series between the counter electrode and the ground.

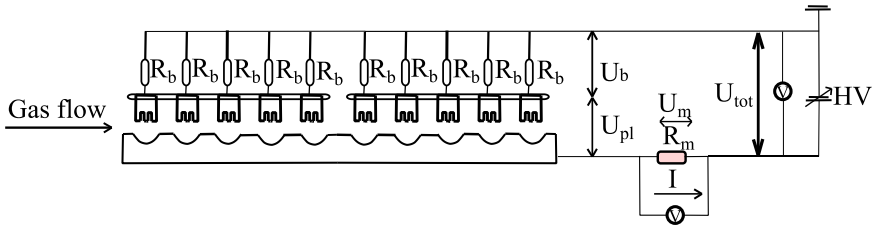

Figure 3.29. Electrical scheme of the multi–pin–to–plate discharge

The anode plate consists of a spherical surface with a radius of 17.5 mm and a depth of 5 mm. A stable and uniform glow discharge was ensured by the gas flow and by ballasting each cathode pin with a 1.5 MΩ resistor R_b. The fraction of the total electrical power that is dissipated in these resistors was amounted to 10% at most. Therefore, the plasma voltage was calculated as following:

$$U_{pl} = U_{tot} - U_b - U_m \quad \text{(Eq. 3.32)}$$

$$U_{pl} = U_{tot} - \frac{R_b I}{N} - RI \quad \text{(Eq. 3.33)}$$

Catalytic reactor

As shown in **Figure 3.30**, the catalytic reactor system consisted of a cylindrical glass tube, an oven and a temperature controller. The glass reactor was made of Pyrex glass with an inner diameter of 20 mm and an effective length of 100 mm. A sintered and porous plate was used inside the tube to held the catalyst powder in place. Measurements were performed after a thermal balance was reached. The oven was an in-house-made model delivered by UCCS from Lille University.

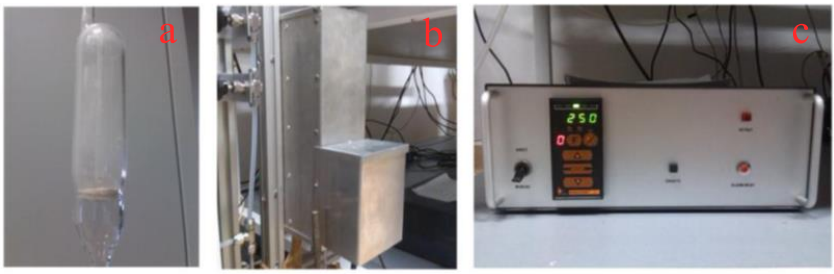

Figure 3.30. Overview of the catalytic reactor components with (a) glass tube, (b) oven and (c) temperature controller

3.4.2.3. Gas analyzing instrumentation

An FT-IR spectrometer (Vertex 70, Bruker) was used as the analysis instrument (figure 3.31). The following experimental conditions were used to

measure the background and the sample spectra. When a steady-state condition was reached by a spectrum, the next measurement was started automatically.

- Instrument type: Vertex 70 Sample Compartment RT-DLaTGS;
- Accessory : General Type-Transmittance;
- Gas cell: 20 cm optical path length
- Resolution: 4 cm^{-1};
- Sample scan number: 10 scans;
- Background scan number: 20 scans;
- Saved data from: 4000 cm^{-1} to 600 cm^{-1}.

Figure 3.31 Gas analyzing instrumentation with (a) FT-IR, (b) gas cell

3.4.3. Catalysis experiment

Generation of stable TCE/air mixture

Firstly, an air flow at 70 mL/min was passed through the distilled water bubbler. Before measuring the background, the gas flow was left running for at least 1 h until a stable gas composition was obtained.

Secondly, the bubbling bottle was placed in a thermostatic water bath maintained at –8 ℃by adding antifreeze to the water to enhance the TCE vapor stabilization.

Thirdly, TCE vapor was generated by passing an air flow of 22 mL/min through the bubbler containing the cooled TCE.

A secondary air flow was mixed with the TCE vapor and the humid air flow. The desired concentration of TCE (300 ppm) was obtained at a relative humidity of 15 % by adjusting the flow rate of air, the flow rate through the water bubbler and the flow rate through the TCE bubbler.

Lastly, the total flow rate was set at 500 mL/min which was the sum of the dry air flow, the flow through the water bubbler and the flow through the TCE bubbler.

Activation step

1. 0.5 g of the catalyst and 3 g of SiC were mixed together and placed into the reactor.
2. The catalyst was pre-calcinated at 300 °C for 4 h (temperature rate 1 °C /min) under an air flow of 200 mL/min.

Catalytic oxidation experiment

1. The reactive flow (TCE: 300 ppm, total flow rate: 0.5 L/min, RH: 15%, GHSV: 60000 $mL*g^{-1}*h^{-1}$) was allowed to stabilize before sending it to the reactor.
2. The reactive flow was initially sent through the by-pass instead of the reactor, until the oven reached the exact temperature.
3. Next, the catalyst was tested at the different temperatures of the experiment (100, 150, 200, 250, 300 ℃). When the exact temperature was reached, the reactive flow was diverted through the catalyst instead of passing through the by-pass (valve 1 and valve 2 in experimental set-up). The temperature was increased from 100 to 300 °C at a rate of 2 ℃/min.
4. For every temperature, the outlet of the reactor was monitored by FT-IR. The number of scans was set at 10 and a new measurement was started every 30 s for each FTIR measurement. The evolution of TCE conversion was measured at each temperature for 1 h.
5. The temperature was cooled back down to room temperature before the actual experiment.

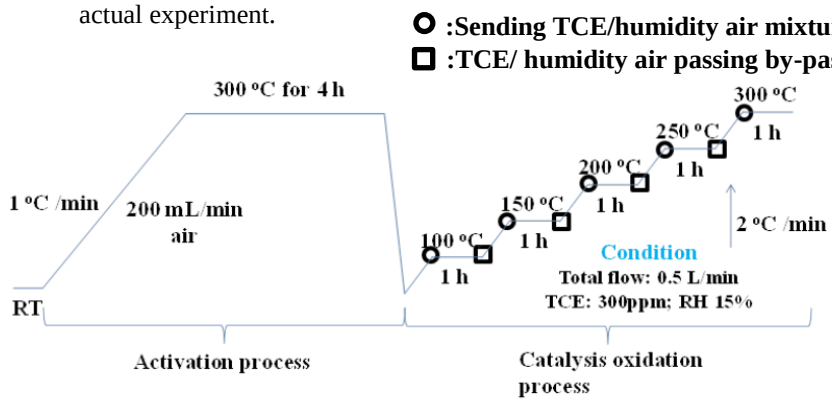

Figure 3.32 Schematic representation of the catalyst alone experiment

Catalyst characterization

For the PPC experiments, the catalyst characterization was mainly focused on the elemental composition, the chemical state and the textural properties before

and after PPC and catalytic oxidation experiments. To do so, ICP, XPS and BET analyses were the characterization techniques of choice. The experimental details are the same as described in section 3.3.2.

3.4.4. The PPC experiments

For the PPC experiments, Cu-Mn oxides were selected: CuMnOx-R3 and $CuMn_2O_4$-P4. Before the actual experiments, 0.5 g of the catalyst was mixed with 3 g of SiC and placed in the reactor. This was followed by a pre-calcination step at 300 °C for 4 h under a synthetic air flow (200 mL/min) to activate the catalyst.

Experimental conditions

The total flow rate was 0.5 L/min, the TCE input concentration 300 ppm and the relative humidity 15%.

Experiment process

1. The reactive flow (total flow = 500 mL/min, 300 ppm TCE, RT = 15%) was stabilized before being fed into the reactor.
2. The catalyst was tested at 150 °C, while the energy density of plasma was varied from 30 to 120 J/l with steps of 30 J/l.
3. First of all, the catalyst temperature was increased to 150 °C. A catalyst test was performed to check the difference in abatement efficiency when the catalyst was fresh at 150 °C.
4. The plasma was turned on and set to 30 J/l (TCE is by-passing the catalyst chamber) until a stable plasma discharge was obtained.
5. TCE was fed into the system and FTIR spectra were recorded for 10 minutes (only plasma involved)
6. The plasma treated effluent was passed through the catalyst (PPC) and FTIR spectra were measured for 1 h at intervals of 30 s.
7. The same procedure was repeated for all the above mentioned energy densities.

CHAPTER 4: STRATEGIC METHODOLOGY

4.1. Introduction

The aim of this chapter is to provide the readers with a clear overview of the strategic methodology that was applied during the course of this PhD. This chapter includes three parts: 1. Plasma-assisted experiments focusing on the analysis of discharge phenomenon and humidity influence as seen figure 4.1; 2. Cu-Mn type catalytic oxidation experiments with a comparison between Cu-Mn oxides prepared in different way as seen figure 4.2; 3. Plasma-catalysis experiments, mainly focusing on the performance of TCE abatement by PPC system as seen figure 4.3.

4.2. Toluene abatement by plasma-assisted technique

In the recent years, the removal of VOCs from air streams has become of great interest as these compounds are known to cause adverse environmental effects as well as serious human health problems [105]. As a result, several VOCs abatement techniques such as adsorption [106], bioprocesses [107], thermal/catalytic oxidation [108, 109] and membrane separation [110, 111] have already been developed at this point, each with its own advantages and limitations. However, for the abatement of dilute VOC streams (< 1000 ppm), the above mentioned conventional techniques are often not suitable due to their very high energy consumption [112]. Over the last three decades, non-thermal plasma (NTP) technology has been identified as a cost and energy efficient alternative for the elimination of low concentration VOCs [113-116]. NTPs are very attractive in such a way that the applied energy is mainly used to create an intense electric field in which electrons are selectively accelerated instead of heating up the entire gas flow [117]. These high energy electrons collide with the present gaseous molecules such as N_2, O_2 and H_2O to induce multiple chemical processes such as excitation, ionization and dissociation. This leads to the creation of active and unstable species like radicals, ions and photons, which can decompose the pollutant molecules [117].

Among various types of NTPs used for VOCs abatement, dielectric barrier discharges (DBDs) are very attractive because of their simplicity, straightforward scalability and capability to treat atmospheric pressure gas streams with a negligible pressure drop [118]. When DBDs are applied for VOCs abatement, the discharge is typically generated between two concentric cylindrical electrodes enclosing a small gas gap which is often filled with dielectric pellets to create a so-called packed bed DBD reactor [113, 119]. Applying a high

voltage to the electrodes leads to the generation of a very strong electric field on each pellet contacting point, resulting in the formation of microdischarges in the void spaces between the pellets and on their surfaces [119, 120]. The dielectric pellets can be either non-catalytic or catalytic, however, the latter system, also referred to as an in-plasma catalysis system do not locate within the scope of the present work.

Packed bed DBD reactors have received considerable attention for VOC abatement since they are able to achieve a very high energy efficiency [113, 119, 121, 122]. This is due to the use of high dielectric constant pellets together with the possibility of reducing the breakdown voltage, which is favorable for industrial applications as higher discharge powers can be obtained at the same applied voltage [119, 120]. In addition, very high electric fields can be obtained in packed bed DBD reactors resulting in discharges with a low electron density, but with high electron energies [119]. The presence of these high energy electrons is a major advantage as they are able to induce electron-impact reactions, which are known to play a major role in plasma-assisted VOC decomposition processes [119] . In this work, a packed bed DBD reactor filled with glass pellets will be used to examine the decomposition of toluene. Toluene is widely used as feedstock in the chemical industry for synthesis of drugs, dyes, explosives,… and as a solvent (e.g. thinner, paints, adhesives) [22, 123]. In addition, exposure to toluene is known to affect the central nervous system and may cause tiredness, confusion, weakness, memory loss and nausea [22, 113, 123]. Moreover, as toluene is water-insoluble, it cannot be scrubbed and should be eliminated from gas streams making use of alternative techniques. Based on its widespread use and its severe health impact, toluene has therefore been chosen as model compound in the current study. In an ideal scenario, toluene should be mineralized into CO_2 and H_2O, however, it is well known that NTP technology often results in incomplete VOC oxidation resulting in the formation of unwanted by-products [14, 124]. Nevertheless, a thorough identification and quantification of these created by-products is often indispensable to elucidate the breakdown mechanism of toluene by NTP. In addition, when the packed bed reactor needs to be filled with catalytic pellets to perform in-plasma catalytic experiments, it is of great importance to know all the by-products of the NTP treatment beforehand to understand the possible synergy between NTP and the used catalyst and to fulfill a complete toluene oxidation at a minimal energy cost. The examination of toluene abatement in the packed bed DBD reactor before combining it with a catalyst will therefore be the topic of this paper. Particular attention will be paid on the influence of air humidity on toluene decomposition process as this parameter can strongly vary in waste streams over time. The influence of humidity on the discharge characteristics will be investigated

making use of optical emission spectroscopy (OES), which is rarely done in the case of plasma reactors for VOC abatement. In addition, the humidity influence on toluene conversion and by-product formation will also be examined with Fourier transform infrared spectroscopy (FTIR), a flue gas analyzer and an ozone monitor. Whenever possible, quantification of the generated by-products will also be conducted. The obtained valuable information will help to unravel the mechanisms occurring during packed bed DBD abatement of toluene and will also be of great value when performing in-plasma catalytic experiments with the same DBD reactor in the near future.

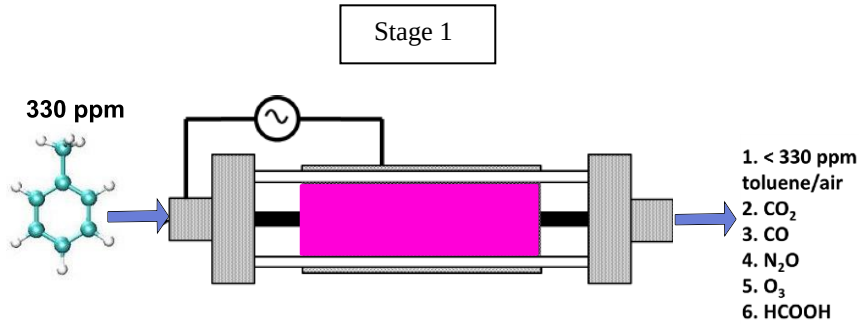

Figure 4.1. Graphical abstract of packed glass beads of plasma-assisted toluene oxidation

4.3. Toluene abatement by catalytic oxidation technique

Catalytic oxidation is one of the most efficient techniques for toluene abatement. For catalyst selection, a promising catalyst should exhibit a high performance in catalytic oxidation as well as a potential to be combined with plasma. Bulk and supported manganese-based catalysts have received increased attention, as they are considered as cheap, environmentally friendly and active materials. Thus, it has been shown that manganese oxides such as Mn_3O_4, Mn_2O_3 and MnO_2 exhibit high activity in the oxidation of hydrocarbons [27] .Some studies, focusing more specifically on the oxidation of toluene, have been performed on such bulk [31, 32, 125, 126] or supported [127-130] catalysts, since toluene is one of the major VOC released by industrial and automotive emissions and since it possesses a high POCP (Photochemical Ozone Creativity Potential) [131, 132]. In an attempt to get more promising catalyst formulations for toluene oxidation, one effective strategy can be the investigation of binary metal oxide containing manganese. Among the different A-Mn-O systems, the Cu–Mn–O system was shown to be attractive since the mixture of

manganese and cupric oxides have led to the discovery of the general name "hopcalite" catalysts. These catalysts are of prime importance in the CO oxidation at ambient temperature, the O_3 destruction [133-136] and the combustion of a wide range of VOCs at elevated temperatures [83, 88, 137, 138]. Improved redox properties were achieved by the formation of copper manganite $Cu_xMn_{3-x}O_4$ exhibiting flexible valences ($Cu^{1+/2+}$and $Mn^{3+/4+}$) and amorphous state. Stabilizing very small particles of copper and manganese oxides have been invoked to explain the good activity of hopcalite for CO oxidation. Based on these studies, Cu-Mn oxides can be viewed as promising catalysts but their performances closely depend on the method of preparation. In order to mainly improve the textural properties and intimate Cu-Mn interaction of copper-manganese oxides, new synthesis routes, capable of replacing the conventional ones such as co-precipitation [139, 140] and solid state reaction, have been developed in literature [141]. The alternative routes include sol–gel [135], redox-precipitation [142, 143], soft reactive grinding [144], synthesis under supercritical water conditions [145], reverse microemulsion [138] and combustion method for formation of Cu–Mn oxide layers on the surface of Al metal foam [146]. W.B. Li *et al* have reported that reverse micro-emulsion method allows to get more efficient catalysts compared to co- precipitation. In particular, $Cu_{0.33}Mn_{0.67}O_x$ gives the highest activity for complete oxidation of toluene due to a better dispersion of the active phase compared to the co-precipitation method [138].

Therefore, the second stage of my Ph.D was focused on the preparation of Cu-Mn oxides and the investigation of their catalytic performance. The details of this part can be found in chapter 6. In this work, the catalytic performances of CuMnOx obtained from the new redox method and the Pt (or Pd) doped CuMnOx for total oxidation of toluene were compared to those of a spinel catalyst $CuMn_2O_4$ prepared by a co-precipitation method in aqueous solution using TMAH as precipitant [100]. The effects of the preparation method and of the noble metal (Pt; Pd) dopants on the catalytic performances were discussed in light of the physicochemical characterizations.

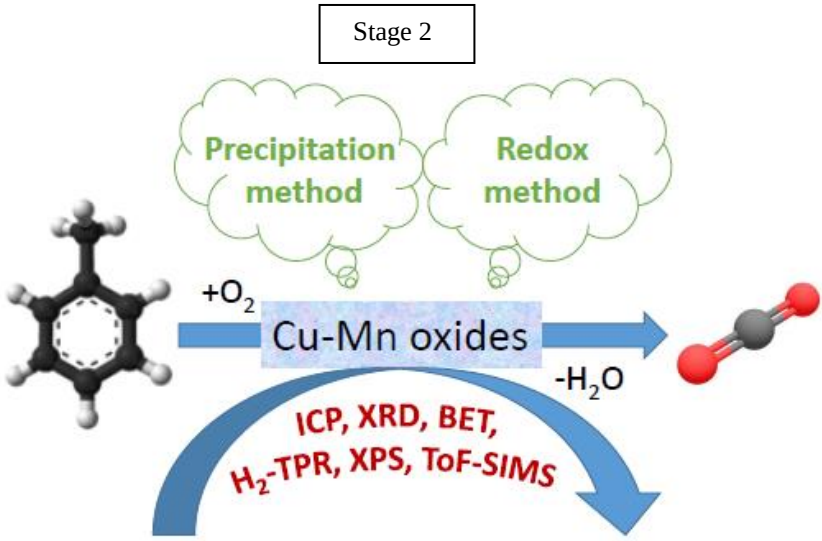

Figure 4.2 Graphical abstract of Cu-Mn catalysts for toluene oxidation

4.4. Improving TCE abatement by plasma-catalysis technique

Despite the widely reported advantages of NTP such as the comparable energy consumption, the easy on-off apparatus, the stable performance and so on, several aspects still need to be improved for future industrial applications, for instance the energy efficiency, the selectivity of CO_2, the unwanted/hazardous byproducts like NOx, CO, ozone and organic byproducts. Moreover, the long-term goals of the catalysis process are a lower reactive temperature and a stable catalytic performance. Therefore, a novel alternative technique is highly demanded. Coupling techniques (plasma-catalysis) come to solve this issue since it has been widely reported that plasma-catalysis has the potential to further improve VOCs when comparing to single techniques. Two combination ways of plasma-catalysis have been described: in plasma-catalysis (IPC) and post plasma-catalysis (PPC).

TCE (C_2HCl_3) is a halocarbon that is commonly used as an industrial solvent . Several environmental and health effects of this non-flammable and sweet smell liquid have been reported [104, 147]. In addition to its neurotoxicity, the International Agency of Cancer (IAC) has reported a TCE carcinogenic effect on humans while stating that its emission in the atmosphere must be prevented in order to secure public health. Moreover, several other maleficent effects have been described such as immunotoxic, hepatic and developmental effects.

Non-thermal plasma produces ozone, phosgene (PG), dichloroacetylchloride (DCAC), trichloroacetaldehyde (TCAA) and hydrochloric acid (HCl) as by-products after the decomposition of TCE. To overcome this disadvantage, NTP is usually coupled with a catalyst that is either placed in the discharge zone (in-plasma catalysis; IPC) or in the downstream after the non-thermal plasma process (post-plasma catalysis; PPC). Depending on the location of the catalyst, different mechanisms improving the synergy, the energy efficiency, the CO_2 selectivity and reducing the formation of by-products, are involved in the decomposition of TCE [21]. Novel advances in the combination of catalyst and NTP are reported in recent reviews [94].

The choice of the catalyst for TCE abatement has to be made taking into account some basic requirements such as ozone decomposition ability, VOC total oxidation capacity, hydrothermal stability and resistance to chlorine. CuMnOx, commonly used for CO and ozone oxidation, has been proved to be a good option for VOCs abatement. Therefore, the main objective of this work is to study the decomposition of low concentration of TCE in humid air using the copper manganese catalysts CuMnOx-R3 and $CuMn_2O_4$-P4 prepared by redox- and co- precipitation methods respectively. The decomposition of TCE and the formation of by-products are studied and compared between different catalysts in different configurations such as single NTP , single catalyst and post plasma catalysis (placing the catalyst in the downstream from the NTP reactor). The detailed studies can be seen in chapter 7.

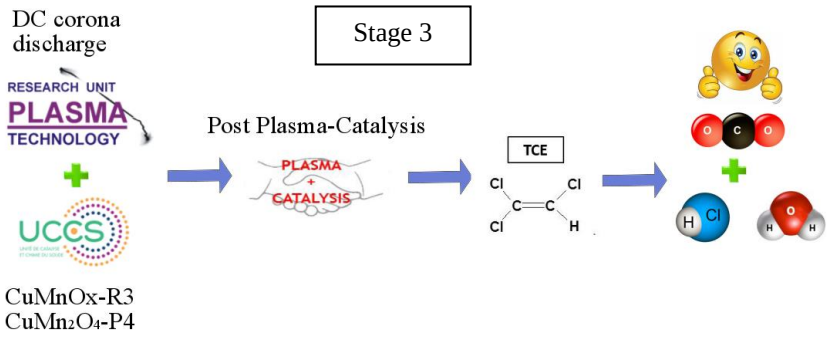

Figure 4.3 The graphic abstract of plasma-catalysis for TCE oxidation

CHAPTER 5: AN IN-DEPTH INVESTIGATION OF TOLUENE DECOMPOSITION WITH A GLASS BEADS PACKED BED DBD REACTOR

The results of chapter 5 were published in the following international peer-reviewed journal:

Z. Ye, S. Kaliya Perumal Veerapandian, I, Onyschchenko, A, Nikiforov, N. De Geyter, J.-M. Giraudon, J.-F. Lamonier, R. Morent

An in-depth investigation of toluene decomposition with a glass beads packed bed DBD reactor

Industrial & Engineering Chemistry Research, 56 (37), pp 10215–10226, 2017

The graphic abstract was chosen to feature on the front page of the October issue of ACS-journal Industrial & Engineering Chemistry Research

5.1. Introduction

The environmental and health problem of toluene has been thoroughly discussed in chapter 1. In an ideal scenario, toluene should be mineralized to CO_2 and H_2O, however, it is well known that NTP technology often results in incomplete VOC oxidation resulting in the formation of unwanted by-products[14, 124]. Nevertheless, a thorough identification and quantification of these created by-products is often indispensable to elucidate the breakdown mechanism of toluene by NTP. In addition, when the packed bed reactor needs to be filled with catalytic pellets in a next step to perform in-plasma catalytic experiments, it is also of great importance to know all the by-products of the NTP treatment alone to understand the possible synergy between NTP and the used catalyst and to fulfill complete toluene oxidation at a minimal energy cost.

As a result, it is thus crucial to first examine toluene abatement in the packed bed DBD reactor alone before combining it with a catalyst, which will therefore be the topic of the chapter 5 and also be the first stage of my Ph.D. Moreover, particular attention will be paid to the influence of air humidity on the toluene decomposition process as this parameter can strongly vary in waste streams over time. The influence of humidity on the discharge characteristics will be investigated making use of optical emission spectroscopy (OES), which is only rarely done in the case of plasma reactors for VOC abatement. In addition, the humidity influence on toluene conversion and by-product formation will also be examined with Fourier transform infrared spectroscopy (FTIR), a flue gas analyzer and an ozone monitor. Whenever possible, quantification of the generated by-products will also be conducted. The obtained valuable information will help to unravel the mechanisms occurring during packed bed DBD abatement of toluene and will also be of great value when performing in-plasma catalytic experiments with the same DBD reactor in the near future.

5.2. Experimental conditions

Table 5.1 summarizes the experimental conditions used in this chapter, and the detailed information can be seen in chapter 3.2

Table 5.1 Experimental conditions

Air source	Air cylinder
Flow rate	1.0050 L/min
Relative Humidity (RH) (20^{o}C)	20%, 40%, 60%
Temperature	Room temperature
Initial toluene concentration	~330 ppm
Energy density (J/L)	75-300

5.3. Experiment results

5.3.1. Discharge characteristics of the reactor

In a first stage of the research, optical emission spectroscopy is used to study the effect of RH of the feeding gas on the generation of excited, radiative species in the discharge. For this purpose, air with different RH containing 330 ppm toluene has been sent through the packed bed DBD reactor operating at a discharge power ranging between 1.5 and 5.0 W. OES spectra were subsequently obtained a few minutes after plasma ignition. As an example, OES spectra of the discharge operating at 5.0 W in gas streams containing toluene for different RH are shown in **Figure 5.1**.

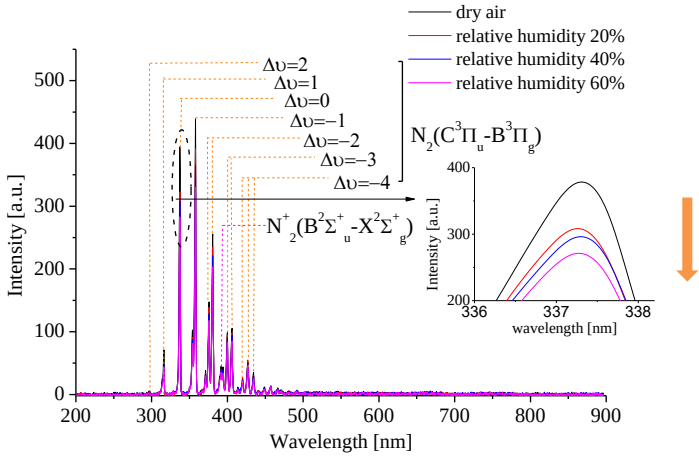

Figure 5.1. OES spectra of the discharge (5.0 W) generated in toluene/air with different relative humidity

From Figure 5.1, it can be concluded that the main component of the spectrum is emission of excited molecular nitrogen under all experimental conditions despite the presence of molecular oxygen and (in some cases) water

vapor in the gas mixture. The main contributions to the spectra presented in **Figure 5.1** are emission of the second positive system of the nitrogen molecule (N_2 ($C^3\Pi_u - B^3\Pi_g$)) and the first negative system of the nitrogen molecular ion (N_2^+ ($B^2\Sigma_u^+ - X^2\Sigma_g^+$)). The intensive N_2 molecular bands in the spectra indicate that the discharge generates abundant metastable electronic excited nitrogen molecules and ionized nitrogen species. In air at atmospheric pressure, stepwise dissociation and ionization of excited nitrogen is however hardly possible because of the very effective collisional quenching of excited states by molecular oxygen [148]. As a result, N_2^+ species are mainly generated by direct electron impact, as shown in the following reaction:

$$e + N_2(X^1\Sigma_g^+)_{v=0} \rightarrow N_2^+(B^2\Sigma_u^+)_{v'=0} + 2e \quad (\Delta E=18.7\ eV) \qquad \text{(Eq. 5.1)}$$

Furthermore, in a dielectric barrier discharge, the mean electron energy is typically ranging between 1 and 10 eV [149]. Hence, only a very small fraction of electrons possesses energies that exceed the threshold value of reaction (5.1), which can explain the relatively low intensity of the peak of the first negative system of N_2^+.

Emission of atomic oxygen ($^5S_0$-^5P at 777 and $^3S_0$-^3P at 845 nm) is hardly detected in the spectra, although the energy required for these transitions (10.7 and 11.0 eV respectively) is well below the threshold for nitrogen emission at 391 nm [150]. Similar results have also been reported by other researchers [150, 151] and can be explained by the fact that the quenching processes of excited oxygen atoms with oxygen and nitrogen molecules are two orders of magnitude faster than the radiative processes, making it very difficult to observe atomic oxygen in the spectra, although it is certainly present in the different air plasma discharges.

The discharge in humid air also contains OH radicals, however, emission of excited OH radicals at 308 nm cannot be detected in the OES spectra. This observation could also be explained by the fact that quenching of excited OH radicals by oxygen and nitrogen molecules is much faster than the de-excitation processes to the ground state.

In the inset of **Figure 5.1**, it can be seen that the intensity of the band at 337.1 nm gradually decreases with increasing humidity and this behavior could be observed for all bands present in the OES spectra. The observed decrease in emission can be attributed to the increased quenching of N_2 ($C^3\Pi_u$) excited

states due to collisions with water molecules before they undergo spontaneous emission to the lower N_2 ($B^3\Pi_g$) excited state.

Unfortunately, since no emission peaks from excited oxygen atoms or OH radicals could be observed in the emission spectra, it is not possible to draw any conclusions on the effect of humidity on the amount of these excited species.

The obtained OES spectra with strong emission of the nitrogen second positive system can however be used to determine the N_2 rotational temperature [152-154] . This temperature is determined by analysis of the rotational structure of a nitrogen molecular band in the second positive system, namely the 0-0 vibrational band of N_2 ($C^3\Pi_u - B^3\Pi_g$) emission at a wavelength of 337.1 nm. The experimental spectra are fitted with simulated ones and a typical fitting procedure of the spectrum in a toluene/dry air mixture is shown in **Figure 5.2**. The experimental spectrum presented in **Figure 5.2** has been simulated with different rotational temperatures ranging from 300 to 900 K in steps of 50 K and the best fit was observed for a rotational temperature of 450 ± 50 K. This rather high temperature is in good agreement with literature, where DBD reactors have also shown to result in the generation of high rotational temperatures [155-157]. It should however be highlighted that this rotational temperature is an overestimation of the bulk gas temperature as it only applies to the central part of the microdischarges and not to the whole gas volume [158, 159]. As a result, the overall gas temperature in the plasma discharge region is much lower than the rotational temperature as was confirmed by measuring the temperature of the DBD reactor wall making use of a thermocouple, which was found to be equal to 323 ± 3 K.

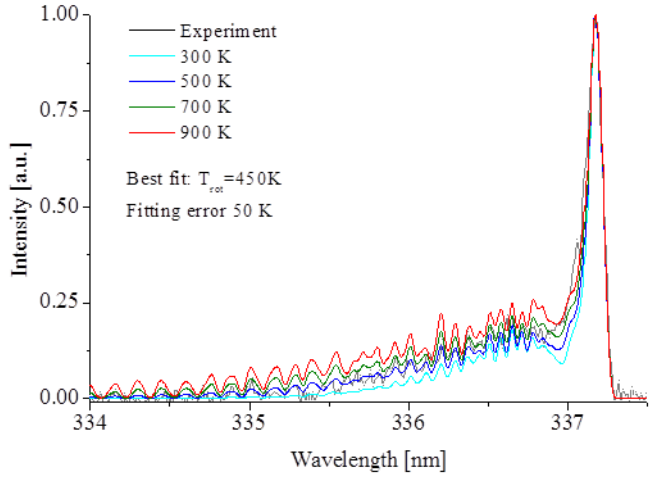

Figure 5.2. Determination of the N_2 rotational temperature by fitting procedure of an experimental spectrum of N_2 ($C^3\Pi_u - B^3\Pi_g, 0-0$) with a calculated spectrum. The plasma is generated in a toluene/dry air mixture at 5.0 W.

Simulations of the experimental spectra have also been performed for discharges generated in toluene containing humid air with different RH at 5.0 W and it was observed that the addition of water vapor to the air feed gas does not result in significant changes in rotational N_2 temperature as well as DBD reactor wall temperature in the range of the applied power from 1.5 to 5 W and sensitivity of the applied spectroscopy method.

5.3.2. Toluene abatement in the packed bed DBD reactor

5.3.2.1. Plasma treatments

After characterizing the DBD itself, plasma-assisted toluene abatement experiments are carried out to study the effect of air humidity. For this purpose, an air gas stream with different RH containing 330 ppm toluene is sent through the packed bed DBD reactor. A constant flow rate of 1.005 l/min is maintained during all experiments while discharge power was varied between 1.2 and 5.0 W enabling a variation in specific input energy (SIE) (= power [J/s] / gas flow rate [L/s]) between 70 and 300 J/l. As previously mentioned, a calibrated FTIR spectrometer is used to analyze the toluene content in the gas stream before and after plasma exposure enabling the determination of the toluene removal efficiency ($\eta_{toluene}$) according to the following formula:

$$\eta_{toluene}(\%) = 100 \times \frac{[toluene]_{in} - [toluene]_{out}}{[toluene]_{in}} \quad \text{(Eq. 5.2)}$$

Where $[toluene]_{in}$ is the toluene concentration introduced into the plasma reactor and $[toluene]_{out}$ the toluene concentration at the exit of the DBD reactor.

The toluene removal efficiency can be seen in **Figure 5.3** as a function of SIE for air streams with different RH. For all cases of humidity, the toluene conversion significantly increases with increasing energy density. This can be attributed to the fact that a higher amount of reactive plasma species, which can initiate and/or promote the decomposition processes of toluene, are available at higher energy density. In addition, the toluene conversions obtained at high SIE values in dry air are comparable with previously reported conversion efficiencies [74, 113, 121, 160]. And the comparison is shown in **table 5.2.**

Table 5.2 Comparison of toluene removal efficiency in glass beads packed bed DBD reactor using dry air non thermal plasma

	Initial toluene conc. (ppm)	Flow rate (L/min)	Energy density (J/L)	Toluene removal efficiency (%)
Present work	330	1.0	300	41
Chang et al. [121]	1100	0.6	370	55
Delagrange et al. [74]	240	0.3	172	36

For a particular SIE value, the removal efficiency significantly increases when the relative humidity is increased from 0 to 40%, while at higher levels of humidity, a trend inversion occurs with the efficiency at 60% RH becoming lower than the one at 40% RH. With increasing humidity levels, an increasing amount of OH radicals are present in the discharge, which are known to be much stronger oxidants than for example atomic oxygen or peroxyl radicals [21, 161]. This in turn results in an increase in removal efficiency with increasing humidity up to 40%. The trend inversion observed for higher humidity levels can be attributed to the saturation and inhibition of OH radical forming reactions for example the dissociation of H_2O molecules by reactions with electrons or atomic oxygen at high humidity levels [161].

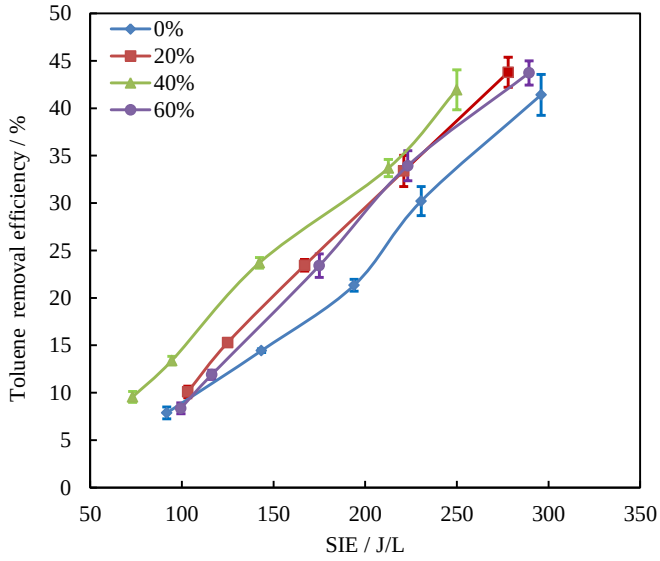

Figure 5.3. Toluene removal efficiency as a function of specific input energy for different relative humidities (RH=0%, 20%, 40% and 60%)

5.3.2.2. Analysis of by-product formation

As previously mentioned in the introduction, incomplete oxidation of VOCs by non-thermal plasma often occurs resulting in the formation of unwanted by-products, such as NO_x, CO, O_3, other VOCs,…[21, 162]. A thorough analysis of the identification of the by-products is thus indispensable to elucidate the plasma-assisted breakdown mechanism of toluene. Therefore, in the following paragraphs, FTIR spectra will be closely examined to qualitatively determine the by-products of toluene abatement with a glass beads packed bed DBD reactor. **Figure 5.4** shows the FTIR spectra of (a) the inlet and (b) the outlet stream when the plasma reactor is operated in a dry air/toluene mixture at two different SIE values (143 and 295 J/L). The inlet stream only shows the characteristic IR bands of toluene, which are listed in **Table 5.3**. On the other hand, several other IR bands appear after plasma abatement thereby suggesting incomplete oxidation of toluene.

To examine the composition of the plasma exhaust stream at both SIE values in detail, wavenumbers values are being used to allocate specific IR bands to the appropriate by-product. An overview of the wavenumbers and the corresponding by-product are presented in **Table 5.4**. By carefully comparing **Figure 5.4 (b)** with NIST reference spectra, several gaseous by-products in the exhaust stream

can be identified after plasma abatement at both SIE values. First of all, CO_2 is clearly present in the outlet stream as confirmed by the double bands at 2337 cm^{-1} and 2361 cm^{-1}. Moreover, toluene is also decomposed into CO which has characteristic FTIR peaks at 2176 and 2106 cm^{-1}. The formation of N_2O is also suggested by the presence of the absorption doublet at 2238 and 2205 cm^{-1}. Ozone is also detectable in the outlet stream since strong absorption bands at 2120, 1055 and 1035 cm^{-1} can be observed in the FTIR spectra. On the other hand, NO and NO_2 cannot be detected in the plasma-treated gas stream as suggested by the absence of strong absorption doublets in the region 1950-1800 cm^{-1} and 1660-1560 cm^{-1}. Additionally, formic acid can also be identified in the outlet stream. This is confirmed by the presence of the peaks, allocated with number 6, at 1106, 1246, 1732 and 3700 cm^{-1}.

Table 5.3 Characteristic FTIR bands of toluene [163, 164]

Wavenumber range (cm^{-1})	Vibration
3140-2975	aromatic ring =C-H stretching
2975-2840	methyl group C-H stretching
1975-1760	overtones
1640-1440	aromatic ring C-C stretching
1130-1010	aromatic in-plane C-H bending
770-660	aromatic out-of-plane C-H bending

Table 5.4 (By)products of plasma-assisted toluene abatement in dry air detected with FTIR spectroscopy

Number	Compound	Structure	Peak locations (cm^{-1})
1	Toluene	C_7H_8	3073, 3040, 2938, 2880, 1608, 1499, 728, 693
2	Carbon dioxide	CO_2	2361, 2337
3	Carbon monoxide	CO	2176, 2106
4	Nitrous oxide	N_2O	2238, 2205
5	Ozone	O_3	2120, 1055, 1035
6	Formic acid	HCOOH	3700, 2938, 2880, 1732, 1246

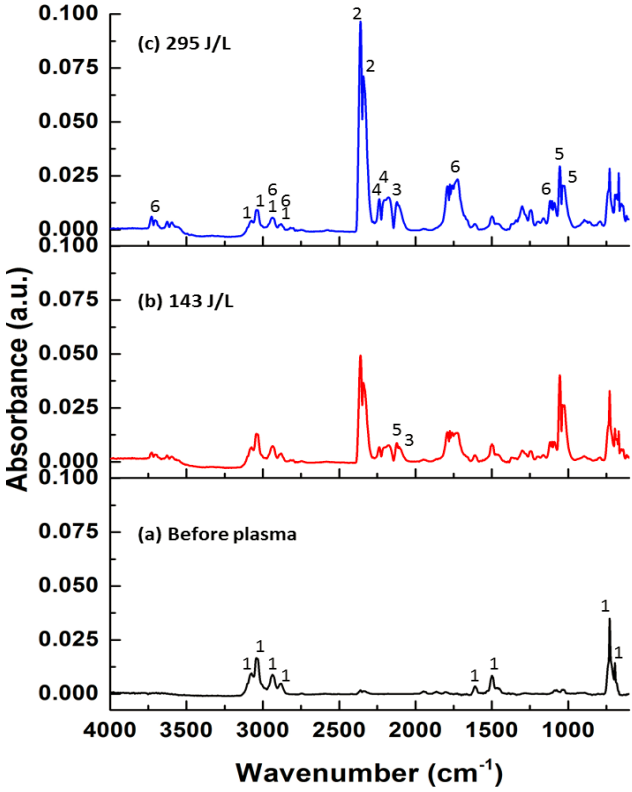

Figure 5.4. FTIR spectra of a dry air/toluene mixture before (black) and after plasma at an energy density of 143 J/l (red) and 295 J/l (blue)

Figure 5.4 also clearly shows that the intensities of the by-product IR bands increase with increasing SIE value suggesting that these by-products are generated in higher amounts at higher SIE values, which is consistent with the increased toluene conversion observed at higher SIE values.

After a close investigation of the outlet FTIR spectra in humid air (not shown here), a great resemblance with the spectra obtained in dry air could be observed. However, two major differences could be clearly observed: (1) a broad absorption band in the region 3600-3000 cm^{-1} due to the presence of water appears in the humid air gas streams and (2) the peaks attributed to formic acid disappear with the introduction of water vapor.

Besides identifying the by-products in the outlet, it is also very important to quantify these products and to examine the influence of applied SIE values and the RH of the air stream on their concentration. These results will therefore be

given in the following paragraphs for the identified by-products (CO_2, CO, ozone, N_2O and HCOOH). First of all, the amount of generated CO_2 will be investigated as this is the targeted degradation product. **Figure 5.5 and 5.6** show the evolution of the CO_2 yield and CO_2 selectivity respectively as a function of SIE for toluene loaded air streams with different RH. The CO_2 yield and selectivity are defined as follows:

$$Y_{CO_2}(\%) = \frac{[CO_2]}{7[toluene]_{in}} * 100 \qquad \text{(Eq. 5.4)}$$

$$S_{CO_2}(\%) = \frac{[CO_2]}{7[toluene]_{conv}} * 100 \qquad \text{(Eq. 5.5)}$$

Where $[CO_2]$ is the amount of CO_2 detected in the outlet gas stream and $[toluene]_{conv}$ the amount of toluene converted by the plasma.

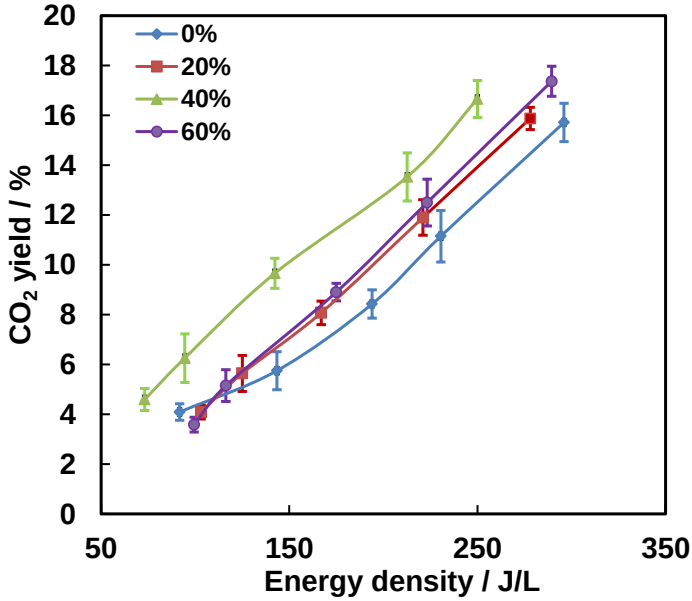

Figure 5.5. CO_2 yield as a function of SIE for different relative humidities (RH = 0%, 20%, 40% and 60%)

Figure 5.5 clearly shows similar trends as the ones depicted in **Figure 5.3**. The CO_2 yield increases with increasing SIE values and with increasing humidity until an RH value of 40%. At higher humidity levels, the CO_2 yield again decreases. These results thus suggest that the more toluene is destroyed due to the addition of extra energy or the increase in humidity, the more CO_2 is produced, which is a rather straightforward conclusion. However, when looking

at the evolution of the CO_2 selectivity as presented in **Figure 5.6**, a completely different behavior can be observed: the CO_2 selectivity first slightly decreases and then remains more or less constant in the range 35-40% with increasing SIE values. In addition, the presence of water vapor also seems to have no significant influence on CO_2 selectivity although it was already observed that it can influence the decomposition efficiency. This result thus means that although more CO_2 is produced in the effluent gas with increasing SIE values and increasing RH up to 40%, these CO_2 molecules will not be more preferentially generated compared to the other by-products. Air humidity can thus not affect CO_2 selectivity, but might have an influence on the formation of other by-products which will be examined in the next few paragraphs.

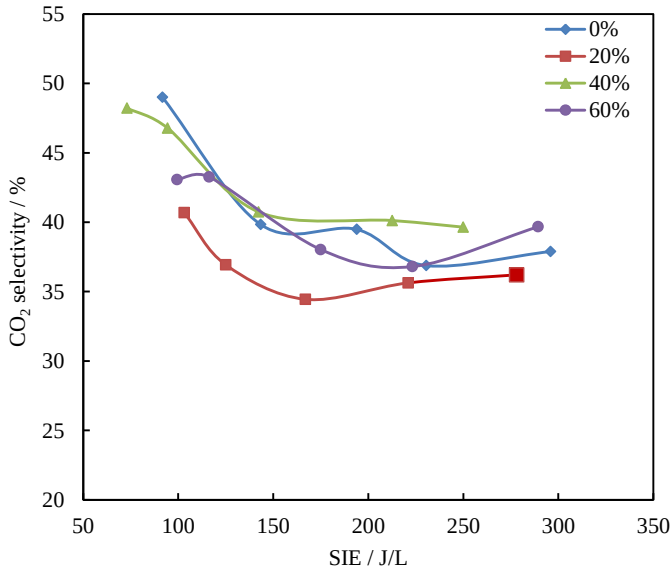

Figure 5.6. CO_2 selectivity as a function of SIE for different relative humidities (RH = 0%, 20%, 40% and 60%)

The second by-product that will be investigated in this work is CO and the results will be presented hereafter. **Figure 5.7** and **Figure 5.8** show the evolution of the CO yield and CO selectivity respectively as a function of SIE for toluene loaded air streams with different RH.

The CO yield and selectivity are defined as follows:

$$Y_{CO}(\%) = \frac{[CO]}{7[toluene]_{in}} * 100 \qquad \text{(Eq. 5.6)}$$

$$S_{CO}(\%) = \frac{[CO]}{7[toluene]_{conv}} * 100 \qquad \text{(Eq. 5.7)}$$

where [CO] is the amount of CO detected in the outlet gas stream and $[toluene]_{conv}$ the amount of toluene converted by the plasma.

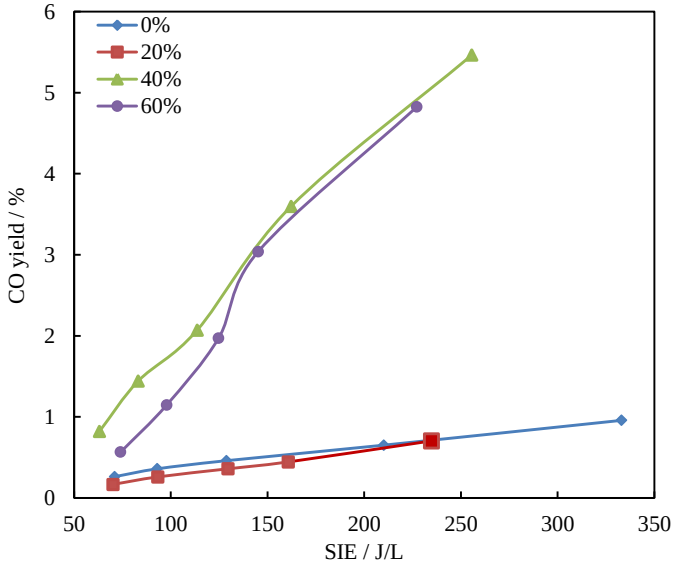

Figure 5.7. CO yield as a function of the SIE for different relative humidities (RH = 0%, 20%, 40% and 60%)

From **Figure 5.7**, it can be clearly observed that the CO yield slightly increases with increasing SIE values for dry air and a RH of 20% while it strongly increases for an RH of 40% and 60%. The evolution of the CO selectivity as presented in **Figure 5.8** shows that the CO selectivity is very low (<5%) for dry air and a RH of 20% and that it remains more or less constant with increasing SIE values. In contrast, a higher CO selectivity (7-20%) can be observed at a RH of 40 and 60% and this CO selectivity slightly increases with increasing SIE values.

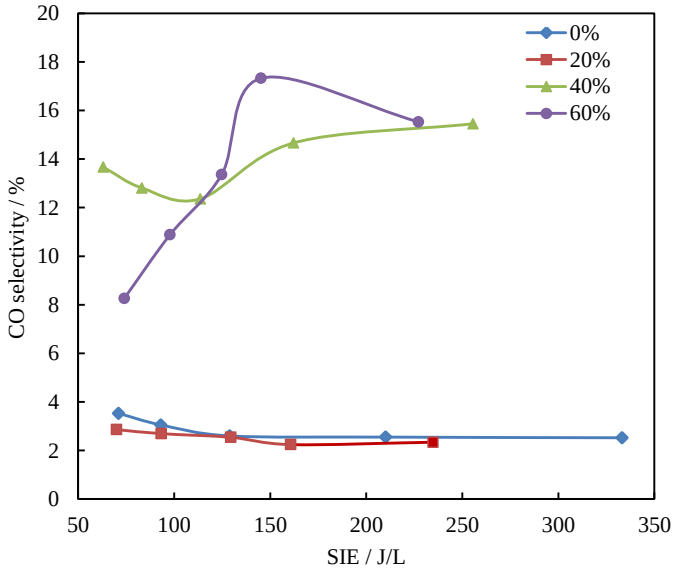

Figure 5.8. CO selectivity as a function of the SIE for different relative humidities (RH = 0%, 20%, 40% and 60%)

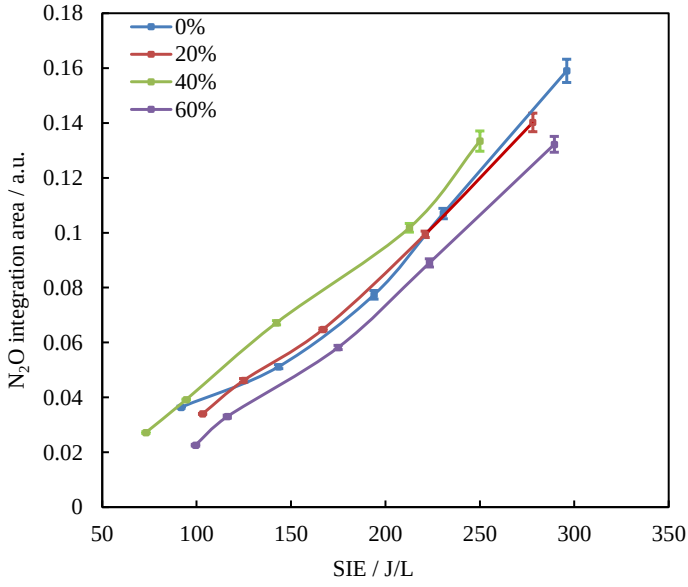

Figure 5.9. Formation of N_2O as a function of SIE for different relative humidities (RH=0%, 20%, 40% and 60%)

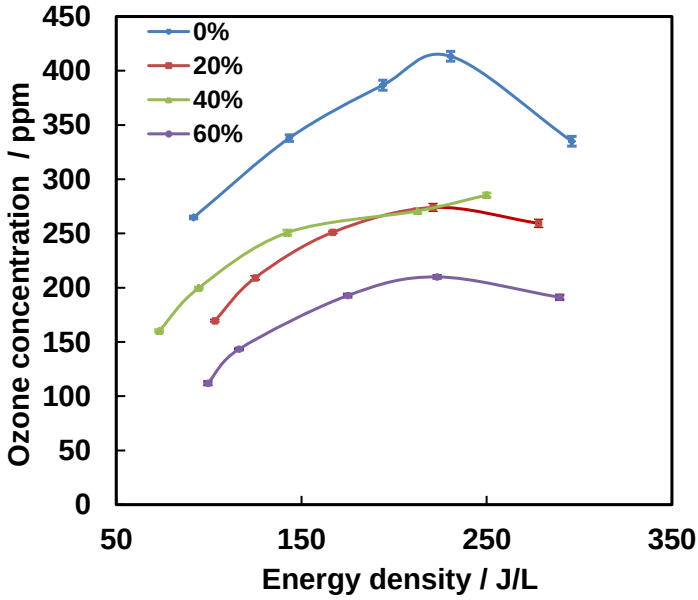

Figure 5.10. Ozone productions as a function of specific input energy for different relative humidities (RH=0%, 20%, 40% and 60%)

During plasma-assisted VOC decomposition, formation of nitrogen oxides is an undesirable process because of their adverse effects on human health. Interestingly, NO and NO_2 have not been detected in the plasma outlet stream under the experimental conditions used in this work. However, the formation of NO_2 was found to occur at very high energy densities (>600 J/l) in both dry as well as humid air (more info will be further given).

In addition, the formation of N_2O was also found to be considerable as could already be observed from the FTIR spectra presented in **Fig.5.4 (b)**. As quantification of N_2O is not possible in this work, the N_2O FTIR peak integration area will be used as a measure for the amount of N_2O and the results as a function of SIE are presented in **Figure 5.9**. As shown in this figure, the formation of N_2O strongly increases with increasing SIE values for all examined RH values. The formation of N_2O does not change when the RH is increased from 0 to 20%, but does increase when the RH is increased to 40%. A higher RH value of 60% however results in a lower N_2O formation.

Figure 5.10 also shows that increasing the humidity of the toluene-loaded air flow results in a noticeable decrease in ozone concentration at the plasma reactor outlet. It is well know from literature [165, 166] that oxygen atoms play a crucial role in the main O_3 formation mechanism, which is shown hereafter:

$$O + O_2 + M \rightarrow O_3 + M \qquad \text{(Eq. 5.8)}$$

However, in humid air, oxygen atoms tend to be rapidly consumed by water related species and the following reaction is believed to be responsible for the largest removal of oxygen atoms [166]:

$$O + H_2O \rightarrow OH + OH \qquad \text{(Eq. 5.9)}$$

As a result, less atomic oxygen atoms are present in humid air resulting into a reduction in O_3 production. In addition, it can also be observed in **Figure 5.10** that the ozone concentration first increases with increasing SIE values to reach a maximal value at approximately 225 J/l after which the ozone concentration starts to decrease. This behavior is in good agreement with former studies performed by Yamamoto et al. [114] and Holzer et al. [115]. The phenomenon that the ozone concentration decreases at high SIE values is peculiar to ozone generation in air DBD discharges as it never appears in pure oxygen DBDs. The reason for this can be twofold: (1) the concentration of NO_x species increases at high SIE values and/or (2) the gas temperature increases with input energy resulting into thermal dissociation of ozone [167]. However, when looking at the FTIR spectra of the gas outlet stream at an SIE value of 290 J/l, no NO_x species can be observed suggesting that in this case most likely the occurring high gas temperature at 290 J/l is responsible for the decreasing ozone generation due to thermal O_3 dissociation. Indeed, the temperature of the DBD reactor wall was found to be equal to 323 ± 3 K under these experimental conditions which is an underestimation of the actual gas temperature in the reactor. As a result, it is expected that the gas temperature in the reactor can be high enough to induce thermal dissociation of ozone which is also in agreement with emission spectroscopy results.

It is observed that when the used DBD reactor is operated in dry air at very high energy densities, like for example 651 J/l, the generation of NO_x species does occur rapidly as can be seen in **Figure 5.11**, where the evolution of the concentration of NO_2 and ozone is shown as a function of plasma operating time. This figure clearly shows that at the time point NO_2 species are being created, the ozone concentration strongly decreases and reaches a concentration close to zero when high amounts of NO_2 species are present in the discharge. Similar trends have also been observed in the examined humid air discharges, but are not

shown in this work. A high concentration of NO_2 is known to completely stop the generation of ozone since it consumes oxygen atoms at a very fast rate according to the following reactions [168]:

$$O + NO_2 \rightarrow NO + O_2 \quad \text{(Eq. 5.10)}$$

$$O + NO + M \rightarrow NO_2 + M \quad \text{(Eq. 5.11)}$$

As a result, at high energy densities, the atomic oxygen reactions with NO_2 become faster than their reaction with molecular oxygen thereby resulting in an ozone generation stop (so-called discharge poisoning) [168]. This observation is thus in good agreement with literature stating that ozone and nitrogen oxides do not coexist well in a non-thermal plasma [169]. Indeed, the used packed bed DBD reactor effectively produces ozone and no NO_2 at low energy densities, while at high energy densities, high amounts of NO_2 are generated without any ozone formation. To avoid the phenomenon of discharge poisoning, the specific input energy of the experiments conducted in this paper has therefore been restricted to 300 J/l.

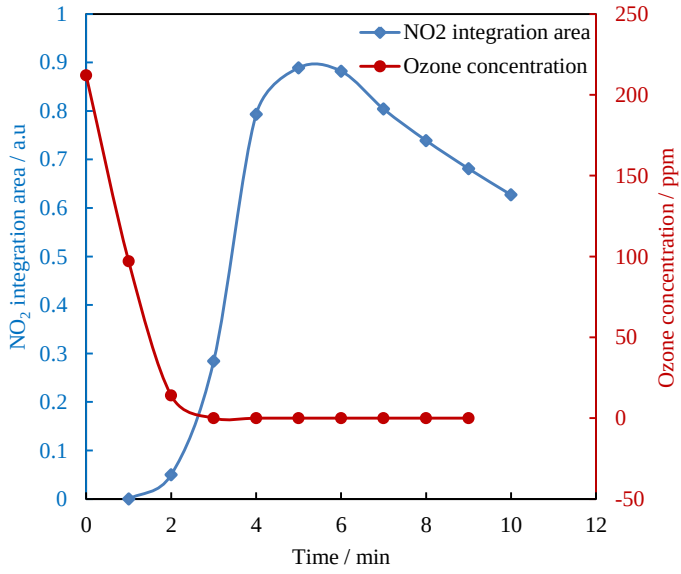

Figure 5.11 Formation of NO_2 and disappearance of ozone as a function of time in a toluene/dry air mixture for a specific input energy of 651 J/l

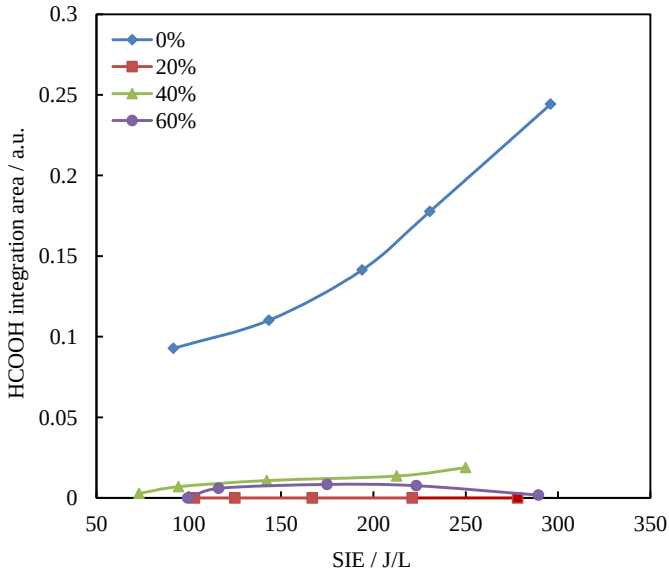

Figure 5.12. Formic acid production as a function of specific input energy for different relative humidities (RH=0%, 20%, 40% and 60%)

The final by-product which will be examined in this paper is formic acid, which has been detected by FTIR (and also confirmed by mass spectrometry, not presented here) in the effluent gas and which has been often reported as an important gaseous byproduct of plasma-assisted toluene removal [170-172]. **Figure 5.12** shows the integrated FTIR peak area of the formic acid ester band (1760 - 1690 cm^{-1}) as a function of specific input energy. This figure clearly shows that in dry air the formation of formic acid is considerable while it also increases with increasing SIE value, whereas in the presence of water vapor, the formation of formic acid becomes almost negligible. This is due to the presence of OH radicals in the humid air discharges which are effectively quenched by formic acid leading into complete oxidation of formic acid to CO_2 and H_2O [172].

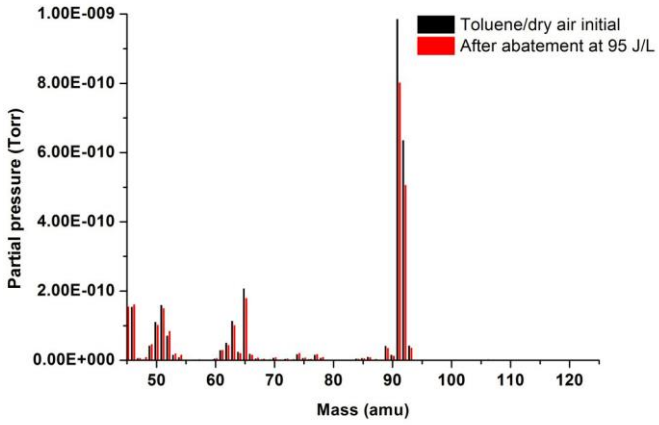

Figure 5.13. Mass spectrum of inlet toluene/dry air before plasma treatment and after plasma treatment at energy density of 95 J/L

The mass spectra of the inlet toluene/dry air before plasma treatment and after abatement at the SIE of 95 J/L are shown in **Figure 5.13**. Before plasma treatment, the mass spectrum shows only the characteristics fragments of toluene. The mass spectrum of the outlet gas after the plasma treatment at the energy density of 95 J/L shows the decrease in the abundance of toluene. From the mass spectrum obtained after the plasma treatment, it is observed that the by-products such as benzene (mass = 78 amu), benzaldehyde (mass = 77, 105, 106 amu) and benzoic acid (mass = 77, 105, 122 amu) are absent.

5.4. Conclusion

In this work, conclusions can be made:Firstly, optical emission spectroscopy has shown that with increasing humidity, less N_2 excited states are present in the discharge, which can be attributed to the increased quenching of these states due to collisions with water molecules before they undergo spontaneous emission to a lower excited state. Unfortunately, it was not able to derive any conclusions on the effect of RH on the amount of excited oxygen atoms as well as excited OH radicals since no corresponding emission peaks have been observed. OES was however able to determine the nitrogen rotational temperature which was found to be equal to 450±50 K for the highest discharge power used in this work (5.0 W). At the same time, under these conditions, the DBD reactor wall temperature was found to be 323±3 K, which is significantly lower than the nitrogen rotational temperature due to the fact that this rotational temperature is an

overestimation of the bulk gas temperature as it only gives an indication of the temperature in the core of the microdischarges. It was also observed that nor the nitrogen rotational temperature nor the reactor wall temperature was influenced by the RH of the gas stream. After characterizing the discharge itself, toluene decomposition experiments were also performed thereby limiting the discharge power to 5.0 W was higher discharge powers were found to result in the formation of the unwanted by-product NO_2. It was observed that the highest toluene removal efficiency was observed at a RH of 40% most likely due to the fact that the OH radical amount in the plasma is the highest under these experimental conditions. In addition, all gaseous products in the plasma reactor outlet have been identified and the main products of the toluene decomposition process were found to be CO_2, CO, N_2O, O_3 (both dry and humid air) and HCOOH (dry air only). Increasing the RH of the air stream was found to completely suppress the formation of formic acid while the formation of ozone was also found to decrease. In contrast, the CO selectivity was found to increase with RH, while the CO_2 selectivity was unaffected by the addition of water to the air stream. The highest N_2O concentration was observed at a RH of 40%: this observation in combination with the observed relatively high amounts of CO_2, CO and O_3 molecules in the gas outlet at a RH of 40% confirm the observed highest removal efficiency at this experimental condition. It can thus be concluded that toluene decomposition in the examined packed bed DBD reactor is the most efficient at a RH of 40%.

CHAPTER 6: INFLUENCE OF THE PREPARATION METHOD ON THE ACTIVITY OF COPPER-MANGANESE OXIDES FOR TOLUENE TOTAL OXIDATION

The results of chapter 6 were published in the following international peer-reviewed journal:

Z. Ye, J.-M. Giraudona, N. Nuns, P. Simon, N. De Geyter, R. Morent, J.-F. Lamonier

Influence of the preparation method on the activity of copper-manganese oxides for toluene total oxidation

Applied Catalysis B: Environmental, in press, 2017

6.1. Introduction

Catalytic total oxidation is one of the most promising approaches for the abatement of toluene owing to its high efficiency and relative low operating temperature [130]. During the course of these experiments, it was opted to use transition metal-based catalysts as these are cheaper and more readily available compared to noble metals. Cu-Mn mixed oxides are promising class of catalysts for VOCs oxidation, ozone decomposition and ambient temperature CO oxidation [8, 173, 174]. The preparation method was considered to be one of the reasons for high catalytic performance [8]. To date, numerous preparation method for Cu-Mn mixed oxides have been reported including co-precipitation [100], sol-gel method [175], solid-grounding method [141], redox [142, 176], thermal format decomposition [177] etc. During the course of this chapter, Cu-Mn oxide catalysts have been synthesized by two different routes: co-precipitation and the redox method. Catalysts $CuMn_2O_4$-P4, CuOx-P4 and MnOx-P4 were prepared as references for co-precipitation, while CuMnOx-R3, CuMnOx-R2 and MnOx-R3 were used to evaluate the calcination temperature and Cu ions effect in the redox method. In addition, the performances of doped noble catalysts (Pd, Pt) were evaluated too.

6.2. Experimental conditions

8 catalysts are prepared and one commercial catalyst is used to compare as-prepared catalysts. For co-precipitation/precipitation method: CuOx-P4, MnOx-P4,$CuMn_2O_4$-P4, For redox-precipitation method: CuMnOx-R3, CuMnOx-R2 and MnOx-R3, and doping 0.5 wt% of noble metals: Pt/ CuMnOx-R3 and Pd/CuMnOx-R3. The commercial catalyst is purelystMD101. The characterization includes ICP-OES, BET, TPR, XRD, SEM, XPS, TGA-MS, ToF-SIMS. And the test in air, test in He, stability test are also performed. The detailed preparation process, characterization process, experiment process and nomenclatures can be seen in chapter 3.3.

Table 6.1 summarizes the basic experimental conditions used in this chapter. The detail also can be found in chapter 3.3.

Table 6.1 Experimental conditions

Air source	Air cylinder
Flow rate	100 ml/min
Initial toluene concentration	~800 ppm
Temperature	300 / 400 ℃ to room temperature
Catalyst weight	200 mg
Stability duration time	24 h
Analyzing apparatus	GC with FID and TCD

6.3. Results and discussion

6.3.1. Catalysts characterization results

ICP-OES results

The elemental composition of the various copper-manganese oxide catalysts is shown in **Table 6.2**. The Mn/Cu atomic ratio of 1.8 is close to the expected value of 2.0 for $CuMnO_4$-P4 sample. Conversely a Mn/Cu atomic ratio of 4.8 for CuMnOx-Ri far exceeding the expected value of 1.0 indicates a copper loss. This result is in agreement with the work of Njagi *et al* [101]. The partial copper loss resulting from the washing step of the preparation can be explained considering that Cu^{2+} ions were not directly involved in the redox reaction. It is also to be noted that small amount of K was detected on MnOx-R3 although intense washing.

Table 6.2 ICP-OES analysis results

	Mn /wt%	Cu /wt%	Mn/Cu[a]	K /wt%	Pd /wt%	Pt /wt%
MnOx-P4	74.43	-				
CuOx-P4	-	80.44				
$CuMn_2O_4$-P4	47.05	30.59	1.8			
MnOx-R3	54.97			4.04		
CuMnOx-R2	45.62	11.05	4.8			
CuMnOx-R3	48.41	11.66	4.8			
Pd/CuMnOx-R3	48.74	11.97	4.7		0.51	
Pt/CuMnOx-R3	46.96	11.26	4.8			0.40

a: atomic ratio

Textural properties

Table 6.3 Textural and H_2-TPR properties of the catalysts

	S_{BET} (m^2/g)	Vp^a (cm^3/g)	H_2 ($mmol/g_{cata}$)	$H_2/(Cu+Mn+M^b)$	Mn AOS
MnOx-P4	27	0.14	5.85	0.43	2.9
CuOx-P4	8	0.05	12.83	1.01	-
$CuMn_2O_4$-P4	48	0.30	9.73	0.73	3.2
MnOx-R3	384	0.66	8.52	0.85	3.7
CuMnOx-R2	194	0.47	9.8	0.98	3.9
CuMnOx-R3	166	0.30	9.84	0.92	3.8
Pd/CuMnOx-R3	118	0.24	9.86	0.91	3.8
Pt/CuMnOx-R3	110	0.23	9.77	0.94	3.9

a: BJH Desorption cumulative volume of pores; b: M = Pt or Pd

Table 6.3 summarizes the textural properties of the different solids. The single oxides, namely CuOx-P4 and MnOx-P4, have BET surface areas of 8 and 27 m^2/g, respectively. Conversely the BET surface area of the Cu-Mn oxide of 48 m^2/g is significantly larger than those of the single oxides as previously observed [100]. The surface area of CuMnOx-Ri increases from 166 m^2/g up to 194 m^2/g with a decreasing calcination temperature of 100 ℃. However these BET surface areas are less than that of MnOx-R3 oxide amounting to 391 m^2/g. The total pore volumes of the "redox-precipitation" samples which ranged from 0.30 to 0.66 cm^3/g are significantly higher than those of the co-precipitated samples ranging from 0.05 to 0.30 m^2/g. It is to be noted that the dispersion of Pt or Pd by wet impregnation on CuMnOx-R3 leads to decreased BET surface areas, most probably due to pore clogging. To sum up the redox-precipitation route allows to get improved textural properties for the catalysts as compared to the co-precipitation one.

X-ray diffraction patterns of the samples

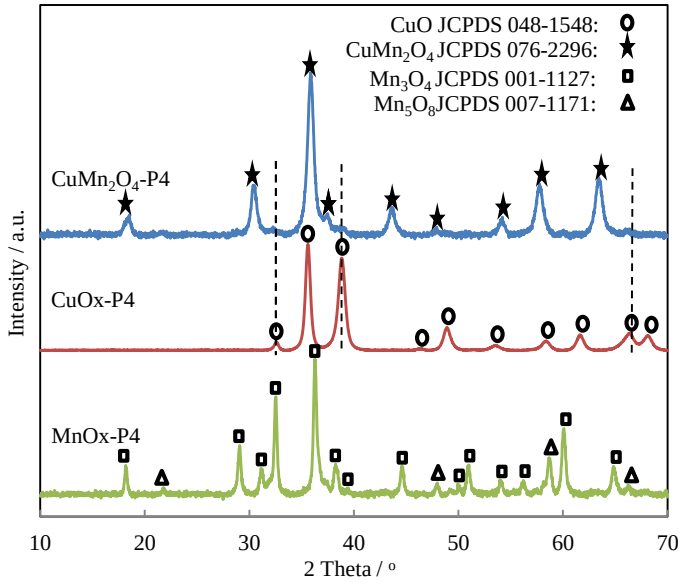

Figure 6.1. XRD patterns of co-precipitated samples

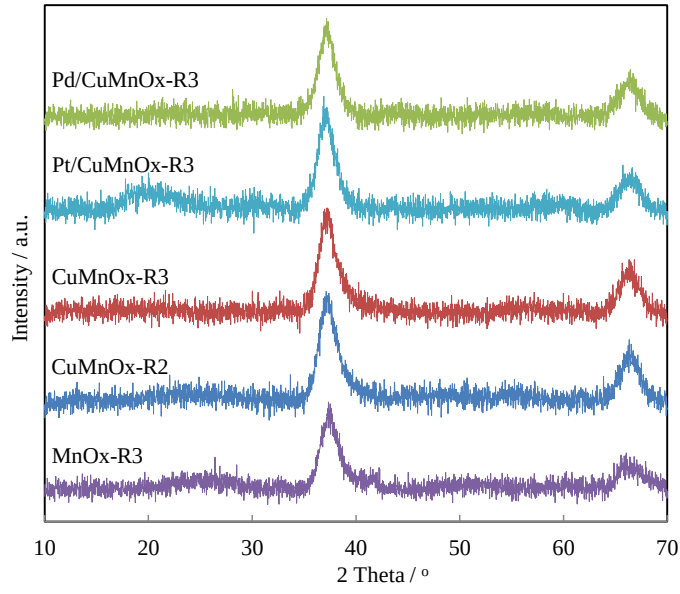

Figure 6.2. XRD patterns of redox samples

The powder X-ray diffraction patterns of the Cu-Mn oxides prepared by the two methods are superposed in **Figure 6.1 and Figure 6.2**, respectively. The characteristic peaks of the spinel $CuMn_2O_4$ were observed for $CuMn_2O_4$-P4 (JCPDS 01-076-2296). Minor peaks due to traces of CuO were also detected. For the Cu single oxide (CuOx-P4), all of the peaks were indexed by the diffraction of CuO phase (JCPDS 048-1548) and no other peaks were detected. For MnOx-P4 sample, Mn_3O_4 (JCPDS 001-1127) along with Mn_5O_8 phase (JCPDS 007-1171), as a minor contribution, were observed. Conversely the MnOx and CuMnOx samples prepared from the redox-precipitation method have similar X-ray diffraction patterns showing two very broad diffraction peaks in the 33-40 and 63-70 2 theta regions implying they are essentially amorphous [101]. This apparently suggests the presence of (i) well dispersed/amorphous CuO_x or/and $Cu_xMn_yO_z$ phases imbedded in an amorphous MnO_x matrix and/or (ii) crystalline particles of above phases with average crystallite sizes or crystalline domains smaller than 2 nm. In order to get some additional information on the evolution of the amorphous phase to crystalline(s) phases with temperature and gas phase composition (air ; N_2) the structural evolution of the CuMnOx-R3 sample has been investigated using *in situ* X-ray diffraction.

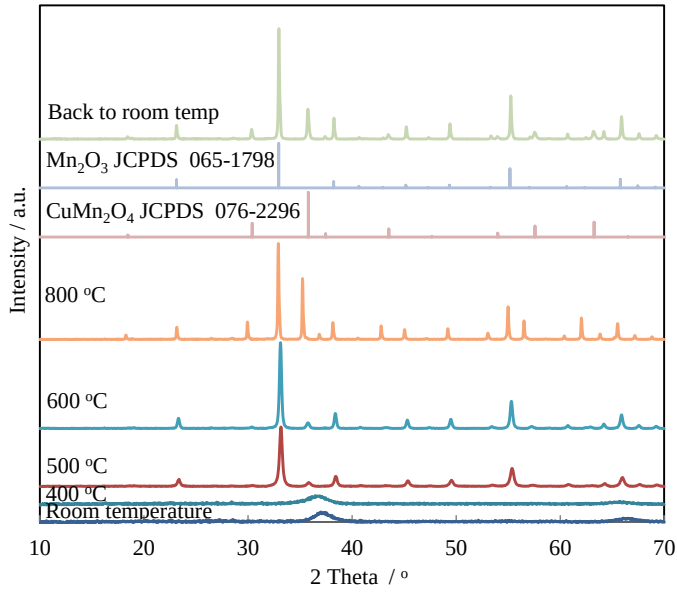

Figure 6.3. In situ XRD patterns of CuMnOx-R3 under flowing air in function of temperature

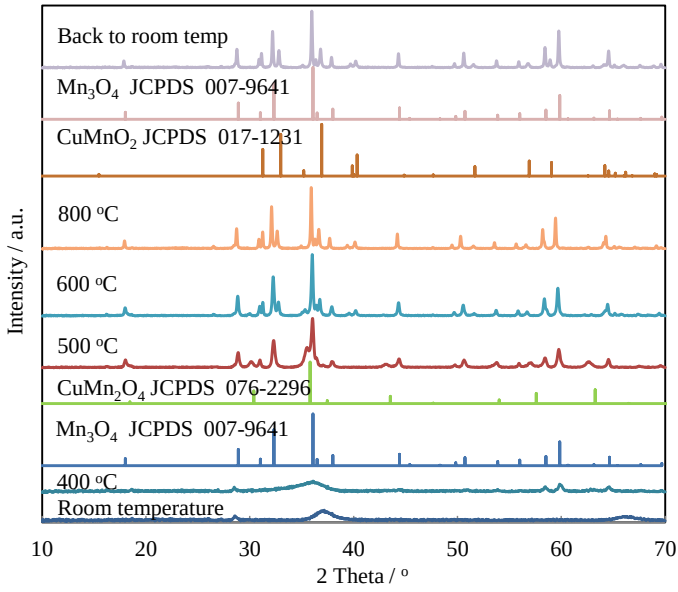

Figure 6.4. In situ XRD patterns of CuMnOx-R3 under flowing N2 in function of temperature

The resulting X-ray diffraction patterns have been plotted against temperature and presented in **Figure 6.3 and 6.4** considering air and N_2 treatment, respectively. As shown in **Figure 6.3** the material heated in air up to 400 ℃ remained amorphous. X-ray diffraction patterns recorded from 500 ℃ up to 800 ℃ revealed that Mn_2O_3 (JCPDS 065-1798) and $Cu_xMn_{3-x}O_4$ spinel oxide were formed and kept thermally stable in that temperature range. The thermal stability of the amorphous phase is also effective up to 400 ℃ when heating in N_2 (**Figure 6.4**). At 500 ℃ the transformation of the amorphous phase takes place into Mn_3O_4 as predominant phase and related spinel $Cu_xMn_{3-x}O_4$ as the minor one. Upon heating at 600 ℃ the X-ray diffraction pattern reveals the presence of additional $CuMnO_2$ oxide (crednerite) at the expense of the $Cu_xMn_{3-x}O_4$ phase. Such a phase has been already observed resulting from the decomposition of $CuMn_2O_4$ when heated at 350 ℃ involving the removal of lattice oxygen according to the formal reaction [178]:

$$2\ CuMn_2O_4 = 2\ CuMnO_2 + Mn_3O_4 + O_2 \qquad \text{(Eq. 6.1)}$$

Back to room temperature does not change the distribution of the related oxide phases.

SEM characterization

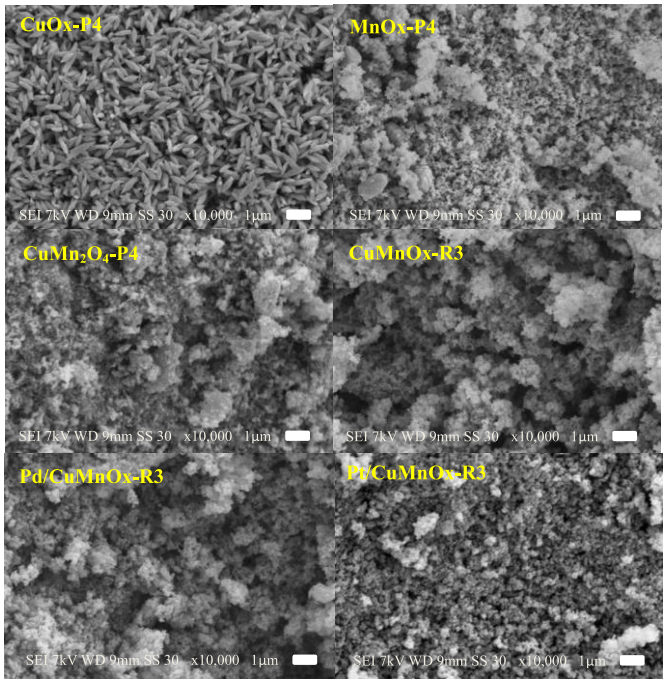

Figure 5. SEM micrographs of prepared catalysts

The SEM image in **Figure 5** clearly displays that CuO particles in CuOx-P4 have an ellipsoidal shape with an average length of 1000 nm and a width of 200 nm. The SEM picture of MnOx-P4 clearly shows randomly distributed spherical grains with small size of 100 nm diameter along with agglomerates. The surface morphology of $CuMn_2O_4$-P4 also shows quasi-spherical grains along with higher agglomerated grain structures as in MnOx-P4 sample. In comparison the SEM image of CuMnOx-R3 shows particles of near spherical morphology with homogeneous size distribution which characteristics are retained in the doped catalysts.

H_2-TPR studies

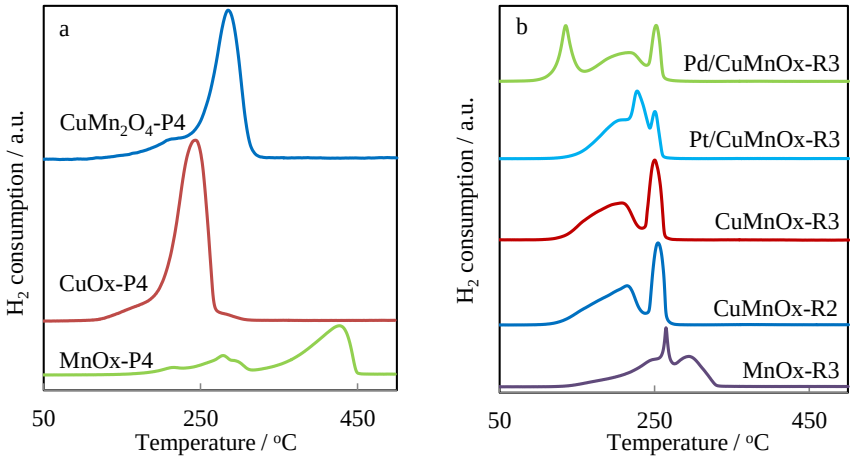

Figure 6.6. H_2-TPR profiles of the fresh catalysts prepared: a) from co-precipitated method; b) from redox method

H_2 temperature-programmed reduction profiles of related CuMn mixed oxides are shown in **Figure 6.6** a and b and the resulting H_2 consumption as well as the Mn AOS are given in **Table 6.3**. The TCD trace relative to $CuMn_2O_4$-P4 showed one asymmetric peak (150–320 ℃) in accordance with the results of Einaga et al. [100]. This suggests that the copper and manganese cations are reduced practically at the same temperature in the spinel lattice. Additionally the low temperature H_2 consumption may possibly arises from the reduction of small crystallites of CuO/MnOx well dispersed on the oxide matrix. We determined a Mn AOS of 3.1 in CuMnOx-P4 based on the corrected H_2 consumption taking into account the reduction of Cu(II) into Cu(0). This is in agreement with the Mn AOS of 3.2 given by H. Einaga *et al* using a linear relationship between the Mn AOS and absorption edge obtained from the Mn K-edge XANES spectra [100].

The CuOx-P4 sample shows only a peak of H_2 consumption in the range 140-300 ℃ indicating its high oxidizing ability. MnOx-P4 shows two reduction regions in the temperature range 160-320 ℃ and 320 - 450 ℃. The first one refers to the reduction of Mn_5O_8 to Mn_3O_4 and the second one to the reduction of Mn_3O_4 to MnO [179] in line with the X-ray diffraction results. The non-observance of the peak at high temperature for $CuMn_2O_4$-P4 has been previously explained by the role of Cu(0) promoting the reduction of manganese oxide by H_2 [100].

The TCD traces relative to $CuMnO_x$-Ri (i = 2,3) samples in **Figure 6.6b** are rather similar showing a broad asymmetric peak in the temperature range 120-

240 ℃ at 210 ± 5 ℃ followed by a symmetric narrow peak at about 250 ± 5 ℃. These curves differ from that of MnOx-R3 which exhibits two broad peaks at 244 and 295 ℃ along with a narrow peak in between at 265 ℃. The Mn AOS of 3.7 for MnOx-R3 increases up to 3.8 and 3.9 for the CuMnOx materials calcined at 200 and 300 ℃, respectively. These findings are consistent with a Mn AOS of 3.8, using potentiometric titration method, performed on a MnO_x catalyst prepared in a similar manner by Njagi *et al* but without calcination by the redox-precipitation method [101]. Consequently a mixed valent environment with Mn^{4+} being predominant can be invoked in this catalyst series. Pd and Pt dispersed on CuMnOx-R3 affect the H_2-TPR profiles while the total amount of consumed H_2 keeps rather constant. The TPR-profile of Pd/CuMnOx-R3 reveals a new peak at 135 ℃ while the remaining shape of the curve resembles that of CuMnOx-R3. The amount of hydrogen consumed in the low temperature peak can be consistent with the total reduction of PdO into metallic Pd promoting the reduction of Cu^{2+} and Mn^{n+} cations at the vicinity of the metallic palladium interface by hydrogen spill-over process. By opposition the H_2-TPR trace of Pt/CuMnOx shows three overlapping peaks at 204, 230 and 251 ℃. The non-observance of a low H_2 consumption can be due here to higher temperature of platinum reduction as compared to palladium. It is to be noted that the Mn AOS keeps at 3.8-3.9 for the doped catalysts shows no significant changes of the state of manganese.

XPS analysis

Table 6.4 XPS results on the fresh samples

Sample	Cu $2p_{3/2}$ BE (eV)	Mn $2p_{3/2}$ BE (eV)	Mn/Cu[a]	AOS Mn	O_1 BE (eV)	O_2 BE (eV)	O_3 BE (eV)	O_1 (%)	O_2 (%)	O_3 (%)	O_2/O_1
MnOx-P4	-	641.7	-	3.0	529.7	531.5	533.4	61.3	28.3	10.4	0.46
CuOx-P4	933.3	-	-	-	529.6	531.3	533.5	55.6	38.6	5.8	0.69
$CuMn_2O_4$-P4	931.2, 934.0	642.0	3.7	3.7	529.8	531.6	533.7	43.8	39.3	8.3	0.90
MnOx-R3		642.4	-	3.4	529.8	531.5	533.8	58.1	38.1	3.8	0.66
CuMnOx-R2	934.3	642.2	5.0	3.3	530.0	531.2	533.7	51.7	43.3	5.0	0.84
CuMnOx-R3	934.3	642.4	5.1	3.5	530.0	531.3	533.8	52.1	43.9	4.0	0.84
Pd/CuMnOx-R3	934.0	642.0	5.1	3.4	529.8	531.5	533.5	47.7	39.3	13.0	0.82
Pt/CuMnOx-R3	934.0	642.2	5.1	3.4	529.8	531.5	533.6	48.5	43.9	7.6	0.90

a: atomic ratio

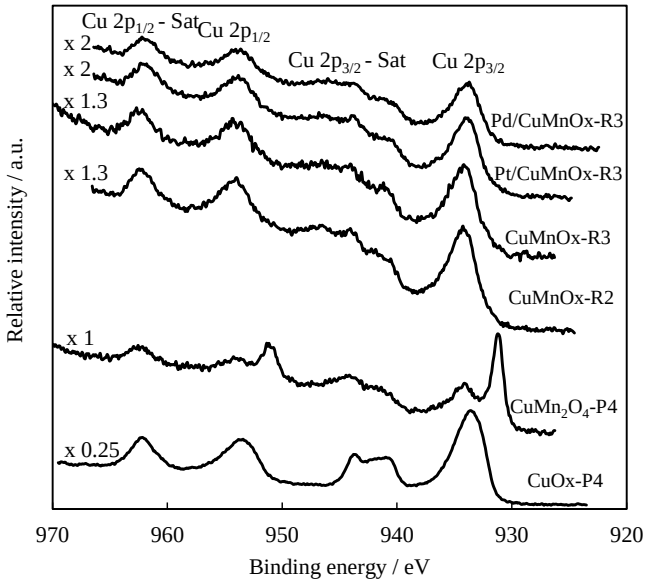

Figure 6.7. XPS Cu 2p core level recorded on the fresh catalysts

XPS data recordings given in **Table 6.4** were used to investigate the oxidation states of copper and manganese in the different catalysts. The Cu $2p_{3/2}$ envelope shows two distinct peaks for the spinel $CuMn_2O_4$-P4 (**Figure 6.7**). The signal at 931.1 eV is due to monovalent copper Cu^+ in accord with previously reported data [180]. The signal of lower intensity at 934.1 eV together with its satellite between 938 and 948 eV is indicative of divalent copper Cu^{2+} [181-183]. Integration of the signals leads to a Cu^+/Cu^{2+} ratio close to 0.5. The formation of Cu^+ takes place owing to the redox equilibrium $Cu^{2+} + Mn^{3+} = Cu^+ + Mn^{4+}$ [180] without excluding some partial reduction of Cu^{2+} under the X-ray beam. This is supported by the XPS Mn AOS of 3.7 which agrees with a mixture of $Mn^{4+/3+}$ with Mn^{4+} as the predominant cation. Additionally the atomic Mn/Cu ratio of 3.7 shows an excess of Mn at the catalyst surface. Conversely the CuMnOx-Ri oxides exhibit one single Cu $2p_{3/2}$ photopeak with BE of 934.2 (± 0.2 eV) ascribed to the presence of Cu^{2+} (**Figure 6.7**). The XPS Mn AOS of 3.3 ± 0.2 eV is in accordance with Mn^{3+} as dominant oxidation state on contrary to H_2-TPR results. The XPS atomic Mn/Cu ratio of 5.1 agrees with that of elemental analysis of 4.8 attesting of a good dispersion of the Cu-Mn oxide particles. The state and dispersion of the metal dopants (Pd ; Pt) dispersed on CuMnOx-R3 have also been investigated. The Pd 3d core level doublet (not shown here) has well separate spin-orbit components Pd $3d_{3/2}$ and Pd $3d_{5/2}$ separated by 5.3 eV. The Pd $3d_{5/2}$ component at about 337.4 eV has been attributed to Pd in a high

oxidation state (+3/+4) existing at the catalyst surface [184]. The Pd/(Mn + Cu) ratio of 0.018 as compared to the value of 0.0044 from elemental analysis shows a surface enrichment of Pd. Regarding Pt/CuMnOx-R3, as the Pt 4f core level is drawn in the Cu 3p envelope, the presence of Pt is only detected by the observance of Pt $4d_{3/2}$ core-level of low intensity precluding quantification and determination of the accurate oxidation state of Pt in the sample. The O1s spectra for all samples were fitted using three contributions. The O_1 component with BE ranging from 529.6 to 530.0 eV was characteristic of lattice oxygen (O^{2-}) [31]. The O_2 component with BE of 531.3–531.5 eV was ascribed to surface oxygen ions with low coordination [31]. While O_3 contribution was related to adsorbed water on the surface. It is to be noted that the formation of oxygen adspecies due to the presence of surface oxygen vacancies is generally believed to be an important parameter to consider in the catalytic activity. The values of the intensity O_2/O_1 ratios listed in **Table 6.4** have been used to quantify such species. It is found the highest values for the redox based catalysts, the $CuMn_2O_4$-P4 and Pt/CuMnOx-R oxides exhibiting the highest value of 0.9 in each series.

ToF-SIMS analysis

Table 6.5 List of the $Cu_xMn_yO_zH_w$ ions in polarity (+) and (-)

$Cu_xMn_yO_zH_w^+$	$CuMn_2O_4$-P4 intensity ($/10^3$ count/s)	CuMnOx-R3 intensity ($/10^3$ count/s)	$Cu_xMn_yO_zH_w^-$	$CuMn_2O_4$-P4 intensity ($/10^3$ count/s)	CuMnOx-R3 intensity ($/10^3$ count/s)
MnCuO	73.82	59.89	$CuMn_2O_4$	3.39	2.00
^{65}CuMnO	34.31	29.07	$CuMn_2O_4H^-$	0.87	1.15
CuMnOH	7.24	11.09	$^{65}CuMn_2O_4$	2.29	1.48
^{65}CuMnOH	3.58	5.13	$CuMn_2O_5$	3.99	1.94
CuMn	15.99	18.62	$CuMn_2O_5H^-$	0.96	1.27
CuMnH	7.97	2.86	$^{65}CuMn_2O_5$	2.17	1.40
$CuMnO_2$	4.00	3.85	$CuMn_3O_5$	3.34	2.30
$CuMnO_2H^+$	6.27	12.87	$CuMn_3O_5H^-$	0.57	0.85
$CuMnO_2H_2$	5.90	13.38	$^{65}Cu\ Mn_3O_5$	1.51	1.02
$^{65}CuMnO_2H$	3.57	6.29	$CuMn_3O_6$	3.84	2.06
$^{65}CuMn\ O_2H_2$	2.51	5.33	$CuMn_3O_6H^-$	0.61	0.70
$CuMn_2O_2$	21.40	13.86	$^{65}Cu\ Mn_3O_6$	1.97	1.12
$^{65}Cu\ Mn_2O_2$	16.97	7.37	$CuMn_4O_6$	1.01	0.82
$CuMn_2O_3$	8.36	5.58	$CuMn_4O_6H^-$	0.31	0.57
$^{65}CuMn_2O_3$	4.95	5.82	$CuMn_4O_7$	1.29	0.73
$CuMn_2O_3H$	4.57	8.45	$CuMn_4O_7H^-$	0.28	0.40
$^{65}CuMn_2O_3H$	2.44	3.73	$^{65}Cu\ Mn_4O_7$	0.83	0.40
$CuMn_3O_3$	8.43	8.29			
$^{65}CuMn_3O_3$	5.21	4.03			
$CuMn_3O_4$	7.22	5.32			
$^{65}CuMn_3O_4$	3.90	3.25			
$CuMn_4O_5$	4.15	3.18			
$^{65}CuMn_4O_5$	2.67	1.84			
$CuMn_4O_4$	3.68	4.14			
$^{65}CuMn_4O_4$	2.60	1.97			
$CuMn_5O_5$	1.58	2.20			
$^{65}CuMn_5O_5$	1.02	1.02			
$CuMn_5O_6$	2.20	1.90			
$^{65}CuMn_5O_6$	1.46	1.10			
Sum	267.97	251.46	Sum	29.23	20.21
$Cu_xMn_yO_zH_w^+$ (%)	9.06	5.99	$Cu_xMn_yO_zH_w^-$ (%)	2.80	2.85

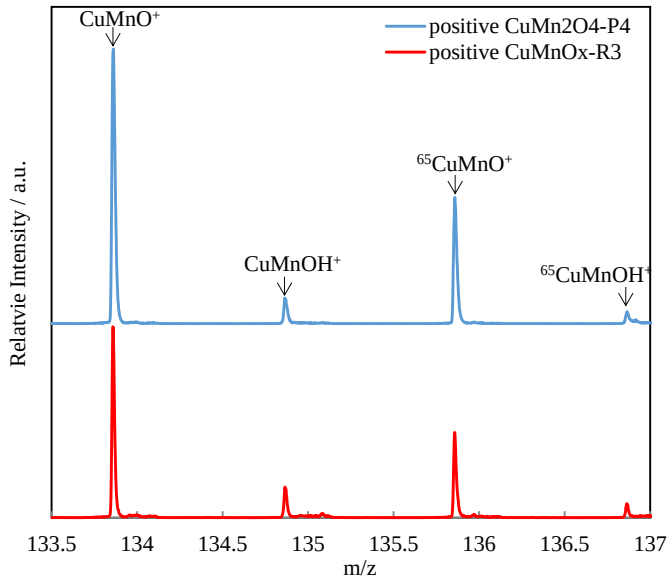

Figure 6.8. ToF-SIMS spectra in polarity (+); m/z range: 133.5-137.0

Time-of-flight secondary ion mass spectrometry (ToF-SIMS) analyses have been performed in static conditions on fresh $CuMn_2O_4$-P4 and CuMnOx-R3 catalysts in order to get molecular information about the surface as ToF-SIMS enables to probe the top layers (1–3 nm) of the catalysts. It is to be noted the detection of $Cu_xMn_yO_zH_w$ secondary ions both in polarities (+) and (-) which have been compiled in **Table 6.5**. As an example the $CuOMn^+$ secondary signal has been reported for the 2 Cu-Mn oxides in **Figure 6.8**. Such family of ions contributes in relative intensity to 9.0% and 6.0% in polarity (+) and to 2.80% and 2.85% in polarity (-) based on the total intensity of significant secondary ions for $CuMn_2O_4$-P4 and CuMnOx-R3, respectively. The detection of such secondary ions in significant amount is indicative of an intimate intermixing of Mn, Cu and O leading to compositionally homogeneous nanoscale materials.

6.3.2. Toluene oxidation experiments

Light-off curves

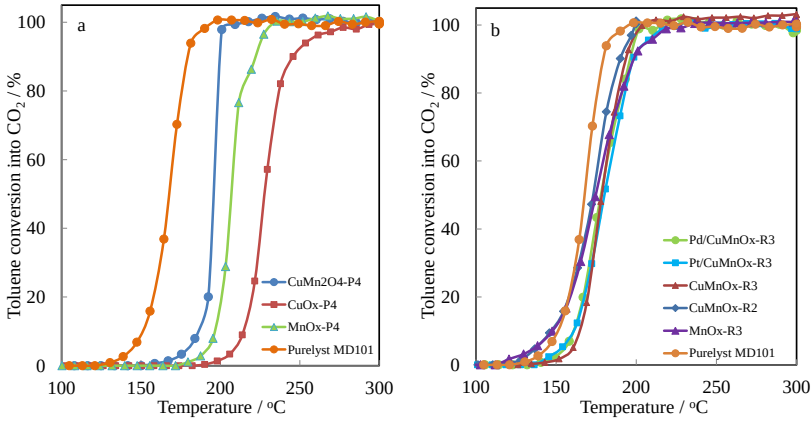

Figure 6.9. Light-off curves of the fresh catalysts prepared: a) from co-precipitated method; b) from redox method – Comparison with commercial Purelyst MD101 sample

Table 6.6 The summary of catalytic results in literature

Catalyst sample	GHSV (h^{-1})	T_{10} (^oC)	T_{50} (^oC)	T_{90} (^oC)	r^a (μmol/h.g)	r^a (μmol/h.m^2)	C_t^c (%)	r_1^b (μmol/h.g)	r_1^b (μmol/h.m^2)
MnOx-P4	21700	196	207	223	-	-	-	-	-
CuOx-P4	29700	215	228	247	-	-	-	-	-
$CuMn_2O_4$-P4	27800	185	195	200	22	0.45	0.14	1.9	0.04
MnOx-R3	16500	147	174	199	401	1.04	-	-	-
CuMnOx-R2	6100	146	173	190	420	2.17	4.41	43	0.22
CuMnOx-R3	8200	164	179	194	205	1.23	2.09	20	0.12
Pd/CuMnOx-R3	7700	160	178	196	289	2.45	2.11	21	0.18
Pt/CuMnOx-R3	8900	160	180	198	251	2.28	2.27	22	0.20
Purelyst MD-101	13200	151	170	180	550	1.90	3.88	38	0.13

Toluene (800 ppmv)/air;
a: reaction rate at 170 ^oC (light-off curves); b: reaction rate at 150 ^oC (stability test) ; c: estimated at the end of stability test

The conversion of toluene into CO_2 as a function of catalyst temperature is plotted in **Figure 6.9**. T_{10}, T_{50} and T_{90}, the temperatures at which respectively 10%, 50% and 90% of toluene is converted into CO_2 as well as the specific and intrinsic rates at 170 °C are listed in **Table 6.6**. Adding copper to manganese by co-precipitation improves the toluene conversion (**Figure 6.9a**). Indeed the activity of the catalysts based on T_{50} value (in °C) decreases as follows: $CuMn_2O_4$-P4 (195) < MnO_x-P4 (207) < CuO_x-P4 (228). This order is maintained when considering T_{10} and T_{90}. Comparatively the redox-precipitation based catalysts are more active with a T_{50} value of 173 °C for the most active CuMnOx-R2 catalyst which compares well with that of Purelyst MD101 catalyst at 170 °C. Although the MnOx-R3 and CuMnOx-Ri catalysts have a similar T_{50}, at about 175 °C, the mixed oxides appear more active at higher temperature as attested by the T_{90} values. The intrinsic rate (in µmol/(h.m^2)) at 170 °C decreased in the following order: CuMnOx-R2 (2.17) > CuMnOx-R3 (1.23) ≈ MnOx-R3 (1.04) as shown in **Table 6.6**. The higher intrinsic rate of CuMnOx-R2 than that of CuMnOx-R3 was ascribed to an improvement of textural properties induced by a decrease of calcination temperature. Hence the good toluene conversion on CuMnOx-R2 was ascribed to the high surface density of catalytic sites in correlation with its high specific surface area and to an improvement of the active site quality.

Adding Pt or Pd to CuMnOx-R3 does not improve the toluene conversion (**Figure 6.9b**). The comparison of the performances of Pt/CuMnOx-R3 or Pd/CuMnOx-R3 catalysts with alumina supported Pt or Pd ones studied in literature is performed through an overview table containing for each study the nature of the support, the noble metal weight percentage, the toluene concentration, the gas hourly space velocity and the T_{50} (**Table 7**). Based on this literature review, the works of Liotta *et al.* [185] (Pt/γ-Al_2O_3) and Kim *et al.* [186] (Pd/γ-Al_2O_3) can be selected for comparison since the experimental test conditions used in both studies are similar to those we have employed. Despite low noble metal loading (0.5 wt%), the catalytic performances of Pt/CuMnOx-R3 and Pd/CuMnOx-R3 can be favorably compared with those of Pt(1wt%)/γ-Al_2O_3 (T_{50} = 180 °C) [185] and Pd(1wt%)/γ-Al_2O_3 T_{50} = 220 °C) [186], respectively (Table S1). It is to be noted that benzene and benzaldehyde are detected as trace amounts in the course of the catalytic reaction.

Table 6.7 Overview of Pd or Pt/Al_2O_3 catalysts used for toluene oxidation

Catalyst	Support	M* wt% * Pt or Pd	Feed	Toluene (ppm)	GHSV/ mL $g^{-1}.h^{-1}$	T_{50}/ ºC	Ref.
$Pt/\gamma\text{-}Al_2O_3$	184 m^2 g^{-1}, Engelhard	0.5	Air	1000	200,000	205[a]	[187]
$Pt/\gamma\text{-}Al_2O_3$		1	Air			235	
$Pd/\gamma\text{-}Al_2O_3$	223 m^2 g^{-1}	1	Air	141	30,000	275	[188]
$Pt/\gamma\text{-}Al_2O_3$	105 m^2 g^{-1},	1	Air	215	34,285	216	[189]
$Pt/\gamma\text{-}Al_2O_3$	120 m^2 g^{-1}, Alfa-Aesar	0.7	20% O_2 in He	300	80,000	162[a]	[190]
Pt/Al_2O_3	107 m^2 g^{-1},	1	Air	1000	8400	200	[191]
$Pd/\gamma\text{-}Al_2O_3$	Asian Catalyst	1	Air	1000	30,000	220	[186]
Pd/Al_2O_3	Wako Chemicals	0.5	Air	9500	1200,000	325	[192]
$Pt/\gamma\text{-}Al_2O_3$	Rhodia-SPH569	1	9% O_2 in He	1000	36,000	180	[185]
$Pd/\gamma\text{-}Al_2O_3$	Asian Catalyst	1	Air	1000	60,000	217	[193]
Pt/Al_2O_3	Soekawa Chemical	2.2	Air	400	18,000	140	[194]
$Pt/\gamma\text{-}Al_2O_3$	120 m^2 g^{-1}, Sumitomo Chemical	1	O_2, 18.5%; H_2O, 1.5%; N_2, balance	500	80,000	167	[195]
Pt/3DOM Al_2O_3[b]	Home-made	1.4	Air	1000	20,000	180	[196]

a: T_{50}: the temperature of toluene conversion to CO_2; b: Three-dimensionally ordered macro - /mesoporous alumina**Reaction without oxygen in the feed**

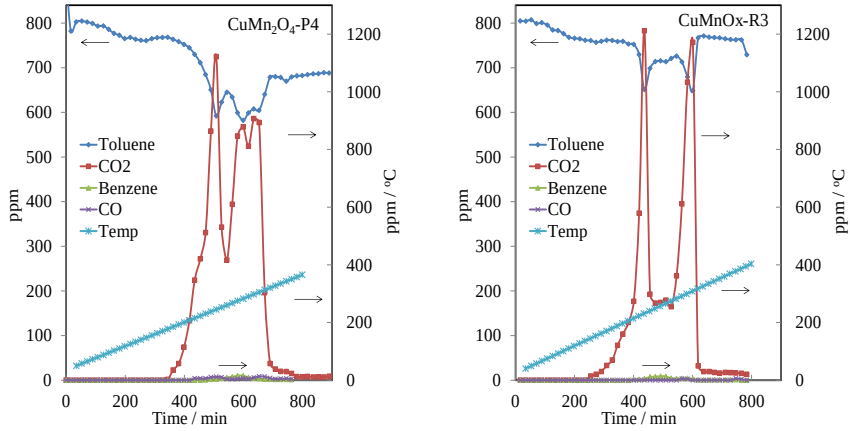

Figure 6.10. Evolution of the gaseous species in function of temperature in toluene oxidation performed in helium in the presence of co-precipitated and redox catalyst

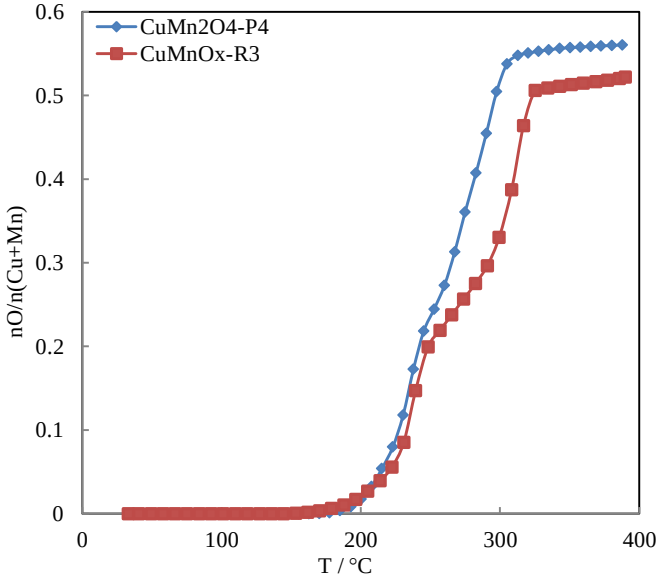

Figure 6.11. Evolution of the atomic O/(Mn + Cu) in function of temperature and toluene oxidation performed in helium

Reactions without oxygen in the feed were also performed over $CuMn_2O_4$-P4 and CuMnOx-R3 catalysts in order to assess the possible participation of catalyst oxygen in toluene oxidation. The evolution of the concentrations of toluene, CO_2,

CO and benzene were recorded as a function of temperature in **Figure 6.10**. Whatever the catalyst under concern the toluene consumption occurred in two steps: one at low temperature with a maximum toluene consumption at about 240-245 ℃ and a second step at higher temperature characterized by 2 maxima at 283 and 298 ℃ for $CuMn_2O_4$-P4 **(Figure 6.10a)** while only a maximum at 317 ℃ was detected for CuMnOx-R3 **(Figure 6.10b)** catalyst. The CO_2/Toluene molar ratio of 6.6 ($CuMn_2O_4$-P4) and 6.8 (CuMnOx-R3) was in accordance with that expected of 7.0, considering the margin of error, in line with a negligible production of CO in the course of the reaction. Hence, the oxidation of toluene occurs in the absence of any gaseous oxygen. The presence of two consecutive peaks separated by about 40 ℃ ($CuMn_2O_4$-P4) and 80 ℃ (CuMnOx-R3) can be explained by the successive participation of surface (sub-surface lattice oxygen) and lattice oxygen in copper-manganese oxides. The amount of oxygen extracted from the solids respective to the metal content O/(Cu+Mn) as a function of temperature was given in **Figure 6.11**. It is found a similar O/(Cu+Mn) trace with temperature regarding the first step to reach a value of 0.22 while in the second step the O/(Cu+Mn) trace was translated to higher temperatures on CuMnOx-R3 to reach a final value at 390 ℃ of 0.53 and 0.56 for CuMnOx-R3 and $CuMn_2O_4$-P4, respectively. It was shown that transformation of the $CuMn_2O_4$-P4 catalyst readily occurred to give MnO and Cu^0 (XRD analysis). By opposition the XRD characteristic peaks of $Cu_{0.1}Mn_{2.9}O_4$ and $Cu_{1.5}Mn_{1.5}O_4$ phases were found for CuMnOx-R3 catalyst.

Test of stability

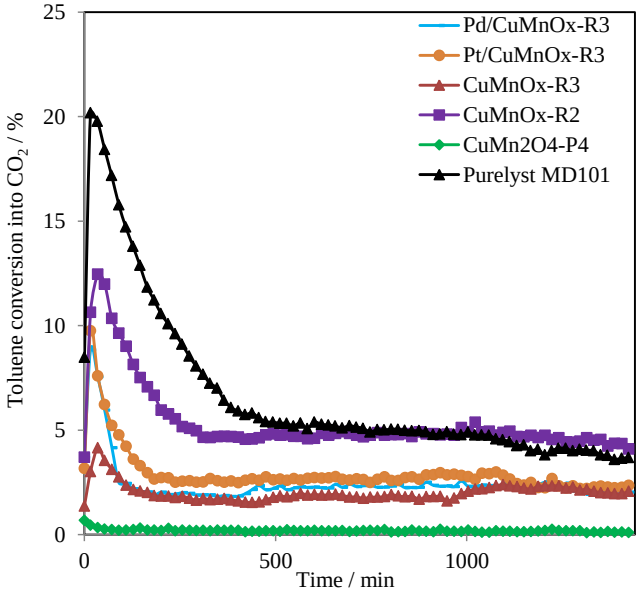

Figure 6.12. Stability tests on the $CuMn_2O_4$-P4, CuMnOx-R3 based catalysts and commercial catalysts at 150 ℃

Table 6.78 Textural and H_2-TPR properties of the catalysts after stability test

	S_{BET} (m^2/g)	Vp^a (cm^3/g)	H_2 (mmol/g)
UCuMnOx-R3	189	0.45	5.26
$UCuMn_2O_4$-P4	30	0.30	8.95
UPd/CuMnOx-R3	167	0.42	6.92
UPt/CuMnOx-R3	188	0.50	6.19

a: BJH Desorption cumulative volume of pores

24h stability tests have been performed at 150 ℃ on all undoped and doped copper-manganese oxides and the toluene conversion into CO_2 as a function of time is given in **Figure 6.12**. The Purelyst MD101 catalyst strongly deactivates in the six first hours and after smoothly linearly deactivates over time. In comparison a partial deactivation at the early stages of the reaction occurs on CuMnOx-Ri and M/CuMnOx-R3 (M=Pt, Pd) before achievement of a quasi-stationary state. At the final stage of the reaction no improvement is observed with the doped catalysts as compared to the CuMnOx-R3 active support. Conversely the low calcining temperature is beneficial as CuMnOx-R2 has the higher specific activity of 43 μmol/(g.h) towards all catalysts even the Purelyst

MD101 (38 µmol/(g.h)). Additionally this beneficial effect is amplified when considering the intrinsic rates which is 1.7 times higher than that of Purelyst MD101.The $CuMn_2O_4$-P4 catalyst for its part seems to be quite stable over time but its activity keeps very low. The physico-chemical characterizations of the used catalysts are displayed in **Table 6.8**. The X-ray diffraction patterns (not shown here) do not change significantly over the course of the reaction. While the BET surface area reduces by one third for $CuMn_2O_4$-P4 those of the "redox-precipitation" series keep stable and even slightly increase.

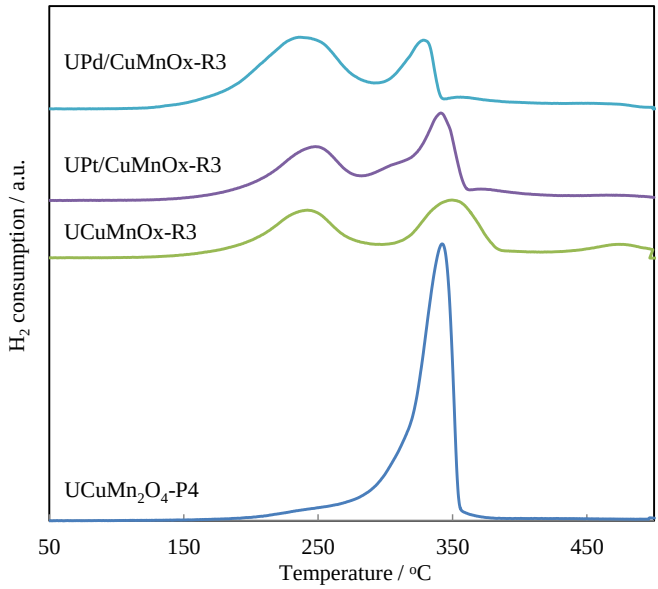

Figure 6.13. H_2-TPR profiles of the used $CuMn_2O_4$-P4 and CuMnOx-R3 based catalysts

By opposition the H_2-TPR profiles of the used catalysts given in **Figure 6.13** as well as the amount of H_2 consumed are significantly affected as compared to those of the fresh catalysts. For CuMnOx-R3 it is found now two broad H_2 consumptions in a larger temperature range 140-380 ℃ to be compared to that of 110 ℃-260 ℃ on the fresh catalyst. It is also to be noted that the amount of H_2 consumption decreases by a factor 2. This clearly indicates a partial reduction of Cu^{2+} and/or Mn^{n+} species due to toluene acting as a reductant in agreement with the previous experiments without oxygen. Similar trends are observed in terms of temperature range and amount of consumed hydrogen when considering the noble metal doped catalysts. In comparison the H_2-TPR profile of $UCuMn_2O_4$-P4

(used $CuMn_2O_4$-P4) is rather similar but shifted to higher temperature with a H_2 consumption slightly affected.

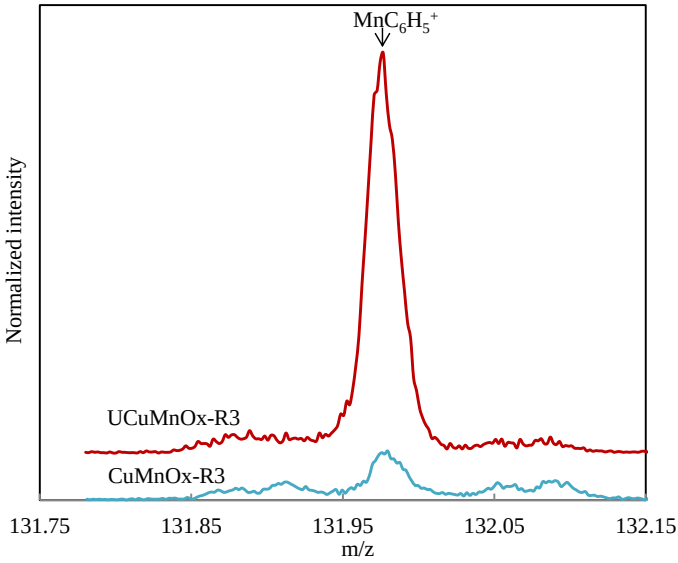

Figure 6.14. Positive ion mass spectra of CuMnO3-R3 and UCuMnO3-R3 in the m/z range:131.8-132.15

ToF-SIMS mass spectra obtained in polarity (+) and (-) of UCuMnOx-R3 (used CuMnOx-R3) showed new secondary peaks compared to that of the fresh catalyst. These secondary ions were found to be derived from toluene (m/z =77.04; $C_6H_5^+$) and to some organic intermediates of the reactions such as benzene (m/z =77.04; $C_6H_5^+$), phenol (m/z = 93.03; $C_6H_5O^-$), benzaldehyde (m/z =105.03; $C_7H_5O^+$) and benzoic acid (m/z =121.03; $C_7H_5O_2^-$). Additionally ToF-SIMS allows to see some metal-organic secondary ions. The detection of such ions gave direct information related to adsorbed organic species on the metal oxide surface. The m/z value at 131.97 identified as $MnC_6H_5^+$ is ascribed to adsorbed benzene on Mn related site (**Figure 6.14**). Quite similarly it is worth to mention the detection of $CuC_6H_4^+$ at m/z = 139.95 but with a relative lower intensity. The m/z value at 163.97 is likely attributed to adsorbed benzaldehyde on Mn ($MnC_6H_5O_2^-$). Hence ToF-SIMS allows to observe fragment ions relative to adsorbed products resulting from the partial oxidation of toluene. It can be proposed that the presence of adsorbed organic species at the surface could also account for the deactivation. This deactivation is less pronounced on CuMnOx-R2 allowing to preserve an activity with time on stream at 150 ℃.

6.4. Conclusion

At least, four relevant conclusions can be drawn from this study:

(i) Whatever the method of synthesis, the CuMnOx catalysts outperformed the reference single oxides in total toluene oxidation. Moreover the CuMnOx-R2 catalyst outclassed the Purelyst MD101 commercial catalyst over time on stream.

(ii) The dispersed copper manganese oxides using the redox-precipitation route exhibit much higher activity as compared to that of the spinel $CuMn_2O_4$-P4 oxide prepared by co-precipitation using TMAH as precipitant. The superior performance of the redox derived Cu-Mn materials was attributed to improved textural properties such as high surface areas, amorphous state and structural disorder (presence of oxygen vacancies).

(iii) From catalytic experiments performed in free oxygen atmosphere it is deduced that surface adsorbed (O_{ads}) oxygen and subsurface oxygen play a role in the activity of the catalyst.

(iv) The ToF-SIMS analysis after test allows to detect metal (M = Mn,Cu) organic secondary ions attesting of strong adsorption of partial oxidation/decomposition products of toluene on activesites inducing partial deactivation.

CHAPTER 7: REMOVAL OF DILUTE TRICHLOROETHYLENE IN AIR BY POST-PLASMA CATALYSIS OVER CU-MN MIXED OXIDES

7.1. Introduction

Chlorinated volatile organic compounds are difficult to eliminate because of their relative high stability in air. These compounds can be easily removed by non-thermal plasma (NTP) [197, 198]. However the process has low energy efficiency and low CO_2 selectivity due to the formation of polychlorinated compounds [199].

This chapter focuses on the combination of non-thermal plasma and a catalyst for trichloroethylene (TCE) removal. This toxic VOC is commonly used as a degreaser in the industry [200]. This combination, known as plasma catalysis, has attracted increasing interest because this process can significantly outperform the plasma alone and thermal catalysis experiments in terms of efficiency, selectivity and energy cost [17, 201]. The catalyst can be placed either directly in the discharge zone (in-plasma catalysis) or after the discharge zone (post-plasma catalysis). For the abatement of TCE, post plasma catalysis (PPC) is more attractive. Using this configuration the preprocessing of TCE by plasma treatment assists the sequential catalytic oxidations by lowering TCE concentration and forming ozone. Catalytic reactions can take advantages of the NTP emitted O_3 as a potential source of active oxygen species enabling further oxidation of both TCE and potential NTP gaseous hazardous by-products.

Hence, the selection of catalysts for TCE abatement in PPC process should consider some important criteria, such as ozone decomposition ability, TCE total oxidation capacity, as well as hydrothermal stability and resistance to chlorine. Copper-Manganese mixed oxides have demonstrated their great ability for ozone decomposition [173, 202], CO oxidation [133, 203] and chlorinated VOCs removal [204], and their resistance to the deactivation caused by chlorinated byproducts [205, 206]. Therefore in this study Cu-Mn based oxides have been selected for TCE abatement in PPC experiments. According to the previous chapter, copper-manganese oxides prepared by a co-precipitation or redox method were proved to be more active than the single oxides for toluene catalytic oxidation. Then Cu-Mn mixed oxides labeled (1) as $CuMn_2O_4$-P4, prepared by a co-precipitation method and (2) as $CuMnO_x$-R3, prepared by a redox route, were selected as catalysts and were placeed in the downstream of the discharge zone in PPC experiments.

The aim of the present study is to investigate the TCE abatement in moist air (RH = 15%) in PPC experiments using two different copper manganese oxides, $CuMn_2O_4$-P4 and $CuMnO_x$-R3, heated at 150 ℃ and positioned in the downstream of the plasma. For better comparison the TCE abatement was also

investigated with plasma alone at 25 ℃ and catalyst alone from 100 to 300 ℃ with analysis every 50 ℃. The performance of each configuration was evaluated in terms of total TCE conversion, CO_2 and CO_x yields and byproducts distribution. The role of ozone was particularly studied in the PPC experiments. Textural and surface characterizations of fresh and used catalysts were performed in order to make some correlations between their physico-chemical properties and their performances in the TCE abatement.

7.2. Experimental conditions

Table 7.1 summarizes the basic experimental conditions used in this chapter and the schematic representation of the experimental set-up is shown in Figure 7.1. The details of experimental process can be found in chapter 3.4.

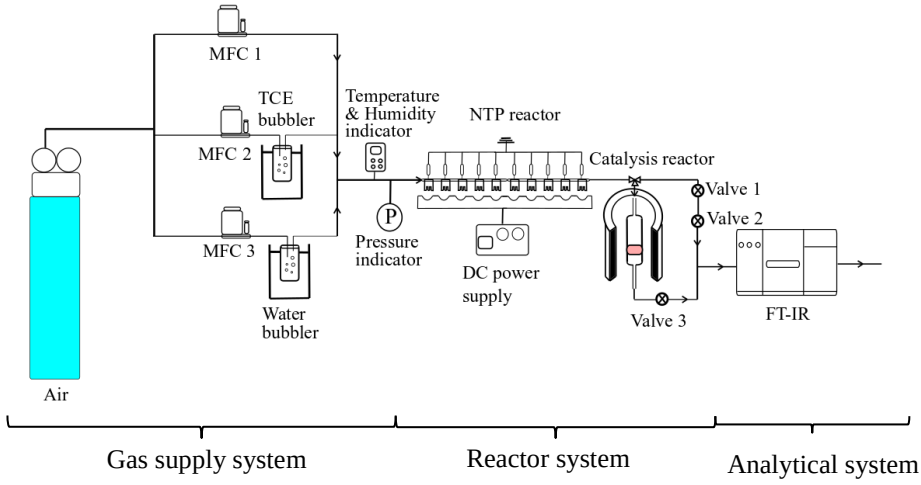

Figure 7.1. Schematic representation of the experimental set–up

Table 7.1 Experimental conditions

Plasma alone	
Air source	Air cylinder
Flow rate	0.5 L/min
Relative Humidity (20 ℃)	15%
Initial TCE concentration	~300 ppm
Energy density (J/L)	60-120
Catalytic oxidation	
Air source	Air cylinder
Activation conditions	200 ml/min, 300 ℃ for 4 h
Temperature for testing	100, 150, 200, 250 and 300 ℃
Experiment flow rate	0.5 L/min
GHSV (ml g^{-1} h^{-1})	60,000
Relative Humidity (20 ℃)	15%
Initial TCE concentration	~300 ppm
Catalyst	0.5 g of catalyst mixed with 3 g SiC
PPC	
Air source	Air cylinder
Flow rate	0.5 L/min
Relative Humidity (20 ℃)	15%
Initial TCE concentration	~300 ppm
Energy density (J/L)	60-120
Temperature for testing	150 ˚C
Catalyst	0.5 g of catalyst mixed with 3 g SiC

7.3. Experimental results and discussions

7.3.1. Catalyst characterization before and after the tests

ICP-OES results

The elemental composition of the fresh and used catalysts is given is Table 7.2. As previously discussed the Mn/Cu atomic ratio of 1.8 for $CuMn_2O_4$-P4 is close to the expected one, while for $CuMnO_x$-R3 it exceeds the expected value due to copper loss during the synthesis [89]. Taking into account the margin of error of the ICP analysis, Mn/Cu atomic ratio of both materials remained constant after PPC experiments.

Table 7.2 summarizes also the textural properties of the fresh and used catalysts. After catalytic or PPC processes, the specific surface areas decrease significantly while the porous volume remains constant or tends to increase.

After the catalytic or PPC processes, the decrease of the specific surface area is less pronounced for $CuMn_2O_4$-P4 sample (~37%) in comparison with $CuMnO_x$-R3 sample (~60%). This decrease in S_{BET} could be explained by pore clogging due to the deposit of chlorine species on the surface of the catalyst (see the XPS analysis).

Table 7.2 Textural properties and ICP-OES results of the catalysts before and after tests

Sample	S_{BET} / m^2/g	Vp[a] / m^3/g	Dp[b] / nm	Mn / wt%	Cu / wt%	Mn/Cu[c]
$CuMn_2O_4$-P4	48	0.30	21.	47.05	30.59	1.8
$CuMn_2O_4$-P4-C	31	0.32	33.5	-	-	-
$CuMn_2O_4$-P4-PPC	30	0.29	39.3	46.87	28.52	1.9
$CuMnO_x$-R3	166	0.30	10.0	48.41	11.66	4.8
$CuMnO_x$-R3-C	63	0.46	28.0	-	-	-
$CuMnO_x$-R3-PPC	68	0.41	21.1	45.13	9.95	5.2

[a] BJH Desorption cumulative volume of pores; [b] BJH Desorption average pore diameter; [c] atomic ratio

XPS analysis

XPS results obtained before and after PPC experiments are summarized in **Table 7.3**. For $CuMn_2O_4$-P4 sample, the Cu $2p_{3/2}$ envelope shows two distinct photopeaks at 931.2 and 934 eV whose values can be attributed to Cu^+ and Cu^{2+} species, respectively. The presence of a satellite structure between 938 and 948 eV allows to confirm the presence of Cu^{2+}. The presence of Cu^{2+} together with Cu^+ could be explained by the following redox equilibrium $Cu^{2+} + Mn^{3+} \rightleftarrows Cu^+ + Mn^{4+}$. This is in accordance with the Mn AOS of 3.7 which suggests the presence of Mn^{4+} and Mn^{3+} species (**Table 7.3**). After PPC process the Cu^+/Cu^{2+} atomic ratio and the Mn AOS decrease from 0.5 to 0.24 and from 3.5 to 2.9, respectively. Conversely $CuMnO_x$-R3 sample exhibits one single Cu $2p_{3/2}$ photopeak with BE of 934.2 eV attributed to the sole presence of Cu^{2+} species. The Mn AOS is close to 3.5. This value decreases to 2.9 after PPC process. Additionally combined decrease of Cu^+/Cu^{2+} atomic ratio and Mn AOS indicates a shift of the above equilibrium toward the +2 and +3 valences of Cu and Mn, respectively. The modification of the species valence is therefore in agreement with possible redox mechanism involving the copper and manganese species during the PPC process.

Table 7.3 XPS results on the fresh and used samples (after PPC tests)

Sample	Cu $2p_{3/2}$ BE /eV	Mn $2p_{3/2}$ BE /eV	Mn/Cu[a]	Cl/(Cu+ Mn)[a]	Mn AOS	Cu^{+}/Cu^{2+}
$CuMn_2O_4$-P4	931.2, 934.0	642.0	3.7	-	3.7	0.5
$CuMn_2O_4$-P4-PPC	931.1, 934.2	642.2	4.6	0.15	2.9	0.24
$CuMnO_x$-R3	934.3	642.4	5.1	-	3.5	0
$CuMnO_x$-R3-PPC	934.8	642.5	11.7	0.25	2.9	0

[a] atomic ratio

For $CuMn_2O_4$-P4 sample the XPS atomic Mn/Cu ratio is higher than the bulk one (**Tables 7.2 and 7.3**), indicating a surface Mn enrichment. For $CuMnO_x$-R3 sample the XPS atomic Mn/Cu is close to the bulk one (**Tables 7.2 and 7.3**), attesting of a good dispersion of Mn and Cu elements. Anyways, after PPC processes both catalysts show a surface Mn enrichment over Cu, but more pronounced over $CuMnO_x$-R3, because the XPS atomic Mn/Cu ratios increase by 20 and 56% for $CuMn_2O_4$-P4 and $CuMnO_x$-R3, respectively.

After PPC processes, chlorine element has been detected at the surface of both catalysts. The detection of chlorine can be explained by the incomplete TCE degradation during the PPC process. Cl $2p_{3/2}$ and Cl $2p_{1/2}$ photopeaks were found at 198.7 and 200.3 eV for $CuMn_2O_4$-P4-PPC and 198.5 and 200.1 eV for $CuMnO_x$-R3-PPC, respectively (**Figure 7.2**). The Cl $2p_{3/2}$ photopeak at 198.7/198.5 eV can be attributed to metal (M) chloride, with M= Cu and/or Mn [207]. As a consequence the presence of organic chloride species can be excluded on both catalysts surfaces. This can be due to the beneficial effect of water enabling the efficient removal of chlorinated organic ad-species [117]. In addition, the XPS atomic Cl/(Cu + Mn) ratio (**Table 7.3**) is 0.15 for $CuMn_2O_4$-P4-PPC, whereas for $CuMnO_x$-R3-PPC, it increases up to 0.25. It is suggested that differences in terms of Cu-Mn interactions and of amorphous-crystallized structure may play a role in the different relative amount of chlorine detected by XPS.

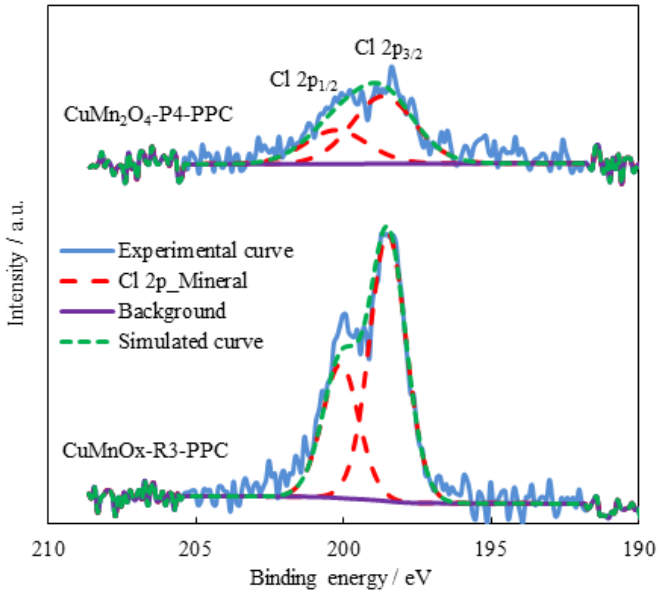

Figure 7.2. Cl 2p spectra obtained for $CuMn_2O_4$-P4 and $CuMnO_x$-R3 samples after PPC process

7.3.2. Non thermal plasma for the abatement of TCE

It was established that increasing humidity up to 20% resulted in enhancement of TCE decomposition efficiency, while the efficiency again decreased when humidity exceeded 20 % [208]. Indeed OH radicals produced by water dissociation can act as highly reactive oxidizing agents for TCE degradation. It was also suggested that reaction of ClO (intermediate of TCE oxidation) with OH could reduce $COCl_2$ production [117]. Therefore the presence of water in the feed at a RH value close to 20% could enhance the activity and the selectivity of the TCE degradation reaction using non-thermal plasma. In that way, NTP experiments have been done in relative humidity of 15%.

Figure 7.3 shows the TCE conversion (defined as the ratio between the reacted TCE over the TCE delivered in the reactor) and the ozone formation obtained during the NTP treatment as a function of energy density. The removal efficiency increases with increasing energy density. This result can be explained by the formation of more energetic electrons which produces more reactive species that are capable of triggering TCE abatement. The highest removal

efficiency of 56% is obtained for the energy density of 120 J/L. An increase of energy density in NTP experiments leads to an increase in the ozone concentration.

Figure 7.4 shows the COx (CO or CO_2) yield obtained during the NTP experiments as a function of energy density. This yield increases with increasing energy density. However a poor mineralization of TCE into COx is observed since the highest yield obtained is 13% for the energy density of 120 J/L. This low COx yield in NTP experiments has been previously explained by the formation of polychlorinated organic by-products such as phosgene ($COCl_2$), dichloroacetylchloride ($CHCl_2$–COCl = DCAC) and trichloroacetaldehyde (Cl_3C-CHO = TCAD) [117].

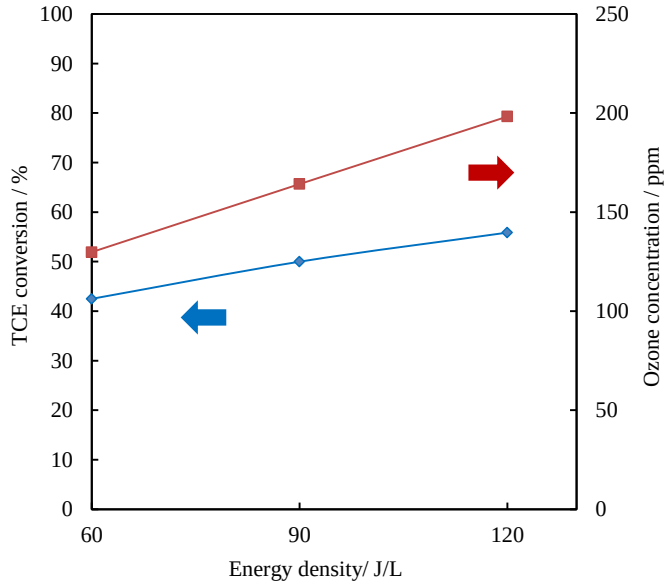

Figure 7.3. TCE conversion and ozone formation as a function of energy density in NTP process

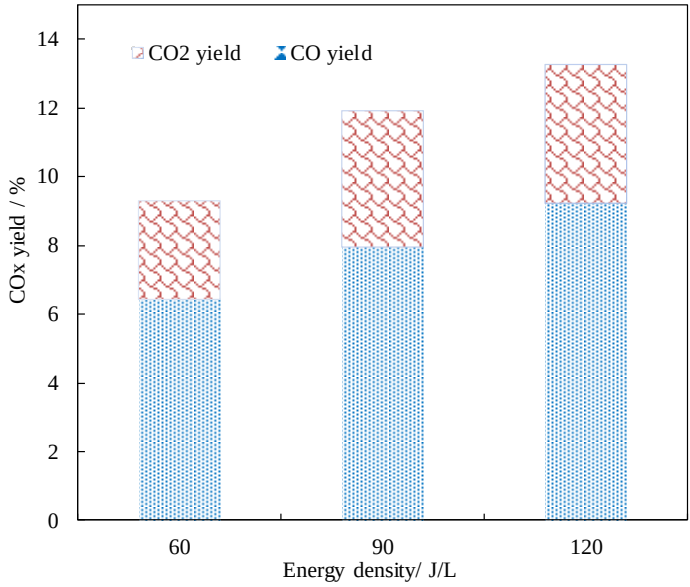

Figure 7.4. CO_x yield as a function of energy density in NTP process

7.3.3. Catalytic abatement of TCE

Figure 7.5 shows the TCE conversion for the catalytic oxidation reaction at different temperatures ranging from 100 to 300 ˚C over $CuMnO_x$-R3 and $CuMn_2O_4$-P4 catalysts. The catalytic performance was evaluated after 1 hour at the studied temperature. In the presence of $CuMn_2O_4$-P4, the catalytic oxidation of TCE started at 250 ℃ where 19% of TCE was converted. At 300 ℃ 50% of TCE was converted over $CuMn_2O_4$-P4 catalyst. A significant improvement in catalytic activity is observed when $CuMnO_x$-R3 is used as catalyst since 45% and 100% of TCE were converted over $CuMnO_x$-R3 catalyst at 250 ℃ and 300 ℃, respectively.

A more detailed analysis shows that the catalyst prepared by redox-precipitation method ($CuMnO_x$-R3) showed a significant decrease in conversion efficiency during one hour. For example, at 150 ℃ the TCE conversion drops from 12% (t = 0h) to 6% (t = 1h), while the activity of the catalyst prepared by co-precipitation method ($CuMn_2O_4$-P4) was stable.

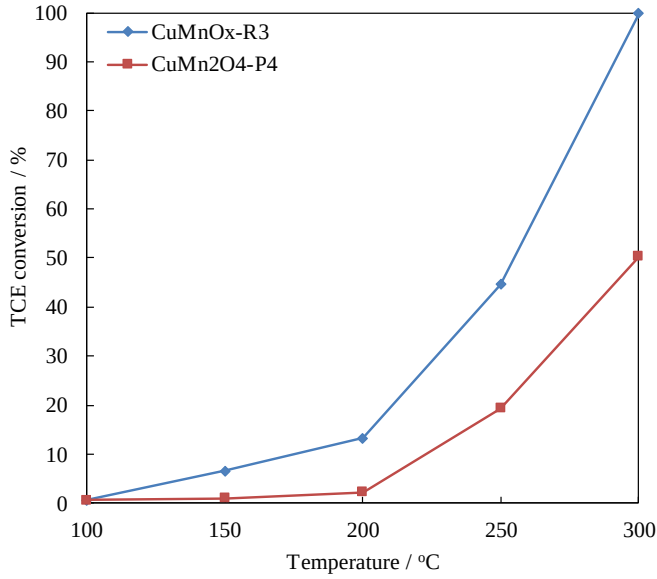

Figure 7.5. TCE conversion in oxidation reaction over $CuMn_2O_4$-P4 and $CuMnO_x$-R3 catalysts at different temperatures

The main oxidation products obtained in the TCE oxidation was CO_2. **Figure 7.6** shows the TCE conversion into CO_2 also called CO_2 yield (defined as the ratio between the CO_2 produced over the TCE delivered in the reactor). The difference between the total toluene conversion (**Figure 7.5**) and TCE conversion into CO_2 (**Figure 7.6**) is partly explained by the detection of the byproduct C_2Cl_4 which has been detected by FT-IR spectra as seen in **Figure 7.7** (strong vibration at 916 cm^{-1} and two medium vibrations at 804 and 781 cm^{-1} [209], but not quantified), at 300 ℃ for $CuMn_2O_4$-P4 and at 250 and 300 ℃ for $CuMnO_x$-R3. At 150 ℃ the difference can be explained by the retained TCE on the surface because no TCE conversion into CO_2 has been observed at this temperature. The amount of retained TCE is in line with the porous character of the catalyst. Additionally CO has been also detected in a few amount (less than 7 ppm) (**Figures 7.8a and 7.8b**) for TCE oxidation over $CuMn_2O_4$-P4 and $CuMnO_x$-R3 catalysts.

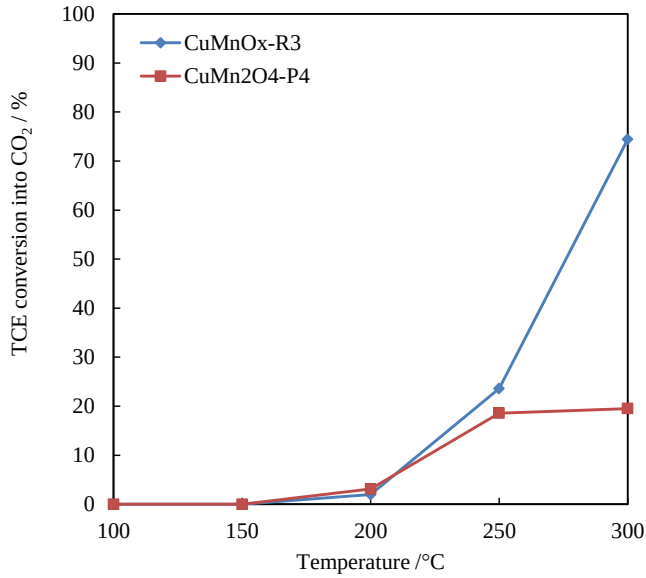

Figure 7.6. TCE conversion into CO_2 in catalytic oxidation reaction over $CuMn_2O_4$-P4 and $CuMnO_x$-R3 at different temperatures

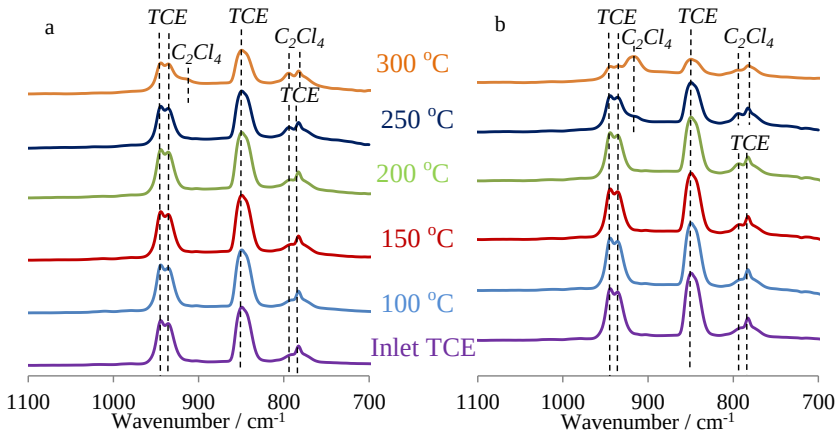

Figure 7.7. FT-IR spectra in the wavenumber range 1000–700 cm^{-1} of inlet TCE polluted air stream and outlet stream after catalytic oxidation (Catalyst : a) $CuMn_2O_4$-P4 and b) $CuMnO_x$-R3; Temperature: 100-300 ℃)

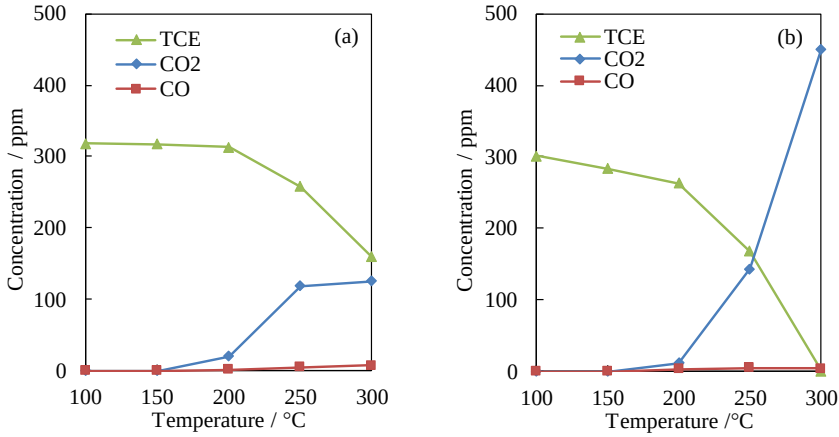

Figure 7.8. TCE, CO_2 and CO distribution obtained during the TCE oxidation reaction over $CuMn_2O_4$-P4 (a) and $CuMnO_x$-R3 (b) at different temperatures

The good CO_2 selectivity of the catalyst could be explained by the ability of the Cu-Mn based catalysts to oxidize efficiently CO into CO_2, even in high humidity condition (RH: 75%) [134]. Similar result has been obtained by R. Cucciniello *et al.* using mayenite catalyst for the TCE oxidation [210].

A comparison between the catalytic performances exhibited by $CuMnO_x$-R3 and $CuMn_2O_4$-P4 (**Figure 7.5**) clearly evidenced the higher activity of $CuMnO_x$-R3 catalyst. It is widely accepted in the literature that acidity and reducibility of the catalyst are related to an efficient TCE removal. Therefore the catalytic activity could be partly associated to its redox behavior evaluated by H_2-TPR experiment [89], H_2 consumption being associated with accessible oxygen species in the temperature range in which the TCE is converted. At low temperature (150-250 ℃) the amount of hydrogen consumed during H_2-TPR analysis is much more important in $CuMnO_x$-R3 sample than in $CuMn_2O_4$-P4 sample. This result suggests that the high quantity of reducible oxygen detected by TPR could be associated to the increase in TCE oxidation.

The high textural properties of $CuMnO_x$-R3 (the value of the specific surface area is 4 times larger) in comparison to $CuMn_2O_4$-P4 could explain the catalytic behavior discrepancy in terms of TCE removal efficiency at low temperature. A direct comparison between the total TCE conversion and conversion of TCE into CO_2 indicates that TCE is most probably retained on the highly porous catalyst surface

The catalytic properties (T_{50}, stability, byproducts formed) of some catalysts obtained in the total oxidation of TCE (various experimental conditions) are listed in **Table 7.4**. This overview highlights the good catalytic activity of $CuMnO_x$-R3 in TCE removal. Indeed the temperature at which 50% of TCE is converted (T_{50}) is around 260 °C. Li et al. [211] obtained clearly a lower T_{50} value (<100 °C) but the experiments have been done with low GHSV (15000 h^{-1})

Table 7.4 Overview of TCE oxidation over different catalysts

Catalyst	Feed	TCE (ppm)	GHSV/ mL $g^{-1}.h^{-1}$	T_{50} [a]/ ^{o}C	stability	byproducts	Ref.
$CuMnO_x$-R3	Humid air RH 15%	300	60,000	255	-	C_2Cl_4 at 250 to 300 ^{o}C, CO, CO_2,	This work
$CuMn_2O_4$-P4	Humid air RH 15%	300	60,000	300	-	C_2Cl_4 at 300 ^{o}C, CO, CO_2	
Co-Al	Dry air	1000	35,294	280	~50% TCE removal for 70 h at 300 ^{o}C	HCl, Cl_2, CO_2, Tetrachloroethylene (C_2Cl_4)	[212]
H–Y zeolite	Humid air RH 60%	1000	35,294	~480	-	CO, CO_2, HCl, and Cl_2, C_2Cl_4	[213]
$Ca_{12}Al_{14}O_{33}$	Humid air RH 60%	1700	8,250	~355	~95% TCE removal for 3 h at 500 ^{o}C, then decrease to ~83% TCE removal from 3 h to 12 h	Cl_2, Cl^{-1}, ClO_x	[210]
1.88 wt% Fe-ZSM-5	Dry air	1000	31,764	~380	100 % TCE removal for 16.7 h at 500 ^{o}C	-	[214]
Cu- β zeolite (pronation)	Dry air	1000	35,294	310	~45% TCE removal for 70 h at 300 ^{o}C	CO, CO_2, HCl, and Cl_2, C_2Cl_4	[215]
H-ZSM-5	Dry air	1000	50,000	510	~38% TCE removal decrease to ~10% in 13.8 h at 500 ^{o}C	-	[216]
0.42 wt% Pd/ Al_2O_3	Dry air	1000	35,294	400	-	CO, CO_2, HCl, and Cl_2, C_2Cl_4	[217]
$CoCr_2O_4$	Humid air RH 60%	1500	48,000	~290	-	-	[218]
Commercial catalyst Pt/Al_2O_3 (Johnson Matthey)	1 vol.% H_2O	200	10,000 h^{-1}	~270	-	$CHCl_3$, CCl_4 and C_2Cl_4	[219]
0.15 wt% Pt/ Al_2O_3 (Chemical Plant OSWIJZCIM)	Dry air	746	10,000 h^{-1}	~280	-	-	[220]
Ce-Mn oxides (Mn/(Mn + Ce) = 0.21)	Dry air	1000	15,000 h^{-1}	87	100 % TCE removal for 20 h at 200 ^{o}C	HCl, Cl_2	[211]

* from total conversion of TCE

7.3.4. Post plasma catalytic abatement of TCE

After studying the TCE abatement performances using NTP and catalytic oxidation, the combination of non-thermal plasma and catalyst was performed through the well-known post-plasma catalysis process.

Figure 7.9 shows the total TCE conversion as a function of energy density (60 - 120 J/L) over the two catalysts ($CuMnO_x$-R3 and $CuMn_2O_4$-P4) in post plasma catalysis configuration. Both catalysts were maintained at 150 ˚C during the experiments. At this temperature, without NTP, the TCE conversion obtained for $CuMnO_x$-R3 and $CuMn_2O_4$-P4 was 10% and 2%, respectively (**Figure 7.5**). This conversion was related to TCE adsorption and/or conversion into intermediates adsorbed at the catalyst surface because no CO and CO_2 were generated at 150 ˚C. When the NTP is turned on, the TCE conversion using PPC configuration was significantly increased and was higher than that of the NTP alone configuration in the range of energy density studied.

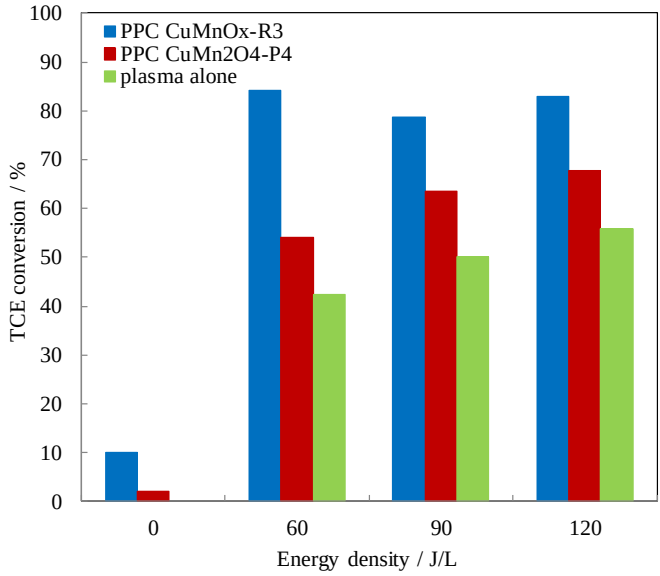

Figure 7.9. TCE conversion for catalysis (ED = 0 J/L; catalyst temperature = 150 ˚C), NTP (ED = 60, 90 and 120 J/L) and post-plasma catalysis (ED = 60, 90 and 120 J/L; catalyst temperature = 150 ˚C) experiments

The superior catalytic performance of $CuMnO_x$-R3 observed in the conventional catalytic oxidation of TCE in air is maintained in PPC configuration. However the difference in total TCE conversion using $CuMnO_x$-

R3 is much less pronounced with different energy density because no significant improvement in TCE abatement using $CuMnO_x$-R3 is observed with increasing the energy density (**Figure 7.9**). The highest TCE conversion efficiency obtained in PPC configuration is 85% and 68% for $CuMnO_x$-R3 and $CuMn_2O_4$-P4 at energy density of 60 and 120 J/L, respectively. As previously mentioned, the activity of the $CuMnO_x$-R3 catalyst for the TCE degradation slightly decreased during the 1h of testing at 150 ℃, evidencing the deactivation of this catalyst during the analysis. This deactivation can be related to the accumulation of chlorine at the surface (see the XPS section). Therefore despite the increase in the energy density from 60 to 120 J/L, the catalytic activity of $CuMnO_x$-R3 remains stable with a compensation effect of energy density towards TCE conversion.

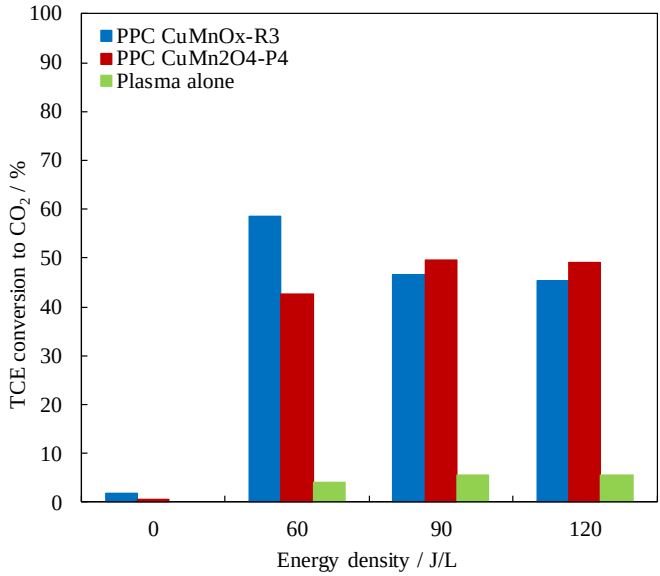

Figure 7.10. TCE conversion into CO_2 for catalysis (ED = 0 J/L; catalyst temperature = 150 ℃), NTP (ED = 60, 90 and 120 J/L) and post-plasma catalysis (ED = 60, 90 and 120 J/L; catalyst temperature = 150 ℃) experiments

Figure 7.10 shows the TCE conversion into CO_2 (or CO_2 yield) as a function of energy density (60-120 J/L) for the two catalysts ($CuMnO_x$-R3 and $CuMn_2O_4$-P4) in post plasma catalysis configuration in comparison with the NTP alone and catalyst alone configuration. Similar trend can be observed for TCE conversion into CO_2 evolution as a function of energy density for the two catalysts. The TCE conversion into CO_2 is significantly improved in PPC configuration when

compared to NTP and TCE conversion into CO_2 increases with energy density in PPC using $CuMn_2O_4$-P4 whereas it decreases using $CuMnO_x$-R3 (**Figure 7.10**).

Interestingly, when comparing to MnO_x and CeMn oxides tested in the same pin-to-plate DC corona plasma reactor, except that the number of pins herein is increased from 5 to 10, [221] $CuMnO_x$-R3 and $CuMn_2O_4$-P4 exhibits better performance in terms of TCE conversion into CO_2 (CO_2 yield). Indeed it has been reported [221] that in the presence of 1 g of MnO_y or $CeMn_x$ catalysts in PPC configuration (catalyst at 150℃ ; RH =10%) the CO_2 yield reached the value of ~30% for ED= 240 J/L. While using 2 times less energy (ED= 120 J/L) and half the catalyst amount (0.5g), $CuMnO_x$-R3 and $CuMn_2O_4$-P4 led to CO_2 yield of ~50% evidencing the high performances of these catalysts in PPC configuration for TCE abatement.

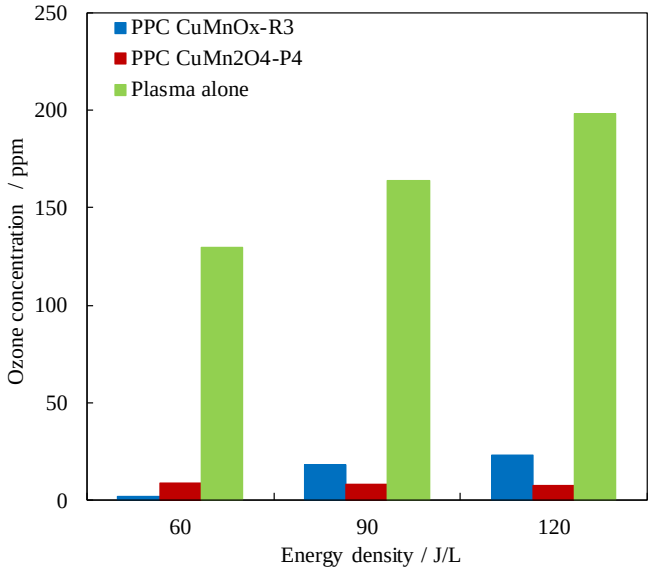

Figure 7.11 Ozone concentration as a function of energy density for plasma alone and PPC experiments

Figure 7.11 shows the amount of ozone in the outlet gas stream after TCE abatement as a function of energy density in NTP and PPC configurations. The comparison between NTP and PPC experiments confirms the ozone decomposition over the catalyst surface. While the ozone concentration measured at the exit of reactor containing $CuMn_2O_4$-P4 catalyst remains constant, the ozone measured at the exit of reactor containing $CuMnO_x$-R3 increases with

energy density. This could be related to the degradation of the $CuMnO_x$-R3 catalyst upon the reaction.

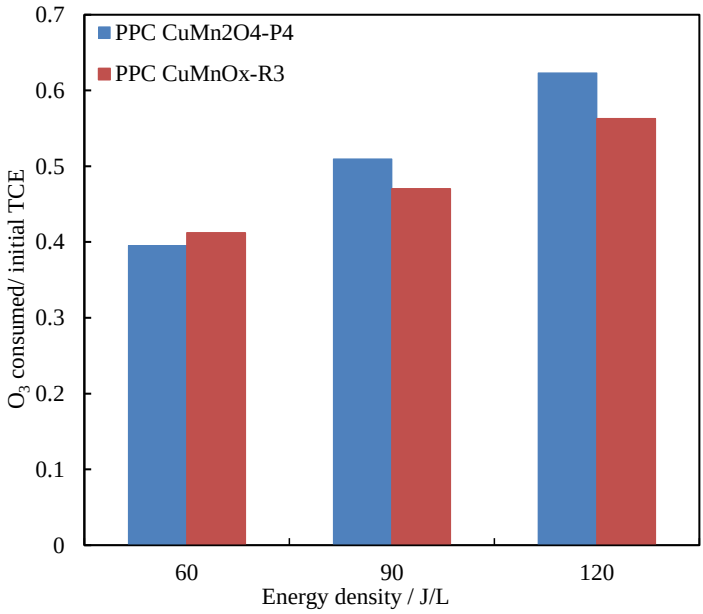

Figure 7.12. Evolution of the molar ratio ($O_{3consumed}$/initial TCE) in function of energy density and of catalyst

The effect of ozone on initial TCE total oxidation was considered as figure 7.12 shown. The molar (O_3consumed/initial TCE) ratio increases as the energy density increases for PPC configuration with both catalysts. As it is known, ozone was the main reactive species after NTP reactor reaching catalyst reactor. And the ozone decomposition over catalysts provides reactive O promoting the TCE/byproducts total oxidation. Hence, the TCE oxidation process should be like the following reaction shown:

$$C_2Cl_3H + 4O_3 = 2CO_2 + Cl_2 + HCl + 4O_2 \quad \text{(Eq. 1)}$$

This indicates for TCE total oxidation, the molar ratio of ozone and TCE is expected to be 4:1. However, the ratio is way lower than 4, suggesting the insufficient supply of ozone in this PPC system. This may be one of the possibilities for catalysts deactivation, which in accord with the finding of mineral Cl on the catalysts surface shown in XPS results.

Figures 7.13 and 7.14 show the FTIR spectra of the inlet TCE polluted humid air, outlet stream after plasma treatment (NTP alone at the energy density of 90 J/L and PPC at the energy density of 60, 90, 120 J/L) and catalyst temperature of 150 ℃. The FTIR spectrum of the inlet TCE shows the characteristic peaks of TCE. When the plasma is turned on (NTP alone), for the energy density of 90 J/L, TCE decomposition is observed by the decrease in intensity of the C-H out of plane deformation band at the wavelength of 945 cm^{-1}. In PPC configuration, the intensity of the band at 945 cm^{-1} decreases further while the intensity of the band corresponding to CO_2 vibration increases, with increase in energy density for both used catalysts. Meanwhile, the formation of ozone is detected from the bands at 1014-1046 cm^{-1} [222, 223] for NTP alone. Although the formation of O_3 decreases in the PPC configuration, the emergence of new bands corresponding to C-Cl bond vibration relative to $CHCl_3$ and CCl_4 are located at the wavenumber of 774 cm^{-1} and 794 cm^{-1} [224]. $HCCl_3$ and CCl_4 formations can be explained by the reaction of $CHCl_2$ and CCl_3 radicals resulting from the easy cleavage of the carbon-carbon bond of DCAC with adsorbed Cl. [225]. Based on the ratio of C-Cl bond vibration intensity the relative proportion of $HCCl_3$ seems to be higher over $CuMnO_x$-R3 despite the higher content of chlorine detected by XPS analysis. The formation of TCAA is difficult to identify due to the presence of water absorption band. The detection and possible reaction schemes of formation of such intermediate oxidation products have already been observed and discussed elsewhere [117, 224].

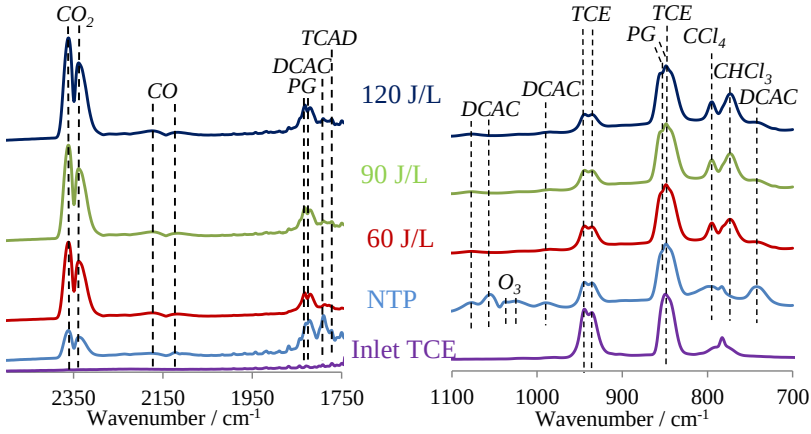

Figure 7.13 FT-IR spectra in the wavenumber range 2500-1750 cm^{-1} and 1000–700 cm^{-1} of inlet TCE polluted air stream and outlet stream after NTP and PPC process (Catalyst:$CuMn_2O_4$-P4; Energy density of PPC: 60-120 J/L; Energy

density of NTP: 90 J/L; PG: phosgene, DCAC: dichloroacetylchloride and TCAD: trichloroacetaldehyde)

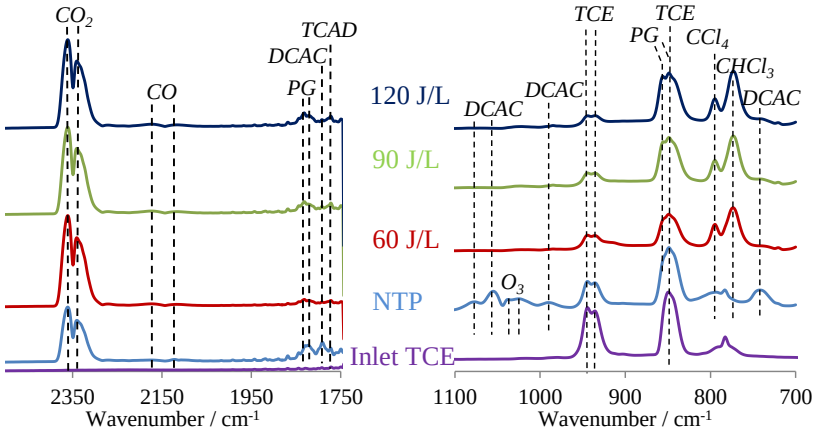

Figure 7.14 FT-IR spectra in the wavenumber range 2500-1750 cm^{-1} and 1000–700 cm^{-1} of inlet TCE polluted air stream and outlet stream after NTP and PPC process (Catalyst:$CuMnO_x$-R3; Energy density of PPC: 60-120 J/L; Energy density of NTP: 90 J/L; PG: phosgene, DCAC: dichloroacetylchloride and TCAD: trichloroacetaldehyde)

7.4. Conclusion

In this chapter, the TCE abatement was investigated in moist air ([TCE] = 300 ppm ; RH=15%) with NTP using a 10-pin-to-plate negative DC corona discharge and with PPC using Cu-Mn mixed oxides as catalysts. In comparison to the catalytic oxidation and NTP process, PPC was found to be the best process to convert TCE into CO_2 with catalyst temperature of 150 ℃. A remarkable increase of CO_2 yield has been observed and explained by the facile oxidation of polychlorinated by-products (adsorbed at the surface) by active oxygen species coming from the O_3 decomposition. Copper manganese oxide prepared by redox-precipitation method ($CuMnO_x$-R3) showed higher TCE conversion into CO_2. However the performance of the catalyst deteriorated by continuous usage due to chlorine poisoning. The catalyst prepared by co-precipitation method ($CuMn_2O_4$-P4) showed better stability (Mn surface enrichment less pronounced) in the PPC process for TCE abatement.

CHAPTER 8: GENERAL CONCLUSIONS AND OUTLOOK

In this thesis, the use of NTP technique for toluene abatement, the different preparations of Cu-Mn oxides for toluene oxidation and PPC process with Cu-Mn oxides for TCE abatement were investigated. The essential objectives of this thesis were:

- Identifying the by–products of VOC abatement with NTP and studying the humidity effect on discharge processes and toluene oxidation.
- Developing high efficient Cu-Mn oxides via using different preparation methods and studying the relations between physicochemical properties of catalysts and toluene oxidation performance.
- Improving the performance of NTP by combination with Cu-Mn oxides and characterization of the used catalyst.

The performance of VOC oxidation using NTP was widely acknowledged. In this thesis, with an IPC reactor the plasma alone case was studied in a glass-beads reactor and was mainly focused on the gaseous byproducts analysis and the effect of humidity on the discharge and the toluene abatement was studied. OES has showed that the amount of N_2 excited states decreases with increasing RH due to the increased quenching of these excited states. The highest toluene removal efficiency of 42±2% was obtained at an optimum RH of 40% at a specific input energy of approximately 250 J/l. The main products of the toluene decomposition process were identified as CO_2, CO, N_2O, O_3 (both dry and humid air) and HCOOH (dry air only). While higher RH suppress the formation of formic acid, the highest CO and CO_2 yields, N_2O and O_3 concentration at an RH of 40% confirm the observed highest removal efficiency at this experimental condition.

In order to prepare appropriate catalysts for a plasma-catalysis system, we investigated the influence of the preparation method on the activity of copper-manganese oxides for toluene total oxidation. Two preparation methods were applied: co-precipitation and redox-precipitation. Thus $CuMn_2O_4$ with spinel structure and amorphous CuMnOx were obtained. Copper manganese oxides were proved to be more active than the single oxides whatever the method of preparation used. CuMnOx prepared via a redox method were more active than the catalysts prepared by co-precipitation and compared favorably with the commercial hopcalite. The overall characterization results revealed that the redox method can ensure a good dispersion of copper in close interaction with manganese preserving more active sites at the outermost layers of the catalyst in comparison with the catalyst obtained via co-precipitation. However, all the catalysts deactivate to some extent at the earlier stages of the reaction before to reach a steady-state. Although the dispersion of trace amount of noble metals does not ensure a better activity, for redox catalysts calcined at 300°C, adding Pt/Pd allowed to get a better resistance to deactivation. Additionally it is noticeable that the catalyst using redox-precipitation method calcined at 200°C outperforms the commercial hopcalite overtime on stream.

It is clearly proved the Cu-Mn oxides can be a good choice for VOCs abatement, and when Cu-Mn oxides are combined with NTP in PPC process, the enhanced performance can also be observed. CuMnOx-R3 via redox-

precipitation method and $CuMn_2O_4$-P4 by co-precipitation method were selected for the PPC process. For the PPC process, the energy was evaluated from 30 J/l to 120 J/l, and the temperature of the catalyst was maintained at 150 ^oC. The performance of TCE oxidation was enhanced by using a plasma-catalysis process. For example, the TCE conversion efficiencies obtained for PPC with $CuMn_2O_4$-P4 and CuMnOx-R3 are 68% and 91% at the energy density of 120 J/L, respectively, which is 56% of the removal efficiency using NTP alone. It is needed to mention that 6.5% and 0% of TCE abatement were obtained using catalytic oxidation with CuMnOx-R3 and $CuMn_2O_4$-P4 at 150 ^oC, respectively. Meanwhile, the formation of by-products such as phosgene, DCAC, TCAA and ozone are significantly reduced by using copper manganese oxide in the PPC configuration for the decomposition of TCE. Although the performance of CuMnOx-R3 in PPC is better than that of $CuMn_2O_4$-P4 at each energy density, performance of CuMnOx-R3 deteriorates by continuous usage. The catalyst prepared by co-precipitation method ($CuMn_2O_4$-P4) showed better stability despite its lower conversion efficiency towards TCE.

Last but not least, after studying these three subjects, some new research ideas have emerged. For a plasma-catalysis system, the role of ozone in the plasma-catalytic process should be a next target. It would be very interesting to investigate for example how ozone is decomposed at the Cu-Mn oxides surface, and how VOCs are oxidized in plasma-catalysis process. From this point of view, development of well-designed instruments specialized in in–situ measurements is essential including discharge characterization by OES, the temperature of reactor/catalyst surface by the infrared thermometer, the determination of ozone concentration by ozone monitor, and mass spectrometer for organic gas byproducts. Additionally, catalyst characterizations are crucial to understand the interaction process between plasma and catalyst, such as XPS, ToF-SIMS, XRD and so on. In my opinion, the IPC mode still needs to be investigated in the future, and structural supported Cu-Mn oxides are required in order to get a better discharge pattern. Alumina or honeycomb structures can be a potential support for this purpose. In addition, further modification of Cu-Mn oxides also can be another interesting topic, such as using high concentrations of HNO_3. It has been reported that the increase of the Mn state, textual properties and activities were observed after such acid treatments.

REFERENCE

[1] "5.14 Toluene," W. R. O. f. Europe, Ed., ed. Copenhagen, Denmark: WHO 2000.
[2] A. f. T. S. a. D. R. (ATSDR), "Toxicological Profile for Toluene," D. o. H. a. H. Services, Ed., ed. Atlanta, GA: U.S. Public Health Service, U.S. Department of Health and Human Services, 2000.
[3] "Environmental Health Criteria 52: Toluene.," ed. Geneva: World Health Organization, 1985.
[4] Y. Guo, X. Liao, M. Fu, H. Huang, and D. Ye, "Toluene decomposition performance and NOx by-product formation during a DBD-catalyst process," *Journal of Environmental Sciences,* vol. 28, pp. 187-194, 2015.
[5] H.-H. Kim, Y. Teramoto, A. Ogata, H. Takagi, and T. Nanba, "Plasma catalysis for environmental treatment and energy applications," *Plasma Chemistry and Plasma Processing,* vol. 36, pp. 45-72, 2016.
[6] J. C. Whitehead, "Plasma–catalysis: the known knowns, the known unknowns and the unknown unknowns," *Journal of Physics D: Applied Physics,* vol. 49, p. 243001, 2016.
[7] B. S. Furniss et al. (1989). *Vogel's Textbook of Practical Organic Chemistry*.
[8] H. C. Genuino, S. Dharmarathna, E. C. Njagi, M. C. Mei, and S. L. Suib, "Gas-Phase Total Oxidation of Benzene, Toluene, Ethylbenzene, and Xylenes Using Shape-Selective Manganese Oxide and Copper Manganese Oxide Catalysts," *The Journal of Physical Chemistry C,* vol. 116, pp. 12066-12078, 2012.
[9] (Jan. 2015, Janunary). *Market Study: Toluene*. Available: http://www.ceresana.com/en/market-studies/chemicals/toluene/
[10] (2008). *Toluene Uses and Market Data*. Available: http://www.icis.com/resources/news/2007/11/07/9076550/toluene-uses-and-market-data/
[11] T. E. Corporation, "Locating and estimating air emissions from soruces of toluene ", U. E. P. Agency, Ed., ed. Chapel Hill, North Carolina, 1994, p. 207.
[12] T. Hobara, M. Okuda, M. Gotoh, K. Oki, H. Segawa, and I. Kunitsugu, "Estimation of the lethal toluene concentration from the accidental death of painting workers," *Industrial health,* vol. 38, pp. 228-231, 2000.

[13] B. Lu, X. Zhang, X. Yu, T. Feng, and S. Yao, "Catalytic oxidation of benzene using DBD corona discharges," *Journal of hazardous materials,* vol. 137, pp. 633-637, 2006.

[14] J. Van Durme, J. Dewulf, C. Leys, and H. Van Langenhove, "Combining non-thermal plasma with heterogeneous catalysis in waste gas treatment: a review," *Applied Catalysis B: Environmental,* vol. 78, pp. 324-333, 2008.

[15] H. H. Kim, "Nonthermal plasma processing for air‐pollution control: a historical review, current issues, and future prospects," *Plasma Processes and Polymers,* vol. 1, pp. 91-110, 2004.

[16] R. McAdams, "Pulsed corona treatment of gases: system scaling and efficiency," *Plasma Sources Science and Technology,* vol. 16, p. 703, 2007.

[17] H. L. Chen, H. M. Lee, S. H. Chen, M. B. Chang, S. J. Yu, and S. N. Li, "Removal of volatile organic compounds by single-stage and two-stage plasma catalysis systems: a review of the performance enhancement mechanisms, current status, and suitable applications," *Environmental science & technology,* vol. 43, pp. 2216-2227, 2009.

[18] M. Magureanu, N. B. Mandache, P. Eloy, E. M. Gaigneaux, and V. I. Parvulescu, "Plasma-assisted catalysis for volatile organic compounds abatement," *Applied catalysis B: environmental,* vol. 61, pp. 12-20, 2005.

[19] G. Xiao, W. Xu, R. Wu, M. Ni, C. Du, X. Gao, Z. Luo, and K. Cen, "Non-thermal plasmas for VOCs abatement," *Plasma Chemistry and Plasma Processing,* vol. 34, pp. 1033-1065, 2014.

[20] H. H. Kim, G. Prieto, K. Takashima, S. Katsura, and A. Mizuno, "Performance evaluation of discharge plasma process for gaseous pollutant removal," *Journal of electrostatics,* vol. 55, pp. 25-41, 2002.

[21] A. M. Vandenbroucke, R. Morent, N. De Geyter, and C. Leys, "Non-thermal plasmas for non-catalytic and catalytic VOC abatement," *Journal of hazardous materials,* vol. 195, pp. 30-54, 2011.

[22] A. M. Vandenbroucke, R. Morent, N. D. Geyter, and C. Leys, "Decomposition of toluene with plasma-catalysis: a review," *Journal of Advanced Oxidation Technologies,* vol. 15, pp. 232-241, 2012.

[23] Z.-Y. Tian, P. Mountapmbeme Kouotou, N. Bahlawane, and P. H. Tchoua Ngamou, "Synthesis of the catalytically active Mn_3O_4 spinel and its thermal properties," *The Journal of Physical Chemistry C,* vol. 117, pp. 6218-6224, 2013.

[24] D. A. Kitchaev, H. Peng, Y. Liu, J. Sun, J. P. Perdew, and G. Ceder, "Energetics of MnO_2 polymorphs in density functional theory," *Physical Review B,* vol. 93, p. 045132, 2016.

[25] P. W. Menezes, A. Indra, P. Littlewood, M. Schwarze, C. Göbel, R. Schomäcker, and M. Driess, "Nanostructured manganese oxides as highly active water oxidation catalysts: a boost from manganese precursor chemistry," *ChemSusChem,* vol. 7, pp. 2202-2211, 2014.

[26] R. Craciun, B. Nentwick, K. Hadjiivanov, and H. Knözinger, "Structure and redox properties of MnOx/Yttrium-stabilized zirconia (YSZ) catalyst and its used in CO and CH_4 oxidation," *Applied Catalysis A: General,* vol. 243, pp. 67-79, 2003.

[27] S. C. Kim and W. G. Shim, "Catalytic combustion of VOCs over a series of manganese oxide catalysts," *Applied Catalysis B: Environmental,* vol. 98, pp. 180-185, 2010.

[28] X. Li, J. Xu, F. Wang, J. Gao, L. Zhou, and G. Yang, "Direct oxidation of toluene to benzoic acid with molecular oxygen over manganese oxides," *Catalysis letters,* vol. 108, pp. 137-140, 2006.

[29] Y. Liu, H. Dai, J. Deng, L. Zhang, Z. Zhao, X. Li, Y. Wang, S. Xie, H. Yang, and G. Guo, "Controlled generation of uniform spherical $LaMnO_3$, $LaCoO_3$, Mn_2O_3, and Co_3O_4 nanoparticles and their high catalytic performance for carbon monoxide and toluene oxidation," *Inorganic chemistry,* vol. 52, pp. 8665-8676, 2013.

[30] J. Deng, S. He, S. Xie, H. Yang, Y. Liu, G. Guo, and H. Dai, "Ultralow loading of silver nanoparticles on Mn_2O_3 nanowires derived with molten salts: a high-efficiency catalyst for the oxidative removal of toluene," *Environmental science & technology,* vol. 49, pp. 11089-11095, 2015.

[31] F. Wang, H. Dai, J. Deng, G. Bai, K. Ji, and Y. Liu, "Manganese oxides with rod-, wire-, tube-, and flower-like morphologies: highly effective catalysts for the removal of toluene," *Environmental science & technology,* vol. 46, pp. 4034-4041, 2012.

[32] C. Lahousse, A. Bernier, P. Grange, B. Delmon, P. Papaefthimiou, T. Ioannides, and X. Verykios, "Evaluation of γ-MnO_2 as a VOC

removal catalyst: comparison with a noble metal catalyst," *Journal of Catalysis,* vol. 178, pp. 214-225, 1998.

[33] W. Si, Y. Wang, Y. Peng, X. Li, K. Li, and J. Li, "A high-efficiency γ-MnO_2-like catalyst in toluene combustion," *Chemical Communications,* vol. 51, pp. 14977-14980, 2015.

[34] Y. Liao, X. Zhang, R. Peng, M. Zhao, and D. Ye, "Catalytic properties of manganese oxide polyhedra with hollow and solid morphologies in toluene removal," *Applied Surface Science,* vol. 405, pp. 20-28, 2017.

[35] C. T. Herbschleb, *ReactorSTM: imaging catalysts under realistic conditions*: Faculty of Science, Leiden University, 2011.

[36] F. N. Aguero, A. Scian, B. P. Barbero, and L. E. Cadús, "Influence of the support treatment on the behavior of MnO_x/Al_2O_3 catalysts used in VOC combustion," *Catalysis letters,* vol. 128, p. 268, 2009.

[37] J. C. Védrine and I. Fechete, "Heterogeneous partial oxidation catalysis on metal oxides," *Comptes Rendus Chimie,* vol. 19, pp. 1203-1225, 2016.

[38] S. Imamura, M. Ikebata, T. Ito, and T. Ogita, "Decomposition of ozone on a silver catalyst," *Industrial & Engineering Chemistry Research,* vol. 30, pp. 217-221, 1991.

[39] B. Dhandapani and S. T. Oyama, "Gas phase ozone decomposition catalysts," *Applied Catalysis B: Environmental,* vol. 11, pp. 129-166, 1997.

[40] W. Li, G. Gibbs, and S. T. Oyama, "Mechanism of ozone decomposition on a manganese oxide catalyst. 1. In situ Raman spectroscopy and ab initio molecular orbital calculations," *Journal of the American Chemical Society,* vol. 120, pp. 9041-9046, 1998.

[41] W. Li and S. T. Oyama, "Mechanism of ozone decomposition on a manganese oxide catalyst. 2. Steady-state and transient kinetic studies," *Journal of the American Chemical Society,* vol. 120, pp. 9047-9052, 1998.

[42] H. Einaga, M. Harada, and S. Futamura, "Structural changes in alumina-supported manganese oxides during ozone decomposition," *Chemical physics letters,* vol. 408, pp. 377-380, 2005.

[43] R. Radhakrishnan, S. T. Oyama, Y. Ohminami, and K. Asakura, "Structure of MnO_x/Al_2O_3 catalyst: A study using EXAFS, in situ

laser Raman spectroscopy and ab initio calculations," *The Journal of Physical Chemistry B,* vol. 105, pp. 9067-9070, 2001.

[44] J. Jia, P. Zhang, and L. Chen, "Catalytic decomposition of gaseous ozone over manganese dioxides with different crystal structures," *Applied Catalysis B: Environmental,* vol. 189, pp. 210-218, 2016.

[45] T. Kameya and K. Urano, "Catalytic decomposition of ozone gas by a Pd impregnated MnO_2 catalyst," *Journal of environmental engineering,* vol. 128, pp. 286-292, 2002.

[46] J. Ma, C. Wang, and H. He, "Transition metal doped cryptomelane-type manganese oxide catalysts for ozone decomposition," *Applied Catalysis B: Environmental,* vol. 201, pp. 503-510, 2017.

[47] R. Radhakrishnan, S. T. Oyama, J. G. Chen, and K. Asakura, "Electron transfer effects in ozone decomposition on supported manganese oxide," *The Journal of Physical Chemistry B,* vol. 105, pp. 4245-4253, 2001.

[48] M. Setvín, U. Aschauer, P. Scheiber, Y.-F. Li, W. Hou, M. Schmid, A. Selloni, and U. Diebold, "Reaction of O_2 with subsurface oxygen vacancies on TiO_2 anatase (101)," *Science,* vol. 341, pp. 988-991, 2013.

[49] E. Rezaei, J. Soltan, and N. Chen, "Catalytic oxidation of toluene by ozone over alumina supported manganese oxides: Effect of catalyst loading," *Applied Catalysis B: Environmental,* vol. 136, pp. 239-247, 2013.

[50] E. Rezaei and J. Soltan, "EXAFS and kinetic study of MnO_x/γ-alumina in gas phase catalytic oxidation of toluene by ozone," *Applied Catalysis B: Environmental,* vol. 148, pp. 70-79, 2014.

[51] E. Rezaei and J. Soltan, "Low temperature oxidation of toluene by ozone over MnOx/γ-alumina and MnOx/MCM-41 catalysts," *Chemical engineering journal,* vol. 198, pp. 482-490, 2012.

[52] M. Hu, K. Hui, and K. Hui, "Role of graphene in MnO_2/graphene composite for catalytic ozonation of gaseous toluene," *Chemical Engineering Journal,* vol. 254, pp. 237-244, 2014.

[53] J. Li, H. Na, X. Zeng, T. Zhu, and Z. Liu, "In situ DRIFTS investigation for the oxidation of toluene by ozone over Mn/HZSM-5, Ag/HZSM-5 and Mn–Ag/HZSM-5 catalysts," *Applied Surface Science,* vol. 311, pp. 690-696, 2014.

[54] K. Sekiguchi, Y. Kurita, K. Sankoda, N. Namiki, F. Yasui, and H. Tamura, "Ozone Catalytic Oxidation of Gaseous Toluene over

MnO_2-Based Ozone Decomposition Catalysts Immobilized on a Nonwoven Fabric," *Aerosol and Air Quality Research,* vol. 17, pp. 2110-2118, 2017.

[55] L. Liping, Z. Jianguo, Y. Lixian, F. Mingli, W. Junliang, B. Huang, and Y. Daiqi, "Room temperature catalytic ozonation of toluene over MnO_2/Al_2O_3," *Chinese Journal of Catalysis,* vol. 32, pp. 904-916, 2011.

[56] K. Ramesh, L. Chen, F. Chen, Y. Liu, Z. Wang, and Y.-F. Han, "Re-investigating the CO oxidation mechanism over unsupported MnO, Mn_2O_3 and MnO_2 catalysts," *Catalysis Today,* vol. 131, pp. 477-482, 2008.

[57] S. Royer and D. Duprez, "Catalytic oxidation of carbon monoxide over transition metal oxides," *ChemCatChem,* vol. 3, pp. 24-65, 2011.

[58] L.-C. Wang, Q. Liu, X.-S. Huang, Y.-M. Liu, Y. Cao, and K.-N. Fan, "Gold nanoparticles supported on manganese oxides for low-temperature CO oxidation," *Applied Catalysis B: Environmental,* vol. 88, pp. 204-212, 2009.

[59] S. Imamura, Y. Tsuji, Y. Miyake, and T. Ito, "Cooperative action of palladium and manganese (III) oxide in the oxidation of carbon monoxide," *Journal of Catalysis,* vol. 151, pp. 279-284, 1995.

[60] S. Liang, F. Teng, G. Bulgan, R. Zong, and Y. Zhu, "Effect of phase structure of MnO_2 nanorod catalyst on the activity for CO oxidation," *The Journal of Physical Chemistry C,* vol. 112, pp. 5307-5315, 2008.

[61] X. Wang and Y. Li, "Selected-control hydrothermal synthesis of α-and β-MnO_2 single crystal nanowires," *Journal of the American Chemical Society,* vol. 124, pp. 2880-2881, 2002.

[62] X. Wang and Y. Li, "Synthesis and formation mechanism of manganese dioxide nanowires/nanorods," *Chemistry-A European Journal,* vol. 9, pp. 300-306, 2003.

[63] V. Iablokov, K. Frey, O. Geszti, and N. Kruse, "High catalytic activity in CO oxidation over MnO_x nanocrystals," *Catalysis letters,* vol. 134, pp. 210-216, 2010.

[64] A. Gervasini, G. Vezzoli, and V. Ragaini, "VOC removal by synergic effect of combustion catalyst and ozone," *Catalysis today,* vol. 29, pp. 449-455, 1996.

[65] H. T. Quoc An, T. P. Huu, T. Le Van, J. M. Cormier, and A. Khacef, "Application of atmospheric non thermal plasma-catalysis hybrid

system for air pollution control: Toluene removal," *Catalysis Today,* vol. 176, pp. 474-477, 2011.

[66] L. Ye, F. Feng, J. Liu, X. Tang, X. Zhang, Y. Huang, Z. Liu, and K. Yan, "Toluene decomposition by a two-stage hybrid plasma catalyst system in dry air," *IEEE Transactions on Plasma Science,* vol. 42, pp. 3529-3538, 2014.

[67] M. Magureanu, N. Mandache, E. Gaigneaux, C. Paun, and V. Parvulescu, "Toluene oxidation in a plasma-catalytic system," *Journal of applied physics,* vol. 99, pp. 123301-1-123301-7, 2006.

[68] J. Van Durme, J. Dewulf, K. Demeestere, C. Leys, and H. Van Langenhove, "Post-plasma catalytic technology for the removal of toluene from indoor air: Effect of humidity," *Applied Catalysis B: Environmental,* vol. 87, pp. 78-83, 2009.

[69] A. M. Harling, D. J. Glover, J. C. Whitehead, and K. Zhang, "The role of ozone in the plasma-catalytic destruction of environmental pollutants," *Applied Catalysis B: Environmental,* vol. 90, pp. 157-161, 2009.

[70] H. Grossmannova, D. Neirynck, and C. Leys, "Atmospheric discharge combined with Cu-Mn/Al_2O_3 catalyst unit for the removal of toluene," *Czechoslovak Journal of Physics,* vol. 56, pp. B1156-B1161, 2006.

[71] J. Van Durme, J. Dewulf, W. Sysmans, C. Leys, and H. Van Langenhove, "Efficient toluene abatement in indoor air by a plasma catalytic hybrid system," *Applied Catalysis B: Environmental,* vol. 74, pp. 161-169, 2007.

[72] Y. Huang, S. Dai, F. Feng, X. Zhang, Z. Liu, and K. Yan, "A comparison study of toluene removal by two-stage DBD-catalyst systems loading with MnO_x, $CeMnO_x$, and $CoMnO_x$," *Environmental Science and Pollution Research,* vol. 22, pp. 19240-19250, 2015.

[73] K. Hayashi, H. Yasui, M. Tanaka, S. Futamura, S. Kurita, and K. Aoyagi, "Temperature dependence of toluene decomposition behavior in the discharge–catalyst hybrid reactor," *IEEE Transactions on Industry Applications,* vol. 45, pp. 1553-1558, 2009.

[74] S. Delagrange, L. Pinard, and J.-M. Tatibouët, "Combination of a non-thermal plasma and a catalyst for toluene removal from air: Manganese based oxide catalysts," *Applied Catalysis B: Environmental,* vol. 68, pp. 92-98, 2006.

[75] X. Tang, F. Feng, L. Ye, X. Zhang, Y. Huang, Z. Liu, and K. Yan, "Removal of dilute VOCs in air by post-plasma catalysis over Ag-based composite oxide catalysts," *Catalysis today,* vol. 211, pp. 39-43, 2013.

[76] H. Huang, D. Ye, and X. Guan, "The simultaneous catalytic removal of VOCs and O_3 in a post-plasma," *Catalysis Today,* vol. 139, pp. 43-48, 2008.

[77] V. Demidyuk and J. C. Whitehead, "Influence of temperature on gas-phase toluene decomposition in plasma-catalytic system," *Plasma chemistry and plasma processing,* vol. 27, pp. 85-94, 2007.

[78] D. Chlala, J.-M. Giraudon, N. Nuns, C. Lancelot, R.-N. Vannier, M. Labaki, and J.-F. Lamonier, "Active Mn species well dispersed on Ca^{2+} enriched apatite for total oxidation of toluene," *Applied Catalysis B: Environmental,* vol. 184, pp. 87-95, 2016.

[79] I. Spasova, P. Nikolov, and D. Mehandjiev, "Ozone decomposition over alumina-supported copper, manganese and copper-manganese catalysts," *Ozone: Science and Engineering,* vol. 29, pp. 41-45, 2007.

[80] S. Vepřek, D. Cocke, S. Kehl, and H. Oswald, "Mechanism of the deactivation of Hopcalite catalysts studied by XPS, ISS, and other techniques," *Journal of Catalysis,* vol. 100, pp. 250-263, 1986.

[81] L. S. Puckhaber, H. Cheung, D. L. Cocke, and A. Clearfield, "Reactivity of copper manganese oxides," *Solid State Ionics,* vol. 32, pp. 206-213, 1989.

[82] W. Li, M. Zhuang, and J. Wang, "Catalytic combustion of toluene on Cu-Mn/MCM-41 catalysts: Influence of calcination temperature and operating conditions on the catalytic activity," *Catalysis Today,* vol. 137, pp. 340-344, 2008.

[83] X. Li, L. Wang, Q. Xia, Z. Liu, and Z. Li, "Catalytic oxidation of toluene over copper and manganese based catalysts: Effect of water vapor," *Catalysis Communications,* vol. 14, pp. 15-19, 2011.

[84] D. A. Aguilera, A. Perez, R. Molina, and S. Moreno, "Cu–Mn and Co–Mn catalysts synthesized from hydrotalcites and their use in the oxidation of VOCs," *Applied Catalysis B: Environmental,* vol. 104, pp. 144-150, 2011.

[85] W. Li, M. Zhuang, T. Xiao, and M. Green, "MCM-41 supported Cu− Mn catalysts for catalytic oxidation of toluene at low

temperatures," *The Journal of Physical Chemistry B,* vol. 110, pp. 21568-21571, 2006.

[86] S. Behar, P. Gonzalez, P. Agulhon, F. Quignard, and D. Świerczyński, "New synthesis of nanosized Cu–Mn spinels as efficient oxidation catalysts," *Catalysis today,* vol. 189, pp. 35-41, 2012.

[87] S. M. Saqer, D. I. Kondarides, and X. E. Verykios, "Catalytic oxidation of toluene over binary mixtures of copper, manganese and cerium oxides supported on γ-Al_2O_3," *Applied Catalysis B: Environmental,* vol. 103, pp. 275-286, 2011.

[88] M. Zimowska, A. Michalik-Zym, R. Janik, T. Machej, J. Gurgul, R. Socha, J. Podobiński, and E. Serwicka, "Catalytic combustion of toluene over mixed Cu–Mn oxides," *Catalysis Today,* vol. 119, pp. 321-326, 2007.

[89] Z. Ye, J.-M. Giraudon, N. Nuns, P. Simon, N. De Geyter, R. Morent, and J.-F. Lamonier, "Influence of the preparation method on the activity of copper-manganese oxides for toluene total oxidation," *Applied Catalysis B: Environmental,* vol. 223, pp. 154-166, 2018.

[90] Z. Lian, J. Ma, and H. He, "Decomposition of high-level ozone under high humidity over Mn–Fe catalyst: The influence of iron precursors," *Catalysis Communications,* vol. 59, pp. 156-160, 2015.

[91] A. Khacef, T. P. Huu, H. T. Quoc An, T. Le Van, and J.-M. Cormier, "Removal of Toluene in Air by Non Thermal Plasma-Catalysis Hybrid System," in *20th International Symposium of Plasma Chemistry*, 2011, pp. 1-4.

[92] J.-S. Chang, P. A. Lawless, and T. Yamamoto, "Corona discharge processes," *IEEE Transactions on plasma science,* vol. 19, pp. 1152-1166, 1991.

[93] J. Chang, K. Kostov, K. Urashima, T. Yamamoto, Y. Okayasu, T. Kato, T. Iwaizumi, and K. Yoshimura, "Removal of NF_3 from semiconductor process flue gases by tandem packed bed plasma-adsorbent hybrid systems," in *Industry Applications Conference, 1998. Thirty-Third IAS Annual Meeting. The 1998 IEEE*, 1998, pp. 1845-1852.

[94] S. K. Veerapandian, C. Leys, N. De Geyter, and R. Morent, "Abatement of VOCs Using Packed Bed Non-Thermal Plasma Reactors: A Review," *Catalysts,* vol. 7, p. 113, 2017.

[95] *IR Spectrum of Toluene*. Available: http://webbook.nist.gov/cgi/cbook.cgi?ID=C108883&Type=IR-SPEC&Index=1#IR-SPEC

[96] *IR Spectrum of CO_2*. Available: http://webbook.nist.gov/cgi/cbook.cgi?ID=C124389&Units=SI&Type=IR-SPEC&Index=1#IR-SPEC

[97] *IR Spectrum of CO*. Available: http://webbook.nist.gov/cgi/cbook.cgi?ID=C630080&Units=SI&Type=IR-SPEC&Index=1#IR-SPEC

[98] *IR Spectrum of TCE*. Available: http://webbook.nist.gov/cgi/cbook.cgi?ID=C79016&Units=SI&Type=IR-SPEC&Index=1#IR-SPEC

[99] *IR Spectrum of O_3*. Available: http://webbook.nist.gov/cgi/cbook.cgi?ID=C10028156&Units=SI&Mask=80#IR-Spec

[100] H. Einaga, A. Kiya, S. Yoshioka, and Y. Teraoka, "Catalytic properties of copper–manganese mixed oxides prepared by coprecipitation using tetramethylammonium hydroxide," *Catal. Sci. Technol.,* vol. 4, pp. 3713-3722, 2014.

[101] E. C. Njagi, C.-H. Chen, H. Genuino, H. Galindo, H. Huang, and S. L. Suib, "Total oxidation of CO at ambient temperature using copper manganese oxide catalysts prepared by a redox method," *Applied Catalysis B: Environmental,* vol. 99, pp. 103-110, 2010.

[102] D. Chlala, "Étude de l'ajout de métaux (Pt, Pd, Mn et Cu) sur hydroxyapatite: apport de la flexibilité du support dans l'oxydation catalytique totale du toluène," Lille 1, 2015.

[103] V. Santos, M. Pereira, J. Órfão, and J. Figueiredo, "Synthesis and characterization of manganese oxide catalysts for the total oxidation of ethyl acetate," *Topics in Catalysis,* vol. 52, pp. 470-481, 2009.

[104] "Product Safety Summary on Trichloroethylene," ed. Brussels, Belgium: European Chlorinated solvent association, 2012.

[105] Y. Wang, Y. Zhang, L. Su, X. Li, L. Duan, C. Wang, and T. Huang, "Hazardous air pollutant formation from pyrolysis of typical Chinese casting materials," *Environmental science & technology,* vol. 45, pp. 6539-6544, 2011.

[106] F.-Y. Yi, X.-D. Lin, S.-X. Chen, and X.-Q. Wei, "Adsorption of VOC on modified activated carbon fiber," *Journal of Porous Materials,* vol. 16, pp. 521-526, 2009.

[107] C. Kennes, E. R. Rene, and M. C. Veiga, "Bioprocesses for air pollution control," *Journal of Chemical Technology and Biotechnology,* vol. 84, pp. 1419-1436, 2009.
[108] K. Everaert and J. Baeyens, "Catalytic combustion of volatile organic compounds," *Journal of Hazardous Materials,* vol. 109, pp. 113-139, 2004.
[109] W.-B. LI and H. GONG, "Recent progress in the removal of volatile organic compounds by catalytic combustion," *Acta Physico-Chimica Sinica,* vol. 26, pp. 885-894, 2010.
[110] M. W. Reij, J. T. Keurentjes, and S. Hartmans, "Membrane bioreactors for waste gas treatment," *Journal of Biotechnology,* vol. 59, pp. 155-167, 1998.
[111] J. Degrève, K. Everaert, and J. Baeyens, "The use of gas membranes for VOC-air separations," *Filtration & separation,* vol. 38, pp. 48-54, 2001.
[112] C. Subrahmanyam, A. Renken, and L. Kiwi-Minsker, "Catalytic non-thermal plasma reactor for abatement of toluene," *Chemical Engineering Journal,* vol. 160, pp. 677-682, 2010.
[113] W. Liang, J. Li, J. Li, and Y. Jin, "Abatement of toluene from gas streams via ferro-electric packed bed dielectric barrier discharge plasma," *Journal of hazardous materials,* vol. 170, pp. 633-638, 2009.
[114] T. Yamamoto, K. Ramanathan, P. A. Lawless, D. S. Ensor, J. R. Newsome, N. Plaks, and G. H. Ramsey, "Control of volatile organic compounds by an ac energized ferroelectric pellet reactor and a pulsed corona reactor," *IEEE Transactions on Industry Applications,* vol. 28, pp. 528-534, 1992.
[115] F. Holzer, F. Kopinke, and U. Roland, "Influence of ferroelectric materials and catalysts on the performance of non-thermal plasma (NTP) for the removal of air pollutants," *Plasma chemistry and plasma processing,* vol. 25, pp. 595-611, 2005.
[116] A. Ogata, N. Shintani, K. Mizuno, S. Kushiyama, and T. Yamamoto, "Decomposition of benzene using a nonthermal plasma reactor packed with ferroelectric pellets," *IEEE Transactions on industry applications,* vol. 35, pp. 753-759, 1999.
[117] A. M. Vandenbroucke, M. T. N. Dinh, J.-M. Giraudon, R. Morent, N. De Geyter, J.-F. Lamonier, and C. Leys, "Qualitative by-product identification of plasma-assisted TCE abatement by mass spectrometry and Fourier-transform infrared

spectroscopy," *Plasma Chemistry and Plasma Processing,* vol. 31, p. 707, 2011.

[118] Z. Ye, C. Wang, Z. Shao, Q. Ye, Y. He, and Y. Shi, "A novel dielectric barrier discharge reactor with photocatalytic electrode based on sintered metal fibers for abatement of xylene," *J Hazard Mater,* vol. 241-242, pp. 216-23, Nov 30 2012.

[119] H. L. Chen, H. M. Lee, S. H. Chen, and M. B. Chang, "Review of packed-bed plasma reactor for ozone generation and air pollution control," *Industrial & Engineering Chemistry Research,* vol. 47, pp. 2122-2130, 2008.

[120] C. H. Lin and H. Bai, "Energy effectiveness of nonthermal plasma reactors for toluene vapor destruction," *Journal of Environmental Engineering,* vol. 127, pp. 648-654, 2001.

[121] C. L. Chang and T. S. Lin, "Decomposition of toluene and acetone in packed dielectric barrier discharge reactors," *Plasma Chemistry and Plasma Processing,* vol. 25, pp. 227-243, Jun 2005.

[122] H.-X. Ding, A.-M. Zhu, X.-F. Yang, C.-H. Li, and Y. Xu, "Removal of formaldehyde from gas streams via packed-bed dielectric barrier discharge plasmas," *Journal of Physics D: Applied Physics,* vol. 38, p. 4160, 2005.

[123] M. Schiorlin, C. Paradisi, R. Brandenburg, M. Schmidt, E. Marotta, A. Giardina, and R. Basner, *Pollutant Degradation in Gas Streams by means of Non-Thermal Plasmas*, 2015.

[124] C.-L. Chang, H. Bai, and S.-J. Lu, "Destruction of styrene in an air stream by packed dielectric barrier discharge reactors," *Plasma Chemistry and Plasma Processing,* vol. 25, pp. 641-657, 2005.

[125] V. Santos, M. Pereira, J. Órfão, and J. Figueiredo, "The role of lattice oxygen on the activity of manganese oxides towards the oxidation of volatile organic compounds," *Applied Catalysis B: Environmental,* vol. 99, pp. 353-363, 2010.

[126] C. Cellier, V. Ruaux, C. Lahousse, P. Grange, and E. M. Gaigneaux, "Extent of the participation of lattice oxygen from γ-MnO 2 in VOCs total oxidation: Influence of the VOCs nature," *Catalysis today,* vol. 117, pp. 350-355, 2006.

[127] S. C. Kim, "The catalytic oxidation of aromatic hydrocarbons over supported metal oxide," *Journal of hazardous materials,* vol. 91, pp. 285-299, 2002.

[128] G. S. P. Soylu, Z. Özçelik, and İ. Boz, "Total oxidation of toluene over metal oxides supported on a natural clinoptilolite-type

zeolite," *Chemical Engineering Journal,* vol. 162, pp. 380-387, 2010.

[129] G. S. Pozan, "Effect of support on the catalytic activity of manganese oxide catalyts for toluene combustion," *Journal of hazardous materials,* vol. 221, pp. 124-130, 2012.

[130] D. Chlala, J. M. Giraudon, N. Nuns, C. Lancelot, R.-N. Vannier, M. Labaki, and J. F. Lamonier, "Active Mn species well dispersed on Ca2+ enriched apatite for total oxidation of toluene," *Applied Catalysis B: Environmental,* vol. 184, pp. 87-95, 2016.

[131] R. Derwent, M. Jenkin, and S. Saunders, "Photochemical ozone creation potentials for a large number of reactive hydrocarbons under European conditions," *Atmospheric Environment,* vol. 30, pp. 181-199, 1996.

[132] R. G. Derwent, M. E. Jenkin, S. M. Saunders, and M. J. Pilling, "Photochemical ozone creation potentials for organic compounds in northwest Europe calculated with a master chemical mechanism," *Atmospheric environment,* vol. 32, pp. 2429-2441, 1998.

[133] A. B. Lamb, W. C. Bray, and J. Frazer, "The Removal of Carbon Monoxide from Air," *Industrial & Engineering Chemistry,* vol. 12, pp. 213-221, 1920.

[134] T. Biemelt, K. Wegner, J. Teichert, M. Lohe, J. Martin, J. Grothe, and S. Kaskel, "Hopcalite nanoparticle catalysts with high water vapour stability for catalytic oxidation of carbon monoxide," *Applied Catalysis B: Environmental,* vol. 184, pp. 208-215, 2016.

[135] M. Krämer, T. Schmidt, K. Stöwe, and W. Maier, "Structural and catalytic aspects of sol–gel derived copper manganese oxides as low-temperature CO oxidation catalyst," *Applied Catalysis A: General,* vol. 302, pp. 257-263, 2006.

[136] A. Marinoiu, M. Raceanu, C. Cobzaru, C. Teodorescu, D. Marinescu, A. Soare, and M. Varlam, "Low temperature CO retention using hopcalite catalyst for fuel cell applications," *Reaction Kinetics, Mechanisms and Catalysis,* vol. 112, pp. 37-50, 2014.

[137] H. Chen, X. Tong, and Y. Li, "Mesoporous Cu–Mn Hopcalite catalyst and its performance in low temperature ethylene combustion in a carbon dioxide stream," *Applied Catalysis A: General,* vol. 370, pp. 59-65, 2009.

[138] W. Li, W. Chu, M. Zhuang, and J. Hua, "Catalytic oxidation of toluene on Mn–containing mixed oxides prepared in reverse microemulsions," *Catalysis Today,* vol. 93, pp. 205-209, 2004.

[139] P. A. Wright, S. Natarajan, J. M. Thomas, and P. L. Gai-Boyes, "Mixed-metal amorphous and spinel phase oxidation catalysts: characterization by x-ray diffraction, x-ray absorption, electron microscopy, and catalytic studies of systems containing copper, cobalt, and manganese," *Chemistry of materials,* vol. 4, pp. 1053-1065, 1992.

[140] P. Porta, G. Moretti, M. Musicanti, and A. Nardella, "Copper-manganese mixed oxides: formation, characterization and reactivity under different conditions," *Solid state ionics,* vol. 63, pp. 257-267, 1993.

[141] J. L. Daniel P. Shoemaker, and Ram Seshadri, "Unraveling Atomic Positions in an Oxide Spinel with Two Jahn-Teller Ions: Local Structure Investigation of CuMn2O4," *J. AM. CHEM. SOC,* vol. 131, pp. 11450–11457, 2009.

[142] E. C. Njagi, C.-H. Chen, H. Genuino, H. Galindo, H. Huang, and S. L. Suib, "Total oxidation of CO at ambient temperature using copper manganese oxide catalysts prepared by a redox method," *Applied Catalysis B: Environmental,* vol. 99, pp. 103-110, 2010.

[143] V. H. Vu, E. Ndzebet, A. Kumar, D. Gilbert, W. C. Bushong, K. Ramaswami, and J. Scherer, "Copper-manganese mixed oxide cathode material for use in alkaline cells having high capacity," ed: Google Patents, 2010.

[144] Q. Liu, L.-C. Wang, M. Chen, Y.-M. Liu, Y. Cao, H.-Y. He, and K.-N. Fan, "Waste-free soft reactive grinding synthesis of high-surface-area copper–manganese spinel oxide catalysts highly effective for methanol steam reforming," *Catalysis Letters,* vol. 121, pp. 144-150, 2008.

[145] D. Rangappa, S. Ohara, M. Umetsu, T. Naka, and T. Adschiri, "Synthesis, characterization and organic modification of copper manganese oxide nanocrystals under supercritical water," *The Journal of Supercritical Fluids,* vol. 44, pp. 441-445, 2008.

[146] J. Papavasiliou, G. Avgouropoulos, and T. Ioannides, "In situ combustion synthesis of structured Cu-Ce-O and Cu-Mn-O catalysts for the production and purification of hydrogen," *Applied Catalysis B: Environmental,* vol. 66, pp. 168-174, 2006.

[147] L. H. Lash, J. W. Fisher, J. C. Lipscomb, and J. C. Parker, "Metabolism of trichloroethylene," *Environmental health perspectives,* vol. 108, p. 177, 2000.

[148] K. V. Kozlov, H. E. Wagner, R. Brandenburg, and P. Michel, "Spatio-temporally resolved spectroscopic diagnostics of the barrier discharge in air at atmospheric pressure," *Journal of Physics D-Applied Physics,* vol. 34, pp. 3164-3176, Nov 2001.

[149] U. Kogelschatz, B. Eliasson, and W. Egli, "Dielectric-barrier discharges. Principle and applications," *Le Journal de Physique IV,* vol. 7, pp. C4-47-C4-66, 1997.

[150] J. Mahoney, W. Zhu, V. S. Johnson, K. H. Becker, and J. L. Lopez, "Electrical and optical emission measurements of a capillary dielectric barrier discharge," *European Physical Journal D,* vol. 60, pp. 441-447, Dec 2010.

[151] J. L. Walsh, D.-X. Liu, F. Iza, M.-Z. Rong, and M. G. Kong, "Contrasting characteristics of sub-microsecond pulsed atmospheric air and atmospheric pressure helium–oxygen glow discharges," *Journal of Physics D: Applied Physics,* vol. 43, p. 032001, 2010.

[152] J. M. Williamson, P. Bletzinger, and B. N. Ganguly, "Gas temperature determination in a N2/Ar dielectric barrier discharge by diode-laser absorption spectroscopy and resolved plasma emission," *Journal of Physics D: Applied Physics,* vol. 37, p. 1658, 2004.

[153] T. Nozaki, Y. Unno, Y. Miyazaki, and K. Okazaki, "Optical diagnostics for determining gas temperature of reactive microdischarges in a methane-fed dielectric barrier discharge," *Journal of Physics D-Applied Physics,* vol. 34, pp. 2504-2511, Aug 21 2001.

[154] Z. Machala, M. Janda, K. Hensel, I. Jedlovsky, L. Lestinska, V. Foltin, V. Martisovits, and M. Morvova, "Emission spectroscopy of atmospheric pressure plasmas for bio-medical and environmental applications," *Journal of Molecular Spectroscopy,* vol. 243, pp. 194-201, Jun 2007.

[155] D. Liu, J. Niu, and N. Yu, "Optical emission characteristics of medium-to high-pressure N2 dielectric barrier discharge plasmas during surface modification of polymers," *Journal of Vacuum Science & Technology A: Vacuum, Surfaces, and Films,* vol. 29, p. 061506, 2011.

[156] A. S. Chiper, V. Aniţa, C. Agheorghiesei, V. Pohoaţa, M. Aniţa, and G. Popa, "Spectroscopic diagnostics for a DBD plasma in He/Air and He/N2 gas mixtures," *Plasma Processes and Polymers,* vol. 1, pp. 57-62, 2004.

[157] X. Tu, H. J. Gallon, and J. C. Whitehead, "Electrical and spectroscopic diagnostics of a single-stage plasma-catalysis system: effect of packing with TiO2," *Journal of Physics D-Applied Physics,* vol. 44, Dec 7 2011.

[158] N. Jidenko, E. Bourgeois, and J. Borra, "Temperature profiles in filamentary dielectric barrier discharges at atmospheric pressure," *Journal of physics D: applied physics,* vol. 43, p. 295203, 2010.

[159] J. Raud, M. Laan, and I. Jogi, "Rotational temperatures of N2 (C, 0) and OH (A, 0) as gas temperature estimates in the middle pressure Ar/O2 discharge," *Journal of Physics D: Applied Physics,* vol. 44, p. 345201, 2011.

[160] C.-H. Lin and H. Bai, "Energy-effectiveness of nonthermal plasma reactors for toluene vapor destruction," *Journal of environmental engineering,* vol. 127, pp. 648-654, 2001.

[161] M. Schiorlin, E. Marotta, M. Rea, and C. Paradisi, "Comparison of toluene removal in air at atmospheric conditions by different corona discharges," *Environmental science & technology,* vol. 43, pp. 9386-9392, 2009.

[162] M. Magureanu, N. Mandache, V. Parvulescu, C. Subrahmanyam, A. Renken, and L. Kiwi-Minsker, "Improved performance of non-thermal plasma reactor during decomposition of trichloroethylene: Optimization of the reactor geometry and introduction of catalytic electrode," *Applied Catalysis B: Environmental,* vol. 74, pp. 270-277, 2007.

[163] J. Coates, "Interpretation of infrared spectra, a practical approach," *Encyclopedia of analytical chemistry,* 2000.

[164] T. V. Ivanova, T. Hoder, M.-L. Kääriäinen, A. Komlev, R. Brandenburg, and D. C. Cameron, "Enhancement of Atmospheric Plasma Decomposition of Toluene Using Porous Dielectric Conformally Coated with Titanium Dioxide by Atomic Layer Deposition," *Science of Advanced Materials,* vol. 6, pp. 2098-2105, 2014.

[165] R. Morent and C. Leys, "Ozone generation in air by a DC-excited multi-pin-to-plane plasma source," *Ozone-Science & Engineering,* vol. 27, pp. 239-245, 2005.

[166] J. H. Chen and P. X. Wang, "Effect of relative humidity on electron distribution and ozone production by DC coronas in air," *Ieee Transactions on Plasma Science,* vol. 33, pp. 808-812, Apr 2005.
[167] W. Mista and R. Kacprzyk, "Decomposition of toluene using non-thermal plasma reactor at room temperature," *Catalysis Today,* vol. 137, pp. 345-349, 2008.
[168] S. Pekarek, "Effect of catalysts on dc corona discharge poisoning," *European Physical Journal D,* vol. 61, pp. 657-662, Feb 2011.
[169] A. Fridman, *Plasma chemistry*: Cambridge university press, 2008.
[170] J. Van Durme, J. Dewulf, W. Sysmans, C. Leys, and H. Van Langenhove, "Abatement and degradation pathways of toluene in indoor air by positive corona discharge," *Chemosphere,* vol. 68, pp. 1821-1829, 2007.
[171] S. Y. Lu, X. M. Sun, X. D. Li, J. H. Yan, and C. M. Du, "Decomposition of toluene in a rotating glidarc discharge reactor," *IEEE Transactions on Plasma Science,* vol. 40, pp. 2151-2156, 2012.
[172] H. B. Huang, D. Q. Ye, D. Y. C. Leung, F. D. Feng, and X. J. Guan, "Byproducts and pathways of toluene destruction via plasma-catalysis," *Journal of Molecular Catalysis a-Chemical,* vol. 336, pp. 87-93, Feb 14 2011.
[173] J. Pei, Y. Lu, and X. Yin, "Catalytic Decomposition of Ozone by CuO/MnO2-Performance, Kinetics and Application Analysis," *Procedia Engineering,* vol. 121, pp. 792-800, 2015.
[174] C. Jones, K. J. Cole, S. H. Taylor, M. J. Crudace, and G. J. Hutchings, "Copper manganese oxide catalysts for ambient temperature carbon monoxide oxidation: Effect of calcination on activity," *Journal of Molecular Catalysis A: Chemical,* vol. 305, pp. 121-124, 2009.
[175] Y.-I. Hasegawa, R.-U. Maki, M. Sano, and T. Miyake, "Preferential oxidation of CO on copper-containing manganese oxides," *Applied Catalysis A: General,* vol. 371, pp. 67-72, 2009.
[176] E. C. Njagi, H. C. Genuino, C. K. King'ondu, S. Dharmarathna, and S. L. Suib, "Catalytic oxidation of ethylene at low temperatures using porous copper manganese oxides," *Applied Catalysis A: General,* vol. 421-422, pp. 154-160, 2012.
[177] D. S. V. Koleva, 1 and D. Mehandjiev, "Formation of Copper–Manganese Oxides from CuxMn12x(HCOO)2á 2H2O Mixed

Crystals," *JOURNAL OF SOLID STATE CHEMISTRY,* vol. 133, pp. 416-422, 1997.

[178] A. M. Azad, A. Hedayati, M. Rydén, H. Leion, and T. Mattisson, "Examining the Cu–Mn–O spinel system as an oxygen carrier in chemical looping combustion," *Energy Technology,* vol. 1, pp. 59-69, 2013.

[179] F. Kapteijn, A. D. Vanlangeveld, J. A. Moulijn, A. Andreini, M. A. Vuurman, A. M. Turek, J.-M. Jehng, and I. E. Wachs, "Alumina-supported manganese oxide catalysts: I. Characterization: effect of precursor and loading," *Journal of Catalysis,* vol. 150, pp. 94-104, 1994.

[180] J. Papavasiliou, G. Avgouropoulos, and T. Ioannides, "Combined steam reforming of methanol over Cu–Mn spinel oxide catalysts," *Journal of Catalysis,* vol. 251, pp. 7-20, 2007.

[181] G. Avgouropoulos and T. Ioannides, "Selective CO oxidation over CuO-CeO 2 catalysts prepared via the urea–nitrate combustion method," *Applied Catalysis A: General,* vol. 244, pp. 155-167, 2003.

[182] A. S. Reddy, C. S. Gopinath, and S. Chilukuri, "Selective ortho-methylation of phenol with methanol over copper manganese mixed-oxide spinel catalysts," *Journal of Catalysis,* vol. 243, pp. 278-291, 2006.

[183] G. Fierro, S. Morpurgo, M. L. Jacono, M. Inversi, and I. Pettiti, "Preparation, characterisation and catalytic activity of CuZn-based manganites obtained from carbonate precursors," *Applied Catalysis A: General,* vol. 166, pp. 407-417, 1998.

[184] Y. Zhu, W. Zhou, Y. Chen, J. Yu, X. Xu, C. Su, M. O. Tadé, and Z. Shao, "Boosting oxygen reduction reaction activity of palladium by stabilizing its unusual oxidation states in perovskite," *Chemistry of Materials,* vol. 27, pp. 3048-3054, 2015.

[185] L. Liotta, M. Ousmane, G. Di Carlo, G. Pantaleo, G. Deganello, A. Boreave, and A. Giroir-Fendler, "Catalytic removal of toluene over Co3O4–CeO2 mixed oxide catalysts: comparison with Pt/Al2O3," *Catalysis letters,* vol. 127, pp. 270-276, 2009.

[186] S. C. Kim and W. G. Shim, "Properties and performance of Pd based catalysts for catalytic oxidation of volatile organic compounds," *Applied Catalysis B: Environmental,* vol. 92, pp. 429-436, 2009.

[187] S. M. Saqer, D. I. Kondarides, and X. E. Verykios, "Catalytic activity of supported platinum and metal oxide catalysts for

toluene oxidation," *Topics in Catalysis,* vol. 52, pp. 517-527, 2009.

[188] A. A. dos Santos, K. M. N. Lima, R. T. Figueiredo, S. M. da Silva Egues, and A. L. D. Ramos, "Toluene deep oxidation over noble metals, Copper and Vanadium Oxides," *Catalysis letters,* vol. 114, pp. 59-63, 2007.

[189] F. Diehl, J. Barbier, D. Duprez, I. Guibard, and G. Mabilon, "Catalytic oxidation of heavy hydrocarbons over Pt/Al 2 O 3. Influence of the structure of the molecule on its reactivity," *Applied Catalysis B: Environmental,* vol. 95, pp. 217-227, 2010.

[190] H. A. Dole, R. J. Isaifan, F. M. Sapountzi, L. Lizarraga, D. Aubert, A. Princivalle, P. Vernoux, and E. A. Baranova, "Low temperature toluene oxidation over Pt nanoparticles supported on yttria stabilized-zirconia," *Catalysis letters,* vol. 143, pp. 996-1002, 2013.

[191] Z. Abbasi, M. Haghighi, E. Fatehifar, and S. Saedy, "Synthesis and physicochemical characterizations of nanostructured Pt/Al 2 O 3–CeO 2 catalysts for total oxidation of VOCs," *Journal of hazardous materials,* vol. 186, pp. 1445-1454, 2011.

[192] K. Okumura, T. Kobayashi, H. Tanaka, and M. Niwa, "Toluene combustion over palladium supported on various metal oxide supports," *Applied Catalysis B: Environmental,* vol. 44, pp. 325-331, 2003.

[193] S. C. Kim, H. Y. Jung, J. W. Nah, and Y. Park, "Complete Oxidation of Toluene Over Supported Palladium Catalysts: Effect of Support," *Journal of Nanoscience and Nanotechnology,* vol. 16, pp. 4638-4642, 2016.

[194] Y. Liao, L. Jia, R. Chen, O. Gu, M. Sakurai, H. Kameyama, L. Zhou, H. Ma, and Y. Guo, "Charcoal-supported catalyst with enhanced thermal-stability for the catalytic combustion of volatile organic compounds," *Applied Catalysis A: General,* vol. 522, pp. 32-39, 2016.

[195] Y. Takamitsu, S. Yoshida, W. Kobayashi, H. Ogawa, and T. Sano, "Combustion of volatile organic compounds over composite catalyst of Pt/γ-Al2O3 and beta zeolite," *Journal of Environmental Science and Health, Part A,* vol. 48, pp. 667-674, 2013.

[196] H. Yang, J. Deng, Y. Liu, S. Xie, P. Xu, and H. Dai, "Pt/Co 3 O 4/3DOM Al 2 O 3: Highly effective catalysts for toluene

combustion," *Chinese Journal of Catalysis,* vol. 37, pp. 934-946, 2016.

[197] D. Evans, L. A. Rosocha, G. K. Anderson, J. J. Coogan, and M. J. Kushner, "Plasma remediation of trichloroethylene in silent discharge plasmas," *Journal of applied physics,* vol. 74, pp. 5378-5386, 1993.

[198] K. Urashima and J.-S. Chang, "Removal of volatile organic compounds from air streams and industrial flue gases by non-thermal plasma technology," *IEEE Transactions on Dielectrics and Electrical Insulation,* vol. 7, pp. 602-614, 2000.

[199] A. M. Vandenbroucke, R. Aerts, W. Van Gaens, N. De Geyter, C. Leys, R. Morent, and A. Bogaerts, "Modeling and Experimental Study of Trichloroethylene Abatement with a Negative Direct Current Corona Discharge," *Plasma Chemistry and Plasma Processing,* vol. 35, pp. 217-230, 2015.

[200] S. S. Papdullo RF, Kincaid L et al., "Survey of Trichloroethylene Emission Sources," E. P. A. Office of Air Quality Planning and Standards, Ed., ed. Research Triangle Park, 1985.

[201] H.-H. Kim, Y. Teramoto, N. Negishi, and A. Ogata, "A multidisciplinary approach to understand the interactions of nonthermal plasma and catalyst: a review," *Catalysis Today,* vol. 256, pp. 13-22, 2015.

[202] H. Einaga, N. Maeda, S. Yamamoto, and Y. Teraoka, "Catalytic properties of copper-manganese mixed oxides supported on SiO 2 for benzene oxidation with ozone," *Catalysis Today,* vol. 245, pp. 22-27, 2015.

[203] C. Jones, K. J. Cole, S. H. Taylor, M. J. Crudace, and G. J. Hutchings, "Copper manganese oxide catalysts for ambient temperature carbon monoxide oxidation: Effect of calcination on activity," *Journal of Molecular Catalysis A: Chemical,* vol. 305, pp. 121-124, 2009.

[204] J. K. Rice, J. R. Wyatt, and L. Pasternack, "Selective catalytic activity toward hydrofluorocarbon refrigerants in mixed oxides of manganese and copper," *Applied Catalysis B: Environmental,* vol. 24, pp. 107-120, 2000.

[205] J. Belkouch, A. Ould-Dris, and B. Taouk, "Removal of hazardous chlorinated VOCs over Mn–Cu mixed oxide based catalyst," *Journal of hazardous materials,* vol. 169, pp. 758-765, 2009.

[206] A. Vandenbroucke, R. Morent, N. De Geyter, M. Tuan, N. Dinh, G. Jean-Marc, L. Jean-Francois, and C. Leys, "Plasma-catalytic

decomposition of TCE," *International Journal of Plasma Environmental Science & Technology,* vol. 4, 2010.

[207] A. M. Vandenbroucke, M. N. Dinh, N. Nuns, J.-M. Giraudon, N. De Geyter, C. Leys, J.-F. Lamonier, and R. Morent, "Combination of non-thermal plasma and Pd/LaMnO 3 for dilute trichloroethylene abatement," *Chemical Engineering Journal,* vol. 283, pp. 668-675, 2016.

[208] Y. Nakagawa, R. Ono, and T. Oda, "Relationship between TCE nonthermal decomposition and OH radical behavior observed by LIF," in *Industry Applications Society Annual Meeting, 2013 IEEE*, 2013, pp. 1-5.

[209] O. Bertrand, G. Weber, S. Maure, V. Bernardet, J. Bellat, and C. Paulin, "Spectroscopic signatures of VOC physisorption on microporous solids. Application for trichloroethylene and tetrachloroethylene adsorption on MFI zeolites," *The Journal of Physical Chemistry B,* vol. 109, pp. 13312-13321, 2005.

[210] R. Cucciniello, A. Intiso, S. Castiglione, A. Genga, A. Proto, and F. Rossi, "Total oxidation of trichloroethylene over mayenite (Ca 12 Al 14 O 33) catalyst," *Applied Catalysis B: Environmental,* vol. 204, pp. 167-172, 2017.

[211] H. Li, G. Lu, Q. Dai, Y. Wang, Y. Guo, and Y. Guo, "Efficient low-temperature catalytic combustion of trichloroethylene over flower-like mesoporous Mn-doped CeO 2 microspheres," *Applied Catalysis B: Environmental,* vol. 102, pp. 475-483, 2011.

[212] N. Blanch-Raga, A. E. Palomares, J. Martínez-Triguero, M. Puche, G. Fetter, and P. Bosch, "The oxidation of trichloroethylene over different mixed oxides derived from hydrotalcites," *Applied Catalysis B: Environmental,* vol. 160, pp. 129-134, 2014.

[213] R. López-Fonseca, J. Gutiérrez-Ortiz, M. Gutiérrez-Ortiz, and J. González-Velasco, "Dealuminated Y zeolites for destruction of chlorinated volatile organic compounds," *Journal of Catalysis,* vol. 209, pp. 145-150, 2002.

[214] M. Romero-Sáez, D. Divakar, A. Aranzabal, J. González-Velasco, and J. González-Marcos, "Catalytic oxidation of trichloroethylene over Fe-ZSM-5: Influence of the preparation method on the iron species and the catalytic behavior," *Applied Catalysis B: Environmental,* vol. 180, pp. 210-218, 2016.

[215] N. Blanch-Raga, A. Palomares, J. Martínez-Triguero, and S. Valencia, "Cu and Co modified beta zeolite catalysts for the

trichloroethylene oxidation," *Applied Catalysis B: Environmental,* vol. 187, pp. 90-97, 2016.

[216] D. Divakar, M. Romero-Sáez, B. Pereda-Ayo, A. Aranzabal, J. A. González-Marcos, and J. R. González-Velasco, "Catalytic oxidation of trichloroethylene over Fe-zeolites," *Catalysis today,* vol. 176, pp. 357-360, 2011.

[217] J. González-Velasco, A. Aranzabal, J. Gutiérrez-Ortiz, R. López-Fonseca, and M. Gutiérrez-Ortiz, "Activity and product distribution of alumina supported platinum and palladium catalysts in the gas-phase oxidative decomposition of chlorinated hydrocarbons," *Applied Catalysis B: Environmental,* vol. 19, pp. 189-197, 1998.

[218] D.-C. Kim and S.-K. Ihm, "Application of spinel-type cobalt chromite as a novel catalyst for combustion of chlorinated organic pollutants," *Environmental science & technology,* vol. 35, pp. 222-226, 2001.

[219] J. Corella, J. M. Toledo, and A. M. Padilla, "On the selection of the catalyst among the commercial platinum-based ones for total oxidation of some chlorinated hydrocarbons," *Applied Catalysis B: Environmental,* vol. 27, pp. 243-256, 2000.

[220] B. Mendyka, A. Musialik-Piotrowska, and K. Syczewska, "Effect of chlorine compounds on the deactivation of platinum catalysts," *catalysis Today,* vol. 11, pp. 597-610, 1992.

[221] M. N. Dinh, J.-M. Giraudon, A. Vandenbroucke, R. Morent, N. De Geyter, and J.-F. Lamonier, "Post plasma-catalysis for total oxidation of trichloroethylene over Ce–Mn based oxides synthesized by a modified “redox-precipitation route”," *Applied Catalysis B: Environmental,* vol. 172, pp. 65-72, 2015.

[222] R. Morent and C. Leys, "Ozone generation in air by a DC-excited multi-pin-to-plane plasma source," *Ozone: science & engineering,* vol. 27, pp. 239-245, 2005.

[223] B. Eliasson, M. Hirth, and U. Kogelschatz, "Ozone synthesis from oxygen in dielectric barrier discharges," *Journal of Physics D: Applied Physics,* vol. 20, p. 1421, 1987.

[224] M. N. Dinh, J.-M. Giraudon, J.-F. Lamonier, A. Vandenbroucke, N. De Geyter, C. Leys, and R. Morent, "Plasma-catalysis of Low TCE Concentration in air Using LaMnO 3+ δ as Catalyst," *Applied Catalysis B: Environmental,* vol. 147, pp. 904-911, 2014.

[225] M. N. Dinh, J.-M. Giraudon, A. Vandenbroucke, R. Morent, N. De Geyter, and J.-F. Lamonier, "Manganese oxide octahedral

molecular sieve K-OMS-2 as catalyst in post plasma-catalysis for trichloroethylene degradation in humid air," *Journal of hazardous materials,* vol. 314, pp. 88-94, 2016.